UNIVERSITY OF SOUTHAMPTON

FACULTY OF ENGINEERING AND APPLIED SCIENCES

INSTITUTE OF SOUND AND VIBRATION RESEARCH

ACTIVE STRUCTURAL ACOUSTIC CONTROL SMART PANEL WITH SMALL SCALE PROOF MASS ACTUATORS

by

Cristóbal González Díaz

A thesis submitted for the award of
Doctor of Philosophy

December 2007

Mi trabajo esta dedicado a mi tía Nati, siempre me dio grandes consejos, incluso ahora desde arriba, se que lo esta haciendo.

UNIVERSITY OF SOUTHAMPTON

ABSTRACT

FACULTY OF ENGINEERING AND APPLIED SCIENCE

INSTITUTE OF SOUND AND VIBRATION RESEARCH

Doctor of Philosophy

ACTIVE STRUCTURAL ACOUSTIC CONTROL SMART PANEL WITH SMALL
SCALE PROOF MASS ACTUATORS

by Cristóbal González Díaz

This thesis presents a comprehensive study of decentralised feedback control on a smart panel with electrodynamic proof mass actuators and velocity sensors at their footprints. The aim is to provide guidance for the design of light, simple, robust and low cost, control units which can be attached in large numbers to flexible structures in order to control their spatially averaged response and sound radiation at low audio-frequencies.

The first part of the thesis is focused on the identification of simple and effective single channel feedback control laws. In particular the stability properties and control performance produced by Proportional, Integral, Derivative, PI, PD, PID feedback control laws are assessed with reference to two simple problems where a single degrees of freedom system is controlled by an ideal reactive force actuator and by a practical proof mass actuator.

Following this introductory study, the implementation of decentralised feedback control on a smart panel with five control units using proof mass electrodynamic actuators is investigated for the best two cases of Proportional and PID control. In parallel the practical design of small scale control units is explored. In particular the scaling of the stability and control performance properties of a single control unit that implements proportional control is examined using a stability–control formula.

The final part of the thesis presents the stability and control performance tests carried out on a single control unit and on five decentralised control units. For the multiple channel control case, the reductions of the spatially averaged vibration measured with a laser vibrometer and the reduction of the total sound power radiation measured in an anechoic room are presented.

TABLE OF CONTENTS

LIST OF ILLUSTRATIONS

LIST OF TABLES

LIST OF SYMBOLS

Abbreviations

j imaginary unit ($=\sqrt{-1}$)

N number of considered mode shapes

n index of mode shape

$\mathbf{I}$ identity matrix

μ_0 $4\pi10^{-7}\text{Hm}^{-1}$

π ~3.1415926535, ratio of circumference to diameter of a circle

g 9.81ms^{-2}, gravity constant

Parameters

$\omega_{0,i}$	fundamental resonance of the inertial actuators	[rad s^{-1}]
$f_{n,i}$	natural frequency of the actuators	[Hz]
ω	circular frequency	[rad s^{-1}]
ω_n	nth natural frequency of the plate	[rad s^{-1}]
$\phi_n(x,y)$	nth mode shape of the plate evaluated at position x, y	[-]
$\boldsymbol{\phi}(x,y)$	row vector with the amplitudes of the modes at position x, y	[-]
ρ_s	mass density of the plate	[kg m^{-3}]
Λ	modal normalization factor	[kg]
η_s	loss factor of the plate	[-]
l_x	plate length	[m]
l_y	plate width	[m]
h_s	plate thickness	[m]
x_p	x coordinate of primary force position	[m]
y_p	y coordinate of primary force position	[m]
x_{c1}	x coordinate of control system 1	[m]
y_{c1}	y coordinate of control system 1	[m]
x_{c2}	x coordinate of control system 2	[m]
y_{c2}	y coordinate of control system 2	[m]
x_{c3}	x coordinate of control system 3	[m]
y_{c3}	y coordinate of control system 3	[m]
x_{c4}	x coordinate of control system 4	[m]
y_{c4}	y coordinate of control system 4	[m]

x_{c5}	x coordinate of control system 5	[m]
y_{c5}	y coordinate of control system 5	[m]
E_s	Young's modulus of plate material	[N m^{-2}]
v_s	Poisson's ratio	[-]
m_i	actuators moving mass	[kg]
$m_{b,i}$	actuators housing mass	[kg]
ψ_i	actuators electrodynamic transducer coefficient of the coil	[N A^{-1}]
k_i	actuators suspension stiffness coefficient	[N m^{-1}]
c_i	actuators viscous damping coefficient	[N s m^{-1}]
$R_{e,i}$	actuators electrical resistance of the driving coil	[Ω]
$L_{e,i}$	actuators electrical self-inductance of the driving coil	[H]
k_P	proportional control constant	[-]
k_I	integral control constant	[-]
k_D	derivative control constant	[-]
g	feedback gain	[various]
$g_{I,max}$	max control gain for the current-driven	[various]
$g_{U,max}$	max control gain for the voltage-driven	[various]
$\mathbf{H}$	diagonal matrix with the feedback control function	[various]
$\varPsi_i$	transducer coefficient of the coil	[N A^{-1}]
$\boldsymbol{\Psi}$	diagonal matrix with the transducer coefficients $\varPsi_i$	[N A^{-1}… N A^{-1}]
T	total kinetic energy	[J]
d	actuator stroke	[m]
B_{go}	magnetic flux density at the outer diameter of the air gap	[Wb m^{-2}]
B_{gi}	magnetic flux density at the inner diameter of the air gap	[Wb m^{-2}]
B_w	magnetic flux density in the outer wall of the yoke	[Wb m^{-2}]
B_m	magnetic flux density in the permanent magnet	[Wb m^{-2}]
A_i	diameter of the hole in the permanent magnet	[m]
A_d	diameter of the permanent magnet	[m]
b	height of the permanent magnet	[m]
s	air gap width	[m]
h_g	air gap height	[m]
h_{gl}	height of the lower yoke	[m]
B_r	remanence of the permanent magnet	[Wb m^{-2}]
H_l	coercivity of the permanent magnet	[A m^{-1}]
p	configuration factor of magnetic circuit	[-]
q	shape factor of magnetic circuit	[-]

ρ_{wi}	electric resistivity of coil wire	[V / (Am)]
P	electrical power dissipated in electrodynamic actuator	[W]
B_g	magnetic flux density in the air gap	[Wb m^{-2}]

Phasors

f_p	primary excitation force	[N]
f_{ai}	secondary excitation force	[N]
$\mathbf{f}_a$	secondary excitation force vector with $f_{a1}\ldots f_{a5}$	[N…N]
$\dot{w}_{cr}$	transverse velocity at the error control position	[m s^{-1}]
$\dot{\mathbf{w}}_c$	transverse velocity vector with $\dot{w}_{c1}\ldots\dot{w}_{c5}$	[m s^{-1}…m s^{-1}]
$\dot{w}_{m,i}$	transverse velocity of the proof-mass	[m s^{-1}]
$\dot{\mathbf{w}}_m$	vector with the transverse proof-mass velocities $\dot{w}_{m1}\ldots\dot{w}_{m5}$	[m s^{-1}…m s^{-1}]
f_{mi}	force between the proof-mass and the suspension spring	[N]
$\mathbf{f}_m$	vector with the forces between the proof-masses and the suspensions springs	[N…N]
$\dot{\mathbf{w}}$	column vector with components $\dot{\mathbf{w}}_c$ and $\dot{\mathbf{w}}_m$	[m s^{-1}…m s^{-1}]
$\mathbf{f}$	column vector with components $\mathbf{f}_a$ and $\mathbf{f}_m$	[N…N]
$f_{c,i}$	reactive forces generated by the linear electro-dynamic motor	[N]
$\mathbf{f}_c$	column vector with the reactive forces $f_{c1}\ldots f_{c5}$	[N…N]
$I_{c,i}$	electrical current in the coil of the ith actuators	[A]
$\mathbf{I}_c$	column vector with five currents in the coils	[A…A]
$U_{s,i}$	electrical driving voltage	[V]
$\mathbf{U}_c$	column vector with the five driving voltage	[V…V]

Impedances and mobilities

$Y_{cp,r}$	transfer mobility of the plate between primary and secondary Actuators	[m s^{-1} / N]
$Y_{cc,r}$	point mobility of the plate at the position of the secondary actuators	[m s^{-1} / N]
$\mathbf{Y}_{cp}$	matrix with the transfer mobility of the plate between primary and secondary Actuators	[m s^{-1} / N]
$\mathbf{Y}_{cc}$	matrix with the point mobility of the plate at the position of the secondary actuators [m s^{-1} / N]	

$Y_{m,ii}$	mobility of the proof-mass	[m s^{-1} / N]
$\mathbf{Y}_m$	matrix with the mobilities of the proof-mass	[m s^{-1}/N…ms^{-1}/N]
$\mathbf{Y}_c$	diagonal matrix with components $\mathbf{Y}_{cc}$ and $\mathbf{Y}_m$	[m s^{-1} / N … m s^{-1} / N]
$\mathbf{Y}_p$	column vector with components $\mathbf{Y}_{cp}$ and $\mathbf{0}$	[m s^{-1} / N … m s^{-1} / N]
$\mathbf{V}$	column vector with components $\mathbf{I}^{5\text{x}5}$ and $-\mathbf{I}^{5\text{x}5}$	
$Z_{s,ii}$	impedance of the spring-damper	[N s m^{-1}]
$\mathbf{Z}_s$	diagonal matrix with the impedances of the springs-damper	[N s m^{-1}]
$Z_{Act,ii}$	impedance of the base mass	[N s m^{-1}]
$\mathbf{Z}_{Act}$	diagonal matrix with the impedance of the base mass	[N s m^{-1}]
$\mathbf{Z}$	square matrix with impedance components	[N s m^{-1}]
$Z_{e,ii}$	electrical impedance of the actuator driving coil	[V / A]
$\mathbf{Z}_e$	diagonal matrix with the electrical impedances of the coils	[V/A…]

ACKNOWLEDGEMENTS

También es necesario dar las gracias a las cinco más importantes personas de este mundo, mis padres y hermanos. Sin su amor y su apoyo financiero durante mis estudios, no habría tenido la oportunidad de continuar mi educación. Gracias a Prisci, Pilar, Mariano, Olga y Pili, y mi familia entera.

Quería agradecer a mi familia adoptiva parisina todo su apoyo, sin ellos no habría sido posible haber llegado tan lejos como he llegado. Gracias a Jesús, Manu Blasco, Octavio, Sara y todos los amigos que allí conocí… incluso a aquellos que casi arruinan mi carrera profesional… gracias David Putero, Alberto Putero, Manu Climent, Fernando y todos los demás.

1   INTRODUCTION

In many engineering systems it is important to control air-borne and structure-borne sound radiation by partitions in order to prevent discomfort. In particular, vibration of panels and shell structures may generate high levels of interior noise in transportation vehicles such as aircrafts, helicopters, cars, trains, etc [1-3]. The background of this study is the control of vibration of thin panels in order to avoid excessive vibration and sound radiation levels. Vibration and sound radiation control can be achieved with passive means such as mass, damping and stiffness treatments applied on the radiating structure [4,5]. In general, these methods have been proved to be efficient in the high audio frequency range. However, they are quite bulky and tend to be less effective in the low audio frequency range [6], where the mechanical responses of structures are characterised by well–separated resonances [7,8]. In order to control low frequency vibration and sound radiation, active control methods have been considered [7,9,10].

'Smart panels' are adaptive structures with sensor and actuator transducers directed by a controller capable of modifying response of the structure in presence of time-varying environmental and operational conditions [11].

This thesis is concerned with the study of a smart panel with decentralised feedback control units using electrodynamic proof mass actuators with a velocity sensors located at their footprints. The feedback control gains are tuned in such a way as to reduce the spatially mean vibration and the sound radiation at low audio frequencies where the response and sound radiation are controlled by lightly damped resonances of the panel. In particular this thesis summarises a comprehensive study of Single Input Single Output (SISO) and Multiple input multiple output (MIMO) active feedback control systems using electrodynamics proof mass actuators mounted on a rectangular panel. The stability and control effects produced by basic feedback control laws such as Proportional, Integral, Derivative and combinations of the three (i.e. PI, PD, PID) are revised. The aim is to identify simple feedback architectures that guarantees stable and robust feedback loops which produces good reductions of vibration and sound radiation in broad band terms. The dynamic response of the proof mass actuator is analysed in great details. In particular the stability and control performance effects produced by miniaturisation of the actuators is

analysed using scaling laws applied to a 'stability-performance' formula specifically derived for this study.

1.1   Short review of Active control of sound and vibration

Frequently both passive and active systems are used together to reduce vibration and sound radiation. Active control essentially tries to eliminate sound or vibration components by adding the exact opposite sound or vibration. The phase describes the relative position of the wave in its rising and falling cycle. If two waves are in phase, they rise and fall together, whilst if they are exactly out of phase, one is rises as the other falls, and so they cancel out. An active control system can alter the amplitude of the control waves to ensure that the primary wave is cancelled. This is usually achieved by monitoring the result of both waves together and adapting the controlled waveform to reduce the total amplitude until cancellation is achieved. The waveforms may represent the acoustic pressure variations in a duct or enclosure, or the displacement of a vibrating structure. The principle of active control of sound and vibration is not new. It was first introduced by Lueg (1936) [12] in a patent as is shown in the Figure 1.1.
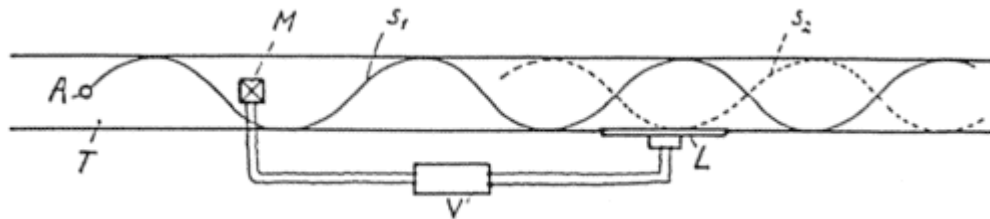
Figure 1.1: *Illustration from active control patent given to Paul Lueg in 1936.*

However it took about two decades before the first single-channel analogue control system was built [13,14]. The wider application of active control and the development of systems with many microphones and many loudspeakers have been made possible by the development of integrated circuits, which implement Digital Signal Processing (DSP) algorithms, such as those used in active control [15-17].

During the last twenty years much progress has been made in the design and development of both digital and analogue active control of sound and vibration. Several control schemas have been proposed which can be divided into two principal families: feed-forward and feedback control systems [9]. A brief review of the two approaches is presented below with reference to active vibration control problems

1.2 Feedback versus Feedforward control

Feed-forward control systems require a reference signal well correlated to the disturbance to be controlled. Thus they normally provide good control effects for tonal disturbances that can be easily characterised far in advance [15,18].

$r(\omega_o)$ $s(\omega_o)$

$-H(\omega_o)$

Primary source with
reference sensor
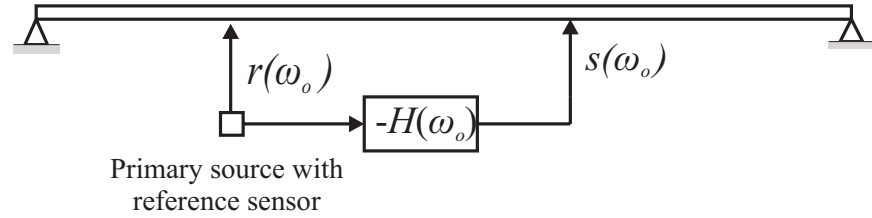
Figure 1.2: *Scheme of a Feed-forward control system.*

As schematically shown in the Figure 1.2, the reference signal, $r(\omega_o)$, is detected by the primary source and used to obtain the signal $s(\omega_o)$ that drives the control actuator.

For random, wide-band disturbances, feedback control schemes should be utilized. The implementation of feedback control system does not require a reference signal. These systems can provide good control performance regardless of the type of disturbance to be controlled, provided the sensor and actuator transducers are collocated and dual [11,19]. Collocation is a geometrical characteristic where point sensors and actuators are placed in the same position on the structure. Duality is a physical property where the actuator and sensor excite and detect the vibrations of a structure in the same manner.

If the sensor-actuator transducers are collocated and dual then the real part of their frequency response function is bound to be positive real, so that large feedback control gains can be implemented with no stability problems [7,11,19]. Therefore most of the work carried out by scientist is focused on the design of collocated and dual sensor-actuator pairs so that a relatively simple feedback controller which is unconditionally stable could be implemented. If the sensor-actuator transducers are not collocated and dual then only a limited range of control could be implemented in order to guarantee stability and this leads to a reduced performance of the system. For this reason, different control functions such as the so-called 'proportional', 'integral' and 'derivative' feedback laws could be used in order to improve the control performances of the control systems. If a collocated velocity sensor and a force actuator is assumed to be used, these four control functions synthesise an 'active damper', an 'active stiffness', an 'active mass' respectively.
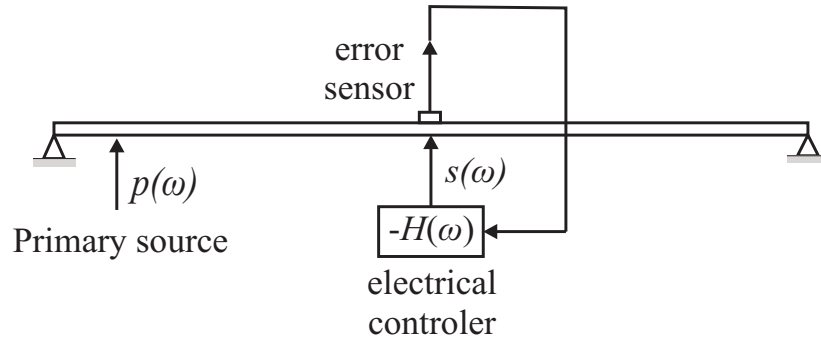
Figure 1.3: *Scheme of a feedback control system.*

The construction of distributed pairs of collocated and dual sensor-actuator transducer is not an easy task. One of the most common ways is by using the same type of transducers and by locating the two transducers in the same position.

1.3   Decentralised versus Centralised control

Feedback control systems for vibro-acoustic control can be classified in three categories:

a) Multiple Input Multiple Output (MIMO) systems with fully coupled arrays of error sensor and actuators,

b) Decentralised MIMO control schemes with arrays of independent sensor–actuator pairs, and

c) Single Input Single Output (SISO) active control schemes, using distributed sensor–actuator pairs [7].

Fully coupled MIMO systems are difficult to implement in practice, since a reliable model of the response functions between all sensors and actuators is required by the controller [11,19]. Moreover they require a lot of cabling to connect all sensors and actuators to the controller. As a result the system tends to be heavy, costly and requires a lot of maintenance. Finally centralised controllers are not robust systems since they would not work properly if one sensor or actuator fails.

MIMO decentralised control systems have been shown to give good control performances which are comparable to those that would be obtained from an ideal fully coupled MIMO control systems [20-23]. The implementation of a decentralised MIMO system is much simpler than that of fully coupled systems, since simple SISO loops need to be implemented. Balas [24] has shown that, provided the sensor–actuator pairs are dual and collocated [25,26], the decentralised MIMO system is bound to be stable if direct velocity

control is implemented. Therefore, the main issue of decentralised MIMO control is concerned with the design of collocated and dual sensor–actuator pairs [7]. When decentralised velocity feedback loops are implemented in such a way as to generate active damping, both the frequency average vibration and sound radiation of the structure are reduced, provided an optimal gain is implemented such that the damping action is maximised without pinning the structure at the control positions [27]. The optimally tuned active dampers reduce the amplitudes of the well separated low frequency resonances of the structure and thus the frequency averaged vibration and sound radiation at low frequencies. Previous work [28] has shown that, to produce the best performances, there is no need of fine tuning of the control gains. Also, when large arrays of control units are used, there is no need to specially position the control systems. The desired active damping effect will be generated provided the units are evenly spread over the whole surface of the structure to be controlled. These properties make decentralised control a very appealing and robust approach where the focus is just on the design of simple and effective feedback control units using closely located sensor–actuator pairs.

In principle, SISO feedback control systems using distributed sensor–actuator pairs specifically designed to minimize the most efficient radiation modes of the radiating structure [29] form the simplest and most convenient solution for active structural acoustic control. However, they normally require strain transducers, such as piezoelectric transducers, which cannot be easily used to form matched and collocated sensors and actuator pairs that guarantee unconditionally stable feedback control loops [30].

In conclusion, decentralised MIMO systems offer a good compromise between the fully coupled MIMO and the distributed transducers SISO control systems. The main issue of this strategy is the design of small collocated and dual sensor-actuator pairs. The purpose of this thesis is to discuss the design of a light, simple, low cost and robust feedback active control unit to be used in a decentralised MIMO control system arranged on a thin panel in order to control both its vibration and sound radiation. The feedback control unit consists of a proof-mass force actuator with a velocity sensor at its base which implement basic feedback control laws that does not need complex electronic systems to be implemented.

1.4 Smart panels for Active Structural Acoustic Control (ASAC)

As schematically shown Figure 1.4 in Active Structural Acoustic Control (ASAC) trough partitions, structural sensors and actuators are closely attached or even integrated into the walls in order to modify or control the vibration of the partitions and reduce the sound transmission [31]. Most of this research was motivated by the reduction of air-borne or structure-borne noise transmission of the fuselage walls or marine hulls in aerospace and naval applications [1-3,32,33]. The first ASAC systems were built using adaptive feed-forward control. In this case a set of error sensors was required for the detection of the total sound power radiated to be minimised. Thus, although the actuators were integrated into the walls, the error signal was taken from the acoustic measurements in the space under acoustic control. ASAC systems tend to be most effective at relatively low frequency where the first radiation mode of the structure under control [7], its volume velocity equivalent, produces most of the sound radiation. Thus, the output of just one error sensor can provide a good estimate of the total sound radiation by a panel. In this way a compact smart panel with both structural actuators and structural sensors can be developed to control the structure-borne and air-borne noise radiated. The great advantage of this system is that it does not require to locate sensor and actuator transducers in the space under control. In other words, it is a not invasive system. Therefore, a lot of work has been carried out to develop smart panels with integrated distributed strain sensors [29,34-37] or with arrays of sensors [11,19] that measure the vibration components of a panel that mostly contribute to the far field sound [29].
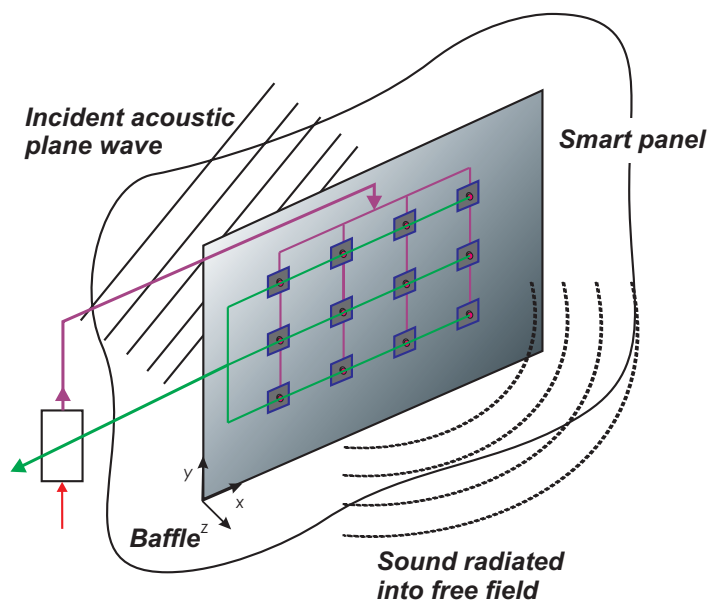
Figure 1.4: *Active Structural Acoustic Control (ASAC) with a large number of centralised sensor-actuators pairs.*

In parallel with the work on ASAC systems with feed-forward control techniques, which are limited to the control of tonal disturbances, work has been carried out to build up ASAC systems where feedback controllers are used. In this case, the reference signal is not required, so these systems can be used to control both tonal and random, wide-band, disturbances. These systems, the signal from the structural sensors are fed back to the structural actuators in such a way as to minimize the vibration component that contributes to the sound radiation. For the case of disturbance rejection feedback control, the most suitable strategy is active damping. This strategy reduces the response of the structure at resonance frequencies. The simplest and most robust way in order to get active damping is by implementing direct velocity feedback (DVFB), in this case the signal from the velocity sensor is directly fed back to the actuators via a fixed control gain. This has led to the design of multichanel feedback controller using state space design [20].
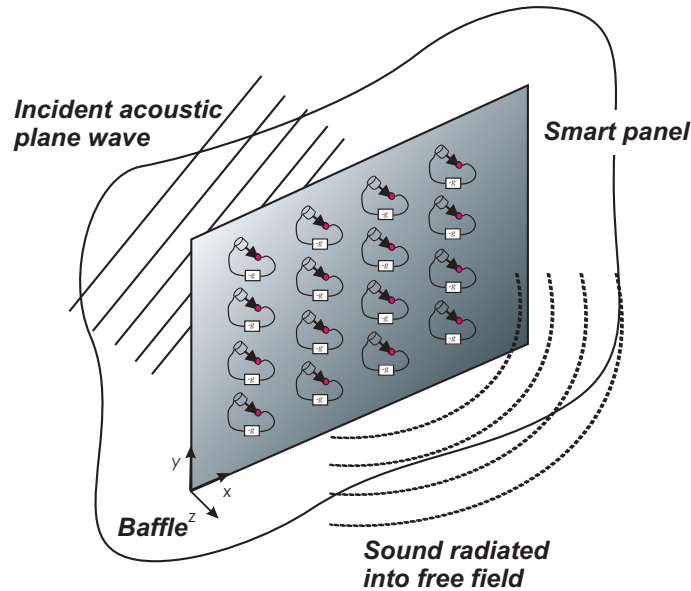
Figure 1.5: *Active Structural Acoustic Control (ASAC) with a large number of decentralised collocated sensor-actuators pairs.*

1.5   Smart panels for Active Vibration Control (AVC)

The problems which have appeared in the development in smart panel with feedback ASAC have motivated the development of alternative control solutions. With velocity feedback control, active damping is produced, which generates control at the resonances frequencies of the structure, where the sound radiation is controlled by the self-radiation of the resonant mode. Also it tends to enhance the vibration at antiresonance frequencies, where the sound radiation is controlled by self- and mutual-radiation effects of a set of modes. Thus, as the feedback gain, and thus the active damping increases from zero, the

frequency averaged kinetic energy and total sound radiation of the panel decreases. This active damping effect on the frequency averaged kinetic energy and total sound power radiation does not grow indefinitely. On the contrary, it tends to decrease for large control gains which tend to pin the structure at the control position. In this way no active damping is injected on the structure. Thus the overall effect is a modification of the spatial response of the structure which becomes pinned at the control position so that, it even radiates more efficiently sound at the new, lightly damped, resonance frequencies.

As shown in Figure 1.5 practical systems can be built using grids of electrodynamic proof mass actuators and closely located accelerometers inertial sensors, as it will be shown later in this thesis. Although these systems are not properly collocated and dual, they enable relatively large feedback control gains, as it will be shown in the chapter 6.

1.6   Sensor-Actuator transducer for smart panels

In the previous sections, the principal features of ASAC and AVC systems have been introduced without taking into account the dynamics of the sensor-actuator transducers used in the smart panels. Therefore, the most common transducers used for the different strategies of active control systems are briefly revised in this subsection.

Mechanical vibration can be both generated and detected by strain and inertial transducers such as piezoelectric patch actuators and sensors or electrodynamic proof mass actuators and inertial accelerometers [38]. Flexural vibration can be both generated and measured in a smart panel by activating strain transducers embedded into the surface. The simplest of these strain transducers are made from a piezoelectric lamina/film sandwiched between two thin layers of metal working as electrodes. Therefore, when a voltage is applied across the two electrodes, and electric field is generated between the piezoelectric lamina, which, because of the piezoelectric effect [9], causes in plane stretching of the piezoelectric lamina. As a result, when lamina is bonded on a thin structure, it causes bending, twisting, stretching [39]. In the same way, when the piezoelectric transducer is employed as strain sensors, the vibrations of the structure where the transducer is bonded produces deformations of the piezoelectric lamina which produces a distribution of charge on the surface of the two electrodes by means of the piezoelectric effects [9,40,41]. Therefore, a charge output proportional to the structure vibration can be measured by connecting a

charge amplifier to the two electrodes. Since these devices have a small mass per unit surface area, they are suited for the construction of distributed sensors.

One way to generate a sky-hook point force on a structure in a smart panel is by means of proof mass electrodynamic actuators [42]. A proof mass actuator can be made with a coil-magnet electrodynamic linear motor, where the coil is fixed to the base or case of the actuator and the magnet is suspended on soft springs so that it provides the inertial reaction necessary to generate a point force on the structure where the proof mass actuator is fixed [19]. These devices will be described in more details later in this thesis. The absolute vibration mode of a structure on a specific point can be measured with inertial accelerometers [38]. This type of devices comprises an elastic transducer with a seismic mass. The transducer normally consists of a piezoelectric element which generates a voltage signal proportional to the relative displacement between the mass and the case respectively. With these devices it is possible to measure the acceleration at a point of a structure provided its natural frequency is well above the measurement range [19].

1.7 Scaling of transducer

In some cases, the scaling of transducers may offer favourable benefits; in fact, smaller devices tend to be faster and consume less power. The smaller they are, the less material is needed in order to be build. They allow new applications where space is confined. As they become smaller, they become portable. Due to batch fabrication technique, they can be mass produced and cost effective. If the production method is compatible with integrated circuit production technique, sensors, actuators, accelerometers and electronics could be integrated on the same chip. By integrating multiple sensors or actuators in one device, reliability can be increased.

However, scaling may also introduce disadvantages: smaller actuators exert less force and smaller sources transmit low power levels. The resonance frequency of mechanical system increases with miniaturisation, which as shown in detail in the chapter 4, is a critical problem for proof mass actuators. Manipulation of miniaturised objects becomes a problem and electrical values like resistance, capacitance, and inductances do not scale in the same way so that the response of the transducers may change drastically with scaling. Besides new forces and physical phenomena appear and become important with miniaturisation such as: Van der Waals forces [43].

When the transducers are scaled down, force, power, speed and other characteristic scale too. However these characteristic do not scale proportionally to the size. Mass and volume, for example, scale with the third power of the size while the surface scales with the second power of the size [43].

1.8 Scope and Objective

The purpose of this thesis is to discuss the design of a light, simple, low cost and robust feedback active control unit to be used in a decentralised MIMO control system arranged on a thin panel in order to control both its vibration and sound radiation. The feedback control unit consists of a proof-mass force actuator with a velocity sensor at its base which implement basic feedback control laws that does not need complex electronic systems to be implemented. The test rig used to study the electrodynamics proof mass actuators consists of a clamped, thin aluminium panel which is excited by either a point force or an acoustic field.

The four main objectives of this thesis are

- to model and study theoretically the stability and control performance properties of one and five feedback control loops on the clamped rectangular panel which, using the velocity error signal, implement [19]:
  1. Proportional Control for the implementation of Velocity Feedback;
  2. Integral Control for the implementation of Displacement Feedback;
  3. Derivative Control for the implementation of Acceleration Feedback and
  4. PID Control (Proportional–Integral–Derivative Feedback).
- to study the scaling effects of the actuator with reference to the implementation of velocity feedback control.
- to present stability and control performance experimental test of a miniaturised prototype actuator specifically designed for this study.
- to assess the practical implementation of decentralised velocity feedback control on a thin aluminium rectangular panel with five prototype miniaturised electrodynamic actuators.

1.9   Structure and organisation

This thesis is divided in five chapters. Chapter 2 presents the main features of SISO feedback control on a single degree of freedom system using either an ideal reactive force actuator or a proof mass actuator. The aim of this chapter is twofold. First, to revise the basic stability and control performance properties of Proportional, Integral, Derivative, PI, PD and PID control laws. Second, to investigate the effects on stability and control performance that are produced by the dynamics of a proof mass actuator.

Chapter 3 presents a simulation study about the stability and performance of a control system with five decentralised feedback control units mounted on a flat panel in order to reduce its vibration and sound radiation. Each control unit consists of a proof-mass electro-dynamic actuator with a velocity sensor at its base. The aim is to design light, simple, robust and low cost, control units which can be attached in large numbers to flexible structures in order to control their spatially averaged response and sound radiation at low audio-frequencies. Thus four basic feedback control functions have been studied: a) Proportional, b) Integral c) Derivative and d) PID. Two types of controllers have been considered which drive the actuators either with current or voltage signals.

The study for the various feedback control laws is organised in a consistent framework which first introduces the mathematical model for the various control schemes, it then presents the stability analysis using the Nyquist criterion [19] and finally it gives the control performance results.

The use of proof mass electrodynamic actuators for decentralised velocity feedback control on a rectangular panel is presented in the next two chapters. In chapter 4 the principal features of a small scale proof mass actuator with a low mounting resonance frequency are first presented. In particular a stability–performance formula is derived which can be effectively used to asses the miniaturisation effects on the stability and control performance of the feedback loop. The design and tests of a velocity feedback loop with a prototype miniaturised proof mass actuator are presented in chapter 5.

Finally in chapter 6 the implementation of five decentralised control loops is analysed, both theoretically and experimentally. The stability properties of the five decentralised control units is assessed with the generalised Nyquist criterion by plotting the loci of the eigenvalues of the fully populated matrix of frequency response functions between the five

error signals and five input signals to the amplifiers driving the actuators. The control performance properties have been assessed in terms of the spatially averaged response of the panel measured with a scanning laser vibrometer and the total sound power radiated measured in an anechoic room.

1.10 Contributions

The main original contributions of this thesis are:

- An investigation of the differences feedback control laws using an electrodynamic proof mass actuator which is driven either by current or voltage signals.

- Derivation of a 'stability–performance' formula that can be used to assess simultaneously the stability and control performance of the feedback control loop with the proof mass actuator.

- Miniaturisation study of the stability and control performance of a direct velocity feedback loop small scale prototype electrodynamic proof mass actuator mounted on a thin panel.

- Experimental study of stability and control performances of a feedback control unit using a prototype miniaturised proof mass electrodynamic actuator.

- Theoretical and experimental investigation of the stability and control performance properties of a five channel decentralised velocity feedback control units using five prototype miniaturised proof mass electrodynamic actuators.

2   FUNDAMENTAL CONCEPTS OF FEEDBACK CONTROL

In this chapter, the steady–state response of a Single Degree of Freedom (SDOF) with a reactive point forces or inertial point force feedback control system is studied. First, the response of the SDOF system will be studied when there is no active vibration control assuming different values of damping ratio. Second, the effect of a feedback control loop using either a reactive force actuator or a proof mass force actuator will be examined assuming a small damping ratio. A number of control architectures will be studied namely: a) Proportional Control for implementation of Velocity Feedback, b) Integral Control for implementation of Displacement Feedback c) Derivative Control for implementation of Acceleration Feedback and d) PID Control (Proportional–Integral–Derivative Feedback Control). The aim of this chapter is to introduce the stability and performance analysis of vibration control using proof mass actuators.

2.1   Single degree of freedom system under harmonic motion of the base

Figure 2.1(a) shows the notation used for the mass–spring–dashpot SDOF system under harmonic motion of the base considered in this section.
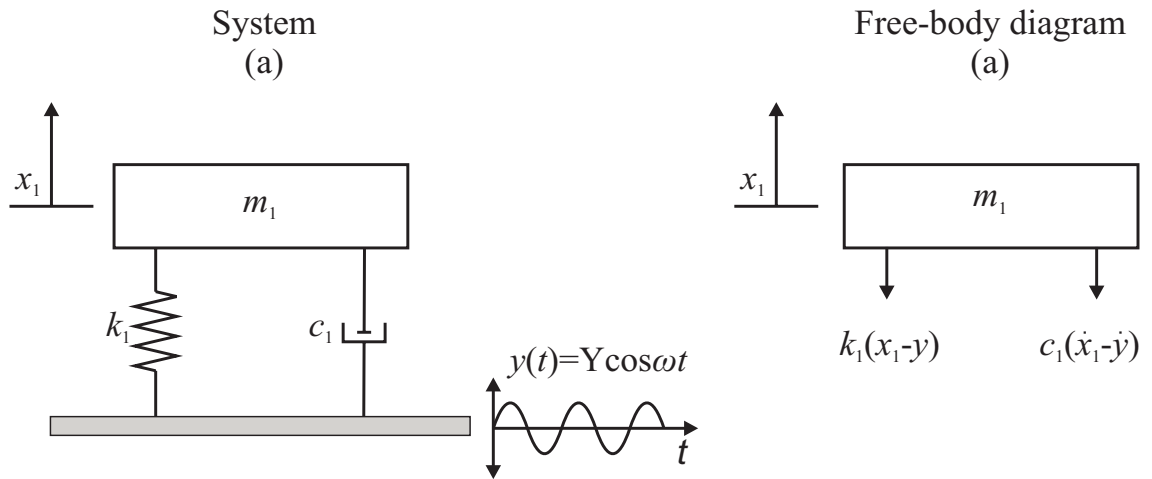
Figure 2.1: *Single degree of freedom system under harmonic motion of the base.*

In this chapter the mechanical kinematics (displacement, velocities, accelerations) or kinetic (force) functions have been taken to be time–harmonic and given by the real part of counterclockwise rotating complex vectors (phasors), so that, for example the displacement and force functions are given by $x(t) = \mathrm{Re}\{X(\omega)e^{j\omega t}\}$, $f(t) = \mathrm{Re}\{F(\omega)e^{j\omega t}\}$, where ω is the

circular frequency [rad/s] and $j = \sqrt{-1}$. Therefore $x(t)$ and $f(t)$ are the time–dependent harmonic displacement and force function while $X(\omega)$ and $F(\omega)$ are the complex frequency–dependent displacement and force phasors. In order to simplify the formulation, the harmonic time dependence is assumed in the mathematical expressions. Also, the first and second derivative of the time–harmonic functions will be represented by velocity and acceleration frequency dependent phasors; $\dot{X}(\omega) = j\omega\, X(\omega)$ and $\ddot{X}(\omega) = -\omega^2 X(\omega) = j\omega\, \dot{X}(\omega)$.

Considering the free–body diagram shown in Figure 2.1(b) and using Newton's second law of motion ($\sum F = m_1 \ddot{x}_1$), the following equation of motion is obtained:

$$m_1 \ddot{x}_1 + c_1 \dot{x}_1 + k_1 x_1 = c_1 \dot{y} + k_1 y \tag{2.1}$$

where m_1 is the proof mass, c_1 is the damping coefficient, k_1 the stiffness, x_1 is the displacement of the proof mass and the base excitation is given by:

$$y = \mathrm{Re}\left\{ Y e^{j\omega t} \right\} \tag{2.2}$$

where Y is the amplitude. The right hand side of the Eq. (2.1) base can be seen as a force $f(t)$ acting on a "classic" SDOF mass–spring–dashpot system with a rigid base:

$$f = c_1 \dot{y} + k_1 y \,. \tag{2.3}$$

The steady state solution of Eq. (2.1) can be found by assuming:

$$x_1(t) = \left\{ X_1 e^{j\omega t} \right\}. \tag{2.4}$$

By substituting Eq. (2.4) into Eq. (2.1) and solving for X_1, the following relation between the phasors of the mass and base displacement is obtained:

$$X_1(\omega) = \frac{k_1 + jc_1\omega}{k_1 - m_1\omega^2 + j\omega c_1} Y(\omega). \tag{2.5}$$

Figure 2.2 shows the variation of the ratio between the velocity of the proof mass and the displacement of the base calculated assuming the physical parameters given in Table 2.1 and for different damping ratios; $\xi = c/c_c$ where c_c is the critical damping:

$$c_c = 2m_1\omega_n \tag{2.6}$$

and ω_n is the natural frequency:

$$\omega_n = \sqrt{\frac{k_1}{m_1}} \,. \tag{2.7}$$

Table 2.1: *Physical parameters for the elements in the SDOF system.*

Parameter	Value
Critical Damping	$c_c = 2.83$ N/ms^{-1}
Mass	$m_1 = 0.015$ Kg
Stiffness	$k_1 = 133.24$ N/m
Natural frequency	$f_n = 15$ Hz

Figure 2.2: *Modulus and phase of the ratio between the velocity of the proof mass and the displacement of the base of the system shown in Figure 2.1(a) when the system is damped by $\xi_1=0.001$ (solid line), $\xi_2=0.1$ (dashed line), $\xi_3=0.4$ (dotted line) or $\xi_4=0.8$ (dash-dot line).*

The key features of the SDOF system under study can summarised in the following points:

- For an undamped system (ξ=0) $|j\omega X_1/Y|$ tends towards infinity at resonance.
- The addition of small amounts of damping lead to important reductions of the response at, or near, resonance but also increase the response at frequencies much higher than resonance.
- Increasing damping causes the frequency of maximum response to move to lower values.
- Increasing the amount of damping leads to a smoother phase transition.

The results shown in Figure 2.2 indicate that, in order to obtain the maximum vibration reduction of the mass, the spring element should be selected in such a way as to keep the natural frequency as low as possible in respect to the limitation imposed on the static displacement $\delta = m_1 g / k_1$, where g is the acceleration due to the gravity, which also depends on the stiffness of the spring. Also the damping effect should be as small as possible, although also in this case a compromise must be found in order to avoid excessive vibrations transmission around the resonance frequency.

2.2 SDOF system under harmonic motion of the base with a reactive force feedback control loop

The design problems highlighted above generate important limitations to the low frequency passive isolation effect introduced by the spring–dashpot element. An interesting and effective way to enhance the vibration isolation is the implementation of an active control system.
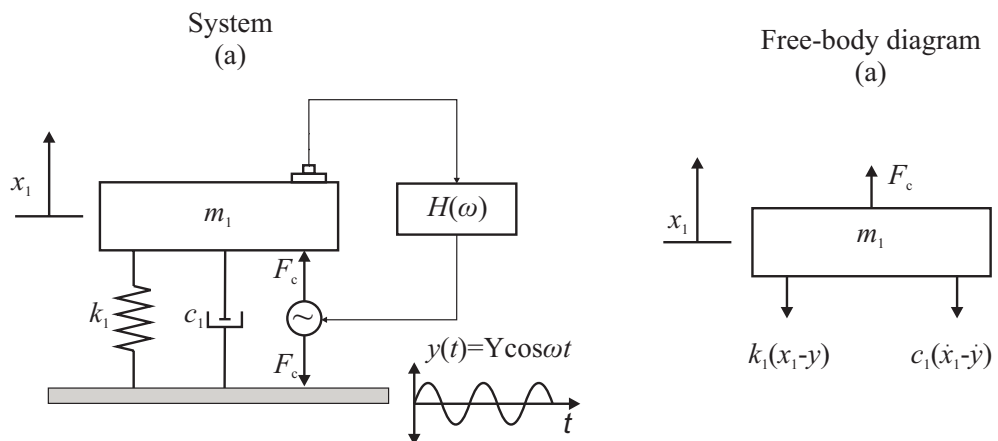
Figure 2.3: *SDOF under harmonic motion in the base with feedback control.*

In this section the effects produced by a feedback control system, which, as shown in Figure 2.3(a), is composed by a) a control sensor that measures the velocity of the mass, b) a control actuator mounted in parallel with the spring–dashpot elements that produces reactive forces between the mass and base and c) a control system that implement a control function –H which in the simplest case is given by a pure gain; –g.

The equation of motion for the system shown in Figure 2.3(a) with a Proportional, Integral, Derivative, or combination among the three control functions can be derived from the free-body diagram shown in Figure 2.3(b) using Newton's second law of motion, which gives:

$$m_1 \ddot{x}_1 + c_1 \dot{x}_1 + k_1 x_1 = c_1 \dot{y} + k_1 y + f_c \tag{2.8}$$

where $f_c = \mathrm{Re}\{F_c e^{j\omega t}\}$ is the feedback reactive control force which depends on the control loop used as it is described in the sections below:

2.2.1 Proportional control for implementation of velocity feedback

In this case, the output signal from the velocity sensor is feedback to the actuator via a negative proportional function, i.e. $H(\omega) = -g_P$, where g_P is a fixed proportional gain, so that the phasor of the control force F_c, is directly proportional to the opposite of the velocity of the mass:

$$F_c = -g_P \dot{X}_1(\omega). \tag{2.9}$$

Therefore substituting the steady state solution $x_1(t) = \{X_1 e^{j\omega t}\}$, (Eq.(2.4)) into the equation of motion (Eq.(2.1)), with $y = Y e^{j\omega t}$, and $F_c = -g_P \dot{X}_1(\omega)$, the following expression for the complex amplitude of the response is obtained:

$$X_{1-P}(\omega) = \frac{k_1 + j c_1 \omega}{k_1 - m_1 \omega^2 + j\omega(c_1 + g_P)} Y(\omega) \tag{2.10}$$

The denominator of this equation indicates that Proportional Control adds active damping. This effect will be further discussed in Section 2.4 where simulations results for this control scheme are presented.

2.2.2 Integral control for implementation of displacement feedback

In this case, the output signal from the velocity sensor is feedback to the actuator via a negative integral control function, i.e. $H(\omega) = -g_I/j\omega$, where g_I is a fixed integral gain, so that the phasor of the control force F_c is directly proportional to the opposite of the displacement of the mass. Hence F_c is given by:

$$F_c = -g_I \frac{\dot{X}_1(\omega)}{j\omega} = -g_I X_1(\omega).$$ (2.11)

Following the same procedure as in the previous subsection, the complex response is found to be in this case:

$$X_{1-I}(\omega) = \frac{k_1 + jc_1\omega}{(k_1 + g_I) - m_1\omega^2 + j\omega c_1} Y(\omega).$$ (2.12)

The denominator indicates that Integral Control adds active stiffness so that the resonance frequency is moved to higher values as it will be further discussed in section 2.4.

2.2.3 Derivative control for implementation of acceleration feedback

In this case, the output signal from the velocity sensor is feedback to the actuator via a derivative control function, i.e. $H(\omega) = -g_D j\omega$, where g_D is a fixed derivative gain, so that the phasor of the control force F_c, is directly proportional to the opposite of the acceleration of the mass. Hence F_c is given by:

$$F_c = -j\omega g_D \dot{X}_1(\omega) = -g_D \ddot{X}_1(\omega).$$ (2.13)

Once more, following the procedure highlighted in the previous subsections the response is found to be:

$$X_{1-D}(\omega) = \frac{k_1 + jc_1\omega}{k_1 - (m_1 + g_D)\omega^2 + j\omega c_1} Y(\omega).$$ (2.14)

2.2.4 Proportional-Integral-Derivative (PID) control

As it will be shown in section 2.4; a) Velocity Feedback Control (Proportional Control) can control the response at resonance, b) Displacement Feedback Control (Integral Control) can reduce vibration at low frequency below resonance and c) Acceleration Feedback Control (Derivative Control) can reduce vibration at higher frequency above resonance. Thus a combination of these three control approaches; Proportional–Integral– Derivative Feedback Control (PID), is expected to enhance the vibration isolation in all frequency range of interest.

With PID control the output signal from the velocity sensor is feedback to the actuator via a control function combining proportional, integral and derivative control so that, the phasor of the control force F_c is directly proportional to the opposite of the velocity– displacement–acceleration of the mass. Hence F_c is given by:

$$F_c = \left\{ -g_P - \frac{g_I}{j\omega} - j\omega g_D \right\} \dot{X}_1(\omega) = -g_P \dot{X}_1(\omega) - g_I X_1(\omega) - g_D \ddot{X}_1(\omega). \qquad (2.15)$$

Following the procedure seen above the response is found to be:

$$X_{1-PID}(\omega) = \frac{k_1 + jc_1\omega}{(k_1 + g_I) - (m_1 + g_D)\omega^2 + j\omega(c_1 + g_P)} Y(\omega). \qquad (2.16)$$

The numerator shows that PID Control adds active damping, active stiffness and active mass so that vibration reduction can be obtained in the three regions, below, at and above resonance as it will be shown in the section 2.4.

2.3 Stability analysis

A critical problem for the design of feedback control system is stability. To address the problem of stability, several graphical techniques have been developed for Single Input Single Output (SISO) control schemes. Two of these techniques are the *Bode* and *Nyquist plots*. The first one consists of plotting the magnitude versus frequency and phase angle versus frequency of the open loop sensor–actuator frequency response function. The second one is a polar plot of the open loop sensor–actuator frequency response function as

ω varies from $-\infty$ to ∞. Both approaches rely on the Nyquist stability criterion which state that *"provided the Nyquist plot of the open loop sensor–actuator frequency response does not encircle the Nyquist point −1+j0, then the control system is stable"*. Therefore in those cases where the sensor–actuator frequency response function enters on the left hand side quadrants of the Nyquist plot, the system could be either unstable or conditionally stable so that only a limited range of control gains can be implemented. If instead the Nyquist plot of the sensor–actuator response function occupies only the right hand side quadrants of the Nyquist plot, i.e. the response function is strictly positive real, then the system is unconditionally stable. The same type of conclusion can be drawn by considering the Bode plot of the open loop sensor–actuator response function. If the phase plot is confined between $\pm 90°$ then the open loop sensor–actuator response function is real positive and thus the system is unconditionally stable. If the phase plot exceed $\pm 90°$ then the system could be either conditionally stable or indeed unstable. Normally the concepts of gain and phase margin [7] are used to assess the level of stability.

There are two necessary requirements in order to have an unconditionally stable system: the sensor–actuator pair must be dual and collocated [25,29]. Indeed in this case the sensor–actuator frequency response function is real positive definite so that its Nyquist plot occupies the right hand side quadrants as ω varies from $-\infty$ to $+\infty$ and thus the Nyquist instability point is never encircled whatever the control gain.
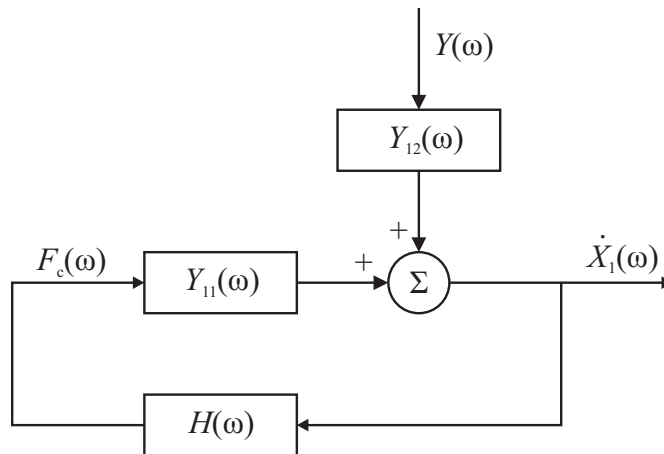
Figure 2.4: *Block diagram of feedback control system implemented on the SDOF system.*

The response of the active system shown in Figure 2.3 can be formulated in terms of mobility frequency response functions: *Y=velocity/force.* In this case, as shown by the block diagram in Figure 2.4, the response at the error sensor can be modelled in terms of the primary disturbance effect plus the closed feedback loop effect. This is a classical

disturbance rejection control loop. Considering Figure 2.4, the following expressions for $\dot{X}_1$ and control force F_c are obtained:

$$\dot{X}_1 = Y_{12}Y + Y_{11}F_c,$$ (2.17)

$$F_c = H(\omega)\dot{X}_1$$ (2.18)

where, the mobility functions Y_{12} and Y_{11} are given by:

$$Y_{12} = \left.\frac{\dot{X}_1}{Y}\right|_{F_c=0} = j\omega\frac{k_1 + jc_1\omega}{k_1 - m_1\omega^2 + j\omega\, c_1} \quad,$$ (2.19)

$$Y_{11} = \left.\frac{\dot{X}_1}{F_c}\right|_{Y=0} = j\omega\frac{1}{k_1 - m_1\omega^2 + j\omega\, c_1} \quad,$$ (2.20)

and $H(\omega)$ is a control function. Substituting Eq. (2.18) into Eq. (2.17), and solving respect the velocity $\dot{X}_1$, the following expression is obtained:

$$\dot{X}_1 = \frac{Y_{12}}{1 + HY_{11}}Y$$ (2.21)

where HY_{11} is the open loop frequency response function between the velocity sensor and the control actuator. If $\mathrm{Re}(HY_{11})>0$, then Eq. (2.21) shows that $\dot{X}_1/Y < 1$ for any control gain and frequency, that is the feedback control monotonically reduces the velocity of the system. Unconditionally stable control systems allow large control gains without causing instability and hence may achieve superior control performance.

In the following sub–sections the stability for the different control architectures listed above is studied.

2.3.1 Proportional Control: velocity feedback

In order to implement negative velocity feedback, the output signal from the velocity sensor is feedback to the actuator via a negative proportional control function; $H(\omega) = -g_P$, and thus:

$$F_c = -g_P \dot{X}_1.$$ (2.22)

Figure 2.5 shows the amplitude–phase and Nyquist plot of the open loop sensor–actuator frequency response function HY_{11} in the frequency range between 0 and 50 Hz.

Figure 2.5: *Frequency response functions; amplitude (top left), phase (bottom left) and Nyquist plot (right) of the open loop sensor–actuator frequency response function in the frequency range between 0-50 Hz when a Proportional control is used.*

The Bode plot in Figure 2.5 confirms that the frequency response function HY_{11} of the SDOF active system is positive real so that the system is unconditionally stable. Alternatively the Nyquist plot of HY_{11} in Figure 2.5 (right plot) shows that the polar plot of the frequency response function is entirely on the right hand side quadrants and thus it is positive real, which also indicates the unconditional stability of proportional, which is negative velocity feedback, control.

2.3.2 Integral Control: displacement feedback

In order to implement negative displacement feedback, the output signal from the velocity sensor is feedback to the actuator via a negative integral control function; $H(\omega) = -g_I/j\omega$, and thus:

$$F_c = -\frac{g_I}{j\omega}\dot{X}_1.$$

(2.23)

As shown in Figure 2.6, in this case the Bode plot indicates that the phase of the open loop sensor–actuator frequency response function HY_{11} exceed $-90°$ at higher frequencies above resonance. Therefore the Nyquist plot of HY_{11} is not confined on the right hand side quadrants which suggest that the system could be unstable.

Figure 2.6: *Frequency response functions; amplitude (top left), phase (bottom left) and Nyquist plot (right) of the open loop sensor–actuator frequency response function in the frequency range between 0-50 Hz when an Integral control is used.*

Indeed the Nyquist plot of HY_{11} in Figure 2.6 is characterised by a circle which occupies the bottom quadrants only. Thus in principle, the system is unconditionally stable although part of the circle is very close to the Nyquist instability point $(-1+j0)$ and thus it is likely to intersect the negative real axis at higher frequencies even with little variations of the response function which can be easily generated by external factors that would cause the system to become unstable. Also, when the polar plot of HY_{11} enters the circle of unit radius and centre $(-1,j0)$, but does not encircle the instability point $(-1,j0)$, then $\mathrm{Re}\{1/(1+HY_{11})\}>1$ and thus, according to Eq.(2.21), even though the system is not unstable, the response $\dot{X}_1$ is magnified rather than minimised. This phenomenon is known

as control spillover. In this thesis the circle of unit radius and centre $-1, j0$, will be referred as the "spillover circle".

2.3.3 Derivative Control: Acceleration feedback

In order to implement negative acceleration feedback the output signal from the velocity sensor is feedback to the actuator via a negative derivative control function; $H(\omega)=-g_D j\omega$ and thus:

$$F_c = -j\omega g_D \dot{X}_1. \tag{2.24}$$

Figure 2.7: *Frequency response functions; amplitude (top left), phase (bottom left) and Nyquist plot (right) of the open loop sensor–actuator frequency response function in the frequency range between 0-50 Hz when a Derivative control is used.*

As shown in Figure 2.7 in this case the Bode plot indicates that the phase of the open loop sensor–actuator frequency response function HY_{11} exceed $+90°$ at lower frequencies below resonance. Therefore the Nyquist plot of HY_{11} is not confined on the right hand side quadrants which suggest that the system could be unstable. Indeed the Nyquist plot of HY_{11} in Figure 2.7 is characterised by a circle which occupies the top quadrants only. Thus in principle, the system is unconditionally stable although part of the circle is very close to the Nyquist instability point $(-1+j0)$ and thus it is likely to intersect the negative real axis at lower frequencies when the response function is modified by the presence of external factors that bring the system to instability. In this case, the polar plot enters the spillover circle at low frequencies where control spillover vibration enhancement effects will therefore be generated for high control gains.

2.3.4 PID Control

In order to implement a combination of negative displacement, velocity and acceleration feedback that reduce vibration in the stiffness, damping and mass controlled regions. The output signal from the velocity control sensor is feedback to the control force actuator via a negative combination of Proportional–Integral–Derivative control function; $H(\omega) = -\{ g_P + g_I/j\omega + j\omega g_D \}$.

Table 2.2: *Physical parameters for the Proportional, Integral and Derivative Control constants.*

Parameter	Value
Proportional Control Constant	$k_P = 0.1$
Integral Control Constant	$k_I = 10$
Derivative Control Constant	$k_D = 0.001126$

These Proportional, Integral and Derivative Control functions have been chosen in such a way that the resonance frequency of the system is kept the same than with no control. Thus the feedback control law has been rewritten in the following form $H(\omega) = -g(k_P + k_I / j\omega + j\omega k_D)$, where g is a fixed gain and k_P, k_I and k_D have been chosen in such a way as to keep the same natural frequency of the system. The undamped resonance frequency of the PID controlled system can be found by setting to zero the denominator in Eq. (2.16) assuming the complex term due to passive and active damping to be zero:

$$k_1 + k_I - \left(m_1 + k_D \right) \omega_n^2 = 0 \quad . \tag{2.25}$$

The undamped resonance frequency of the PID active system is therefore given by:

$$\omega_n = \sqrt{\frac{k_1 + k_I}{m_1 + k_D}} \quad . \tag{2.26}$$

Table 2.2 gives the values of k_P, k_I and k_D chosen to keep constant the resonance in the following simulation results.

Figure 2.8: *Frequency response functions; amplitude (top left), phase (bottom left) and Nyquist plot (right) of the open loop sensor–actuator frequency response function in the frequency range between 0-50 Hz when a PID control is used.*

In this case, the Bode plot in Figure 2.8 indicates that the phase of the open loop sensor–actuator frequency response function HY_{11} is positive real. Alternatively the Nyquist plot in Figure 2.8 (right plot) and Figure 2.9 show that the open loop response function HY_{11} is entirely on the right hand side quadrants, which also indicates the unconditional stability of the system. This is due to the fact that the system adds the same percentage of Integral control (Active stiffness) and Derivative control (Active mass); so that their phase lag and phase lead effects are balanced.
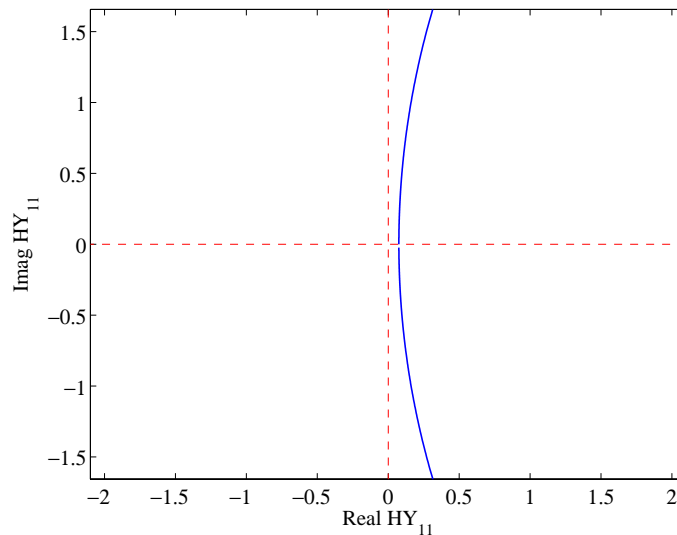
Figure 2.9: *Zoom of the Nyquist plot shows in Figure 2.8.*

In general it can be concluded that if the Integral and Derivative Control gains are chosen in such a way as to maintain the same resonance frequency of the system, then the Nyquist

plot of the open loop sensor–actuator frequency response function HY_{11} will be characterised by a circle in the right hand side quadrants as in the case of no control.

2.4 Control performances.

In this section the control performances for the different control architectures introduced above will be studied. In the following points the ratio between the velocity of the mass and the base

$$\frac{\dot{X}_1}{Y} = \frac{Y_{12}}{1 + H(\omega)Y_{11}} \tag{2.27}$$

will be plotted using the various control functions $H(\omega)$.

2.4.1 Proportional Control

In this case the control function utilised is a Proportional function; $H(\omega) = -g_P$. Figure 2.10 shows that the addition of small amounts of control gain lead to consistent reduction of the response at, or near, resonance without producing any harm at higher frequencies. Also the phase transition is smoothened out.
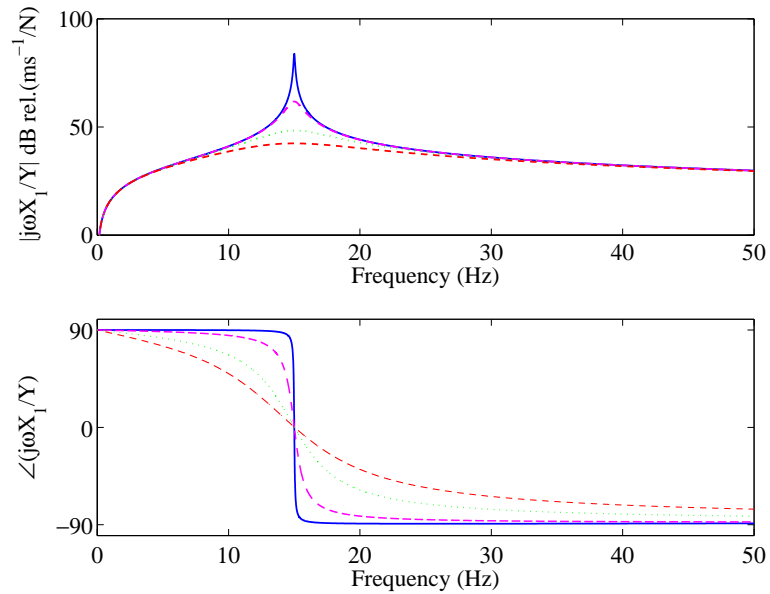
Figure 2.10: *Modulus and phase of the ratio between the velocity of the proof mass and displacement of the base of the system shown in Figure 2.3(a) when the system has a small damping ratio ($\xi=0.001$) and different values of gain; $g_1=0$; no-gain (solid line), $g_2=0.1$ (dashed line), $g_3=0.5$ (dotted line) or $g_4=1$ (dash-dot line) when a Proportional control is used.*

In summary, Proportional Control adds active damping such that vibrations reductions are generated at resonances frequencies without side effects below and above resonance frequencies.

2.4.2 Integral Control

In this case the control function is an Integral function; $H(\omega) = -\dfrac{g_I}{j\omega}$.
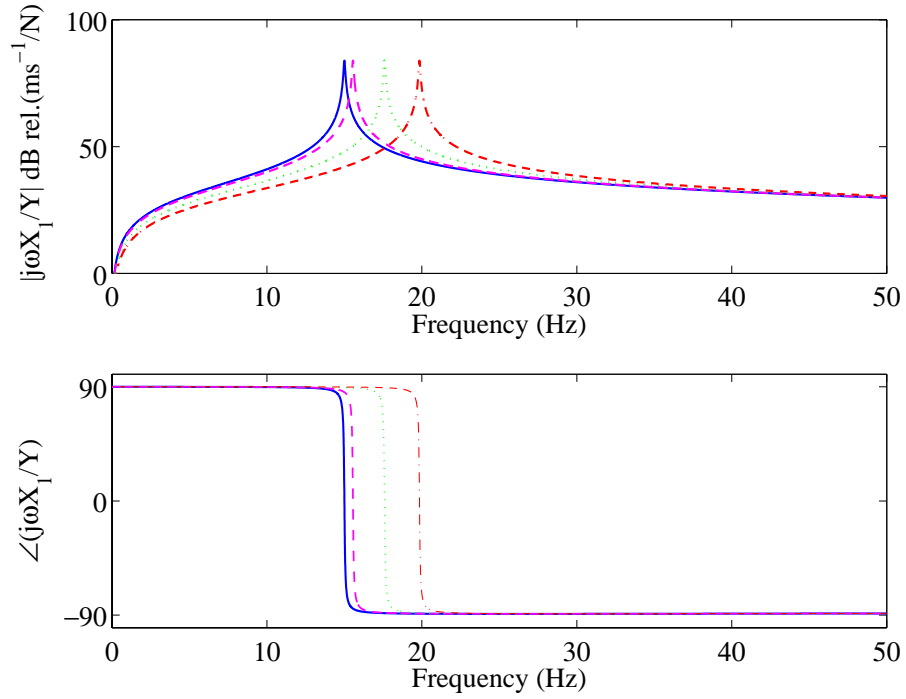
Figure 2.11: *Modulus and phase of the ratio between the velocity of the proof mass and the displacement of the base of the system shown in Figure 2.3(a) when the system has a small damping ratio (ξ=0.001) and different values of gain; g_1=0; no-gain (solid line), g_2=10 (dashed line), g_3=50 (dotted line) or g_4=100 (dash-dot line) when an Integral control is used.*

Figure 2.11 shows that using Integral control the system adds active stiffness moving the resonance frequency to higher values. Thus the system produces vibration reductions at low frequencies below resonance only. The increase of the resonance frequency can be interpreted as a result of the control spillover effect discussed in section 2.3, which is confirmed by the Nyquist plot in Figure 2.6 which shows that part of the Nyquist plot of the open loop sensor–actuator response function enters the spillover circle of centre $-1+j0$ and radius 1.

2.4.3 Derivative Control

In this case the control function is a Derivative function given by $H(\omega) = -j\omega g_D$.
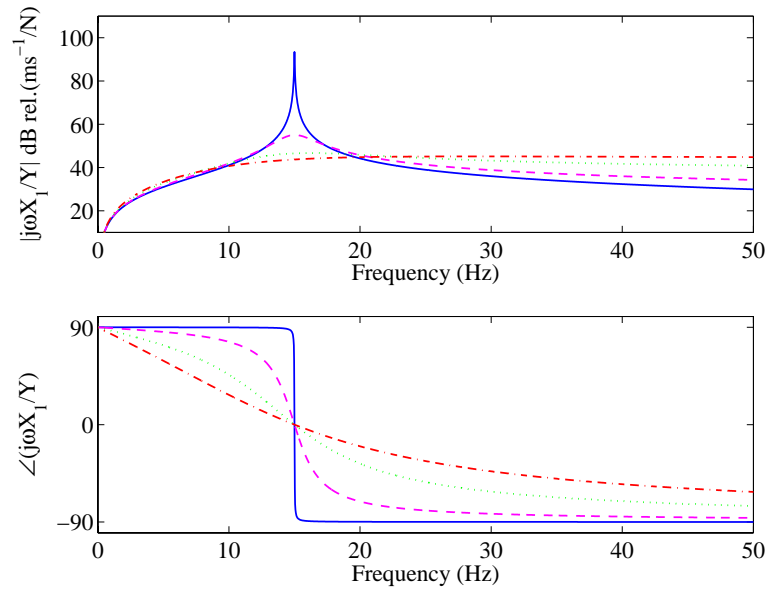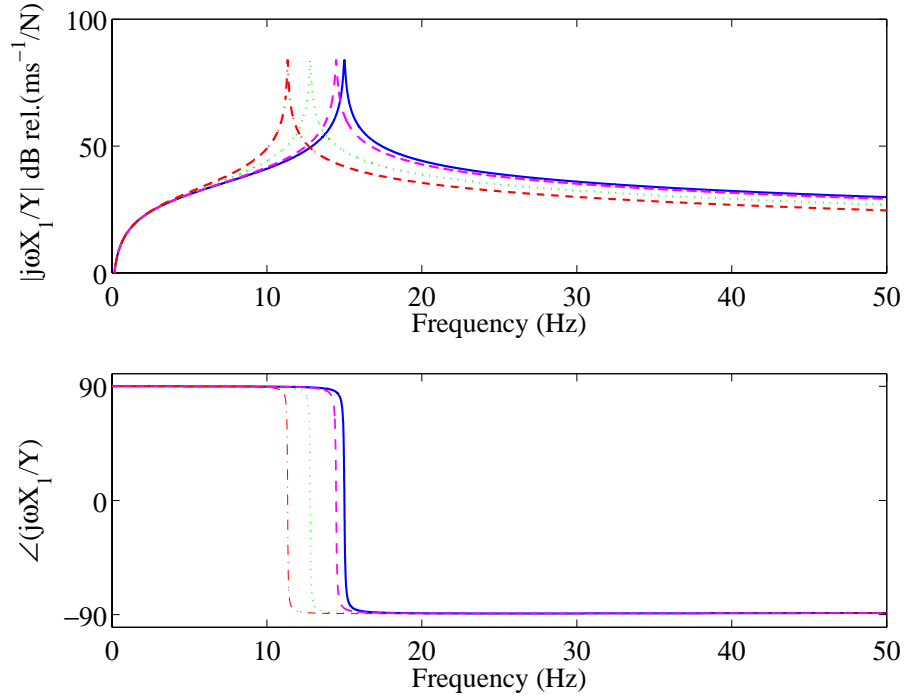

Figure 2.12: *Modulus and phase of the ratio between the velocity of the proof mass and the displacement of the base of the system shown in Figure 2.3(a) when the system has a small damping ratio ($\xi=0.001$) and different values of gain; $g_1=0$; no-gain (solid line), $g_2=0.001$ (dashed line), $g_3=0.005$ (dotted line) or $g_4=0.01$ (dash-dot line) when a Derivative control is used.*

Figure 2.12 shows that using Derivative control the system adds active mass moving the resonance frequency to lower values. Thus the system produces vibration reductions at high frequencies above resonance only. Also in this case, the lowering of the resonance frequency can be interpreted as a control spillover effect as suggested by the Nyquist plot in Figure 2.7 which shows that the low frequency part of the Nyquist plot of the open loop sensor–actuator response function enter the spillover circle of centre $-1+j0$ and radius 1.

2.4.4 PID Control

In this case the control function used is a combination of Proportional–Integral–Derivative

function $H(\omega) = -g\left\{k_P + \dfrac{k_I}{j\omega} + j\omega k_D\right\}$.
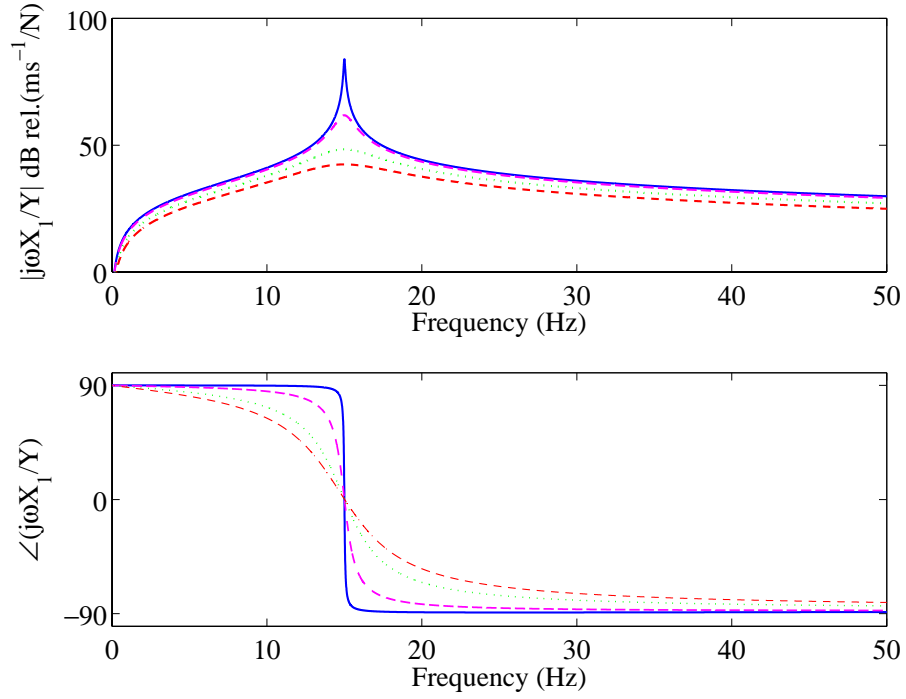
Figure 2.13: *Modulus and phase of the ratio between the velocity of the proof mass and the displacement of the base of the system shown in Figure 2.3(a) when the system has a small damping ratio (ξ=0.001) and different values of gain; g_{k1}=0, g_{c1}=0, g_{m1}=0; no-gain (solid line), g_{k2}=10, g_{c2}=0.1, g_{m2}=0.001; (dashed line), g_{k3}=50, g_{c3}=0.5, g_{m3}=0.005 (dotted line) or g_{k4}=100, g_{c4}=1, g_{m4}=0.01 (dash-dot line) when a PID control is used.*

As it was seen in previous sections; a) Proportional Control reduces vibration at resonance, b) Integral Control reduces the vibration at low frequency below resonance and c) Derivative Control reduces the vibration at high frequency above resonance. Therefore, as shown in Figure 2.13, using a combination among the three will reduce the vibration in the three regions.

2.5 SDOF system under harmonic force with a proof mass force actuator

In this section, the dynamic response of a single degree of freedom system excited by a point force and controlled by a feedback loop using a proof mass actuator will be

considered. The aim of this study is to introduce the analysis of vibration control using proof mass actuators. Therefore, considering the drawing in Figure 2.14, the bottom mass–spring–dashpot elements represent the system to be controlled which is excited by the force f_1. The proof mass actuator is composed by an additional mass–spring–dashpot system placed on top of the system to be controlled, so that, as will be shown in section 2.6, a control force is generated on the mass m_1 by reacting on the mass m_2. The form of this excitation will be $f_1(t) = \text{Re}\{F_1(\omega)e^{j\omega t}\}$, where $F(\omega)$ is the complex amplitude. In this section the response of this system is studied when there is no feedback active vibration control. In the next sections the stability and control performance of various control functions will be investigated.
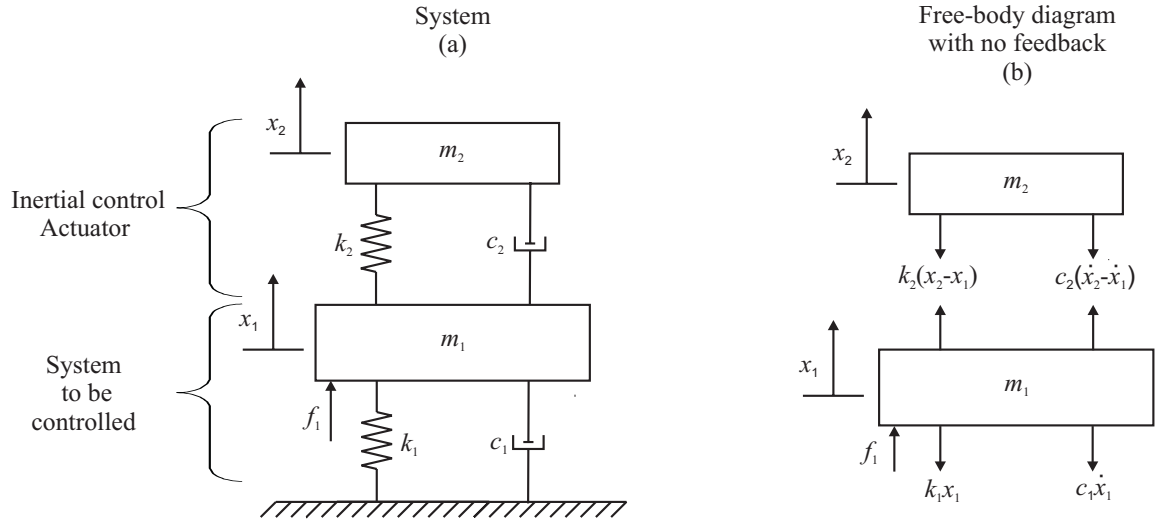
Figure 2.14: *DOF system under harmonic force when Fc=0.*

Considering the free–body diagram with F_c=0 shown in Figure 2.14(b) above and using Newton's second law of motion to each of the masses gives the equations of motion:

$$\begin{cases} m_1\ddot{x}_1 + (c_1 + c_2)\dot{x}_1 - c_2\dot{x}_2 + (k_1 + k_2)x_1 - k_2x_2 = f_1 \\ m_2\ddot{x}_2 - c_2\dot{x}_1 + c_2\dot{x}_2 - k_2x_1 + k_2x_2 = 0 \end{cases} \tag{2.28}$$

Eq. (2.28) can be written in matrix form as:

$$\mathbf{M}\ddot{\mathbf{x}} + \mathbf{C}\dot{\mathbf{x}} + \mathbf{K}\mathbf{x} = \mathbf{h}_1 f_1 \tag{2.29}$$

where:

$$\mathbf{M} = \begin{pmatrix} m_1 & 0 \\ 0 & m_2 \end{pmatrix}, \tag{2.30}$$

$$\mathbf{C} = \begin{pmatrix} c_1 + c_2 & -c_2 \\ -c_2 & c_2 \end{pmatrix}, \tag{2.31}$$

$$\mathbf{K} = \begin{pmatrix} k_1 + k_2 & -k_2 \\ -k_2 & k_2 \end{pmatrix}, \tag{2.32}$$

$$\mathbf{h_1} = \begin{pmatrix} 1 \\ 0 \end{pmatrix}, \tag{2.33}$$

$$\ddot{\mathbf{x}} = \begin{pmatrix} \ddot{x}_1 \\ \ddot{x}_2 \end{pmatrix}, \quad \dot{\mathbf{x}} = \begin{pmatrix} \dot{x}_1 \\ \dot{x}_2 \end{pmatrix} \quad \text{and} \quad \mathbf{x} = \begin{pmatrix} x_1 \\ x_2 \end{pmatrix}. \tag{2.34}$$

The steady state solution of Eq. (2.28) can be found by assuming:

$$\mathbf{x}(t) = \mathrm{Re}\left\{ \mathbf{X} e^{j\omega t} \right\} \tag{2.35}$$

where:

$$\mathbf{X} = \left\{ \begin{matrix} X_1 \\ X_2 \end{matrix} \right\}. \tag{2.36}$$

By substituting Eq. (2.35) into Eq.(2.29), and solving for $\mathbf{X}$, the following expression is obtained:

$$\mathbf{X}(\omega) = \left\{ -\omega \mathbf{M} + j\omega \mathbf{C} + \mathbf{K} \right\}^{-1} \cdot \mathbf{h_1} F_1. \tag{2.37}$$

The physical parameters used in the simulation study presented in this chapter are summarized in Table 2.3.

Table 2.3: *Physical parameters for the elements in the SDOF system.*

Parameter	Value
Resonance frequency of the structure to be controlled	$f_{n1} = 40$ Hz
Resonance frequency of proof mass actuator	$f_{n2} = 15$ Hz
Mass of Structure to be controlled	$m_1 = 0.350$ Kg
Mass of the proof mass actuator	$m_2 = 0.030$ Kg
Stiffness of the structure to be controlled	$k_1 = 2.21 \ 10^4$ N/m
Stiffness of the proof mass actuator	$k_2 = 266.5$ N/m
Critical Damping of the structure to be controlled	$c_{c1} = 175.9$ N/ms^{-1}
Critical Damping of proof mass actuator	$c_{c2} = 5.65$ N/ms^{-1}
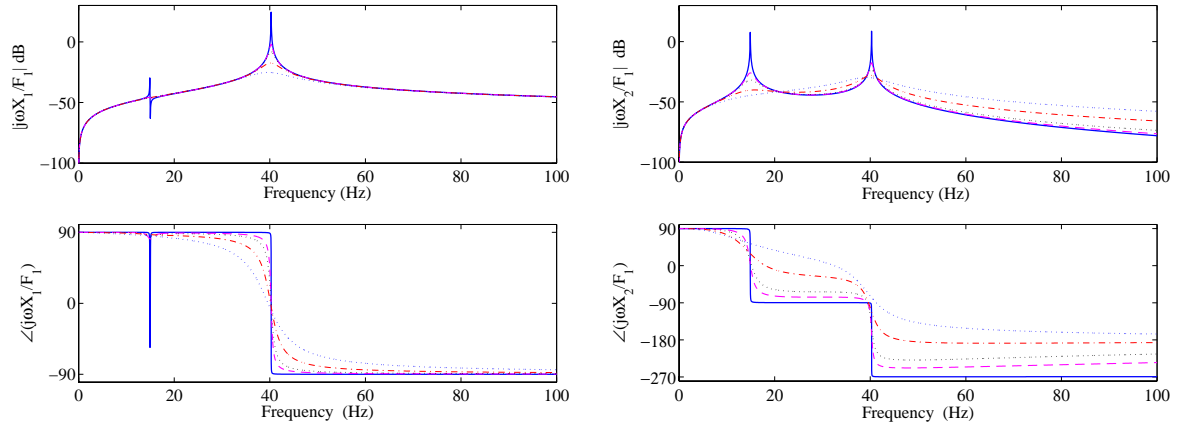
Figure 2.15: *Modulus and phase of the velocities per unit force F_1 of the system to be controlled (m_1) (left plots) and the proof mass actuator (m_2) (right plots) of the system shown in Figure 2.14(a) when there is no active vibration control considering different values of damping ratio; $\xi_{1,1}=0.0001$ and $\xi_{2,1}=0.001$ (solid line), $\xi_{1,2}=0.005$ and $\xi_{2,2}=0.05$ (dashed line), $\xi_{1,3}=0.01$ and $\xi_{2,3}=0.1$ (dotted line), $\xi_{1,4}=0.03$ and $\xi_{2,4}=0.3$ (dash-dot line) or $\xi_{1,5}=0.08$ and $\xi_{2,5}=0.8$ (dotted line).*

The mass and stiffness of the actuator has been chosen much smaller compared to that of the system to be controlled. In order to obtain the maximum vibration reduction a constant force actuation in the frequency of control, the natural frequency of the actuator must be lower than that frequency range [21]. Therefore, in order to control the response at the resonance frequency of the SDOF system under control the mass/stiffness ratio of the actuator should be selected in such a way as to keep the natural frequency of the actuator much lower than the natural frequency of the system to be controlled. As shown in Figure 2.15, the first resonance, at about 15 Hz, is primarily a control actuator resonance since $X_2 > X_1$. The second resonance, at about 40 Hz, is mainly linked to the response of the base

system to be controlled since $X_1 > X_2$. As seen for the SDOF problem, when the damping level in the system to be controlled, c_1, is increased then the response at its fundamental resonance frequency at about 40 Hz goes down although in this case there is no degrading effect at higher frequencies as was noted for the base vibration SDOF problem considered above.

2.6   SDOF system under harmonic force with a proof mass force feedback control loop

In this section the effects produced by the feedback control system are investigated. As done in the previous sections, different Control architectures will be studied; a) Proportional Control, b) Integral Control, c) Derivative Control, d) PID Control (Proportional–Integral–Derivative Feedback Control), e) PI Control (Proportional–Integral Feedback Control) and f) PD Control (Proportional–Derivative Feedback Control).
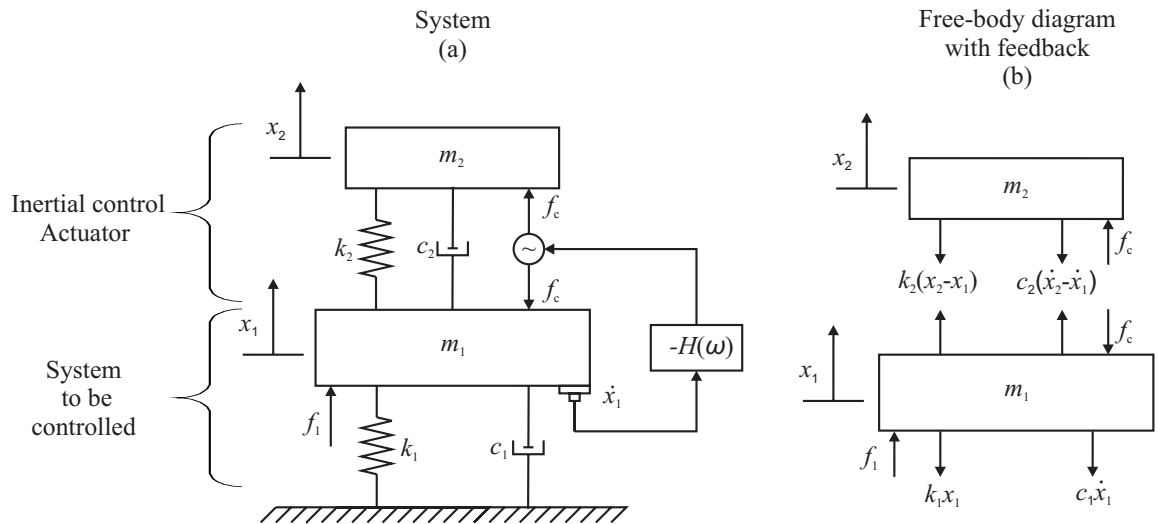
Figure 2.16: *Two DOF under harmonic force with feedback.*

In this case the response of the active system shown in Figure 2.16 will only be formulated in terms of mobility frequency response functions.

2.7   Stability analysis

As done in section 2.3, the stability of the feedback control loop will be assessed with reference to the Nyquist criterion considering the Bode and Nyquist plots of the open loop HY_{11} sensor–actuator frequency response function.
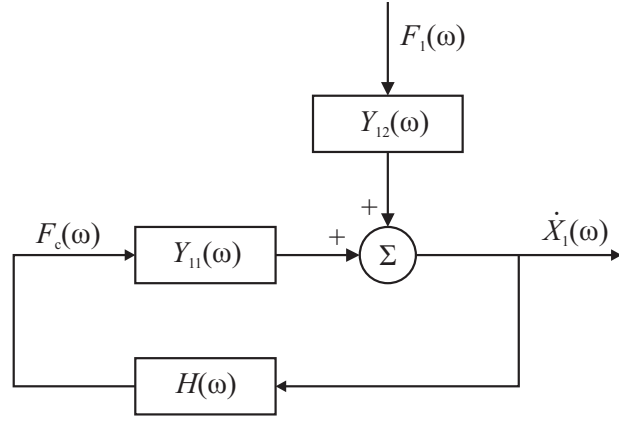
Figure 2.17: *Block diagram of Feedback Control implemented on the Two DOF system.*

Following the same procedure as in section 2.3, the response of the system shown in Figure 2.16 can be formulated in terms of mobility functions. From Figure 2.17 the following expression for $\dot{X}_1$ and control force F_c are obtained:

$$\dot{X}_1 = Y_{12}F_1 + Y_{11}F_c,$$ (2.38)

$$F_c = H(\omega)\dot{X}_1$$ (2.39)

where the mobility functions Y_{21} and Y_{22} are given by:

$$Y_{12} = \frac{\dot{X}_1}{F_1}\bigg|_{F_c=0} = j\omega \lfloor 1 \quad 0 \rfloor \left(\{-\omega\mathbf{M} + j\omega\mathbf{C} + \mathbf{K}\}^{-1} \cdot \mathbf{F} \right),$$ (2.40)

$$Y_{11} = \frac{\dot{X}_1}{F_c}\bigg|_{F_1=0} = j\omega \lfloor 1 \quad 0 \rfloor \left(\{-\omega\mathbf{M} + j\omega\mathbf{C} + \mathbf{K}\}^{-1} \cdot \left\{ \begin{matrix} -1 \\ 1 \end{matrix} \right\} \right),$$ (2.41)

and **F** is the excitation force vector defined by:

$$\mathbf{F} = \left\{ \begin{matrix} F_1 \\ 0 \end{matrix} \right\}.$$ (2.42)

The open loop sensor–actuator frequency response function HY_{11} depends on the specific control function H implemented in the feedback loop. The stability of the different control functions will be studied in the following subsections. Substituting Eq. (2.39) into

Eq.(2.38), and solving respect to the velocity of the mass to be controlled (m_1), the following expression is obtained:

$$\dot{X}_1 = \frac{Y_{12}}{1 + HY_{11}} F_1$$ (2.43)

where HY_{11} is the open loop frequency response function between the velocity sensor on the mass of the system to be controlled (m_1) and the control force. As anticipated in the previous chapter if $\mathrm{Re}(HY_{11}) > 0$, then Eq. (2.43) shows that $\dot{X}_1 / F_1 < 1$ for any control gain and frequency, that is the feedback control decrease the velocity of the base system for any control gain and frequency.

2.7.1 Proportional control

In order to implement negative velocity feedback, the output signal from the velocity control sensor on the mass of the structure to be controlled (m_1) is feedback to the actuator via a negative Proportional control function $H(\omega) = -g_P$, and thus:

$$F_c = -g_P \dot{X}_1 .$$ (2.44)

Figure 2.18 shows the amplitude–phase and Nyquist plots of the open loop sensor–actuator frequency response function HY_{11} in the frequency range between 0 and 100 Hz.
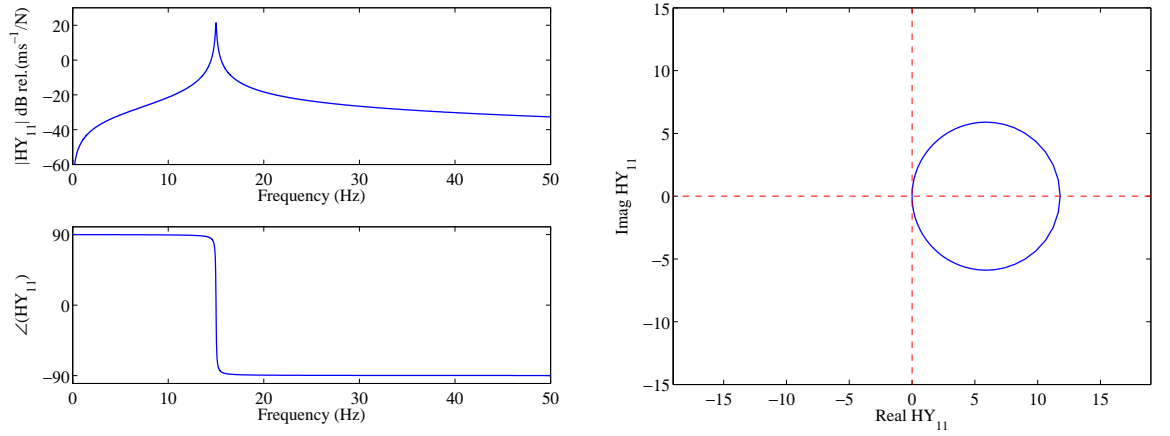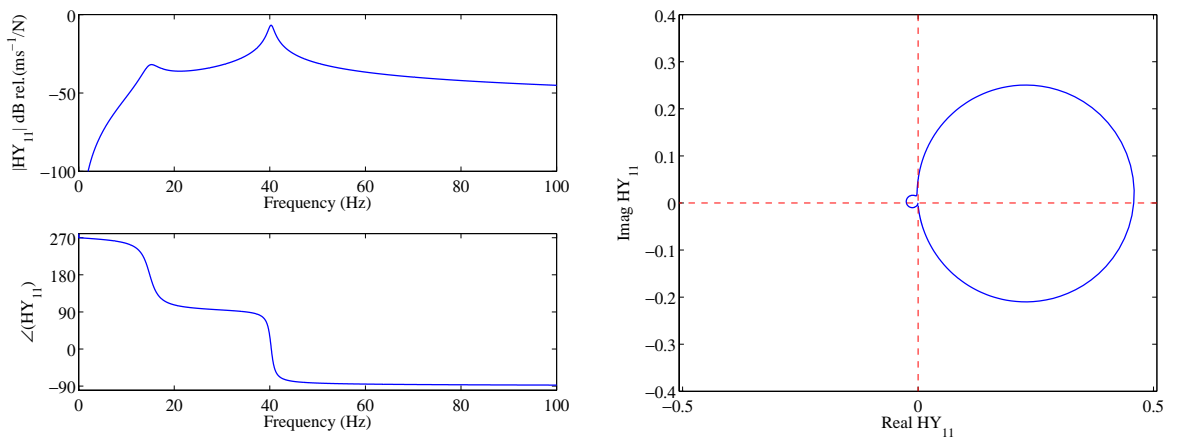

Figure 2.18: *Frequency response functions; amplitude (top left), phase (bottom left) and Nyquist plot (right) of the open loop sensor–actuator frequency response function in the frequency range between 0-100 Hz when a Proportional control is used.*

In this case, the Bode plot in Figure 2.18 indicates that the phase of the open loop sensor–actuator frequency response function starts from +270°, drops to +90° after the first resonance of the actuator and then goes to –90° after the resonance of the system to be controlled. Therefore the Nyquist plot shows two circles (one for each resonance); the left hand side circle is "controlled" by the resonance of the actuator and the right hand side circle is "controlled" by the resonance of the mass of the system to be controlled. The actuator circle is confined on the left hand side quadrants which suggest that the system is only conditionally stable. Indeed the Nyquist plot in Figure 2.18 indicates that for large control gains the Nyquist instability point (–1+j0) can be encircled, so that, the control system goes unstable.

2.7.2 Integral control

In order to implement negative displacement feedback, the output signal from the velocity control sensor on the mass to be controlled (m_1) is feedback to the actuator via a negative Integral control function $H(\omega)=-g_I/j\omega$, and thus:

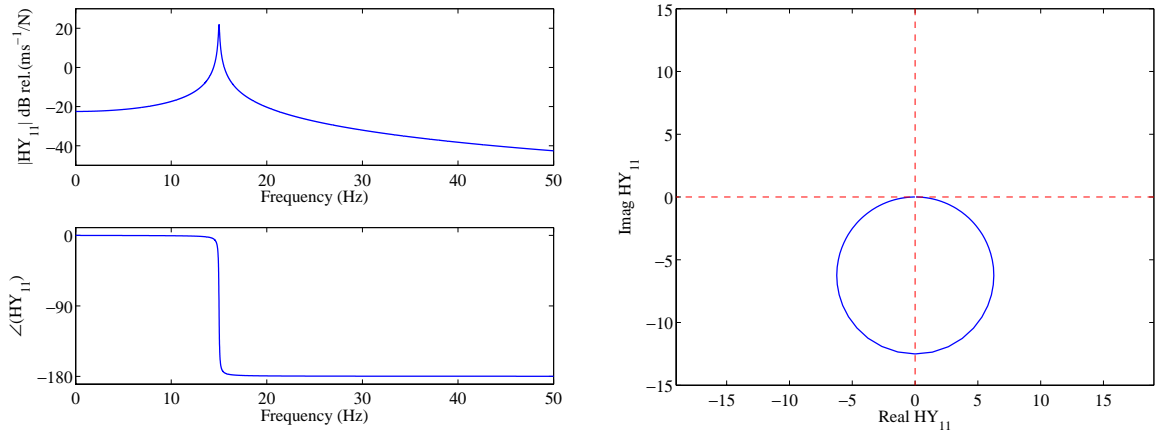$$F_c = -\frac{g_I}{j\omega}\dot{X}_1.$$ (2.45)
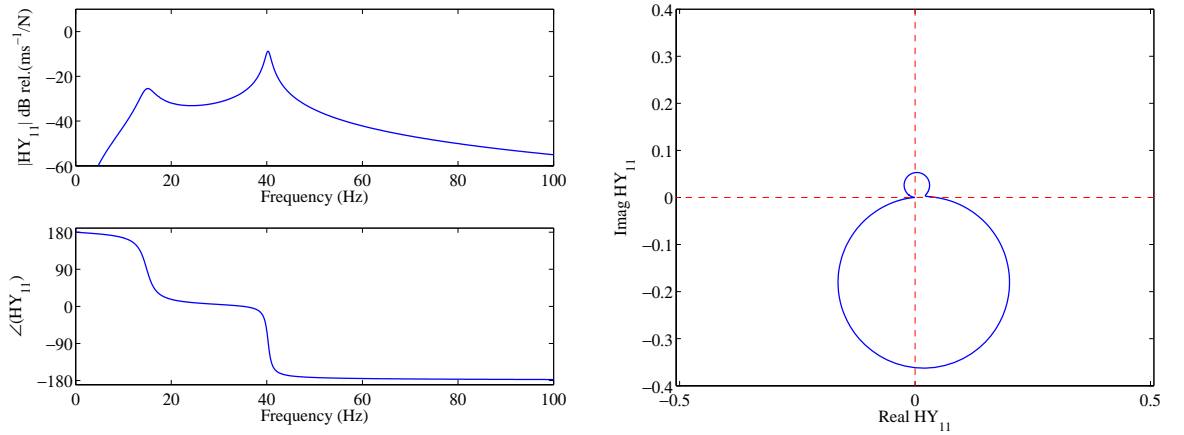
Figure 2.19: *Frequency response functions; amplitude (top left), phase (bottom left) and Nyquist plot (right) of the open loop sensor–actuator frequency response function in the frequency range between 0-50 Hz when an Integral control is used.*

In this case, the Bode plot in Figure 2.19 indicates that the phase of the open loop sensor–actuator frequency response function exceed +90° at lower frequencies below the resonance of the proof mass actuator and –90° at higher frequencies above the resonance of the mass to

be controlled. This is due to the fact that with Integral Control the system adds $-90°$ phase lag to the open loop sensor–actuator response function of the Proportional control system. Therefore the Nyquist plot shows two circles one on the top side quadrants, which is due to the actuator resonance, and the other on the bottom side quadrants, which is due to the resonance of the system to be controlled. Considering the details of the Nyquist plot at low frequency, it is found that the locus does not cross over the real negative axis. Thus the system can be considered unconditionally stable, although the vicinity of the locus with the real negative axis suggests that the control system could go unstable, both at low and high frequency. In fact part of the circles are very close to the Nyquist instability point $(-1+j0)$ and thus even with little variations of the response function which can be easily generated by external factors the system can become unstable. Besides, the two circles enter the spillover circle so that the control spillover effects are likely to happen at low and high frequencies when the high control gains are implemented. The larger size of the lower loop suggests that the spillover effect associated to the second resonance, and thus at higher frequencies, is likely to be more effective.

2.7.3 Derivative Control

In order to implement negative acceleration feedback, the output signal from the velocity control sensor on the mass to be controlled (m_1) is feedback to the actuator via a negative Derivative control function $H(\omega)=-g_D j\omega$, and thus:

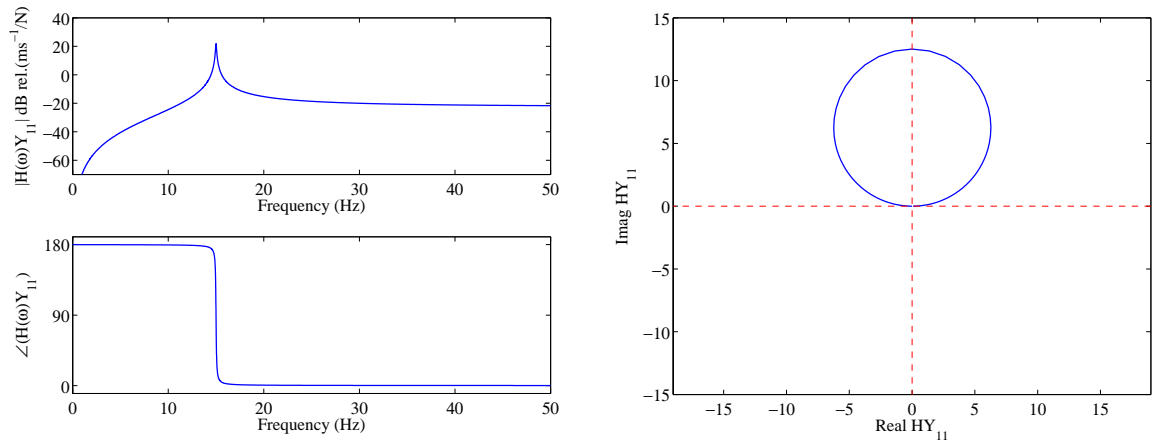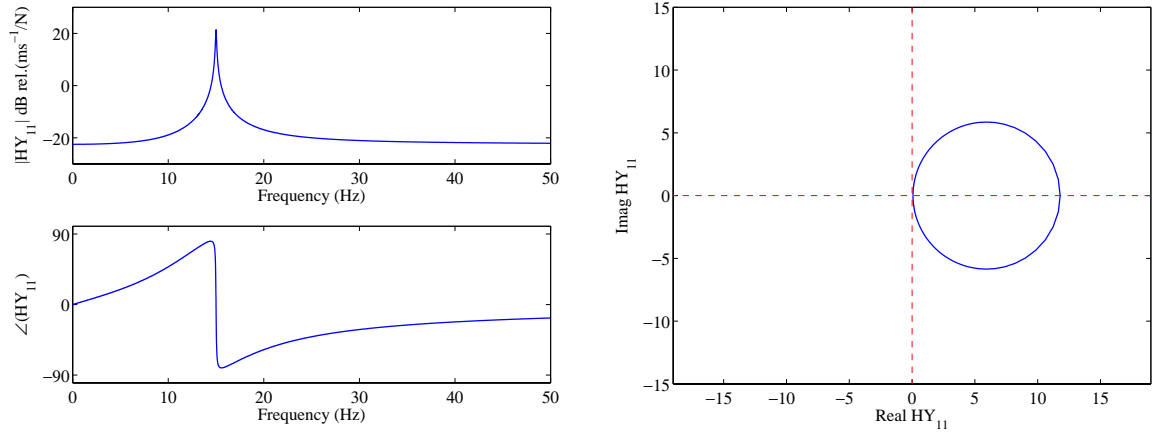$$F_c = -j\omega g_D \dot{X}_1 \tag{2.46}$$
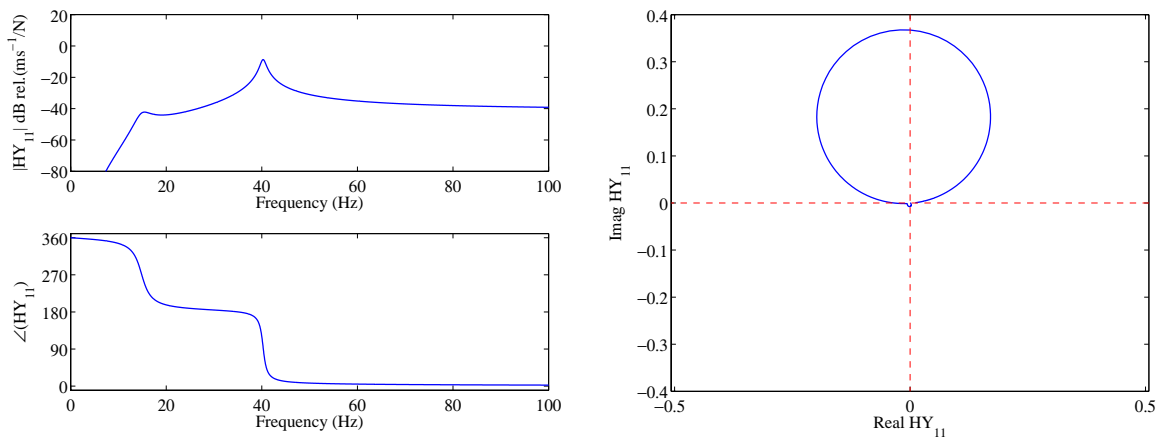
Figure 2.20: *Frequency response functions; amplitude (top left), phase (bottom left) and Nyquist plot (right) of the open loop sensor–actuator frequency response function in the frequency range between 0-100 Hz when a Derivative control is used.*

In this case, the Bode plot in Figure 2.20 indicates that the phase of the open loop sensor–actuator frequency response function is about +360° at lower frequencies below the resonance frequency controlled by the actuator. This is due to the fact that with Derivative Control the system adds +90° phase lead to the Proportional system.

Therefore the Nyquist plot in Figure 2.20 shows two circles one on the top side quadrants due to the resonance of the system to be controlled and another much smaller on the bottom side quadrants due to the resonance of the proof mass actuator. According to the plot in Figure 2.20, the locus crosses over the real negative axis, thus the system is only conditionally stable and thus for too high control gains could go unstable. Similarly to the previous control case, control spillover is likely to happen both at low and higher frequencies although, as seen for the integral control the larger size of the top circle indicates that the bigger spillover effect occurs at higher frequencies.

2.7.4 PID Control

In order to implement a combination of negative displacement velocity and acceleration feedback control, the output signal from the velocity sensor on the mass to be controlled (m_1) is feedback to the control force actuator via a negative mix of Proportional–Integral–Derivative control function $H(\omega) = -g\{ k_P + k_I/j\omega + j\omega k_D\}$ and thus:

$$F_c = -g\left\{ k_P + \frac{k_I}{j\omega} + j\omega k_D \right\} \dot{X}_1 \tag{2.47}$$

where k_P, k_I and k_D are Proportional, Integral and Derivative Control constants respectively and their values are summarized in Table 2.4. Figure 2.21 shows the spectrum of this control function.

Figure 2.21 shows that a) at the second resonance $H(\omega)$ is a proportional function controls the response; b) below the second resonance $H(\omega)$ is an integral function, and c) above resonance the second resonance $H(\omega)$ is a derivative function.
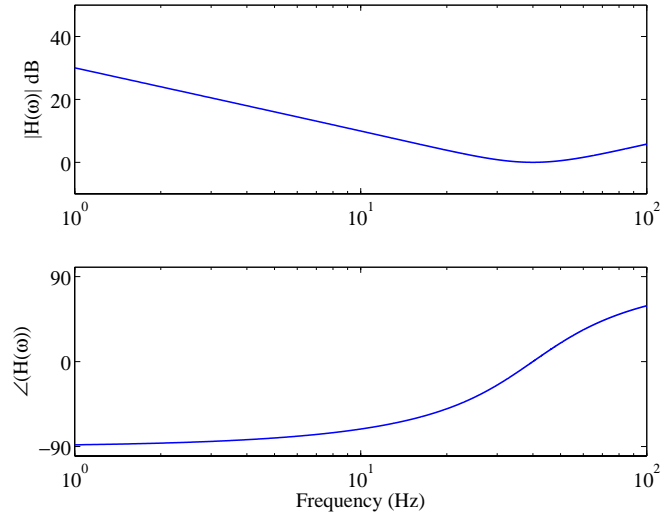
Figure 2.21: Control *function when a PID Control is used.*

Table 2.4: *Physical parameters for the Proportional, Integral and Derivative Control constants used in the two DOF system.*

Parameter	Value
Proportional Control Constant	$k_P = 1$
Integral Control Constant	$k_I = 1000$
Derivative Control Constant	$k_D = 0.01583$

The Integral and Derivative Control constants have been chosen in such a way to maintain constant the undamped resonance frequency of the system to be controlled.
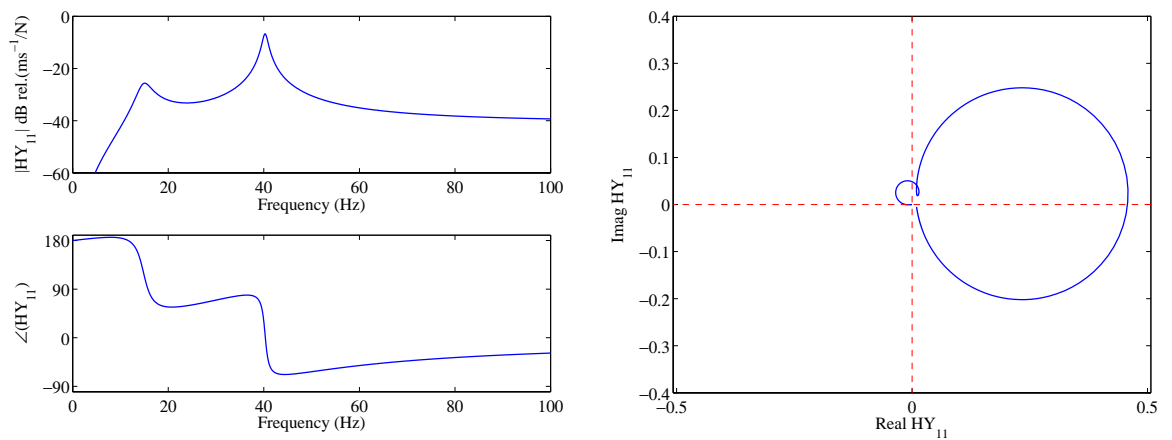
Figure 2.22: *Frequency response functions; amplitude (top left) and phase (bottom left). Nyquist plot (right plot) for the frequency response functions between a collocated ideal velocity sensor in the mass to be controlled (m_1) and force actuator in the 0-100 Hz frequency range in a two DOF when a PID Control is used.*

The Bode plot in Figure 2.22 shows that the phase of the open loop response is about 180º below the first resonance of the actuator, it then goes down to about 0º and rises to +45º at about the second resonance linked to the system to be controlled. Finally it moves down to –45º above this resonance and it gradually moves back to 0º as the frequency rises.

Therefore the Nyquist plot in Figure 2.22 shows two circles one on the right hand side quadrants due to the resonance of the system to be controlled and other much smaller on the top side quadrants due to the resonance of the proof mass actuator. The zoom of the Nyquist plot shown in Figure 2.23 indicates that the sensor–actuator response function does not cross over the real negative axis. Thus the system is unconditionally stable, although the locus is very close to the real negative axis at low frequency so that external disturbances could easily lead to instability problems.
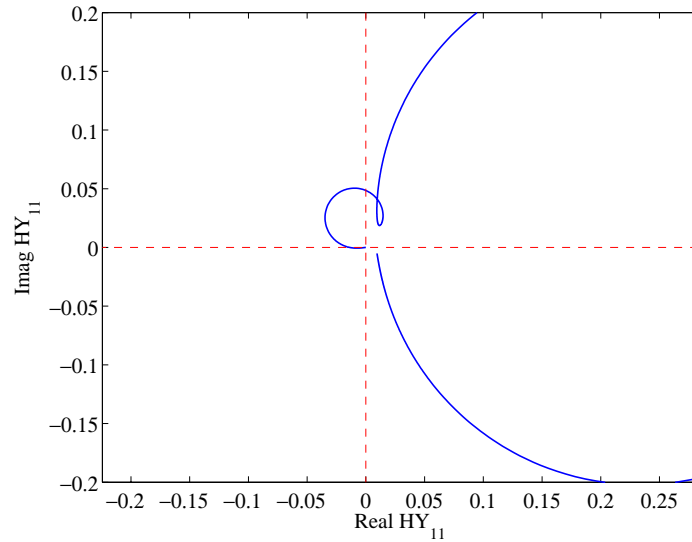
Figure 2.23: *Zoom of the Nyquist plot shown in Figure 2.22.*

In order to keep the same resonance frequency of the base system, the proportional k_I and derivative k_D constants have been chosen in such a way to satisfy the following relation:

$$
\begin{aligned}
\omega_n^2 = \frac{1}{2} & \left\{ \frac{\left(\left(k_1 + k_I \right) + k_2 \right) m_2 + k_2 \left(m_1 + k_D \right)}{\left(m_1 + k_D \right) m_2} \right\} \\
& + \frac{1}{2} \sqrt{ \left\{ \frac{\left(\left(k_1 + k_I \right) + k_2 \right) m_2 + k_2 \left(m_1 + k_D \right)}{\left(m_1 + k_D \right) m_2} \right\}^2 - 4 \left\{ \frac{\left(\left(k_1 + k_I \right) + k_2 \right) k_2 - k_2^2}{\left(m_1 + k_D \right) m_2} \right\} }
\end{aligned}
$$

(2.48)

where ω_h is the second natural frequency which is primarily linked to the vibration of the base system. As a result, the integral constant k_I is much higher than the derivative constant k_D so that the integral control effect at higher frequencies is likely to be more effective than the derivative control at lower frequencies.

2.7.5 PI Control

In order to implement a combination of negative velocity and displacement feedback the output signal from the velocity control sensor in the mass to be controlled (m_1) is feedback to the control force actuator via a negative combination of Proportional–Integral control function $H(\omega)= -g\{ k_P + k_I/j\omega\}$ and thus:

$$F_c = -g\left\{ k_P + \frac{k_I}{j\omega}\right\} \dot{X}_1 \qquad (2.49)$$

where k_P and k_I are Proportional and Integral constants respectively and their values are summarized in Table 2.4. Figure 2.24 shows the spectrum of the control function.
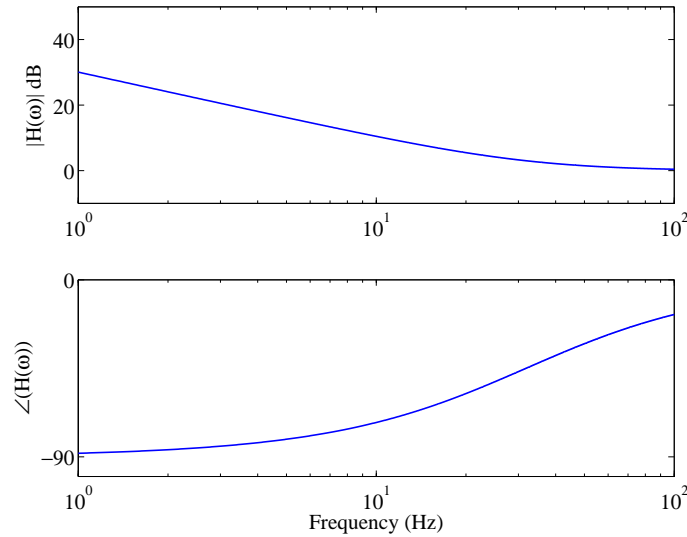
Figure 2.24: *Control function when a PI Control is used.*

Figure 2.24 shows that up to approximately 50 Hz the Integral function controls the response which then starts to move towards a Proportional function.
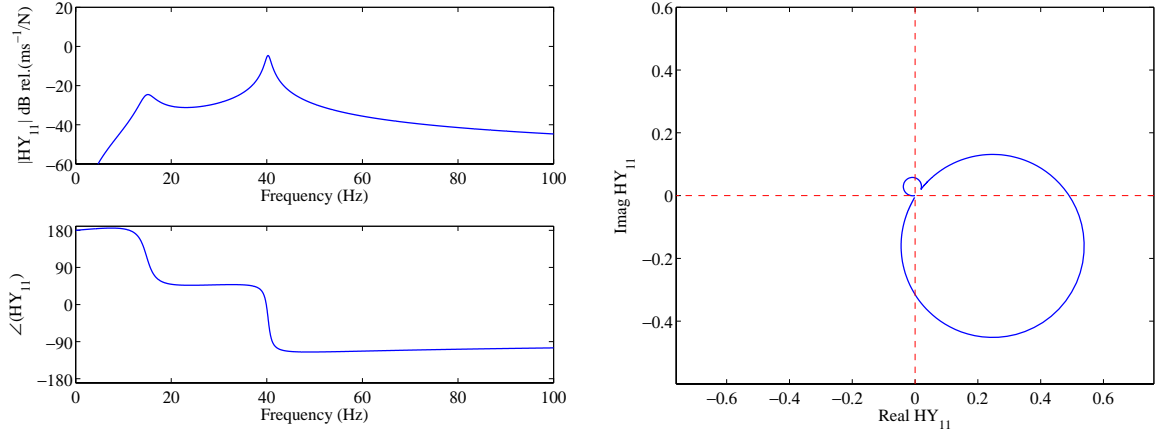
Figure 2.25: *Frequency response functions; amplitude (top left) and phase (bottom left). Nyquist plot (right plot) for the frequency response functions between a collocated ideal velocity sensor in the mass to be controlled and force actuator in the 0-100 Hz frequency range in a two DOF when a PI Control is used.*

As shown in Figure 2.25, in this case the Bode plot indicates that the phase of the open loop sensor–actuator frequency response function exceed +90° at lower frequencies below the resonance frequency of the proof mass actuator and –90° at higher frequencies above the resonance frequency of the system to be controlled. This is due to the fact that with PI Control the system adds almost –90° phase lag to the open loop frequency response function of the proportional control loop.
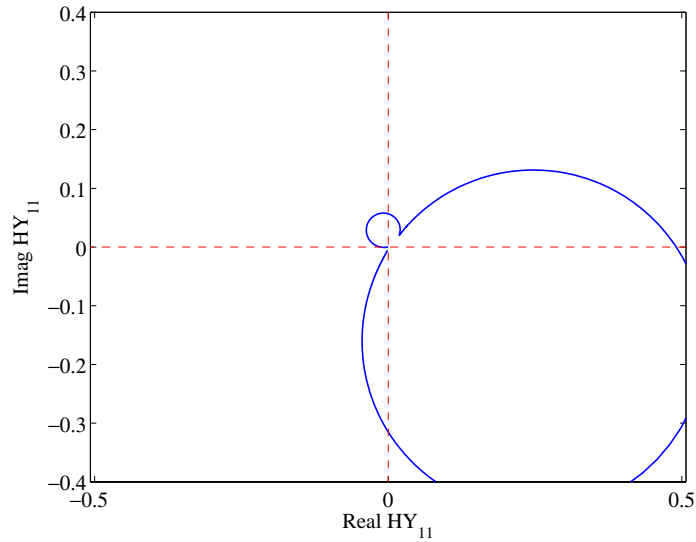
Figure 2.26: *Zoom of the Nyquist plot shown in Figure 2.26.*

The Nyquist plot shows two circles one on the top side quadrants due to the actuator resonance and the other on the bottom side quadrants due to the resonance of the system to be controlled. As shown in the zoom of Figure 2.26 the actuator circle is turned clockwise

away from the Nyquist instability point (–1+j0). The big loop due to the resonance of the system under control is also turned clockwise although not enough to threaten stability. In conclusion PI control enhances the stability although it should degrade the control effectiveness since the circle linked to resonance of the system under control is not aligned along the real positive axis.

2.7.6 PD Control

In order to implement a combination of negative velocity and acceleration feedback the output signal from the velocity control sensor on the mass to be controlled (m_1) is feedback to the control force actuator via a negative combination of Proportional–Derivative control function $H(\omega) = -g\{ k_P + j\omega k_D\}$ and thus:

$$F_c = -g\left\{k_P + j\omega k_D\right\} \dot{X}_1 \tag{2.50}$$

where k_P and k_D are Proportional and Derivative Control gains respectively and their values are summarized in Table 2.4. Figure 2.27 shows that below about 40 Hz $H(\omega)$ is proportional function while at higher frequencies above 10 Hz it is a derivative function.
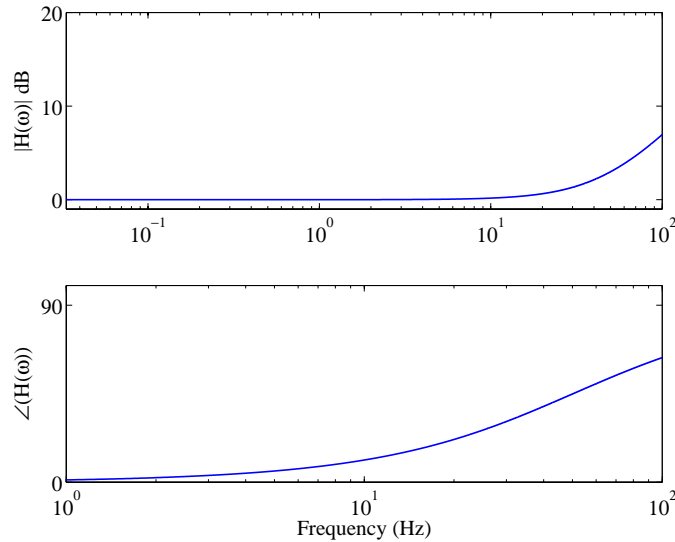
Figure 2.27: *Control function when a PD Control is used.*
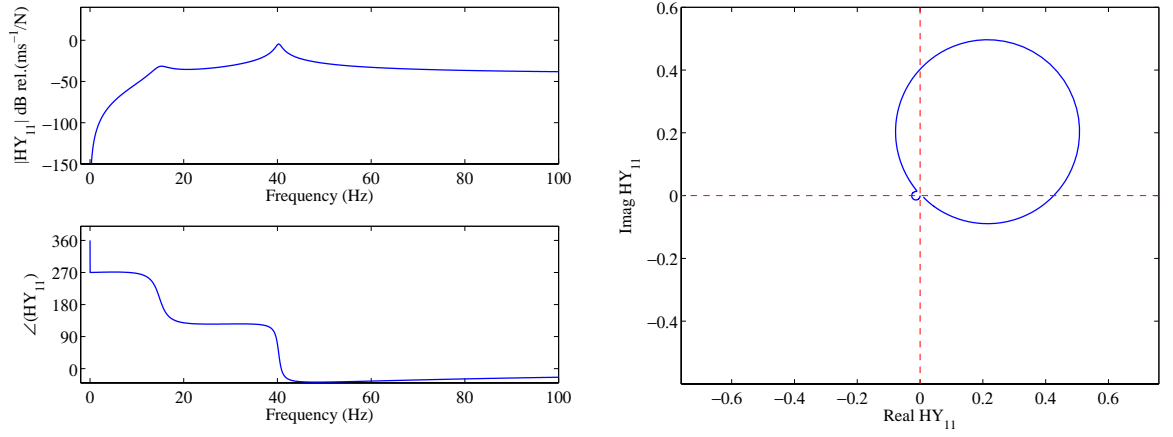
Figure 2.28: *Frequency response functions; amplitude (top left) and phase (bottom left). Nyquist plot (right plot) for the frequency response functions between a collocated ideal velocity sensor in the mass to be controlled and force actuator in the 0-100 Hz frequency range in a two DOF when a PD Control is used.*

In this case the Bode plot in Figure 2.28 indicates that the phase of the open loop sensor–actuator frequency response function exceed even 180° at lower frequencies below the resonance frequency of the proof mass actuator. This is due to the fact that with PD Control the system adds almost +90° phase lead to the open loop sensor–actuator frequency response function of the proportional control.

Therefore as shown in Figure 2.28 the Nyquist plot show two circles one on the top side quadrants due to the resonance of the base system to be controlled and the other much more smaller on the bottom side quadrants due to the resonance of the proof mass actuator.
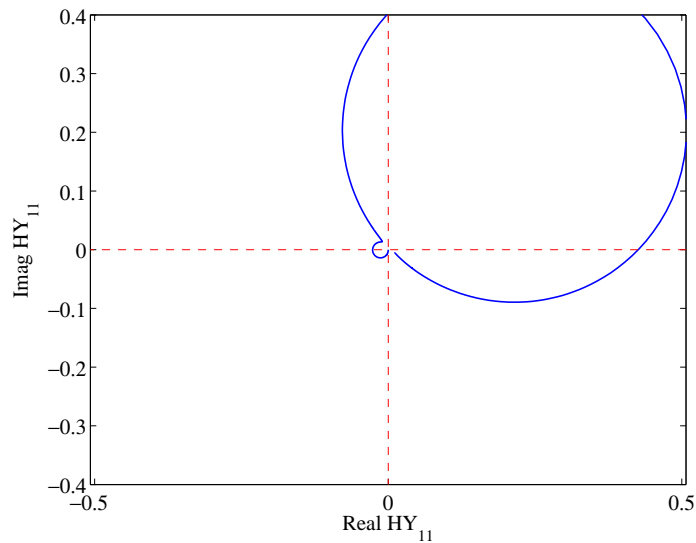
Figure 2.29: *Zoom of the Nyquist plot shown in Figure 2.28.*

The zoom in Figure 2.29, shows that the circle due to the low frequency actuator clearly intersects the real–negative axis which indicates that the system is conditionally stable and thus for too large control gains the system may go unstable.

2.8 Control performances

In this section the control performances for the various control architectures discussed in the previous section will be studied. In the following points the ratio between the velocity of the mass of the system to be controlled (m_1) and the harmonic force F_1, $\dot{X}_1/F_1 = Y_{12}/(1 + HY_{11})$ will be plotted with reference to the various $H(\omega)$ control function.

2.8.1 Proportional Control

Figure 2.30 shows the active control effects produced by a proportional control function $H(\omega) = -g_P$. From this figure it is possible to highlight that the addition of small amounts of control gain lead to large reductions of response at the resonance of the system to be controlled. This is because the control force generated by the proof mass actuator produces an active damping effect that, as seen in the previous chapter, tends to reduce the vibration of the base system at resonance frequencies. However it also produces a spillover effect at the proof mass actuator resonance as was highlighted by the left hand side circle in the Nyquist plot in Figure 2.18.
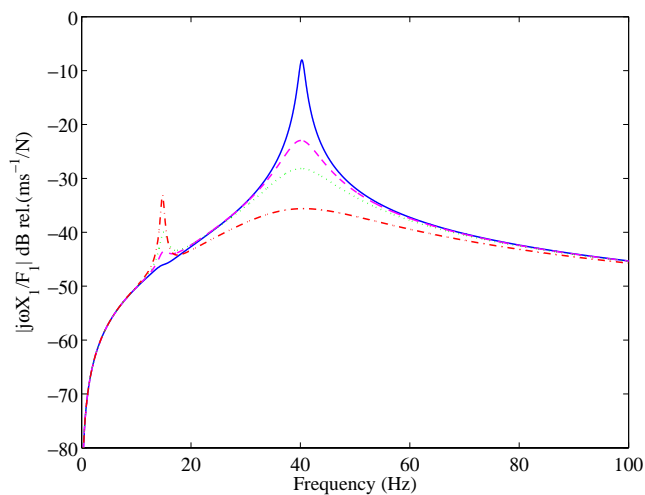
Figure 2.30: *Modulus of the ratio between velocity of the mass of the system to be controlled and the harmonic force of the system shown in Figure 2.16(a) when a Proportional Control is used and different values of gain; $g_1=0$; no-gain (solid line), $g_2=10$ (dashed line), $g_3=50$ (dotted line) or $g_4=100$ (dash-dot line).*

2.8.2 Integral Control

Figure 2.31 shows the effect of an Integral control function $H(\omega) = -g_I/j\omega$. From this Figure it is possible to highlight that Integral control adds "Active Stiffness" moving the resonance frequency of the system to be controlled to higher values and the resonance frequency of the actuator to lower values. Thus the system produces vibration reductions at low frequencies below the resonance of the system to be controlled, also spillover on the resonance of the actuator is generated as indicated by the Nyquist plot in Figure 2.19.
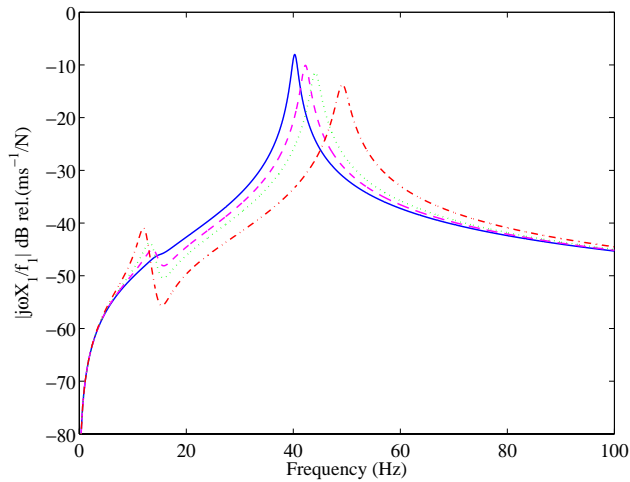
Figure 2.31: *Modulus of the ratio between velocity of the mass of the system to be controlled and harmonic force of the system shown in Figure 2.16(a) when a Integral Control is use and different values of gain; $g_1=0$; no-gain (solid line), $g_2=10$ (dashed line), $g_3=20$ (dotted line) or $g_4=60$ (dash-dot line).*

2.8.3 Derivative Control

Figure 2.32 shows the effects generated by a Derivative control function $H(\omega) = -j\omega g_D$.
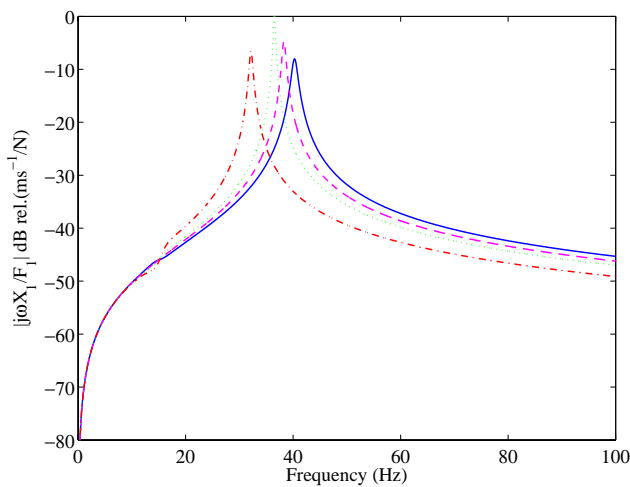
Figure 2.32: *Modulus of the ratio between velocity of the system to be controlled and harmonic force of the system shown in Figure 2.16(a) when a Derivative Control is use and different values of gain; $g_1=0$; no-gain (solid line), $g_2=10$ (dashed line), $g_3=20$ (dotted line) or $g_4=60$ (dash-dot line).*

In this case Derivative Control adds "Active Mass" moving the resonance of the structure to be controlled to lower values, so that vibration reductions are produced at higher frequencies above the resonance of the system to be controlled. Also the resonance frequency of the actuator is moved up so that for high control gain it merges with the resonance of the system to be controlled which, is actually decreasing under the effect of the active control action.

2.8.4 PID Control

Figure 2.33 shows the control effects generated by a combination of Proportional–Integral–Derivative functions; $H(\omega) = -g\{k_P + k_I / j\omega + j\omega k_D\}$. This Figure highlights that PID Control adds: "Active damping", "Active Stiffness" and "Active mass" keeping constant the resonance of the system to be controlled. This system produces vibration reductions in the three regions; below, at and above the resonance of the structure to be controlled. Also, it produces large control spillover effect at the actuator resonance. However the control performance of this loop is not limited by stability as it was seen in section 2.7.
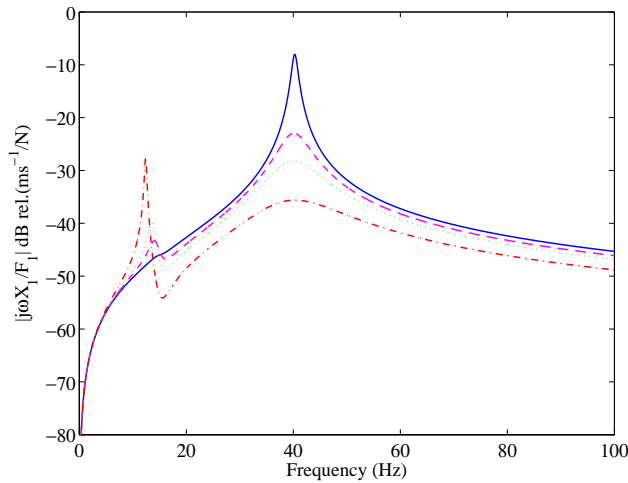
Figure 2.33: *Modulus of the ratio between velocity of the system to be controlled and the harmonic force of the system shown in Figure 2.16(a) when a PID Control is use and different values of gain; g_1=0; no-gain (solid line), g_2=10 (dashed line), g_3=20 (dotted line) or g_4=60 (dash-dot line).*

2.8.5 PI control

Figure 2.34 shows the control effects produced by a combination between Proportional–Integral functions; $H(\omega) = -g\{k_P + k_I / j\omega\}$. This figure highlights that PI Control adds "Active damping" and "Active Stiffness" moving the resonance of the system to be

controlled to higher values. This Control moves down the resonance of the actuator and produces spillover due to the Integral Control effect at low frequencies. Thus, the system produces vibration reductions in two regions; below and at resonance of the system to be controlled. However PI control slightly detriment the response above the resonance of the system to be controlled.
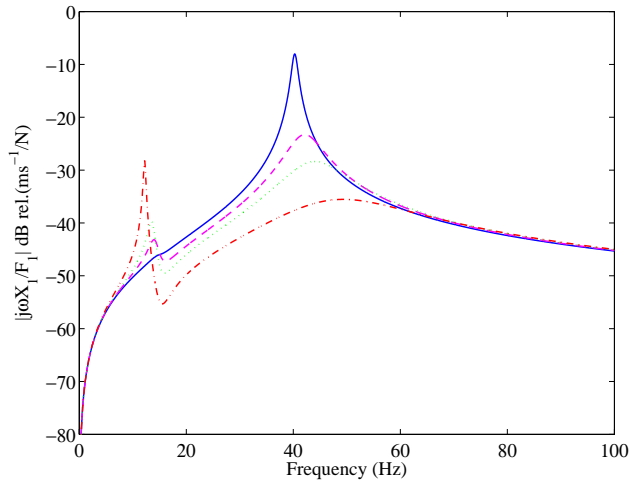
Figure 2.34: *Modulus of the ratio between velocity of the system to be controlled and harmonic force of the system shown in Figure 2.16(a) when a PI Control is use and different values of gain; g_1=0; no-gain (solid line), g_2=10 (dashed line), g_3=20 (dotted line) or g_4=60 (dash-dot line).*

2.8.6 PD Control

Figure 2.35 shows the control effects produced by a combination between a Proportional–Derivative functions; $H(\omega) = -g\{k_P + j\omega k_D\}$.
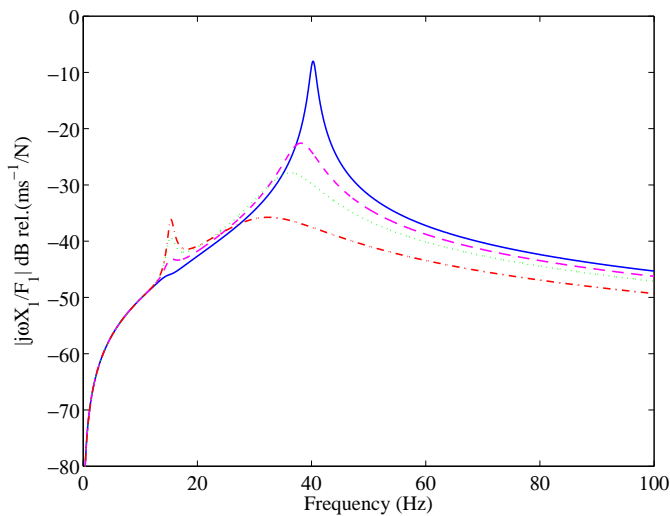
Figure 2.35: *Modulus of the ratio between velocity of the system to be controlled and harmonic force of the system shown in Figure 2.16(a) when a PD Control is use and different values of gain; g_1=0; no-gain (solid line), g_2=10 (dashed line), g_3=20 (dotted line) or g_4=60 (dash-dot line).*

This figure highlights that PD Control adds "Active damping" and "Active mass" moving the resonance of the system to be controlled to lower values. Also the resonance of the actuator is moved up, so that for high control gain it merges with the resonance of the system as it was explained above in Derivative Control case. Thus, the system produces vibration reductions in two regions; at and above the resonance of the system to be controlled.

2.9 Summary

This chapter has presented the modelling of two simple feedback controllers on a SDOF system using either a reactive force actuator or a proof mass force actuator. For each system, the effect produced by velocity, displacement, acceleration, a combination among the three or between two of them control loops have been considered in detail.

In the first part of the chapter; sections 2.1 and 2.2, the first control problem is considered, which consists of a single degree of freedom (SDOF) system under harmonic motion of the base. In these sections the inconveniences of using a passive control and the advantages of employing active control are highlighted. Passive control shows that the addition of small amounts of damping leads to important reductions of the response at resonance but also detriment the response at higher frequencies. The effects of active control depend on which control function is implemented. For instance the vibration response could be reduced at resonance (Proportional Control, i.e. active damping), below resonance (Integral Control, i.e. active stiffness), above resonance (Derivative Control, i.e. active mass) and below, at and above resonance (PID Control, i.e. active damping–stiffness–mass) without detriment in the others regions. However the control performances of theses loops are limited by stability. Proportional and PID control are unconditionally stable and do not show control spillover effects. Integral and Derivative Control are also unconditionally stable but affected by control spillover effect respectively at higher or lower frequencies.

The second part of this chapter introduces the control of a SDOF mechanical system with a proof mass actuator. As an example, the SDOF system to be controlled could be a simplified model of a simple supported plate taking into account just one mode of vibration. In this case, stability problems due to the actuator dynamics have been found, since the actuator adds a new resonance frequency which produces an extra 180° phase lag in the sensor–actuator frequency response function. As a result, proportional and PD

controls are not anymore unconditionally stable. Thus only a limited range of control gains can be implemented with, in any case, control spillover effects at the actuator resonance. In order to reduce this stability and control spillover problem, this resonance should be much lower than the resonance to the system to be controlled. In general PID feedback control can avoid this instability problem leaving unaltered the control performance.

3   MODELLING AND STUDY OF SMART PANELS WITH DECENTRALISED FEEDBACK CONTROL USING PROOF MASS ELECTRODYNAMIC ACTUATORS

The objective of this chapter is to study in a consistent framework the principal stability and control performance properties of decentralised feedback control loops on a thin panel using proof-mass force actuators with base velocity sensors. The aim is to develop a simple and robust multichanel feedback control system formed by an array of decentralised control units that implement basic feedback laws, which can be straightforwardly implemented with analogue control circuits. Previous work has shown that, in order to generate significant reductions of the spatially average response and sound radiation of a panel at low audio-frequencies, i.e. up to 1 kHz, a rather dense array of decentralised control units should be used [28]. Thus it is essential to investigate the feasibility of light and low cost control units to be attached in large numbers on flexible structures. In this chapter attention is focused on direct single channel feedback control loops with fixed feedback gains, which can be implemented by simple and robust analogue controllers. The theoretical study is based on a fully coupled electromechanical model of the proof-mass electro-dynamic actuators and plate structure that includes the back electromotive effect of the coil transducer. As discussed in this chapter, this plays an important role on the stability properties of the feedback control loops.

The principal stability features of Proportional, Integral, Derivative, PI, PD and PID feedback control laws are first analyzed using the Nyquist criterion. The control performances produced by these feedback control laws are then assessed in terms of the total kinetic energy of the panel which gives an indication of its spatially averaged vibration. The stability and control performance results are interpreted in terms of mass, stiffness and damping laws, which provide a physical insight of the six control approaches considered. Particular attention is dedicated to the passive effects of the mechanical and electrical components of the actuator on stability and performance of the control system. In this way, general guidelines are provided for the design of simple feedback control loops using proof-mass force actuators with base velocity sensors.

The chapter is structured into four sections. Section one presents the mobility model that has been developed to take into account the fully coupled response between the five

control units and the panel. The dynamic effects of the principal components of the proof-mass actuator, i.e. base mass, suspension spring and proof-mass, have been taken into account. Also, the fully coupled electro-magnetic response of the coil-magnet linear motor has been modelled for two cases where the coil is either current- or voltage-driven. In section two, the stability of a single and five decentralised control units is then analysed using the classic and generalized Nyquist criteria respectively [15,19]. In section three, the global control performances produced by just one or five decentralised control units are presented and discussed in terms of the kinetic energy of the panel.

3.1 Model problem

The system studied in this chapter is shown in Figure 3.1; it consists of a simply supported rectangular plate with five decentralised feedback vibration control units. Each control unit is made of a proof-mass electro-dynamic actuator with an ideal velocity error sensor at its base. The velocity error signal is fed back to the actuator by a voltage or current amplifier which implements the six feedback laws for Proportional, Integral, Derivative, PI, PD and PID control. The material and geometrical properties of the aluminium panel and electro–mechanical components of the proof-mass actuators are summarised in Table 3.1 and 3.2.
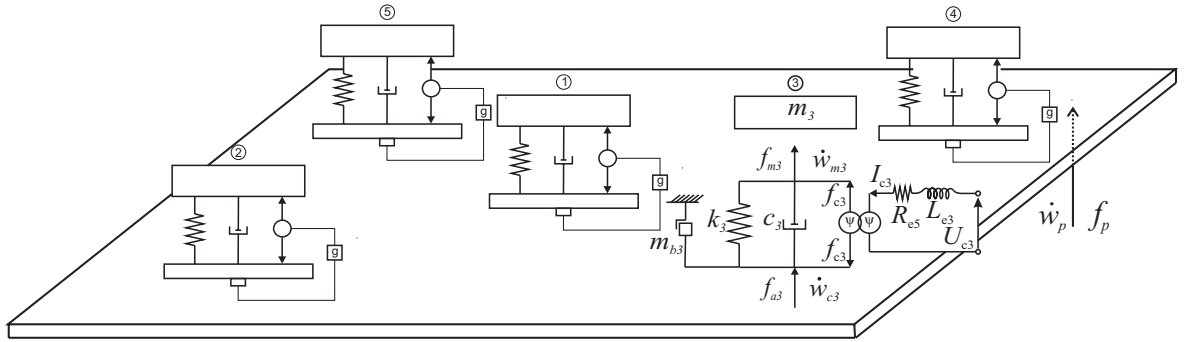
Figure 3.1: *Schematic view of the smart panel with five control units made of a proof-mass electro-dynamic actuator with an ideal velocity error sensor at its base.*

The steady–state spatially averaged flexural response of the rectangular panel when it is excited by a harmonic primary force will be used as a model problem to illustrate the active vibration control effects produced by mounting on the panel either one or five control units. As shown in Figure 3.1, the panel has been modelled as a distributed structure while the electro-mechanical components of the control units have been modelled by lumped mechanical and electrical elements.

Table 3.1: *Geometry and physical parameters for the panel.*

Parameter	Value
Dimensions	l_x x l_y = 0.414 x 0.314 m
Thickness	h_s = 1mm
Mass density	ρ_s = 2700 kg/m^3
Young's modulus	E_s = 7.1x10^{10} N/m
Poisson ratio	v_s = 0.33
Loss factor	η = 0.02
Position of the primary excitation	x_p, y_p = 0.341m , 0.246m
Position of the control system 1	x_{c1}, y_{c1} = 0.207m, 0.156m
Position of the control system 2	x_{c2}, y_{c2} = 0.129m, 0.095m
Position of the control system 3	x_{c3}, y_{c3} = 0.274m, 0.095m
Position of the control system 4	x_{c4}, y_{c4} = 0.274m, 0.206m
Position of the control system 5	x_{c5}, y_{c5} = 0.129m, 0.206m

Table 3.2: *Physical parameters for the actuators.*

Parameter	Value
Moving mass	m_i = 0.022 Kg
Housing mass	$m_{b\,i}$ = 0.008 Kg
Suspension stiffness	k_i = 86.85 N/m
Suspension damping	c_i = 2.76 N/ms^{-1}
Natural frequency	$f_{n,i}$ = 10 Hz
Transducer coefficient of the coil	Ψ_i = 2.6 N/A
Resistance of the coil	$R_{e,i}$ = 20 Ω
Inductance of the coil	$L_{e,i}$ = 0.002 H

The steady state response of the panel has been derived assuming the primary force disturbance to be harmonic, with time dependence of the form Re{exp($j\omega t$)} where ω is the circular frequency and $j = \sqrt{-1}$. The mechanical and electrical functions in the model have therefore been taken to be the real part of anticlockwise rotating complex vectors $x(\omega)$, i.e., phasor, given in the form Re$\{x(\omega)e^{j\omega t}\}$. The phasors of velocity and acceleration time harmonic functions have been denoted by $\dot{x}(\omega) = j\omega x(\omega)$ and $\ddot{x}(\omega) = j\omega \dot{x}(\omega)$. For brevity, the term phasor will be omitted in the text and the mechanical and electrical functions will all be assumed to be phasors.

Considering the notation shown in Figure 3.1, the transverse velocities at the error control positions, $\dot{w}_{cr}(\omega)$, have been grouped into a column vector $\dot{\mathbf{w}}_c(\omega) = \lfloor \dot{w}_{c1}(\omega) \quad \cdots \quad \dot{w}_{c5}(\omega) \rfloor^T$. The flexural vibration at these error positions can be expressed in terms of the primary force, $f_p(\omega)$, and the column vector $\mathbf{f}_a(\omega) = \lfloor f_{a1}(\omega) \quad \cdots \quad f_{a5}(\omega) \rfloor^T$ with the secondary excitations generated by the proof-mass actuators, $f_{as}(\omega)$, with the following mobility matrix relation:

$$\dot{\mathbf{w}}_c = \mathbf{Y}_{cc}\mathbf{f}_a + \mathbf{Y}_{cp}f_p . \tag{3.1}$$

The elements in the two mobility matrices Y_{cc} and Y_{cp}, can be expressed with the following modal expansions [44]:

$$Y_{cc,rs}(\omega) = j\omega\sum_{n=1}^{N}\frac{\phi_n(x_{c,r},y_{c,r})\phi_n(x_{c,s},y_{c,s})}{\Lambda\left[\omega_n^2(1+j\eta)-\omega^2\right]}, \tag{3.2}$$

$$Y_{cp,r}(\omega) = j\omega\sum_{n=1}^{N}\frac{\phi_n(x_{c,r},y_{c,r})\phi_n(x_p,y_p)}{\Lambda\left[\omega_n^2(1+j\eta)-\omega^2\right]}, \tag{3.3}$$

with $r,s=1$, ... , 5. In these equations (x_p,y_p) are the coordinates of the primary excitation and $(x_{c,r},y_{c,r})$, $(x_{c,s},y_{c,s})$ are the coordinates of the rth and sth control positions respectively; $\Lambda = \rho_s h_s l_x l_y /4$ is the modal normalization factor, ρ_s is the density, l_x, l_y and h_s are respectively the dimensions and the thickness of the plate, and η is the loss factor. Finally ω_n and $\phi_n(x,y)$ are respectively the nth natural frequency and nth natural mode, which, for a simply supported panel, are given by [44-46]:

$$\omega_n = \sqrt{\frac{E_s h_s^2}{12\rho_s(1-v_s^2)}}\left[\left(\frac{n_1\pi}{l_x}\right)+\left(\frac{n_2\pi}{l_y}\right)\right], \tag{3.4}$$

$$\phi_n(x,y) = 2\sin\left(\frac{n_1\pi x}{l_x}\right)\sin\left(\frac{n_2\pi y}{l_y}\right) \tag{3.5}$$

where E_s is the Young's modulus, and v_s is the Poisson ratio of the material of the plate.

Considering the lumped parameter model of the actuators shown in Figure 3.1, the velocities of the proof-masses are given by the following mobility matrix relation:

$$\dot{\mathbf{w}}_m = \mathbf{Y}_m \mathbf{f}_m \tag{3.6}$$

where $\dot{\mathbf{w}}_m(\omega) = \lfloor \dot{w}_{m1}(\omega) \quad \cdots \quad \dot{w}_{m5}(\omega) \rfloor^{\mathrm{T}}$ is a vector with the velocities of the proof-masses, $\mathbf{Y}_m$ is a diagonal matrix with the mobilities of the proof-masses; $Y_{m,ii}(\omega) = 1/j\omega m_i$, and $\mathbf{f}_m(\omega) = \lfloor f_{m1}(\omega) \quad \cdots \quad f_{m5}(\omega) \rfloor^{\mathrm{T}}$ is a column vector with the forces between the proof-masses and the suspension springs.

Eqs. (3.1) and (3.6) can be compiled in one mobility equation:

$$\dot{\mathbf{w}} = \mathbf{Y}_c \mathbf{f} + \mathbf{Y}_p f_p \tag{3.7}$$

where:

$$\dot{\mathbf{w}} = \begin{Bmatrix} \dot{\mathbf{w}}_c \\ \dot{\mathbf{w}}_m \end{Bmatrix}, \tag{3.8}$$

$$\mathbf{Y}_c = \begin{bmatrix} \mathbf{Y}_{cc} & \mathbf{0} \\ \mathbf{0} & \mathbf{Y}_m \end{bmatrix}, \tag{3.9}$$

$$\mathbf{f} = \begin{Bmatrix} \mathbf{f}_a \\ \mathbf{f}_m \end{Bmatrix}, \tag{3.10}$$

$$\mathbf{Y}_p = \begin{bmatrix} \mathbf{Y}_{cp} \\ \mathbf{0} \end{bmatrix}, \tag{3.11}$$

and $\mathbf{0}$ is a 5x5 matrix of zeros. The forces transmitted to the plate and to the proof-masses, which are grouped in the vector $\mathbf{f}$, can be expressed in terms of the velocities of the bases and proof-masses, which are grouped in the vector $\dot{\mathbf{w}}$, by the following impedance matrix expression:

$$\mathbf{f} = -\mathbf{Z}\dot{\mathbf{w}} + \mathbf{V}\,\mathbf{f}_c \tag{3.12}$$

where $\mathbf{f}_c = \lfloor f_{c1} \quad \cdots \quad f_{c5} \rfloor^T$ is a column vector with the reactive forces generated by the linear electro-dynamic motors of the five control actuators, $\mathbf{Z} = \begin{bmatrix} \mathbf{Z}_s + \mathbf{Z}_{Act} & -\mathbf{Z}_s \\ -\mathbf{Z}_s & \mathbf{Z}_s \end{bmatrix}$,

$\mathbf{V} = \begin{bmatrix} \mathbf{I} \\ -\mathbf{I} \end{bmatrix}$ and $\mathbf{I}$ is a 5×5 identity matrix. The elements in the diagonal matrix $\mathbf{Z}_s$ are given by the impedances of the spring–damper (k_i, c_i) mounting systems: $Z_{s,ii}(\omega) = k_i / j\omega + c_i$, and the elements in the diagonal matrix $\mathbf{Z}_{Act}$ are given by the impedances of the masses ($m_{b,i}$) of the case and base-coil parts of the actuators: $Z_{Act,ii}(\omega) = j\omega m_{b,i}$. The coupled response of the plate and mechanical components of the actuator can be derived by substituting Eq. (3.12) into Eq. (3.7), so that:

$$\dot{\mathbf{w}} = \mathbf{Q}_c \mathbf{f}_c + \mathbf{Q}_p f_p \qquad (3.13)$$

where $\mathbf{Q}_c$ and $\mathbf{Q}_p$ are given by $\mathbf{Q}_c = (\mathbf{I} + \mathbf{Y}_c\mathbf{Z})^{-1} \mathbf{Y}_c \mathbf{V}$ and $\mathbf{Q}_p = (\mathbf{I} + \mathbf{Y}_c\mathbf{Z})^{-1} \mathbf{Y}_p$. The coil of the actuator is immersed in a constant radial magnetic field that is generated by the permanent magnet which in proof-mass actuators also acts as the moving mass.

When there is an electrical current $I_{c,i}(\omega)$ in the coil of the ith actuator, as schematically shown in Figure 3.1, a reactive pair of forces $f_{c,i}(\omega)$ is produced between the coil and magnet components of the actuator, which are directly proportional to the current via the so called voice coil coefficient ψ_i [19]:

$$f_{c,i} = \psi_i I_{c,i} . \qquad (3.14)$$

Therefore, the vectors with the forces generated by the electro-magnetic motors of the actuators can be expressed in terms of the following matrix expression:

$$\mathbf{f}_c = \mathbf{\psi} \mathbf{I}_c \qquad (3.15)$$

where $\mathbf{\psi}$ is a diagonal matrix with the transducer coefficients ψ_i and $\mathbf{I}_c(\omega) = \lfloor I_{c1}(\omega) \quad \cdots \quad I_{c5}(\omega) \rfloor^T$ is a column vector with the five currents in the coils. A coil-magnet actuator is characterised by a back electromotive force (back e.m.f.) effect which is

generated by the relative motion between the magnet and the coil. As discussed in References [7,19], considering time harmonic motion, the current $I_{c,i}$ in the coil of the ith actuator is governed by the following relation [7,19]:

$$\left(R_{ei} + j\omega L_{ei}\right)I_{ci} = U_{si} - \psi_i \begin{bmatrix} -1 & 1 \end{bmatrix} \begin{Bmatrix} \dot{w}_{ci} \\ \dot{w}_{mi} \end{Bmatrix} \tag{3.16}$$

where R_{ei} is the resistance and L_{ei} is the inductance of the jth coil, U_{si} is the applied voltage and $-\psi_i \begin{bmatrix} -\dot{w}_{ci} & \dot{w}_{mi} \end{bmatrix}$ is the back e.m.f. due to the vibration of the proof-mass with respect to the bases of the ith actuator. Considering the set of five actuators, the relation between the back e.m.f. and the current and driving voltage in the coil of each actuator can be cast in the following matrix expression:

$$\mathbf{Z}_e \mathbf{I}_c = \mathbf{U}_c - \mathbf{\psi} \mathbf{T}_w \dot{\mathbf{w}} \tag{3.17}$$

where $\mathbf{Z}_e$ is a diagonal matrix with the electrical impedances of the coils $Z_{e,ii}(\omega) = R_{e,i} + j\omega L_{e,i}$, $\mathbf{U}_c(\omega) = \begin{bmatrix} U_{s1}(\omega) & \cdots & U_{s5}(\omega) \end{bmatrix}^{\mathrm{T}}$ is a column vector with the five driving voltage signals and $\mathbf{T}_w = \begin{bmatrix} -\mathbf{I} & \mathbf{I} \end{bmatrix}$ where $\mathbf{I}$ is a 5×5 identity matrix.

Considering first the case where the five actuators are driven by current amplifiers, which set the driving currents in the coils, then, substituting Eq. (3.15) into Eq. (3.13), the velocities at the five control positions can be expressed in terms of the following matrix equation

$$\dot{\mathbf{w}}_c = \mathbf{R}_c \mathbf{I}_c + \mathbf{R}_p f_p \tag{3.18}$$

where: $\mathbf{R}_c = \mathbf{T}_c \mathbf{Q}_c \mathbf{\psi}$, $\mathbf{R}_p = \mathbf{T}_c \mathbf{Q}_p$ and $\mathbf{T}_c = \begin{bmatrix} \mathbf{I} & \mathbf{0} \end{bmatrix}$ where $\mathbf{I}$ is a 5×5 identity matrix.

In the second case, where the five actuators are driven by voltage amplifiers, which set the driving voltages in the coils, the velocities at the five control positions can be derived in two steps. First, Eq. (3.17) is substituted into Eq. (3.15) to give the vector with the reactive forces generated by the coil and magnet linear motors

$$\mathbf{f}_c = \mathbf{\psi} \mathbf{Z}_e^{-1} \mathbf{U}_c - \mathbf{\psi} \mathbf{Z}_e^{-1} \mathbf{\psi} \mathbf{T}_w \dot{\mathbf{w}} .$$

(3.19)

Eq. (3.19) is then substituted into Eq. (3.13) so that the velocities at the control positions can be expressed in terms of the following matrix relation

$$\dot{\mathbf{w}}_c = \mathbf{S}_c \mathbf{U}_c + \mathbf{S}_p f_p$$

(3.20)

where $\mathbf{S}_c = \mathbf{T}_c \left[\mathbf{I} + \mathbf{Q}_c \mathbf{\psi} \mathbf{Z}_e^{-1} \mathbf{\psi} \mathbf{T}_w \right]^{-1} \mathbf{Q}_c \mathbf{\psi} \mathbf{Z}_e^{-1}$ and $\mathbf{S}_p = \mathbf{T}_c \left[\mathbf{I} + \mathbf{Q}_c \mathbf{\psi} \mathbf{Z}_e^{-1} \mathbf{\psi} \mathbf{T}_w \right]^{-1} \mathbf{Q}_p$.

The signals feed to the driving coils depends on the type of control loop (i.e. proportional, integral, derivative, PI, PD PID) and type of controller (current and voltage amplifier). The response of both current- and voltage-driven actuators is considered in this chapter. In the first case, where the actuators are current-driven, the currents in the coils can be expressed in terms of the following matrix relation

$$\mathbf{I}_c = -\mathbf{H} \dot{\mathbf{w}}_c$$

(3.21)

where $\mathbf{H}$ is a diagonal matrix with the feedback control functions (P, I, D, PI, PD and PID). Thus, when the five feedback control loops are closed, the velocities at the five control positions can be derived by substituting Eq. (3.21) into Eq. (3.18)

$$\dot{\mathbf{w}}_c = \left(\mathbf{I} + \mathbf{R}_c \mathbf{H} \right)^{-1} \mathbf{R}_p f_p .$$

(3.22)

Also, substituting Eq. (3.22) into Eq. (3.1) the vector with the secondary forces generated by the proof-mass actuators is given by

$$\mathbf{f}_a = \mathbf{Y}_{cc}^{-1} \left[\left(\mathbf{I} + \mathbf{R}_c \mathbf{H} \right)^{-1} \mathbf{R}_p - \mathbf{Y}_{cp} \right] f_p .$$

(3.23)

In the second case, where the actuators are voltage-driven, the voltage applied to the coils can be expressed in terms of the following matrix relation:

$$\mathbf{U}_c = -\mathbf{H} \dot{\mathbf{w}}_c .$$

(3.24)

Thus, when the five feedback control loops are closed, the velocities at the five control positions can be derived by substituting Eq. (3.24) into Eq. (3.20), so that

$$\dot{\mathbf{w}}_c = \left(\mathbf{I} + \mathbf{S}_c\mathbf{H}\right)^{-1}\mathbf{S}_p f_p. \tag{3.25}$$

Also, substituting Eq. (3.25) into Eq. (3.1) the vector with the secondary forces generated by the proof-mass actuators is derived as follows

$$\mathbf{f}_a = \mathbf{Y}_{cc}^{-1}\left[\left(\mathbf{I} + \mathbf{S}_c\mathbf{H}\right)^{-1}\mathbf{S}_p - \mathbf{Y}_{cp}\right]f_p. \tag{3.26}$$

3.2   Stability analysis

A critical problem for the implementation of feedback control systems is stability. To assess this problem, graphical techniques have been developed for both SISO and MIMO control schemes. In this section, the stability of one and five decentralised control units is considered. The stability analysis of a single control unit is carried out by studying the Bode and Nyquist plots of the open loop sensor-actuator response function with reference to the Nyquist stability criterion [11,19,47]. The stability of the five decentralised control systems is also studied graphically with reference to the generalised Nyquist criterion by plotting the determinant and the five eigenvalues of the return difference matrix of the feedback control loop [15].
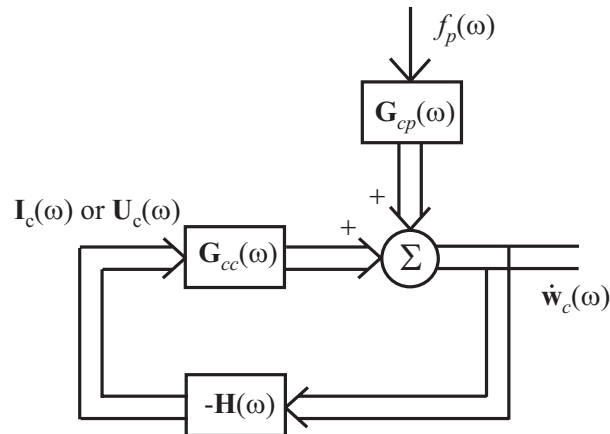
Figure 3.2: *Block diagram of a multichanel feedback control system implemented on the plate.*

The stability of the five channel feedback control system can be analysed in terms of the block diagram shown in Figure 3.2 which indicates that the closed loop error signals can be expressed by the relation

$$\dot{\mathbf{w}}_c(\omega) = \left[\mathbf{I} + \mathbf{G}_{cc}(\omega)\mathbf{H}(\omega)\right]^{-1}\mathbf{G}_{cp}(\omega)f_p(\omega) \qquad (3.27)$$

where $\left[\mathbf{I} + \mathbf{G}_{cc}(\omega)\mathbf{H}(\omega)\right]$ is the return difference matrix [15] and, according to Eq. (3.22) and (3.25), the matrix $\mathbf{G}_{cc}$ of point (diagonal terms) and transfer (off-diagonal terms) frequency response functions (FRFs) between the five control sensors and five actuators when there is no primary excitation and the vector $\mathbf{G}_{cp}$ of FRFs between the five control sensors and the primary excitation when there is no control action are given by

$$\mathbf{G}_{cc} = \mathbf{R}_c, \qquad (3.28)$$

$$\mathbf{G}_{cp} = \mathbf{R}_p, \qquad (3.29)$$

for the case of current-control system and

$$\mathbf{G}_{cc} = \mathbf{S}_c, \qquad (3.30)$$

$$\mathbf{G}_{cp} = \mathbf{S}_p, \qquad (3.31)$$

for the case of voltage-control system.

When a single control unit is implemented, Eq. (3.27) reduces to the following scalar expression:

$$\dot{w}_c(\omega) = \frac{G_{cp}(\omega)}{1 + G_{cc}(\omega)H(\omega)}f_p(\omega) \qquad (3.32)$$

where the mobility functions G_{cc} and G_{cp} for the current- and voltage-driven actuator system can be derived from Eqs. (3.28) to (3.31) respectively assuming only one control unit.

3.2.1 Stability of a single control unit

Although the stability analysis of each control unit does not provide a clear indication on the stability of the whole set of five control systems, it is instructive to start with this type of study, which gives a physical understanding of possible causes of instability in each control unit. The Nyquist stability criterion states that, assuming the controller is stable, a closed feedback loop is bound to be stable provided the open loop sensor–actuator FRF, $G_{cc}H$, does not encircle the Nyquist instability point (-1+j0). Moreover, considering the closed loop response, which for a single channel control system is given by equation (3.32) it can be noticed that if Re$\{G_{cc}H\}$>0 then $\dot{w}_c / f_p \leq 1$ for any control gain and frequency, i.e. the system is unconditionally stable. In this case the Bode plot of $G_{cc}H$ is minimum phase in the range between ±90°. Also the Nyquist plot of $G_{cc}H$ occupies the right hand side quadrants as ω varies from –∞ to +∞ and thus the Nyquist instability point (-1+j0) is never encircled regardless of the control gain [11,19,47]. Keeping in mind these observations, the stability of the four types of control loops listed in the introduction are analysed by plotting the Bode and Nyquist graphs of the open loop sensor–actuator FRF $G_{cc}H$.
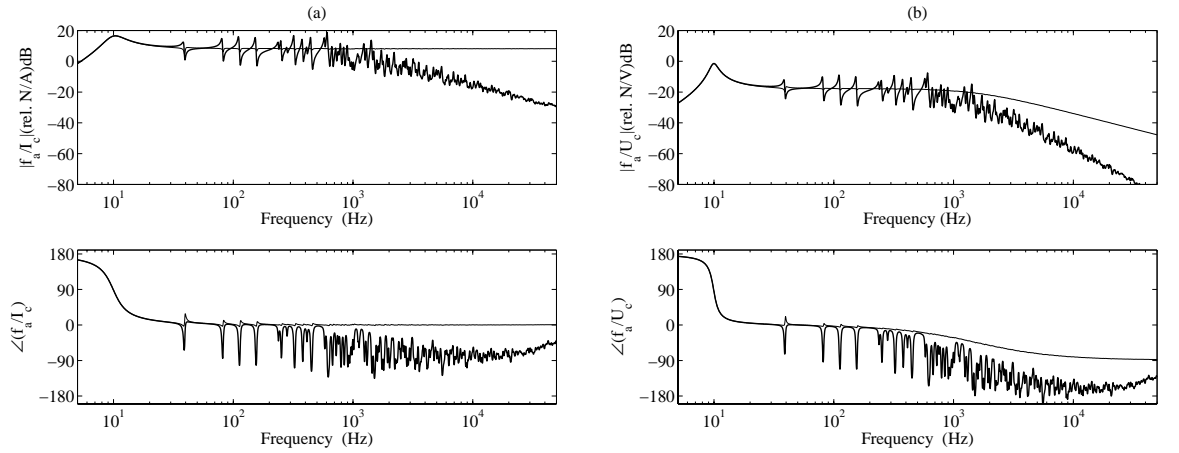
Figure 3.3: *Force transmitted to the base structure per unit driving current (a) or voltage (b) by an electrodynamic actuator when the dynamic effect of the base and coil masses, m_b, are (solid lines) or are not (faint lines) taken into account.*

Before entering into the details of the six types of feedback control laws, it is also useful to examine the plots of the transmitted force to the base of the proof-mass actuator with reference to the driving current or voltage, which have been derived using the formulation of Section 3.2 in two cases; where the dynamic effects of the base and coil masses are or are not taken into account. Considering first the case where the base and coil mass effects are not taken into account, the two plots in Figure 3.3 show that the spectrum of the transmitted force increases monotonically with frequency up to a maximum value at the

resonance frequency of the mass-spring actuator system, which in the case under study is approximately 10 Hz. At higher frequencies, the transmitted force f_a levels down to a value that is approximately constant [48]. Above about 2 kHz, the transmitted force by the voltage-driven actuator is characterised by an amplitude roll off and a constant phase lag which are due to the inductance of the driving coil. This tends to decrease the current in the driving coil, consequently lowering the actuation force. At frequencies below the fundamental resonance frequency of the actuator, the transmitted force is out of phase with the driving signal of the actuator while, at frequencies above the actuator resonance, it is in phase with the driving signal.

A number of small troughs are shown in correspondence to the low frequency resonances of the plate, which are due to the fact that at these resonance frequencies the plate produces little reaction to the actuator excitation and thus the transmitted force falls down. This effect is more marked for the voltage-driven actuator where the strong back e.m.f. effects generated by the large vibration levels at resonances also contribute to enhance these troughs. When the base and coil mass effects are taken into account, the amplitudes of these troughs and peaks become much more pronounced. Also, the dynamic effects of the base and coil masses produce a constant amplitude roll off above 1.5 kHz for both cases of current- and voltage-driven actuators.

These two plots already give some indications about the stability of a constant negative gain feedback loop, i.e. negative velocity control loop. In fact, for this type of control function, at frequencies below the fundamental resonance of the actuator, the force transmitted to the structure by the actuator is actually out of phase with the control velocity signal and thus produces a negative damping effect, which tends to enhance the response of the system (spillover effect) and can even lead to a condition of instability for too high control gains. In contrast, at frequencies above the fundamental resonance of the actuator, the force transmitted to the structure by the actuator is in phase with the control velocity signal and thus produces active damping which reduces the response of the structure in corresponding to of its resonance frequencies.

This simple analysis indicates that in order to efficiently use proof-mass actuators for feedback control, it is important that the actuator has a very low fundamental resonance so that, in the frequency range of control, there is a constant force actuation in phase with the driving signal to the actuator which exactly implements the desired feedback control law.

3.2.1.1 Proportional control: Velocity feedback

In order to implement negative velocity feedback, the output signal from the velocity sensor is fed back to the actuator via a negative proportional control function; $H_P(\omega) = -g$, which can be seen in Figure 3.4.
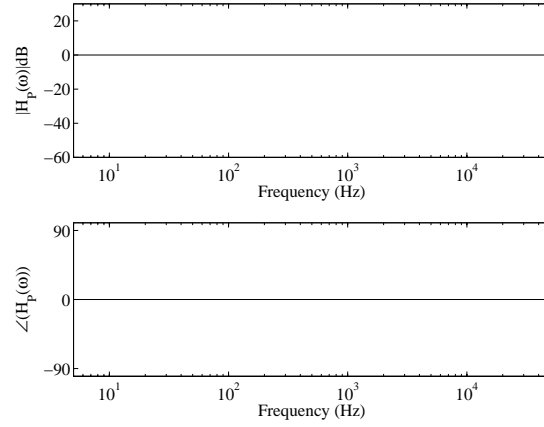
Figure 3.4: *Proportional control function.*

Figure 3.4 shows that an ideal proportional control function equally amplifies the signal at all frequencies and does not add any extra phase lag or lead to the feedback loop.

In order to have an unconditionally stable control system, the open loop sensor–actuator FRF $G_{cc}H$ must be real positive definite [24], that is, the sensor–actuator transducers must be collocated and dual [25,26]. Assuming the sensor is an ideal velocity sensor, then the collocation and duality property with the proof-mass actuator are entirely determined by the response of the actuator which, as shown by the plots in Figure 3.3a,b, is characterised by a 180° phase change across its fundamental resonance frequency. This suggests that the ideal velocity sensor and proof-mass actuator could be considered neither collocated nor dual. Therefore, even for the implementation of a direct velocity feedback control loop with an ideal velocity sensor, the feedback loop using a proof-mass actuator is likely to be affected by stability issues.

Figure 3.5a,b show the Bode plots of the open loop sensor–actuator FRFs $G_{cc}H$ without (solid faint line) and with (solid thick line) the mass effects of the actuator case and coil. The two plots show that, in both cases of current- and voltage-driven, the mass of the case and coil tends to reduce the amplitude of the response function above about 1.5 kHz. This is an important effect since it tends to reduce the stability problems at higher frequencies despite it also generates an additional phase lag.
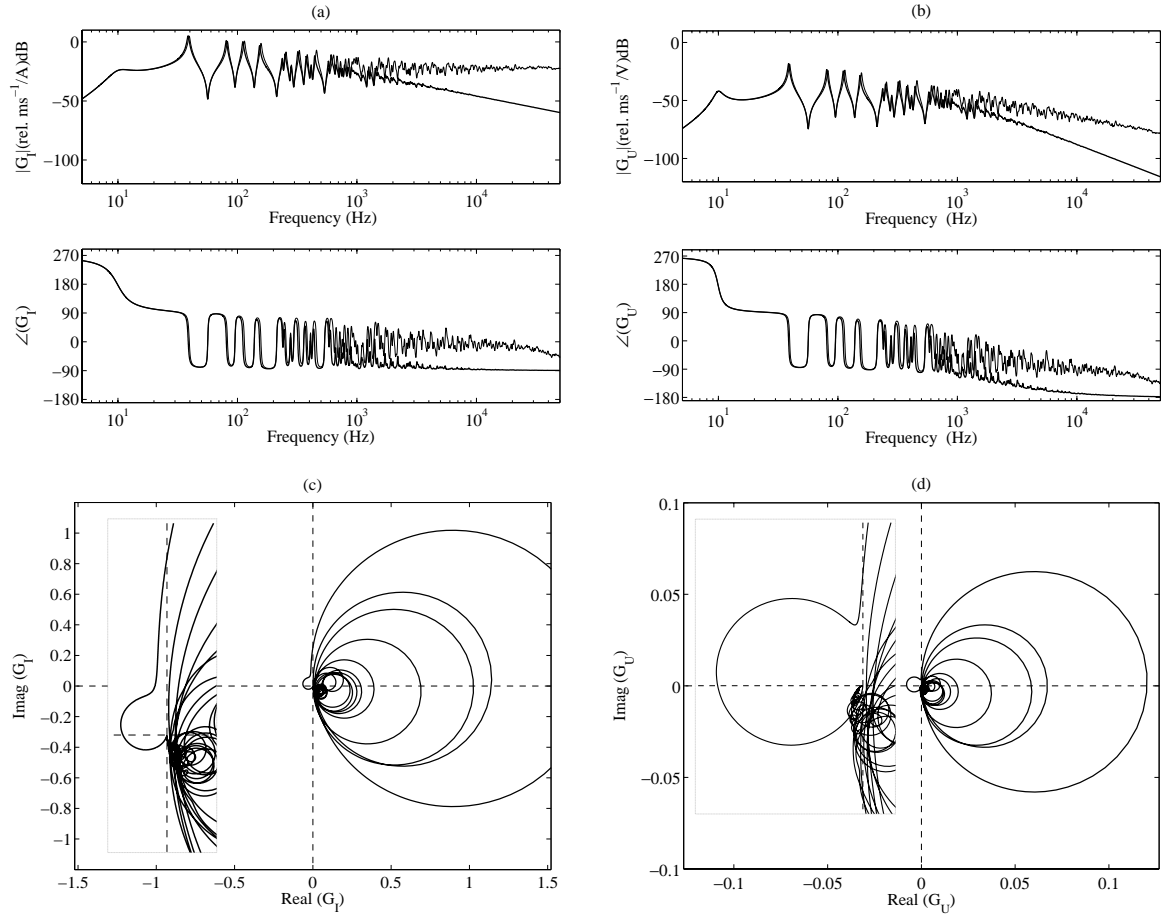
Figure 3.5: *Bode (a, b) and Nyquist plots (c, d) of the open loop sensor–actuator FRF when a Proportional feedback loop is implemented for current-driven (a, c) and voltage-driven (b, d) control actuators when the dynamic effect of the base and coil masses, m_b, are (solid lines) or are not (faint lines) taken into account (a, b).*

Considering in more detail the open loop sensor–actuator FRFs $G_{cc}H$ when the mass effects of the case and coil are taken into account, the Bode plots in Figure 3.5 indicate that, for both current- and voltage-driven actuators, the phase of the open loop sensor–actuator FRF starts from +270° at low frequency, drops to +90° beyond the resonance of the actuator and then alternates between +90° and –90° for the resonances of the plate. The first 180° phase drop, from +270° to +90°, is due to the mechanical response of the proof-mass actuator which, as shown in Figure 3.3, produces a swap of sign of the transmitted force f_a at the fundamental resonance of the actuator. In the voltage control case, at higher frequencies above 1 KHz, the phase plot goes to values beyond –90° because of the coil inductance. This inductance also further decreases the amplitude of the open loop response function.

The loci of the open loop sensor–actuator FRF shown in Figure 3.5c,d are characterised by one circle in the left hand side quadrants, which is due to the resonance of the actuator, and

many circles in the right hand side quadrants, which are due to the resonances of the plate. Thus the control system is bound to be only conditionally stable since, for relatively high control gains, the circle on the left hand side due to the fundamental resonance of the actuator can enclose the Nyquist instability point.

In conclusion, in order to obtain a stable proportional velocity control loop with large control gains, it is necessary to have a low-amplitude actuator resonance frequency. This condition is also important to minimise the control spillover effects at low frequencies around the resonance of the actuator. This low-amplitude resonance of the actuator is normally obtained by designing an actuator with fundamental natural frequency well below the first resonance of the structure. There is however an intrinsic limit to achieve this result since the stiffness of the actuator must be strong enough to hold the proof-mass without a big static deflection; therefore a compromise must be found between a stiff enough spring to support the static weight of the suspended mass and a soft enough spring to guarantee a low fundamental resonance frequency of the actuator [49]. Further improvements can be obtained by adding an internal velocity feedback loop to the actuator which generates relative active damping in the actuator that reduces the amplitude of its resonance [42]. Alternatively a very soft mount can be used in combination with an integral displacement feedback control loop, which acts as a self levelling system that limits the extent of the static displacement [50].

3.2.1.2 Integral control: Displacement feedback

In order to implement negative displacement feedback, the output signal from the velocity sensor is fed back to the actuator via a negative integral control function; $H(\omega) = -g / j \omega$ which can be seen in Figure 3.6.
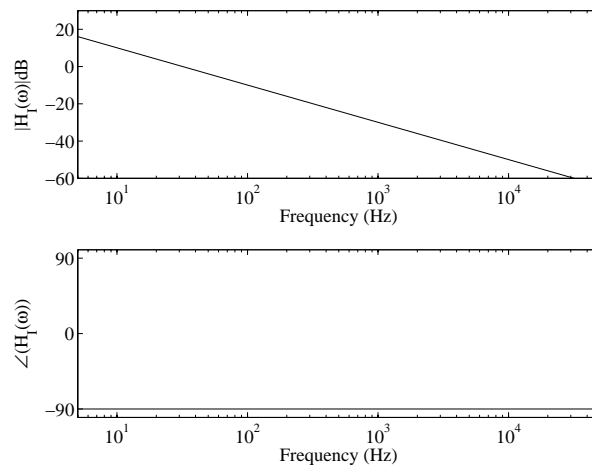
Figure 3.6: *Integral control function.*

Figure 3.6 shows that an ideal integral function will decrease the amplitude of the sensor-actuator FRF with frequency and will add a –90° phase lag to the case where the proportional control function is used.

Figure 3.7: *Bode (a, b) and Nyquist plots (c, d) of the open loop sensor–actuator FRF when an Integral feedback loop is implemented for current-driven (a, c) and voltage-driven (b, d) control actuators.*

The Bode plots in Figure 3.7a,b indicate that the phase of the open loop sensor–actuator FRF starts from +180°, drops to 0° at the resonance of the proof-mass actuator and then alternates between 0° and –180° at higher frequencies above the first resonance of the plate. As discussed above, this is due to the actuator dynamics which, as shown in Figure 3.3, transmits to the plate a force f_a which is +180° out of phase with the driving signal at frequencies below its fundamental resonance. In this control case, the amplitude of the open loop tends to decrease with frequency because of the integration $1/j\omega$. For the voltage–driven proof-mass actuator this effect is even higher because of the coil inductance which introduces an extra phase lag and amplitude drop at frequencies above 1 kHz.

The loci of the open loop sensor–actuator RFR shown in Figure 3.7c,d are characterised by one circle in the top side quadrants, which is due to the actuator–resonance, and many other circles on the bottom side quadrants which are due to the resonance of the plate. Thus, compared to proportional control, the effect of integral control is to rotate in the clockwise direction the locus in the Nyquist plot and to reduce the size of the higher frequencies circles. This should improve the stability of the system since the circle due to the actuator resonance no longer lies exactly along the real negative axis. However, as shown by the magnified plot, for very low frequencies, this circle gets very close to the negative real axis. Although it never crosses the negative real axis, it may cause instabilities when small external perturbations slightly change the dynamics of the actuator. The circles due to the plate resonances are moved to the bottom half of the Nyquist plots so that they pass close to the Nyquist critical point at higher frequencies. When the actuator is current-driven, the locus of the open loop sensor–actuator FRF does not cross the negative real axis and thus guarantees an unconditionally stable system. However when the actuator is voltage-driven, because of the extra phase shift introduced by the inductance effect of the driving coil; as shown by the magnified plot, at higher frequencies it crosses the negative real axis so that stable control is guaranteed only for a limited range of feedback control gains.

In general, the vicinity of both top and bottom circles to the negative real axis makes integral feedback quite difficult to implement. Even small phase lead or lag effects due to external disturbances will cause the top and bottom circles to cross the negative real axis and thus only a limited range of control gains can be implemented in a stable control loop. Also, control spillover effects are likely to occur at those frequencies such that the Nyquist plot enters the circle of radius one centred at the critical point (-1+j0) [11,19,47].

3.2.1.3 Derivative control: Acceleration feedback

In order to implement negative acceleration feedback, the output signal from the velocity sensor is fed back to the actuator via a negative derivative control function; $H(\omega) = -j\,\omega\,g$ which can be seen in Figure 3.8.

Figure 3.8 shows that an ideal derivative function will increase the amplitude of the sensor-actuator FRF with frequency and will add a +90° phase lead to the case where the proportional control function is used.
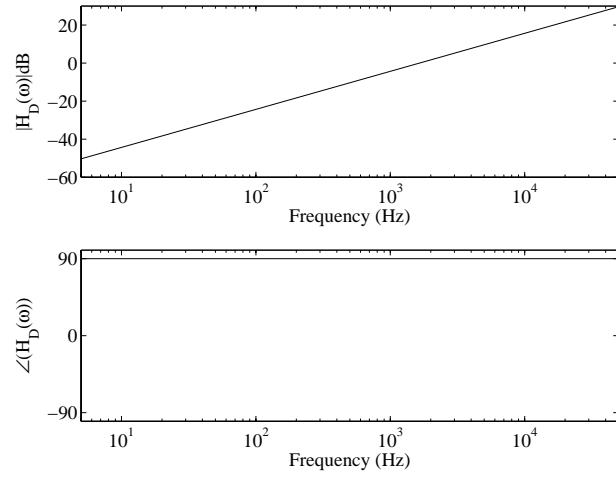
Figure 3.8: *Derivative control Function.*
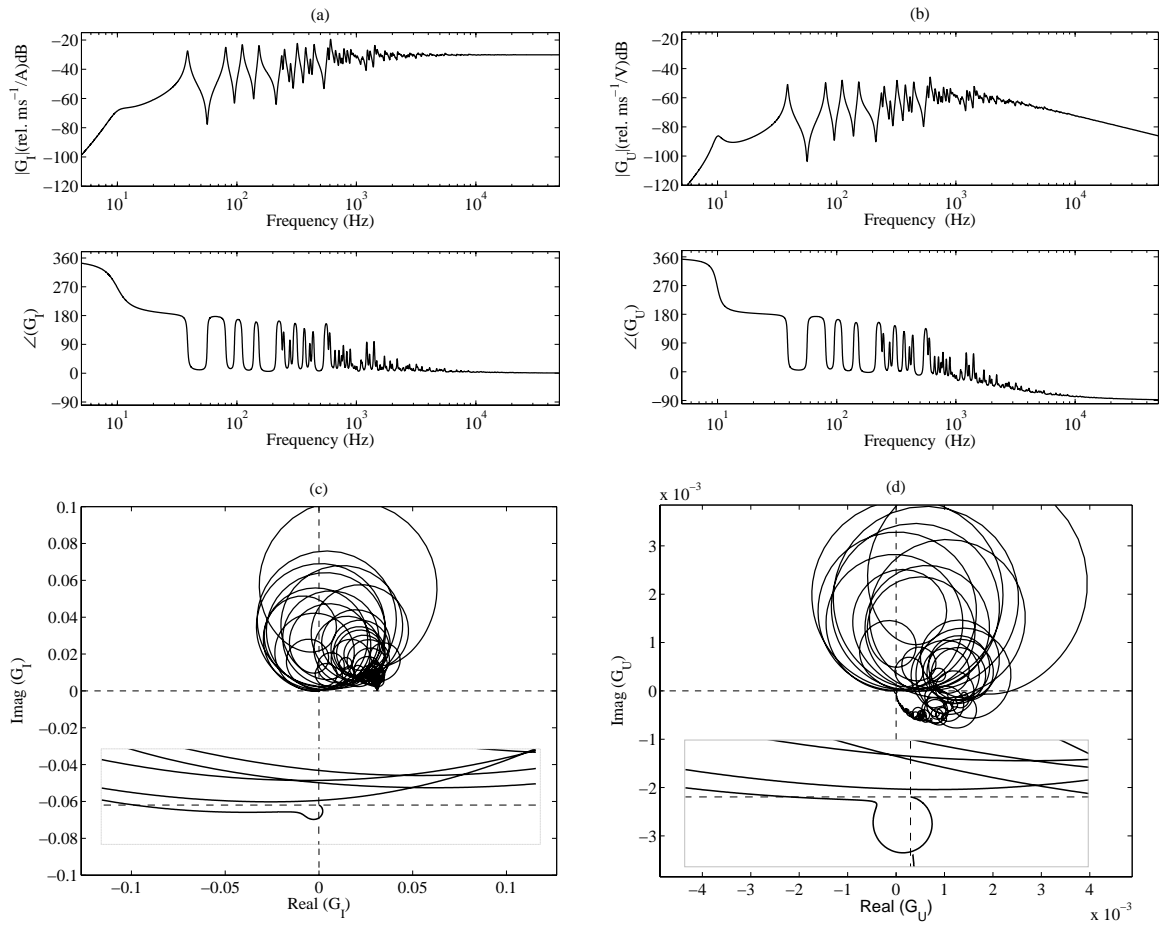
Figure 3.9: *Bode (a, b) and Nyquist plots (c, d) of the open loop sensor–actuator FRF when a Derivative feedback loop is implemented for current-driven (a, c) and voltage-driven (b, d) control actuators.*

In this case, the Bode plots in Figure 3.9a,b indicate that the phase of the open loop sensor–actuator FRF starts from +360° and drops to +180° at the resonance of the proof-mass actuator. This is because, as shown in figure 3, the transmitted force f_a flips sign with the control signal. At higher frequencies, above the first resonance of the plate, the phase alternates between +180° and 0°. The implementation of a derivative control function

produces a constant rise of the open loop sensor–actuator FRF with frequency as it has been pointed above. This effect is however mitigated by the coil inductance effect of the voltage-driven system.

The loci of the open loop sensor–actuator FRF shown in Figure 3.9c,d are characterised by one circle on the bottom quadrants, which is due to the resonance of the actuator, and other circles for the resonances of the plate on the top quadrants. Thus, in contrast to proportional control, the effect of derivative control is to rotate the Nyquist plot in the anti-clockwise direction and to enlarge the higher frequency circles. In principle this should also improve the stability of the system since the circle due to the actuator resonance no longer lies exactly along the real negative axis. However, in this case, as shown by the magnified plot, the transition from the circle due to the actuator resonance to the circle of the first resonance of the plate crosses the negative real axis, so that the control loop is bound to be stable only for a limited range of feedback control gains. Also, control spillover is likely to occur at low frequencies since the locus enters the circle of radius one and centre (-1+j0). For current-driven actuators, the higher frequency part of the locus tends to form a sequence of circles along the imaginary axis so that the complex part rises monotonically. This effect is less pronounced when the actuator is voltage-driven because of the coil inductance which tends to decrease the amplitude and to enhance the phase lag of the open loop sensor–actuator FRF. In any case having a control system with such a large locus of the open-loop sensor-actuator FRF in the higher frequency range could be a problem since high frequency phase lags introduced by the control circuit may lead to instabilities even for very small control gains.

3.2.1.4 PID control

In this case the output signal from the velocity control sensor is fed back to the control actuator via a negative combination of Proportional–Integral–Derivative functions: $H(\omega) = g\{k_P + k_I / j\omega + j\omega k_D\}$ which can be seen in Figure 3.10.

The integral and derivative control parameters, k_I and k_D have been tuned with reference to the first few resonances of the plate in such a way as that a) below the first resonance the control is set to be integral controlled, b) at the first few resonances to be proportional controlled and c) above 1kHz to be derivative controlled. Also k_P has been set to 1. At low

frequencies, below the first resonance of the plate, integral control is implemented so that the locus circle due to the fundamental resonance of the actuator is rotated away from the instability point and spillover circle in clockwise direction. Proportional control is then implemented in the frequency band of the first few, well separated, resonance frequencies of the plate where the active damping control action is desired. Finally, at higher frequencies derivative control is implemented in order to prevent the intrinsic phase lag effect that tends to drift the locus circles towards the left hand side quadrants of the Nyquist diagram. It should be emphasised that derivative control also tends to magnify the amplitude of the control signal, so that the natural roll off offered by the response of the plate to a point force is lost.
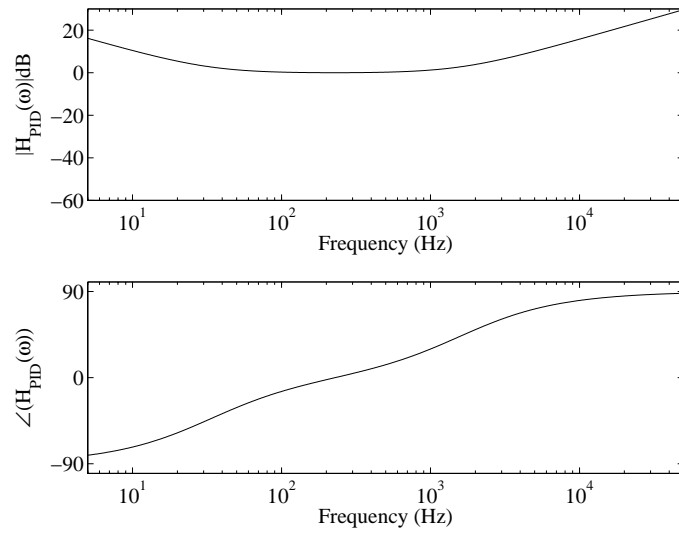
Figure 3.10: *PID control function.*

The Bode plots in Figure 3.11a,b indicate that the phase of the open loop sensor–actuator FRF starts from +180°, drops approximately to +45°, alternates between almost −90° and +90° in the frequency band where proportional control is implemented and then alternates between 0° and 180° above the first few resonances of the plate. Thus, the integral control component tends to produce a +90° phase lead effect at lower frequencies and the derivative control component produces a -90° phase lag at higher frequencies above the first few resonances of the plate. The derivative effect produces a constant increase of the amplitude of the open loop sensor–actuator FRF with frequency, which is less pronounced with the voltage-driven actuator because of the driving coil inductance effect.
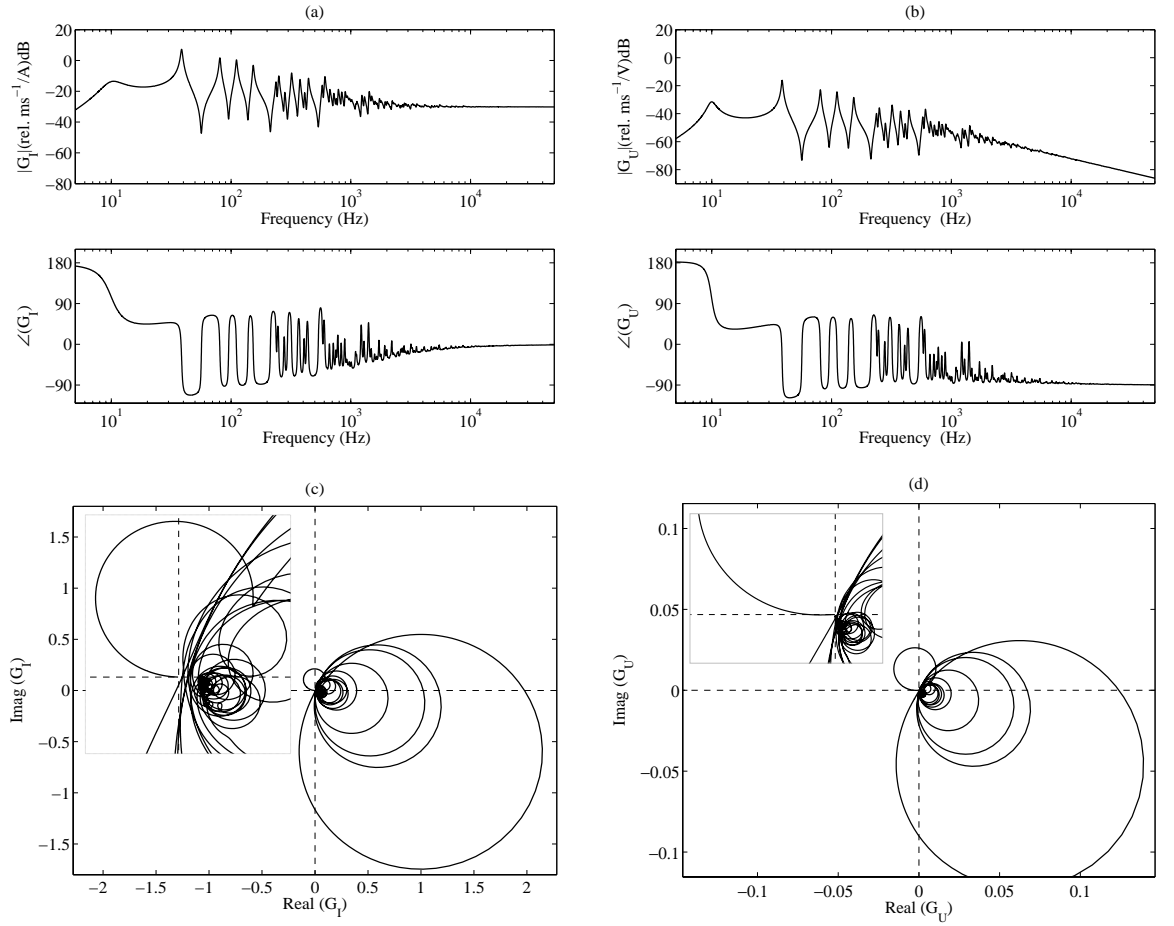
Figure 3.11: *Bode (a, b) and Nyquist plots (c, d) of the open loop sensor–actuator FRF when a PID feedback loop is implemented for current-driven (a, c) and voltage-driven (b, d) control actuators.*

The loci of the open loop sensor–actuator FRFs in Figure 3.11 indicates that, at low frequencies below the first resonance of the plate, the integral control effect in the PID controller locates the locus–circle for the actuator resonance in the top quadrants as seen in Figure 3.7 for the purely integral control case (see magnified plot). Also, the proportional effect in the PID controller locates the locus–circle for the resonances of the plate in the frequency band where proportional control is implemented on the right hand side quadrants, as typically happens with purely proportional control (see Figure 3.5). At higher frequencies, the derivative effect in the PID controller rotates the circles in counter clockwise direction and produces the typical amplification effect proportional to frequency of purely derivative control. When the voltage–driven proof-mass actuator is used, it is found that the typical higher frequencies phase lag and amplitude drop effects are counterbalanced by the amplification effect of the derivative control. In summary this PID control function is bound to be unconditionally stable. At very low frequencies the locus-circle related to the actuator resonance can pass close to the Nyquist critical point when large control gains are implemented. This has two drawbacks since control spillover is

likely to occur and also instability effects may be generated by low frequency external disturbances. Nevertheless these problems are less important that those that would happen with proportional control.

3.2.1.5 PI control

The effects generated by a combination of two control function, between negative displacement, negative velocity and negative acceleration feedback are also studied in this chapter. In this section, the PI control function is studied more in detail. The output signal from the velocity control sensor is fed back to the control actuator via a negative combination of Proportional–Integral functions: $H(\omega) = g\{k_P + k_I / j\omega\}$, which can be seen in the Figure 3.12.
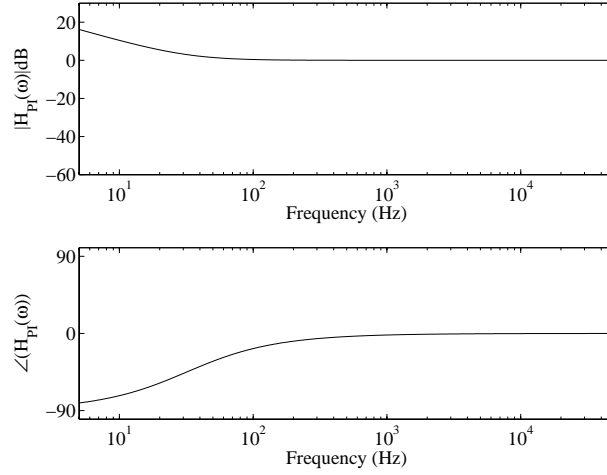
Figure 3.12: *PI control function.*

Figure 3.12 shows that at low frequency, below 100 Hz, the PI control function is mainly integral, decreasing the amplitude with frequency and adding -90° phase lag to the system, above the frequency mentioned, this control function behaves as the Proportional control function.

In this case, the integral and proportional control parameters, k_I and k_P have not been changed from those which were used for the previous feedback loop case, therefore, below the first resonance the control is set to be integral controlled and from this value is set to be proportional. In this case, the Bode plots in Figure 3.13 indicate that the phase of the open loop sensor-actuator FRF starts from +180°, drops to 45° and alternates once over the value −90° in the frequency band where integral control is implemented. Then in the

frequency band where proportional control is implemented, the phase alternates between approximately +45 and –90° and at higher frequency the phase tends to –90° for the current-driven case and –180° for the voltage-driven case, which is due, as found above, to the driving coil inductance effect. Thus, the integral control component tends to produce a +90° phase lead effect at lower frequencies up to the first resonance of the plate approximately.
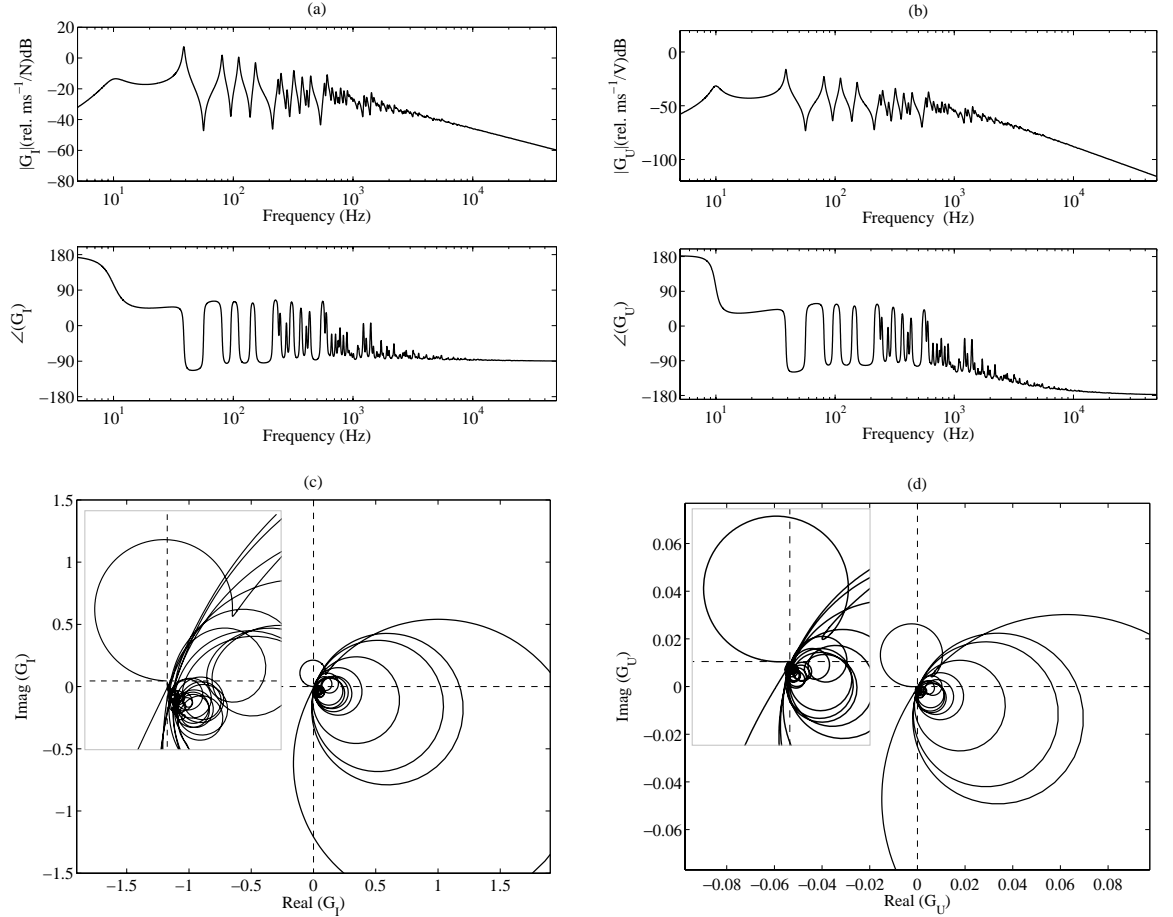
Figure 3.13: *Bode (a, b) and Nyquist plots (c, d) of the open loop sensor–actuator FRF when a PI feedback loop is implemented for current-driven (a, c) and voltage-driven (b, d) control actuators.*

The loci of the open loop sensor–actuator FRFs in Figure 3.13 indicates that, at low frequencies below the first resonance of the plate, the integral control effect in the PI controller locates the locus–circle for the actuator resonance in the top quadrants as seen in Figure 3.7 for the purely integral control case (see magnified plot) and Figure 3.11 for the PID control case. Also, the proportional effect in the PI control function case locates the locus–circle for the resonances on the right hand side quadrants, as typically happens with purely proportional control (see Figure 3.5). In summary this PI control function is bound to be unconditionally stable for the current-driven case and it is conditional stable for the

voltage-driven case since the locus-circle related to the actuator cross the negative axis at low frequency. Moreover, for the current-driven case, at very low frequencies the locus-circle related to the actuator resonance can pass close to the Nyquist critical point when large control gains are implemented. This has two drawbacks since control spillover is likely to occur and also instability effects may be generated by low frequency external disturbances.

3.2.1.6 PD control

In this case, the output signal from the velocity control sensor is fed back to the control actuator via a negative combination of Proportional–Derivative functions: $H(\omega) = g\{k_P + j\omega k_D\}$, which can be seen in the Figure 3.14.
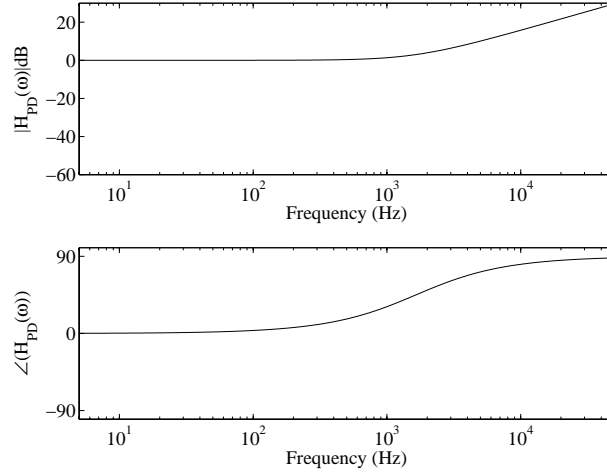
Figure 3.14: *PD control function.*

Figure 3.14 shows that at low frequency, below 1 kHz, the PD control function behaves as the proportional control function would do and above this value as a derivative control function.

The derivative and proportional control parameters, k_D and k_P have not been changed from those which were used for the previous feedback control loop case, therefore, for the actuator and the first few resonances of the plate the PD control is set to be almost proportional controlled and at higher frequencies above the first few resonances of the plate is set to be derivative. In this case, the Bode plots in Figure 3.15 indicate that the phase of the open loop sensor-actuator FRF starts from almost +270°, drops to +90° and alternates between +90° and −90° in the frequency band where proportional control is

implemented. Then in the frequency band where derivative control is implemented, that is above 1 kHz approximately, the alternation of phase decreases with frequency and tends to a constant value, 0° for the current-driven case and –90° for the voltage-driven case. This different is due, as found in previous case, to the driving coil inductance effect.
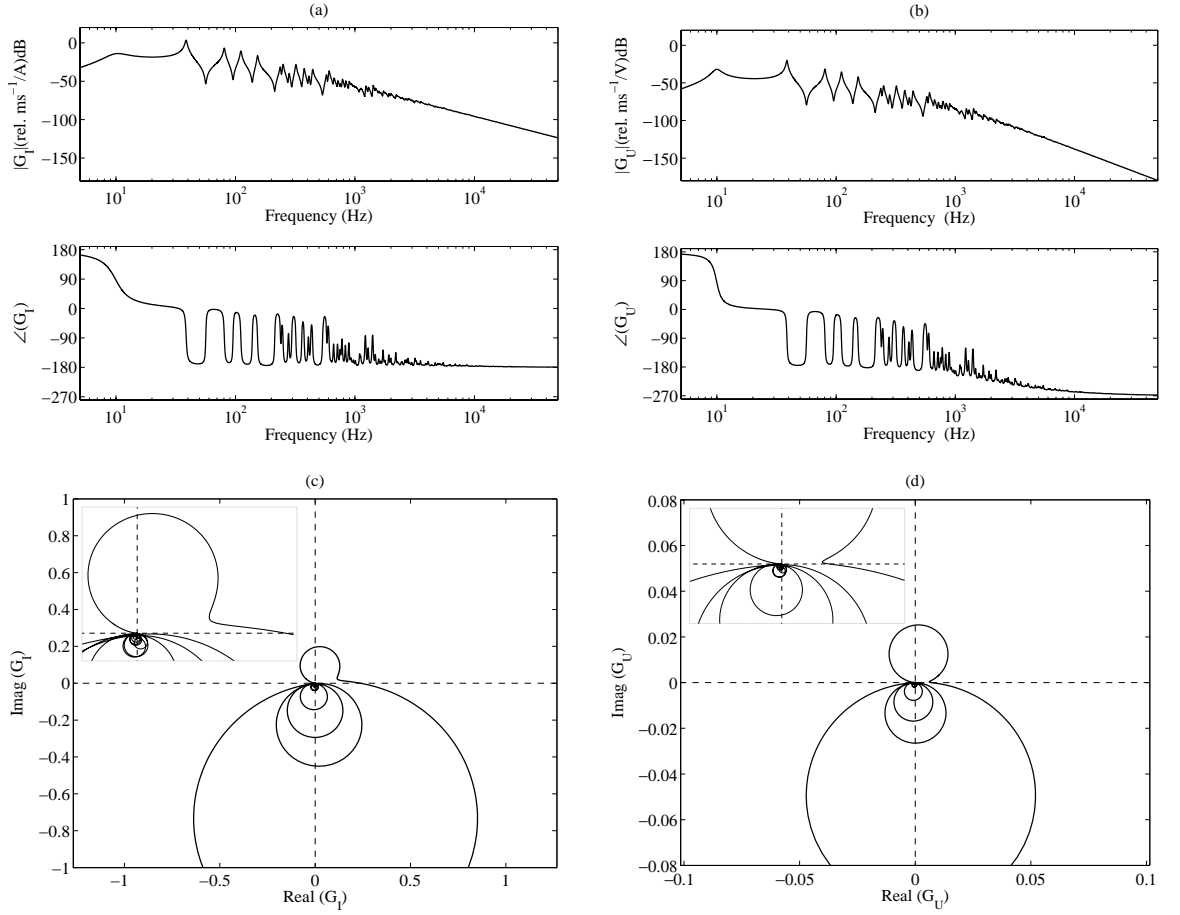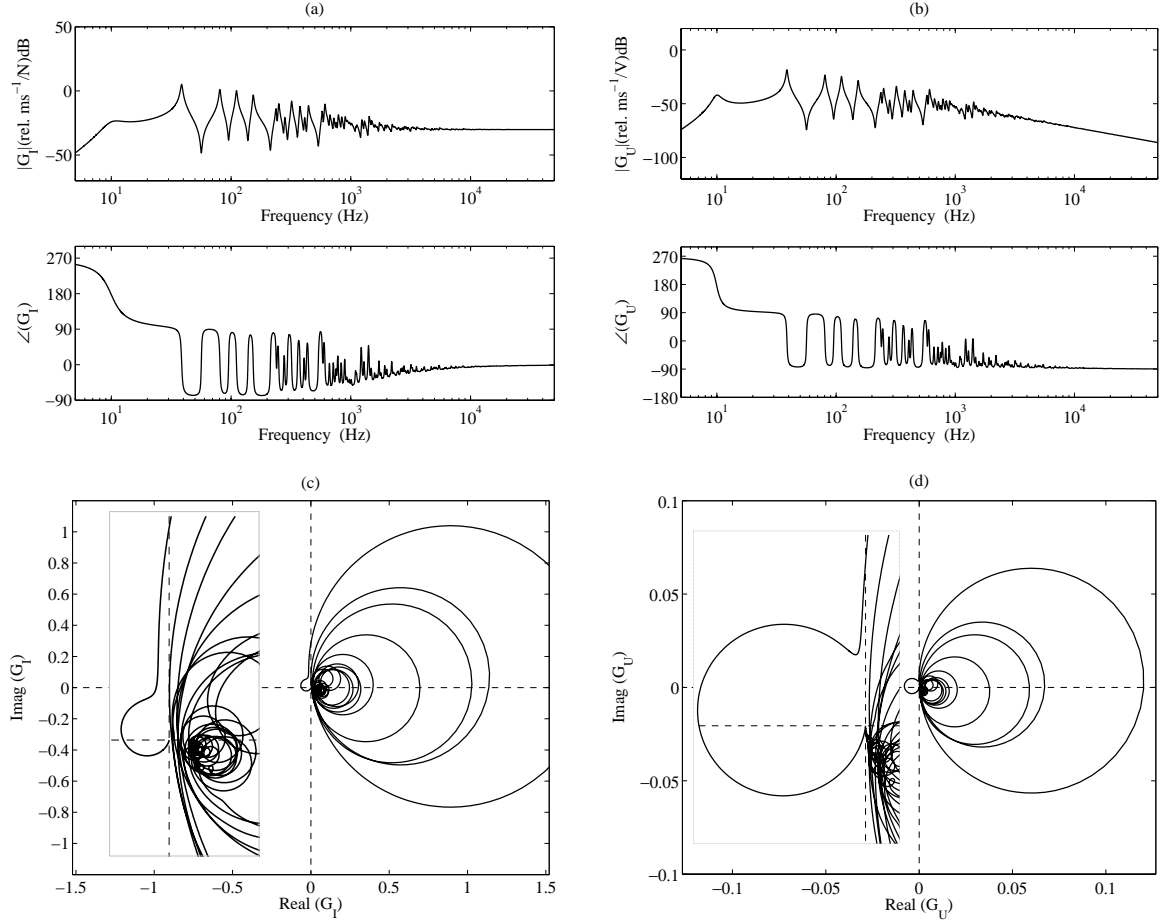

Figure 3.15: *Bode (a, b) and Nyquist plots (c, d) of the open loop sensor–actuator FRF when a PD feedback loop is implemented for current-driven (a, c) and voltage-driven (b, d) control actuators.*

The loci of the open loop sensor–actuator FRFs in Figure 3.15c, d indicates that, at low frequencies below the first few resonances of the plate, the proportional control effect in the PD controller locates the locus–circle for the actuator resonance in the left hand side quadrants and few circles in the right hand side quadrants, which are due to the first few resonances of the plate as seen in Figure 3.5 for the purely proportional control case (see magnified plot). Also, the derivative effect in the PD control function case locates the locus–circle for the plate resonances above 1 kHz on the right hand side quadrants. Thus the PD control system is bound to be only conditionally stable, since for relatively high control gains, the circle on the left hand side due to the fundamental resonance of the actuator can enclose the Nyquist instability point.

In summary, the differences between the purely proportional control system and the PD one are at higher frequencies, where the PD control system is set to be derivative. Therefore, in this frequency range the system adds a +90° phase lead. Hence, in order to obtain a stable PD control loop with large control gains, it is necessary to have a low-amplitude actuator resonance frequency as it has been already discussed in section 3.2.1.1.

3.2.2 Stability of five decentralised control units

In order to assess the stability when the five decentralised control units operate simultaneously, the 5x5 fully populated matrix $\mathbf{G}_{cc}\mathbf{H}$ with the open loop sensor–actuator FRFs between the five sensors and five actuators has been studied. Also in this case the stability analysis has been carried out graphically by considering the plot of the determinant of the return matrix $[\mathbf{I}+\mathbf{G}_{cc}\mathbf{H}]$. In fact, according to the generalised Nyquist stability criterion, a multichanel feedback system is bound to be stable provided the plot of $\det[\mathbf{I}+\mathbf{G}_{cc}\mathbf{H}]=0$ does not encircle the instability point $(0,j0)$ as ω varies from $-\infty$ to $+\infty$ [15,51] and taking into account that the controller is stable. Thus in this case the so called left and right hand quadrants of the polar plot refers to the vertical axis passing through the point $(1,j0)$ as highlighted by the dashed lines in the following plots.

The locus of $\det[\mathbf{I}+\mathbf{G}_{cc}\mathbf{H}]=0$ does not always give information about the maximum control gains that can be implemented before instability is reached. In fact, for integral, derivative, PID and PI control the size of the locus of $\det[\mathbf{I}+\mathbf{G}_{cc}\mathbf{H}]=0$ is not directly proportional to the control gain, g, implemented in the five control actuators. Moreover the shape of the loci itself changes as the control gain is varied. Thus, there is no way to get the maximum control gain that guarantees stability unless a sequence of plots of the locus of $\det[\mathbf{I}+\mathbf{G}_{cc}\mathbf{H}]=0$ are produced for continuously increasing control gains in the actuators. This is a rather inefficient approach to derive the stability limits of the system. A much simpler approach can be implemented by noting the fact that assuming the five control loops implements the same control gains, g, then $\det[\mathbf{I}+\mathbf{G}_{cc}\mathbf{H}]=(1+g\lambda_1)(1+g\lambda_2)\cdots(1+g\lambda_5)$, where $\lambda_i(\omega)$ is the ith eigenvalues of $\mathbf{G}_{cc}\mathbf{H}$. Thus the stability criterion of a decentralised multichanel control system with equal control gains can be assessed with reference to the polar plots of the eigenvalues of $\mathbf{G}_{cc}\mathbf{H}$ which, similarly to the Nyquist stability criterion for single channel control loops, indicate a stable control system provided none of the eigenvalues encloses the instability point

(-1,j0) as ω varies from $-\infty$ to $+\infty$. In this case the shapes of the loci of the eigenvalues remain unchanged as the control gains are increased and also the size of the loci linearly depends on the control gain of the five control units. Therefore, the maximum control gain that guarantees stability can be derived graphically by considering the plot with the real axis crossover closer to the critical point (-1,j0). It should be emphasised that the numerical calculation of the eigenvalues is not obvious, since their spectra intersect and thus special algorithms needs to be develop in order to extract the eigenvalues in the right order from the eigenvalues-eigenvector expression at each frequency.

The stability analysis carried out for a single control unit has already provided evidence that integral and derivative control are likely to be characterised by instability problems. The control performance study, which is reported in the following section, has also shown that poor vibration reduction effects are generated by these two types of control laws. Thus, it has been decided to limit the stability and control performance analysis to multichanel system that implement decentralised Proportional or PID feedback loops. The effects of Integral, Derivative, PI and PD will not consider for brevity.

3.2.2.1 Proportional Control: Velocity feedback

The two plots in Figure 3.16 show the loci of the $\det[\mathbf{I} + \mathbf{G}_{cc}\mathbf{H}] = 0$ functions, as ω varies from $-\infty$ to $+\infty$, in the two cases where the five decentralised proof-mass actuators implement local velocity feedback loops using current (a) and voltage (b) amplifiers. The two plots are quite similar to the co respective loci of the open loop sensor–actuator FRF $G_{cc}H$ of a single control unit shown in Figure 3.5. Therefore the stability of five decentralised control units is only conditional and depends on the low frequency response of the sensors–actuators systems which is the cause of the small loops of the loci on the left of the vertical axis (dotted line) passing through the point (1,j0), which can encircle the critical point (0,j0) when too high control gains are implemented.

The loci for the current-driven actuators is characterised by a relatively big loop located in the lower part of the graph which tends to enter the left hand side part of the plot. This is probably the result of the integration between neighbour actuators which can effectively interfere in such a way as to degrade the stability of the control system so that the locus of $\det[\mathbf{I} + \mathbf{G}_{cc}\mathbf{H}] = 0$ rotates in a clockwise direction towards the instability side of the plot [52].
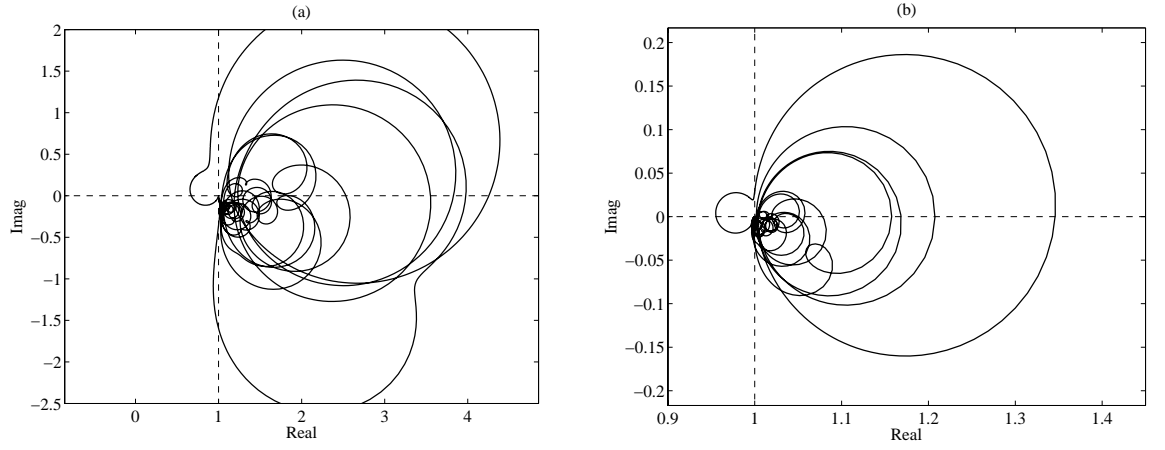
Figure 3.16: *Loci of det[**I**+**G**$_{cc}$**H**]=0 when five Proportional Control loops are implemented by current-driven (a) and voltage-driven (b) control actuators.*

In conclusion, the two plots shown in Figure 3.16 indicate that for both current- and voltage-driven actuators only a limited range of control gains can be implemented in order to guarantee the stability of the feedback control loop. As discussed in the introductory part of this section the maximum control gain that can be implemented by the five control loops can be derived from the loci of the five eigenvalues of the matrix of open loop sensors–actuators FRFs **G**$_{cc}$**H** which are shown in Figure 3.17 and Figure 3.18 for the current and the voltage driven actuators.

The polar plots of the five eigenvalues in Figure 3.17 indicate that the maximum control gains that guarantee stable feedback loops are $g_{I,\max}=3.9$ for the current-driven actuators and the polar plots of the five eigenvalues in Figure 3.18 show that the maximum control gains that guarantee stable feedback loop are $g_{U,\max}=30.2$ for the voltage-driven actuators.
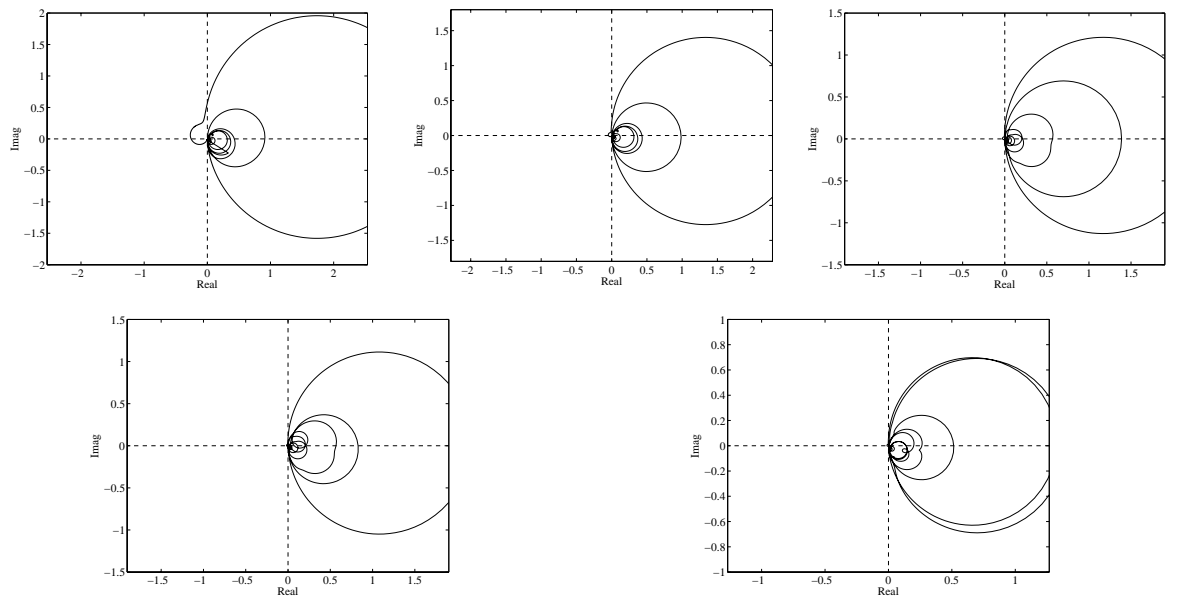
Figure 3.17: *Loci of the eigenvalues of the matrix **G**$_{cc}$ (jω)**H**(jω). Current-driven actuators.*

Figure 3.18: *Loci of the eigenvalues of the matrix $G_{cc} (j\omega)H(j\omega)$. Voltage-driven actuators.*

3.2.2.2 PID control

The stability when five decentralised control systems implementing PID control laws with either current-driven or voltage-driven actuators is also assessed by considering loci of the $\det[\mathbf{I} + \mathbf{G}_{cc}\mathbf{H}] = 0$ functions, as ω varies from $-\infty$ to $+\infty$ as shown in Figure 3.19.
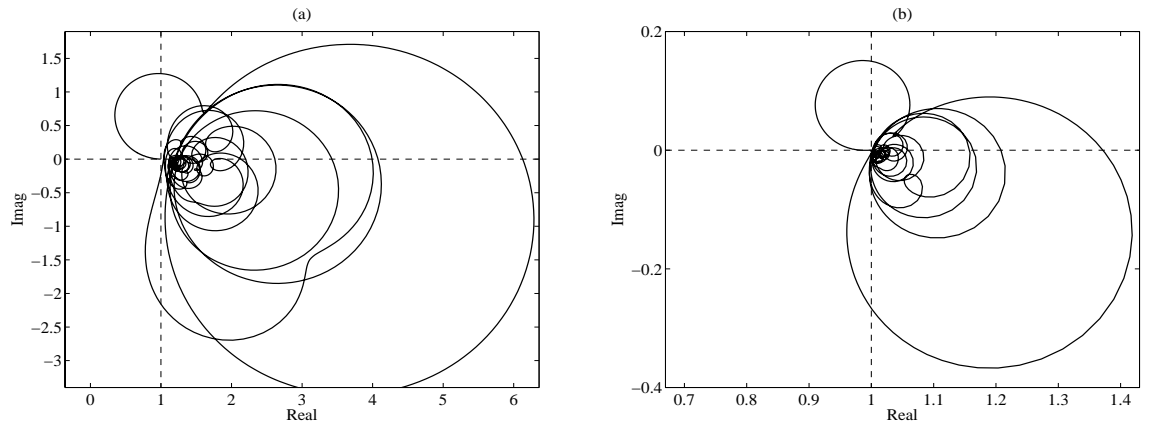
Figure 3.19: *Loci of det[I+G_{cc}H]=0 when five PID Control loops are implemented by current-driven (a) and voltage-driven (b) control actuators.*

Comparing these two plots with the co respective Nyquist plots for the single control systems shown in Figure 3.11, also in this case there is a clear analogy between the two types of polar plots. Thus similarly to the single channel PID control loop, the loci of the five decentralised control systems are characterised by one loop on the left hand side quadrants which are however rotated by about 90$^{\rm o}$ in clockwise direction. As a result, for

the system with current-driven actuators, the loci does not cross over the real axis in the left hand side quadrants, which indicates that the system is unconditionally stable as one can see also from the loci of the five eigenvalues of $\mathbf{G}_{cc}\mathbf{H}$ of Figure 3.20.
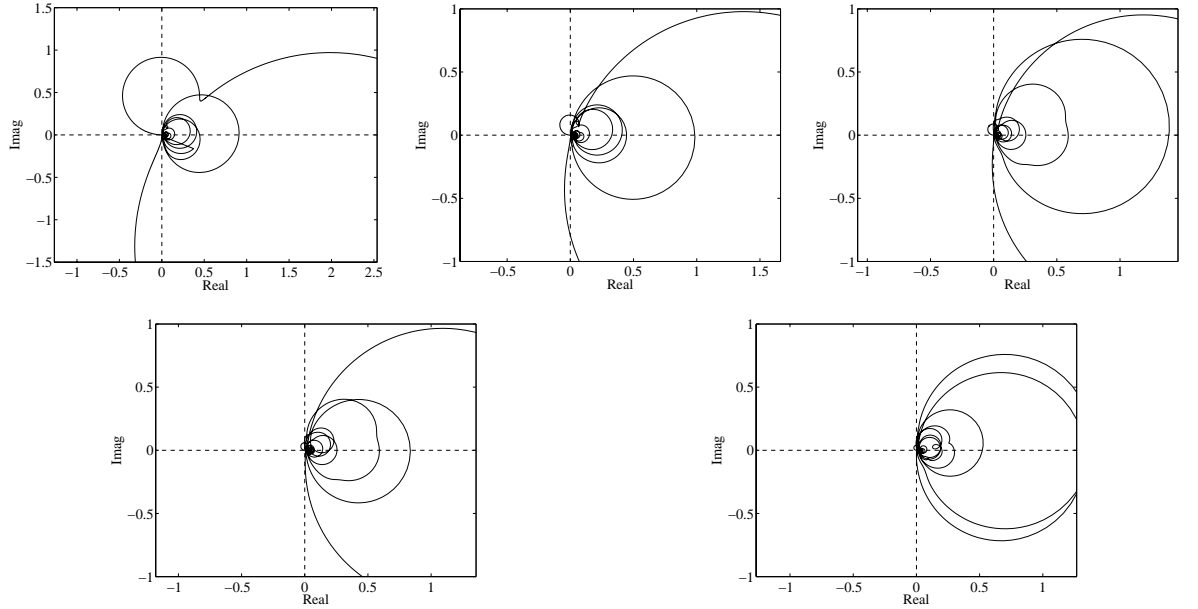
Figure 3.20: *Loci of the eigenvalues of the matrix $\boldsymbol{G}_{cc}(j\omega)\boldsymbol{H}(j\omega)$. Current-driven actuators.*
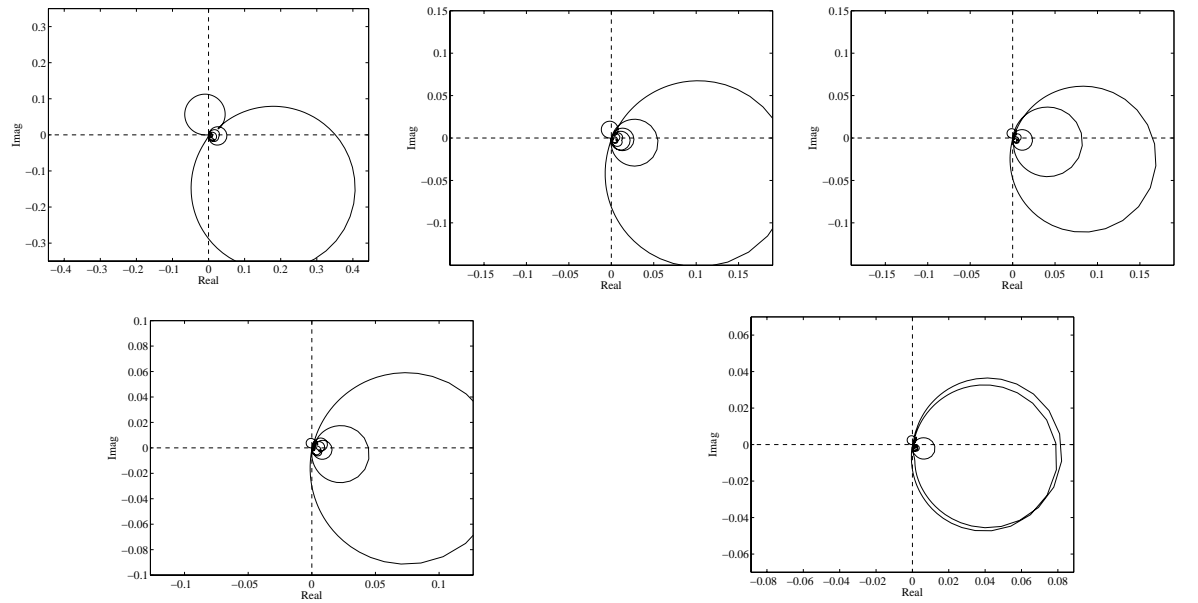
Figure 3.21: *Loci of the eigenvalues of the matrix $\boldsymbol{G}_{cc}(j\omega)\boldsymbol{H}(j\omega)$. Voltage-driven actuators.*

The system with voltage-driven actuators is instead only conditional stable. This can be clearly assessed from the polar plots of the five eigenvalues of $\mathbf{G}_{cc}\mathbf{H}$ in Figure 3.21, where the loci of the eigenvalues cross over the real negative axis. Nevertheless the gain margin is rather large and confirms that with PID control functions even with voltage-driven

actuators the system is characterised by good stability properties. The polar plots of the five eigenvalues in Figure 3.20 and Figure 3.21 indicate that the maximum control gains that guarantee stable feedback loops are $g_{I,\max} = \infty$ for the current-driven actuators and $g_{U,\max} = 82.6$ for the voltage-driven actuators.

3.3 Global control performances

In order to assess the response of a distributed structure it is convenient to represent its overall vibration in terms of the total kinetic energy which, for the plate considered in this study, is given by the following formula [7]:

$$T(\omega) = \frac{1}{4} \int_A \rho_s h_s |\dot{w}(x,y,\omega)|^2 dA \tag{3.33}$$

where $\dot{w}(x,y,\omega)$ is the transverse velocity over the plate surface and A is the surface of the plate. The flexural vibration on a generic point of the panel due to the primary force and the secondary excitations generated by the proof-mass actuators can be expressed with the following mobility matrix relation:

$$\dot{w}(x,y) = \boldsymbol{\phi}(x,y)\mathbf{A}_a \mathbf{f}_a + \boldsymbol{\phi}(x,y)\mathbf{a}_p f_p \tag{3.34}$$

where $\boldsymbol{\phi}(x,y) = \lfloor \phi_1(x,y) \quad \cdots \quad \phi_R(x,y) \rfloor$ is a row vector with the amplitudes of the modes at the generic point (x,y) and $\mathbf{A}_a$ is the matrix with the complex modal excitations functions generated by the forces transmitted by the actuators to the plate and $\mathbf{a}_p$ is a column vector with the complex modal excitation functions generated by the primary force excitation. The elements in the two matrices are given by:

$$A_{a,ns}(\omega) = j\omega \frac{\phi_n(x_{c,s}, y_{c,s})}{\Lambda \left[\omega_n^2 (1 + j\eta_s) - \omega^2 \right]}, \tag{3.35}$$

$$a_{p,n}(\omega) = j\omega \frac{\phi_n(x_p, y_p)}{\Lambda \left[\omega_n^2 (1 + j\eta_s) - \omega^2 \right]}. \tag{3.36}$$

For the two control configurations where the actuators are either current- or voltage-driven, the vectors with the secondary forces generated by the five actuators are given respectively by equations (3.23) and (3.26). Thus, substituting these two expressions in equation (3.34) and then substituting the resulting expression into equation (3.33) the following equaton is found for total kinetic energy of the panel with the five control units:

$$T(\omega) = \frac{1}{4} M f_p^* \left[\mathbf{a}_a^H + \mathbf{a}_p^H \right] \left[\mathbf{a}_p + \mathbf{a}_a \right] f_p \tag{3.37}$$

where for the current-driven actuators

$$\mathbf{a}_a = \mathbf{A}_a \mathbf{Y}_{cc}^{-1} \left[\left(\mathbf{I} + \mathbf{R}_c \mathbf{H} \right)^{-1} \mathbf{R}_p - \mathbf{Y}_{cp} \right] \tag{3.38}$$

and for the voltage-driven actuators

$$\mathbf{a}_a = \mathbf{A}_a \mathbf{Y}_{cc}^{-1} \left[\left(\mathbf{I} + \mathbf{S}_c \mathbf{H} \right)^{-1} \mathbf{S}_p - \mathbf{Y}_{cp} \right]. \tag{3.39}$$

3.3.1 Control performance produced by single control unit

Figure 3.22 and Figure 3.23 shows the kinetic energy of the plate in the frequency range between 5 Hz and 1 kHz when it is excited by the primary point force and the sole control unit at position 1 (see Figure 3.1), considering the two types of control arrangements (current- and voltage-driven actuators) and the six control functions (P, I, D, PID, PI and PD). The response with control is considered for three values of control gains: first a rather low gain, second, an intermediate control gain and third the control gain that gives the best reduction of the kinetic energy averaged in the range 5 Hz and 1 kHz for a stable feedback loop.

When there is no control, the spectrum of the kinetic energy is characterised by well separated resonances which are determined by the modes of the plate. It is interesting to note that there is nearly no peak for the actuator resonance at 10 Hz, that is due to the fact of the fairly high damping value of the actuator.

Considering first the effect of proportional control, for both cases of current- and voltage-driven control, the plots in the top row of Figure 3.22 show that when the control gain rises

the response at the first few resonance frequencies of the panel decreases. This is due to the active damping effect [7] of the control system which tends to reduce the resonant response of the lower order modes which are well coupled with the control actuator. As expected, the resonance due to the actuator produces a control spillover effect so that, although the control system is stable, the peak of the actuator resonance is amplified rather than lowered [49].
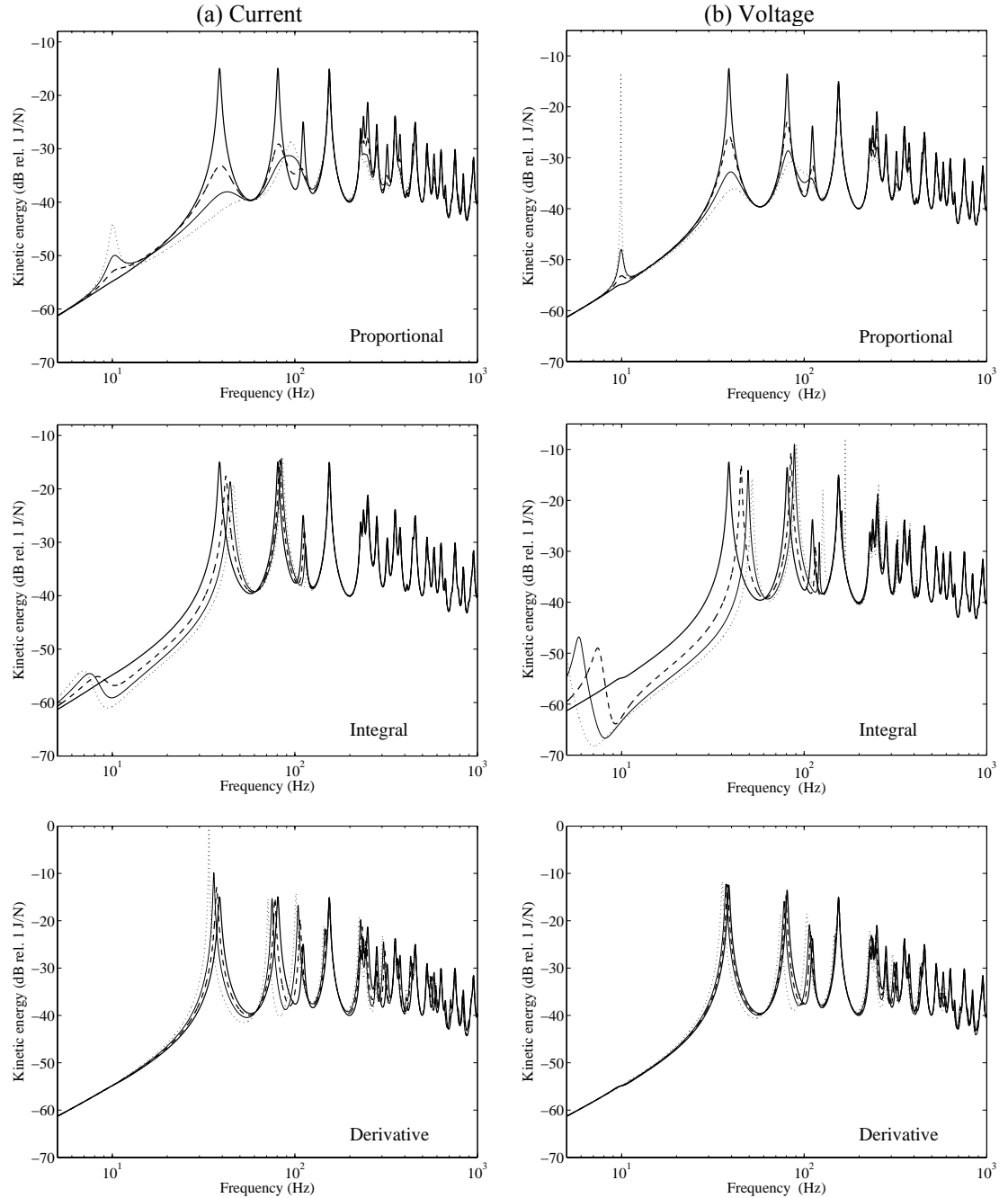
Figure 3.22: *Total flexural kinetic energy of the plate when the control actuator number 1, as shown in Figure 3.1, is current- or voltage-driven (respectively left- and right-hand side plots) and Proportional, Integral, Derivative control functions are implemented with a set or rising control gains up to that which produces the best frequency averaged reduction of vibration with a stable feedback loops.*

Comparing the effects produced by the current- and voltage-driven control loops, the two plots in Figure 3.22 indicate that the control spillover effect at the fundamental resonance of the actuator is more pronounced for the voltage control system. This is probably due to the high frequency filtering effect on the open loop sensor-actuator FRF (see Figure 3.5) so that in order to generate the same active damping levels as with the current-driven control system, much larger control gains must be implemented and thus much larger control spillover effects are generated at the fundamental resonance frequency.

In summary, considering the thick solid lines of the two plots in Figure 3.24, the normalised frequency averaged total kinetic energy[1] monotonically decreases as the control gains rises from zero up to the optimal control gain where the maximum reduction of about -2dB is obtained. For higher gains, the curves have been interrupted because the system would go to unstable values.

The second row of plots in Figure 3.22 shows that the integral control, which implements active stiffness [7], tends to move up the resonances of the panel. The control spillover effect is relatively smaller than that found with the proportional control system and occurs at much lower frequency than that when the feedback control loop is left open. Nevertheless comparing these results with those obtained with the proportional control system, it is evident that with integral control there is a consistent reduction of vibration only at frequencies below the first resonance of the panel where the response of the panel is indeed controlled by stiffness. At higher frequencies there is a shift of the resonance frequencies of the panel low order modes which may result in vibration reductions or enhancements in narrow frequency bands. This trend is confirmed by the plots in Figure 3.24 (dashed lines) which highlights how the integral control produces smaller maximum reductions of the frequency averaged kinetic energy of the panel, although this maximum is obtained with smaller control gains. The dashed line in the plot for the voltage-driven actuator in Figure 3.24 is interrupted because the closed loop would be unstable for higher control gains.

The third row of plots in Figure 3.22 shows the effect of derivative control that implement active mass [7]. The overall result is a shift of the resonance frequencies of the panel which

---

[1] Normalised with respect to the frequency averaged total kinetic energy of the panel when the five control loops are left open.

in this case are decreased. The dotted lines in Figure 3.24 show that in this case the reduction of the frequency averaged total kinetic energy is negligible for the current-driven control system and very small for the voltage-driven control system. This is due to the fact that the derivative control system acts in a frequency range where the vibration of the panel is characterised by multiple resonances so that the response is controlled by both mass and stiffness effects. As a result the sole active mass effect does not produce an effective reduction of the vibration in a wide frequency band. It just produces small vibration reductions in narrow frequencies bands where the response is mass controlled, as for example just above the first three resonances. The dotted lines in Figure 3.24 are interrupted for relatively low control gains since, as highlighted in the previous section, the derivative control loop goes unstable for relatively small control gains.

The first row of plots in Figure 3.23 shows the effect of PID control. The integral component in the controller reduces the vibration of the panel at frequencies below the first resonance. The proportional component is then effective at the first and second resonances of the plate. As found in the previous case the derivative component produces some control effects only in narrow band frequencies. Thus, the reduction of the total kinetic energy averaged in a range between 5 Hz and 1 kHz is lower than that obtained with proportional control (dashed-dotted line). However, the reduction in the frequency range between 5 and 100 Hz is much higher. This type of control unit is specifically tuned to produce active damping on a relatively small frequency band. Thus, it may be possible that, by using an array of these control systems centred at different frequencies, a relatively higher control performance is generated than by using an array with fixed gain proportional feedback control loops.

The second row of the plots in Figure 3.23 shows the effect of PI control. As found for the PID case, the integral component reduces the vibration of the panel at frequencies below the first resonance and the Proportional component is effective at the first and second resonances of the plate.

Finally, the third row of the plots in Figure 3.23 shows the effect of PD controls which is quite similar to the Proportional control (see first row in Figure 3.22) since the derivative component is effective at higher frequencies.
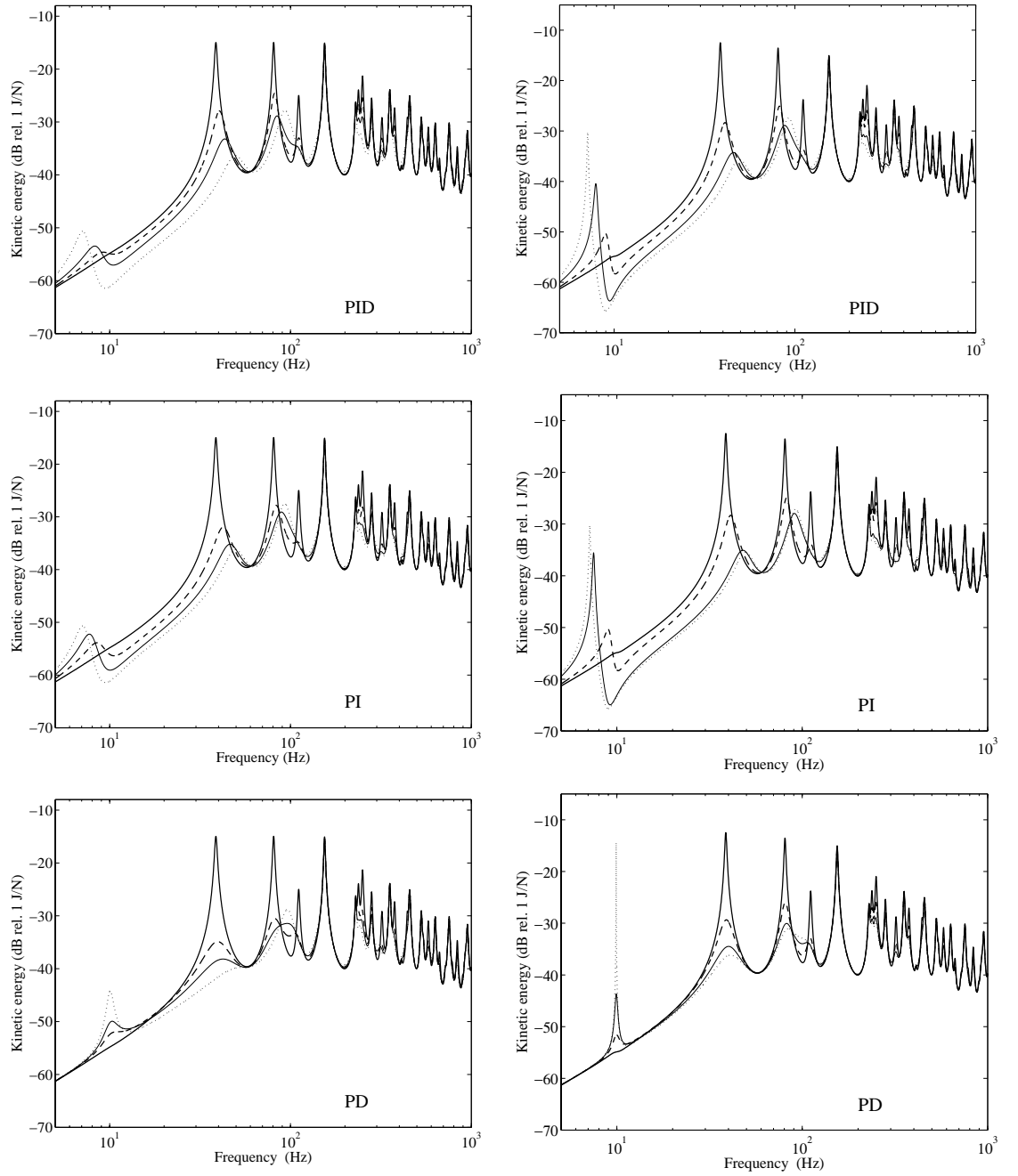
Figure 3.23: *Total flexural kinetic energy of the plate when the control actuator number 1, as shown in Figure 3.1, is current- or voltage-driven (respectively left- and right-hand side plots) and PID, PI and PD control functions are implemented with a set or rising control gains up to that which produces the best frequency averaged reduction of vibration with a stable feedback loops.*
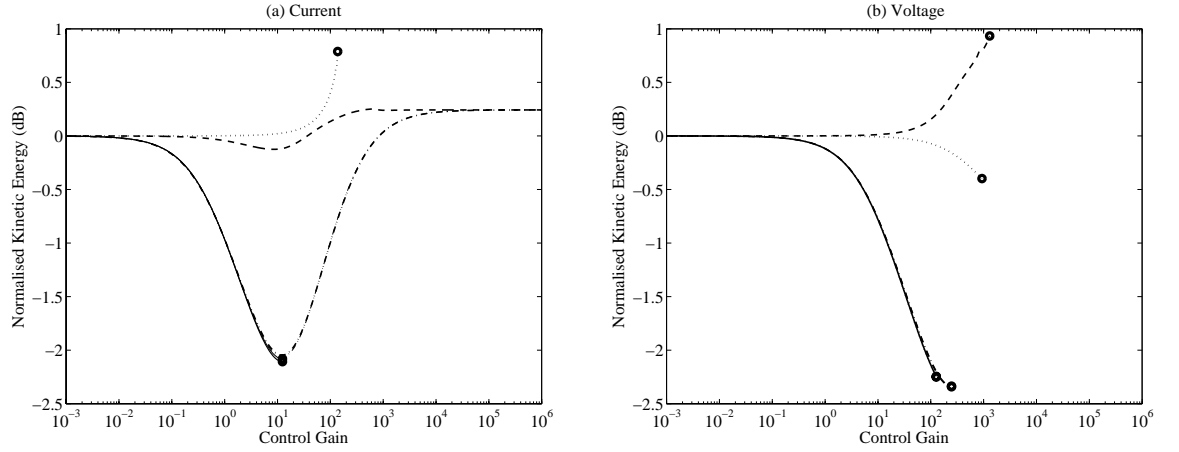
Figure 3.24: *Normalized frequency averaged total kinetic energy in the range between 5 Hz and 1 kHz as a function of the control gain produced by the control unit number 1, as shown in Figure 3.1, when the actuator is driven by current (a) or voltage (b). Solid lines: proportional control; dashed lines: integral control; dotted lines: derivative control; faint line: PI control; faint dash-dotted lines: PD control dash-dotted lines: PID control, these two last lines are overlapped by the PID and Proportional lines respectively.*

3.3.2 Control performance produced by five decentralised control units

The control performances produced by five decentralises control units are now considered. The effects produced by either current- or voltage-driven actuators are analysed when either proportional or PID control loops are implemented. The effects produced by integral and derivative control loops are not analysed since the single loop case analysed above has shown that these control loops produces vibration reductions only very for narrow frequency bands.

The first row of plots in Figure 3.25 show that, as found for the single control unit, as the gains of the five proportional control loops are raised, the active damping effect produces a reduction of vibration at resonance frequencies which is, however, accompanied by a control spillover effect at the fundamental resonance of the actuator at about 10 Hz. The solid lines in the two plots of Figure 3.26 show that the two control systems with current- and voltage-driven actuators produce maximum frequency averaged reductions of the kinetic energy of about 3 dB and 2.5 dB respectively.
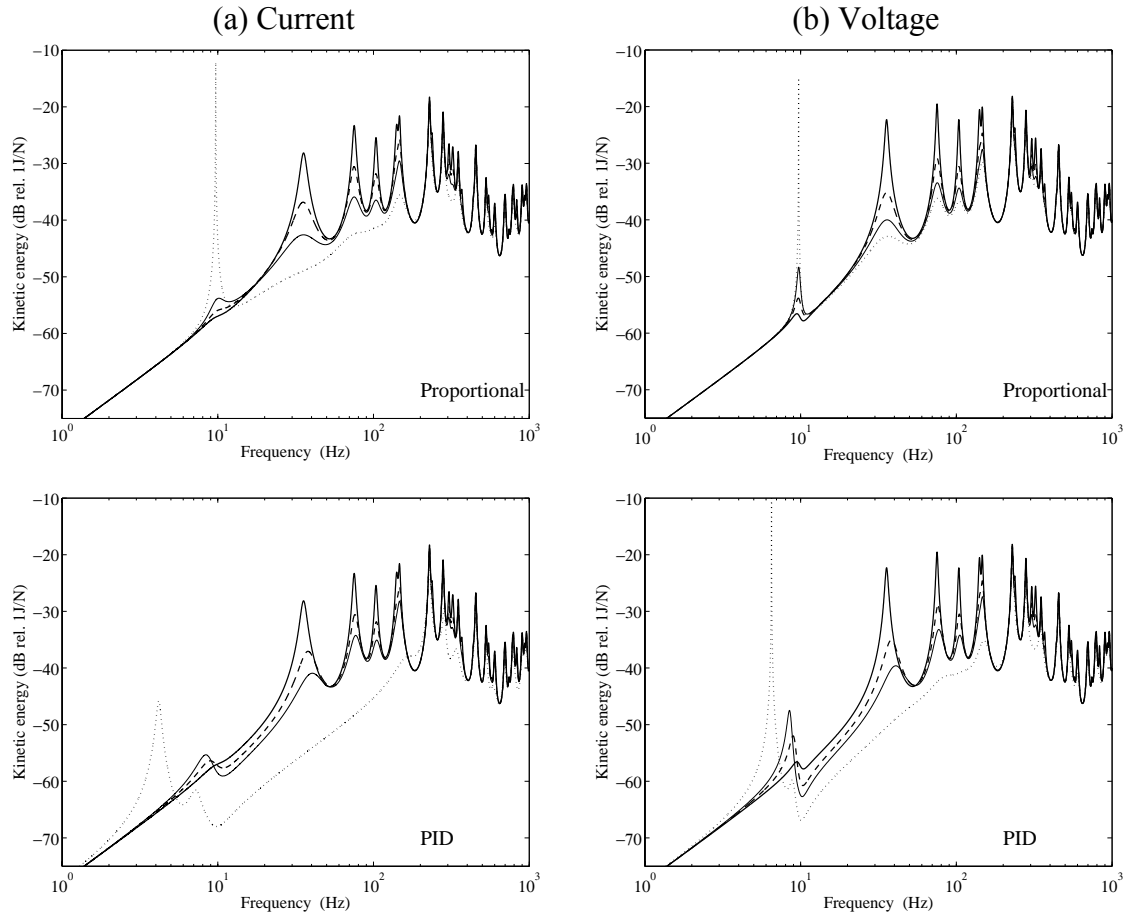
Figure 3.25: *Total flexural kinetic energy of the plate when the five control actuators shown in figure 1 are current- or voltage-driven (respectively left- and right-hand side plots) and Proportional and PD control functions are implemented with a set or rising control gains up to that which produces the best frequency averaged reduction of vibration with five stable feedback loops.*

The second row of plots in Figure 3.25 show the response of the panel when the five control loops implement a PID controller which has been set in such a way as to have integral control below the first resonance of the plate, i.e. up to about 50 Hz, proportional control between the first and tenth resonance, i.e. between about 60 Hz and 800 Hz, and then derivative control above the tenth resonance, i.e. above 800 Hz. With this type of control loop the current-driven control units are bound to be unconditionally stable and thus, according to Figure 3.26, can produce maximum reduction of the frequency averaged kinetic energy of the panel of 4.2 dB. The system with voltage-driven actuators is not unconditionally stable, thus, according to Figure 3.26, the maximum reduction of the frequency averaged kinetic energy of the panel is about 3.6 dB. The two bottom plots in Figure 3.25 show that both types of control systems are affected by control spillover effects at the fundamental resonance of the actuators around 10 Hz. This effect is less important for current-driven actuators.
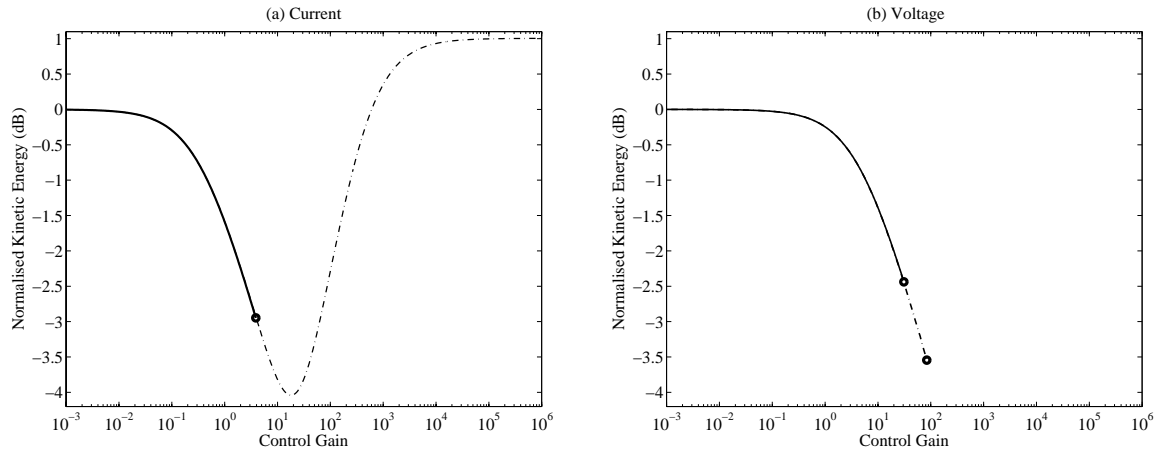
Figure 3.26: *Normalized frequency averaged total kinetic energy in the range between 5 Hz and 1 kHz as a function of the control gains when the five actuators shown in Figure 3.1 are current- (a) or voltage-driven (b). Solid lines: proportional control; dash-dotted lines: PID control.*

3.4 Summary

The stability analysis of the single control unit has highlighted that when proportional control is implemented then the locus of the sensor–actuator open loop response function is characterised by one circle in the left hand side quadrants of the Nyquist plot, which is due to the actuator resonance, and many other circles in the right hand side quadrants which are due to the plate resonances. Thus the system is bound to be conditionally stable with gain margin dependent on the amplitude of the actuator resonance. Integral and Derivative control functions produce a rotation by 90° of the locus, respectively in the clockwise and in the anti-clockwise directions. In principle this should reduce the stability problem but the integration and derivative effects on the amplitude of the open loop response function produce some limitations on the maximum control gains that guarantee stability.

The stability analysis of five decentralised control units has shown similar results to those found for the single control unit, although the maximum gain margins are normally reduced. This is due to the mutual effects between actuators which are particularly important in correspondence to the actuator resonances.

The control performance analysis has shown that, when the error sensor measures velocity, proportional control implements active damping so that the response of the panel is reduced at the resonance frequencies. Integral and derivative control produce active stiffness and active mass respectively so that the resonance frequencies of the plate are moved up and down respectively and vibration reductions are obtained in the frequency bands where the response of the plate is stiffness and mass controlled respectively. The

PID control scheme provides a combination of active stiffness, damping and mass effects which produces better results than just proportional control. This is due to the fact that the integration at low frequency reduces the instability effects generated by the fundamental resonances of the actuators. Also, the derivative effect at higher frequencies reduces the instabilities that would be produced by phase lags effects, particularly those characteristic of voltage-driven actuators due to the inductance and mass effects in the actuators.

The overall outcome of this study suggests that velocity feedback provides the best compromise for the construction of simple and robust decentralised control units. PID control produces some improvements at the cost of a more complex controller. Also, current control requires much smaller feedback gains to reach the optimal control gains that produce the best control performance.

4   STABILITY AND CONTROL PERFORMANCE SCALING STUDY

This chapter is focused on the physics of a feedback control loop using a small scale proof mass electrodynamic actuator. Particular emphasis is given to the scaling effects on stability and control performance when direct velocity feedback is implemented.

The stability and performance study of a small prototype electrodynamic proof mass actuator for the implementation of a direct velocity feedback loop on a thin panel structure is introduced. First, a mobility/impedance formulation is presented which provides a simple 'stability–performance' formula that can be used to assess simultaneously the stability and control performance of the feedback control loop with the proof mass actuator. The model derived in this chapter is a simplified version of that presented in Chapter 3. In particular it does not take into account the mass effect of the base of the actuator. In this way it has been possible to derive a simple "stability/performance" formula that can be interpreted when the size of the control unit is scaled down. After that, the principal scaling and design issues of the proof mass actuator are discussed in view of the stability requirements and control performance properties of the feedback loop. In particular, the scaling laws are derived for: a) the fundamental natural frequency, b) static displacement, c) the generation of electrodynamic force f_a and transmitted force f_c, d) the gain margin g_{max} and the so called 'control performance ratio' R_k.

The study presented in this chapter highlights how the scaling of the actuator may produce contrasting effects with reference to the implementation of velocity feedback control. For instance the down scaling produces a rise of the fundamental resonance frequency which tends to destabilise the feedback control loop. However, it also enhances the damping effect which, in contrast, tends to stabilise the feedback loop.

4.1   Actuation mechanism

Before entering into the details of the scaling study, the principal characteristics of force actuation with the proof mass actuator mounted on the smart panel are revised with reference to a mobility formulation that will be used later in this Chapter for the scaling study. The geometrical and material properties of the panel considered in the experimental study presented in Chapter 6 are summarised in Table 4.1. Also the physical properties of

the actuator are given in Table 4.2. The actuator is mounted at position x_c=109 mm, y_c=75 mm (actuator N.2, Figure 6.1). The stability and control performance of a negative velocity feedback loop using this type of actuator are examined with a simple stability-performance formula which derives the reduction of vibration at the control position for the maximum gain of the feedback control loop that guarantees stability. The scaling laws of the principal mechanical and electrodynamic components are then derived and used in combination with the stability-performance formula to assess the scaling effect on the stability and control performance of a single control unit.

Table 4.1: *Geometry and physical parameters for the panel.*

Parameter	Value
Dimensions	$l_x \times l_y = 414 \times 314$ mm
Thickness	$h = 1$ mm
Mass density	$\rho = 2720 \, \text{Kg}/\text{m}^3$
Young's modulus	$E = 7.1 \times 10^{10} \, \text{N}/\text{m}^2$
Poisson ratio	$\nu = 0.33$
Damping loss factor	$\eta = 0.02$
Coordinates of primary force excitation	$x_p, y_p = 0.341, 0.246$ mm
Mass of the force transducer for the primary excitation	$M_s = 30$ g

Table 4.2: *Geometry and Physical parameters for the actuators.*

Parameter	Value
Housing and base disk mass	$M_b = 8$ g
Proof mass	$M_a = 22$ g
Suspension system stiffness	$K_a = 347.4$ N/m
Suspension system damping	$C_a = 3.3 \, \text{N}/\text{ms}^{-1}$
Fundamental natural frequency	$\omega_a = 125.7$ rad/s
Voice coil coefficient	$\psi = 2.6$ N/A

In order to build a smart panel whose sound insulation effect competes with passive sound insulation treatments, the electrodynamic proof mass actuators used to generate active damping must be light, provide large control forces and guarantee large control gains when velocity feedback is implemented. As schematically shown in Figure 4.1a, the control system considered in this study uses a coil-magnet electrodynamic linear motor. The coil is

fixed to the base of the actuator and the magnet is suspended on springs so that it provides the inertial reaction necessary to generate a point force f_c on the structure where the actuator is fixed [19].
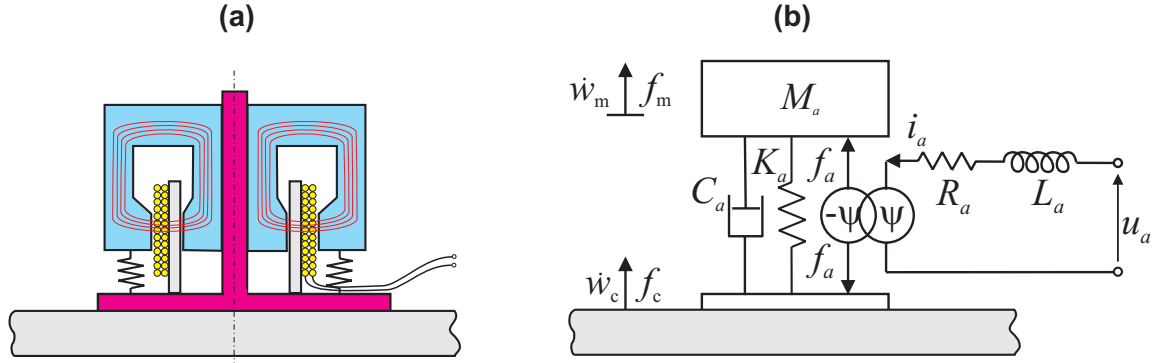
Figure 4.1: *Proof mass electrodynamic force actuator: a) sketch b) electro-mechanical schematic.*

Figure 4.1b shows the equivalent electro-mechanical schematic that has been used to model the response of this actuator when it is fixed on a clamped rectangular aluminium plate. The model takes into account the inertial effect of the proof mass and stiffness-damping effects of the suspension system. In order to keep the formulation simple, the inertial effect of the base and coil masses is instead neglected in this part of the study. Assuming time harmonic vibratory motion of the form exp($j\omega t$), where ω is the circular frequency and $j = \sqrt{-1}$, the fully coupled response of the plate and actuator system has been derived by considering the following mobility and impedance equations:

$$\dot{w}_c = Y_{cc} f_c + Y_{cp} f_p , \tag{4.1}$$

$$\dot{w}_m = Y_a f_m , \tag{4.2}$$

$$f_c = -Z_a \dot{w}_c + Z_a \dot{w}_m + f_a , \tag{4.3}$$

$$f_m = Z_a \dot{w}_c - Z_a \dot{w}_m - f_a \tag{4.4}$$

where $\dot{w}_c(\omega)$, $\dot{w}_m(\omega)$, $f_c(\omega)$ and $f_m(\omega)$, are respectively the complex velocities and forces at the base and proof mass components of the actuator and $f_p(\omega)$ is the complex primary force excitation acting on the plate. $Y_{cc}(\omega)$ and $Y_{cp}(\omega)$ are the plate mobility functions, respectively, at the point where the actuator is attached and between the point

where the actuator is attached and the location of the primary force. The two mobility functions have been derived in terms of the following modal summations [44]:

$$Y_{cc} = j\omega \sum_{n=1}^{N} \frac{\left[\phi_n(x_c, y_c)\right]^2}{M_p \left[\omega_n^2(1+j\eta) - \omega^2\right]}, \tag{4.5}$$

$$Y_{cp} = j\omega \sum_{n=1}^{N} \frac{\phi_n(x_c, y_c)\, \phi_n(x_p, y_p)}{M_p \left[\omega_n^2(1+j\eta) - \omega^2\right]} \tag{4.6}$$

where M_p is the mass of the plate, η is the loss factor and ω_n, $\phi_n(x, y)$ are respectively the n-th natural frequency and n-th natural mode of the plate at position (x, y), which have been taken from reference [44-46] for a clamped plate. Finally $Z_a(\omega)$ and $Y_a(\omega)$ are the impedance and mobility functions for the spring-dashpot and proof mass components of the actuator:

$$Z_a = \frac{K_a}{j\omega} + C_a, \tag{4.7}$$

$$Y_a = \frac{1}{j\omega M_a} \tag{4.8}$$

where K_a, C_a and M_a are respectively the stiffness, viscous damping coefficient and mass of the three components of the actuator.

Assuming the actuator is driven by current, i_a, so that:

$$f_a = \psi\, i_a \tag{4.9}$$

where ψ is the voice coil factor of the actuator [19], then using Eqs. (4.1) to (4.4) the force generated by the proof mass actuator per unit driving current is given by [53]:

$$f_c = \frac{\psi}{1 + Z_a\left(Y_a + Y_{cc}\right)} i_a. \tag{4.10}$$

The plot in Figure 4.2 shows the spectrum of the transmitted force f_c per unit driving current i_a derived when only the actuator N.2 is mounted on the smart panel considered in the chapter 3.
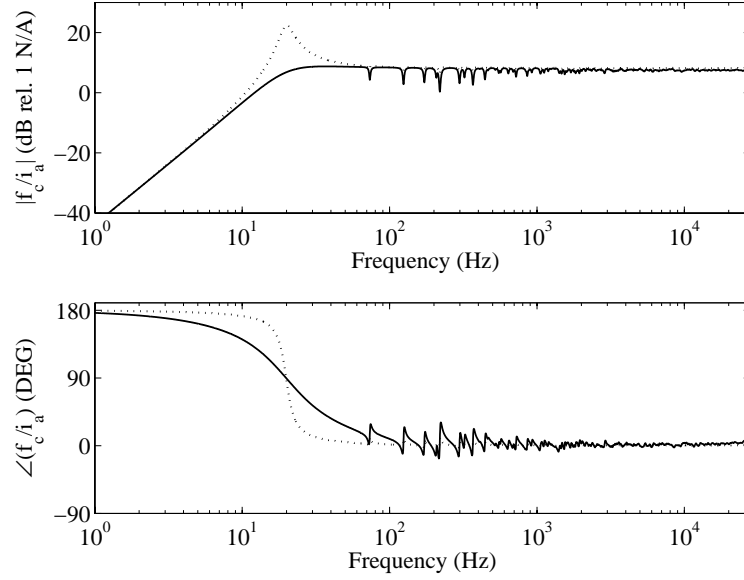
Figure 4.2: *Force transmitted to the base structure per unit driving current. Thick line heavily damped actuator (C_a=3.3 N/ms^{-1}), dotted line lightly damped actuator (C_a=0.5 N/ms^{-1}).*

Considering first the case where the actuator is lightly damped (dotted line), at frequencies below the fundamental resonance frequency of the actuator, the transmitted force f_c is out of phase with the driving current signal and monotonically rises from zero up to a maximum value at the fundamental resonance of the actuator at about 20 Hz. At higher frequencies, the transmitted force f_c is in phase with the driving current signal and its amplitude levels down to a constant value which is approximately equal to the reactive forces $\pm f_a$ generated by the coil–magnet linear motor [19]. The narrow band troughs of the amplitude are produced by the low impedance effect offered by the plate at resonance frequencies. When the actuator is heavily damped, then the actuator resonance peak is smoothed down and can hardly be seen. Also the transition from out of phase to in phase force actuation is stretched out over a wider frequency band. In conclusion, if negative velocity feedback is implemented, the desired damping action is produced only above the fundamental resonance of the actuator. In contrast, below this frequency, negative damping is generated, which tends to destabilise the control loop. This observation already offers a key indication about the fundamental issues of this type of actuator, that is, the actuator should be designed with the smallest possible fundamental resonance frequency in order to

ensure a constant force excitation in a wider range of low frequencies where the active damping effect is mostly desired.

4.2   Stability of a direct velocity feedback loop

In order to prepare the background theory for the scaling study, the stability analysis of a direct velocity feedback loop is also revised using a mobility function based on a classic disturbance rejection feedback block diagram.

Assuming the error sensor for the feedback loop is an ideal velocity sensor located at the base of the actuator, in which case it measures exactly $\dot{w}_c$, the response of the panel measured by the error sensor can be modelled in terms of the classic disturbance rejection feedback block diagram shown in Figure 4.3, where $G_{cc}(\omega)$ and $G_{cp}(\omega)$ are the fully coupled FRFs between the error sensor velocity $\dot{w}_c$ and either the control current i_a or primary force excitation f_p which can be derived from Eqs. (4.1) to (4.4) [53]:

$$G_{cc}(\omega) = \frac{\dot{w}_c}{i_c} = \frac{Y_{cc}\psi}{1 + Z_a\left(Y_a + Y_{cc}\right)}, \tag{4.11}$$

$$G_{cp}(\omega) = \frac{\dot{w}_c}{f_p} = \frac{\left(1 + Z_a Y_a\right)Y_{cp}}{1 + Z_a\left(Y_a + Y_{cc}\right)}. \tag{4.12}$$
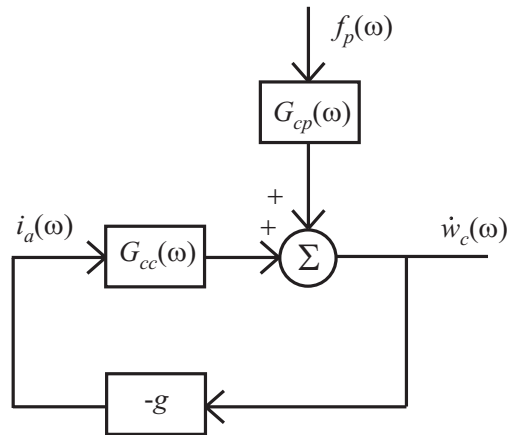
Figure 4.3: *Block diagram of the velocity feedback control loop using a current driven electrodynamic proof mass actuator.*

Figure 4.4 shows the Bode and Nyquist plots of the open loop sensor-actuator FRF $gG_{cc}(\omega)$ assuming g=1. The Bode plot shows that the modulus of $G_{cc}(\omega)$ is characterised by a heavily damped resonance at about 20 Hz, which is due to the actuator fundamental mode, and then a sequence of resonance peaks which are due to the low order natural modes of the plate. The phase of $G_{cc}(\omega)$ starts from +270° at low frequency, drops to +90° beyond the resonance of the actuator and then it alternates between +90° and –90° for the resonances of the plate. As a result the Nyquist plot shows that the loci of $G_{cc}(\omega)$ is characterised by one circle in the left hand side quadrants, which is due to the resonance of the actuator, and many circles in the right hand side quadrants, which are due to the resonances of the plate. Therefore, using the Nyquist stability criterion [47], the control system is found to be only conditionally stable since, for relatively high control gains, the circle on the left hand side due to the fundamental resonance of the actuator can enclose the Nyquist instability point. Also, for moderate control gains that ensure stability, the circle in the left hand side indicates that control spillover is bound to occur around the fundamental resonance frequency of the actuator.
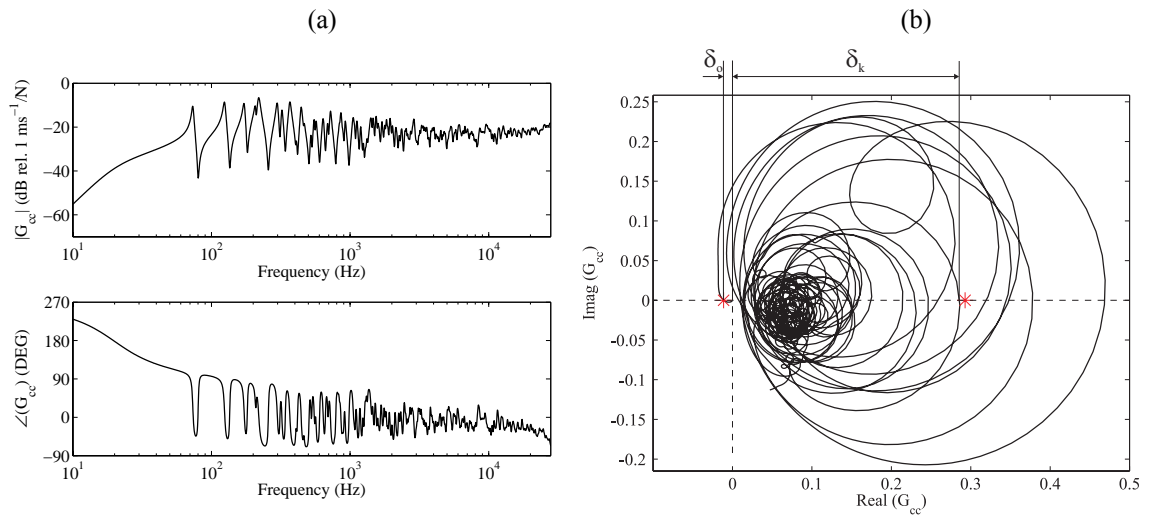
Figure 4.4: *Bode (a) and Nyquist (b) plots of the open loop sensor-actuator FRF $gG_{cc}(\omega)$, assuming g=1 when a proportional feedback loop is used for current control.*

In summary the stability and control performance of a velocity feedback control loop with a proof mass actuator are heavily affected by the presence of the fundamental resonance of the actuator. In order to guarantee a stable feedback control loop with high control gains it is necessary to reduce the amplitude of the actuator resonance so that the left hand side circle in the Nyquist plot is small. Nevertheless, when large control gains are implemented the undesired control spillover effect takes place.

In order to reduce the amplitude of the first resonance peak of $G_{cc}(\omega)$, the fundamental natural frequency of the actuator should be kept as low as possible: ideally it should be brought down to zero. This can be achieved by designing the proof mass suspension system with very soft springs. However, with a too soft suspension system, the static displacement of the proof mass becomes too big so that practical problems, such as non linearity due to the proof mass striking the housing of the actuator may disrupt the stability of the feedback control loop [54]. The amplitude of the fundamental resonance of the proof mass actuator can also be lowered by increasing the damping effect in the actuator. However, this approach is also affected by practical problems, which again may involve non linearity.

4.3   Control performances

The velocity feedback control system considered in this chapter is devised to produce active damping, which efficiently reduces the response at the resonance frequencies of the panel. Thus the effectiveness of the control system can be assessed by looking to the reduction of vibration that can be achieved at each resonance frequency rather than over the whole frequency band. The active damping effect produced by each control unit can be assessed by considering the reduction of vibration at the control position, although, it should be noted that this does not directly correspond to a mean reduction of vibration over the panel surface. In fact, as discussed in reference [27] for too high control gains, the control units produce a pinning effect at the control position which simply rearranges the spatial vibration of the panel and does not inject damping to the structure.

According to the block diagram in Figure 4.3, the responses at the control position per unit primary excitation with and without feedback control are respectively given by:

$$\frac{\dot{w}_{c/c}}{f_p} = \frac{G_{cp}}{1 + gG_{cc}},$$

(4.13)

$$\frac{\dot{w}_{c/nc}}{f_p} = G_{cp}.$$

(4.14)

Therefore, the maximum reduction of vibration at the control position at the k-th resonance frequency ω_k is given by the following expression:

$$\rho_k = \frac{\left|\dot{w}_{c/c}^{f_p}(\omega_k)\right|}{\left|\dot{w}_{c/nc}^{f_p}(\omega_k)\right|} = \frac{1}{\left|1 + g_{\max} G_{cc}(\omega_k)\right|} \qquad (4.15)$$

where $g_{\max}$ is the maximum feedback control gain that guarantees stability which, approximately, can be taken as the reciprocal of the real part of the open loop sensor–actuator FRF, G_{cc}, at the fundamental natural frequency of the actuator $\omega_a = \sqrt{K_a/M_a}$;

$$g_{\max} \approx -\frac{1}{\mathrm{Re}\{G_{cc}(\omega_a)\}} . \qquad (4.16)$$

The response at the resonance frequencies of the low order natural modes of the plate can also be approximated by the real parts of the open loop sensor–actuator FRF, G_{cc}, at the resonance frequencies, i.e. $G_{cc}(\omega_k) \approx \mathrm{Re}\{G_{cc}(\omega_k)\}$, so that the ratio ρ_k can be expressed as

$$\rho_k \approx \frac{1}{1 + \delta_{k0}} \qquad (4.17)$$

where $\delta_{k0} = \delta_k / \delta_0$ with $\delta_k = \mathrm{Re}\{G_{cc}(\omega_k)\}$ and $\delta_0 = -\mathrm{Re}\{G_{cc}(\omega_a)\}$. Normally the control performance is expressed in terms of a dB reduction with the following formula:

$$R_k \equiv 20 \log_{10}\left(\frac{1}{\rho_k}\right) \approx 20 \log_{10}\left(1 + \delta_{k0}\right). \qquad (4.18)$$

This simple expression will be referred as the 'stability-performance' formula since it contains both information on the stability and control performance of the feedback system. The stability and control performance effects are often analyses separately. Normally the design of a feedback loop is focused on getting stability with large control gains although this does not automatically correspond to large control performance over the targeted frequency band. Indeed, as one can notice from Eqs. (4.17) and (4.18), the true objective is to maximise the ratio $\delta_{k0} = \delta_k / \delta_0$, that is the ratio between $\mathrm{Re}\{G_{cc}(\omega_k)\}$ and $\mathrm{Re}\{G_{cc}(\omega_a)\}$. This simple and compact way of presenting the result will be used in the following analysis

to assess the true effect of the actuator scaling on the performance of a velocity feedback control loop.

The plot in Figure 4.5 illustrates the reduction of vibration at the control when either a moderate feedback gain, (dotted line), or the maximum feedback gain that guarantees stability (dashed line) is implemented. With the moderate gain, the control unit produces a good damping effect which generates significant reduction of vibration up to 850 Hz (between 5 and 10 dB) and nearly no control spillover effect at the fundamental resonance frequency ω_a of the actuator.
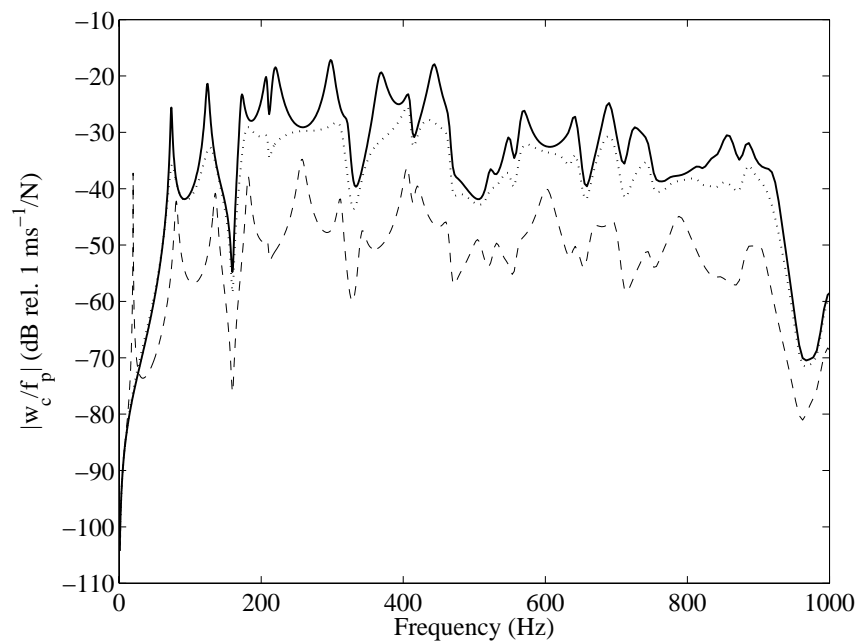
Figure 4.5: *Amplitude of the response at the control position per unit primary force when there is no control (thick line), and when the feedback control loop implements a)moderate control gain (dotted line) and b) the maximum control gain that guarantees stability (dashed line).*

When the maximum control gain is implemented, there is a consistent active damping action which produces very large reductions (up to 25 dB) at the control position within the whole frequency range considered in the plot. However, this result is obtained at the expense of a pronounced peak at the fundamental resonance frequency ω_a of the actuator which is due to the control spillover effect generated by the resonant dynamics of the actuator at low frequency.

4.4   Electrodynamic actuation force scaling laws

Normally the scaling study of a control system is carried out by assessing how the force generated by an actuator varies as the size of the actuator is scaled. Although at first sight this looks as the obvious approach, it is also important to analyse how the stability and active control, i.e. active damping, effects vary with the scaling of the actuator [53]. In this way it is possible to get a clear indication whether it would be convenient to use few, large scale, control units or many, small scale, control units over the surface of the panel. In the following sections the scaling laws for the principal components of the actuator are first revised. The stability–performance formula derived in the previous section is then used to assess how the maximum control performance varies with the scaling of the actuator.

The scaling laws of the actuation force produced by a linear electrodynamic motor have been presented by Trimmer[55] who has considered three cases:

    a)   constant current density, J_a, in the coil;

    b)   constant heat flow, ΔQ, per unit surface area of the windings in the coil and

    c)   constant temperature difference, ΔT, between the windings of the coil and the surrounding environment.

For, these three cases the scaling of current density, J_a, in the windings of the coil with reference to dimension, here expressed as 'L', are given by:

    a)   constant J_a in the windings $\hspace{3cm} J_a \propto \left[L^0 \right]$,

    b)   constant ΔQ per unit surface area of the windings $\hspace{0.3cm} J_a \propto \left[L^{-0.5} \right]$,

    c)   constant ΔT between windings and environment $\hspace{0.5cm} J_a \propto \left[L^{-1} \right]$.

Assuming the proof mass is made of a permanent magnet material that, because of its cross sectional shape (see Figure 4.1a), generates a constant magnetic field B across the windings of the coil, the actuation force is given by Eq. (4.10) with the voice coil coefficient given by $\psi = Bl$, where l is the total length of the windings, and the current is given by $i_a = J_a A$, where A is the cross sectional area of the winding. Thus

$$f_a = BlAJ_a .$$
$$\hspace{6cm} (4.19)$$

As a result, the scaling laws with reference to dimension of the actuation force are given by:

a) constant J_a in the windings $\qquad\qquad\qquad\qquad f_a \propto \left[L^3 \right]$,

b) constant ΔQ per unit surface area of the windings $\quad f_a \propto \left[L^{2.5} \right]$,

c) constant ΔT between windings and environment $\quad f_a \propto \left[L^2 \right]$.

These three expressions indicate that the force generated by a coil–magnet linear motor scales poorly when one scales down the system. Indeed, it is common to assume that, for micro-scale systems, it is preferable to adopt other types of actuation such as for example electrostatic actuation which scales with $\left[L^2 \right]$ or $\left[L \right]$, when the electric field scales respectively with $[L^0]$ and $[L^{-0.5}]$, as described by Trimmer [55].

4.5   Scaling laws of the mechanical components of the actuator

According to the schematic shown in Figure 4.1b and the analytical formulation for the response of the system presented in previous section, the principal mechanical components of the actuator are the proof mass, the suspension system and, although it does not correspond to a self contained mechanical component, the viscous damper which describes the damping effect produced by the squeeze film of lubricant between the guiding stinger and the central hole in the proof mass (see Figure 4.1a). The scaling laws for the mass, stiffness and damping effects of these three components can be derived by inspection of the formulae for these quantities.

Despite the cross section of the magnet proof mass is rather involved, it can be readily shown that its scaling law is

- Proof mass scaling $\qquad M_a \propto \left[L^3 \right]$.

In order to minimise the deformation stress effect in the mounting spring [56], a spring with ring shape has been chosen for the suspension of the mass in the prototype system studied in this thesis. According to Young and Budynas [57], the stiffness of a ring to a diametric load is given by

$$K_a = \frac{EI}{R^3}\left(\frac{4\pi}{k_1\pi^2 - 8k_2^2}\right) \tag{4.20}$$

where E is the Young's modulus of the material of the spring, R is the radius of the ring, I is the area moment of the cross section of the ring (for rectangular section of dimensions $b \times h$, it is $I = bh^3/12$) and k_1, k_2 are dimensionless constants [57]. As a result the scaling law for the suspension system is given by:

- Suspension stiffness scaling $K_a \propto [\,L\,]$.

Finally, the coefficient for the damping effect produced by the squeeze film of lubricant between the guiding stinger and the central hole in the proof mass results directly proportional to the linear dimension [43], thus:

- Squeeze film damping scaling $C_a \propto [\,L\,]$.

4.6 Scaling laws of the dynamic characteristic of the proof mass actuator

The principal dynamic characteristics of the proof mass actuator are given by its fundamental natural frequency, static displacement and damping ratio, which are given by the following expressions:

$$\omega_a = \sqrt{\frac{K_a}{M_a}} \quad , \quad \delta_a = \frac{M_a g}{K_a} \quad , \quad \zeta_a = \frac{C_a}{2\sqrt{K_a M_a}} \, . \tag{4.21}$$

Thus, the scaling laws for these three functions are given by:

a) fundamental natural frequency scaling $\quad \omega_a \propto \left[L^{-1}\right]$,

b) static displacement scaling $\quad\quad\quad\quad \delta_a \propto \left[L^2\right]$,

c) damping ratio scaling $\quad\quad\quad\quad\quad \zeta_a \propto \left[L^{-1}\right]$.

These three expressions indicate that as the size of the actuator is scaled down the fundamental natural frequency and the damping effect tends to rise proportionally to the scaling of dimension, while the static displacement falls down with the square of dimension. The first effect is certainly undesirable since, as we have seen in the previous section, it is of critical importance to design the actuator with the smallest possible

fundamental natural frequency. In contrast, the fact that the static displacement falls down with the square of scaling is a positive effect since it reduces the problems associated to quasi static vibrations of the actuators which can be associated to a rigid body motion of the structure under control [54]. Finally the increase of the damping effect proportionally to the scaling should be regarded as a positive effect since, according to the discussion presented in previous section, the higher is the damping the smaller is likely to be the amplitude at the fundamental resonance of the actuator and thus the higher should be the maximum control gain for a stable feedback control loop.

The last fundamental characteristic of the proof mass actuator is the force it can transmit to the base. Remembering that, $\psi i_a = f_a$, the scaling of the force transmitted to the plate can be readily derived by assuming $C_a = 0$, in which case Eq. (4.10) can be rewritten in the following form:

$$f_c = \frac{f_a}{1 - \frac{\omega_a^2}{\omega^2} + \frac{K_a}{j\omega}Y_{cc}} .$$

(4.22)

Considering frequencies above ω_a, Eq. (4.22) gives the following scaling laws:

   a) constant J_a in the windings $\hspace{4em} f_c \propto \left[L^3 \right]$,

   b) constant ΔQ per unit surface area of the windings $\hspace{1em} f_c \propto \left[L^{2.5} \right]$,

   c) constant ΔT between windings and environment $\hspace{1em} f_c \propto \left[L^2 \right]$.

Thus, the scaling produces the same type of effects on the force effectively transmitted to the structure to be controlled as for the actuation force f_a.

4.7 Scaling laws for the stability and performance parameters

The crucial analysis to assess the effect of scaling on the implementation of a velocity feedback control loop using an electrodynamic proof mass actuator should be carried out considering the control performance with reference to the maximum stable feedback control gain. As discussed in Section 4.3, this can be done by using the stability–performance formula in Eq. (4.18). The ratio $\delta_{k0} = \delta_k/\delta_0$ can be derived in a simplified form by making some assumptions about the driving point mobility function of the plate

structure $Y_{cc}(\omega)$. In fact, assuming $\omega = \omega_a < \omega_k$, where ω_k is the k-th natural frequency, the mobility function for $Y_{cc}(\omega)$ given in Eq. (4.5) can be approximated by

$$Y_{cc}(\omega_a) \approx \frac{j\omega}{K_p} \tag{4.23}$$

where

$$\frac{1}{K_p} = \sum_{n=1}^{N} \frac{\left[\phi_n(x_c, y_c)\right]^2}{M_p \omega_n^2} . \tag{4.24}$$

Thus, using Eqs.(4.7), (4.8) and (4.11), the value of δ_0 is found to be

$$\delta_0 = -\text{Re}\{G_{cc}(\omega_a)\} \approx \frac{-\omega_a \psi}{2\zeta_a K_p - C_a \omega_a} . \tag{4.25}$$

Assuming now $\omega = \omega_k > \omega_a$, the mobility function for $Y_{cc}(\omega)$ in Eq. (4.5) can be approximated by

$$Y_{cc}(\omega_k) \approx \frac{1}{C_{p,k}} \tag{4.26}$$

where

$$\frac{1}{C_{p,k}} = \frac{\left[\phi_k(x_c, y_c)\right]^2}{M_p \omega_k \eta} . \tag{4.27}$$

Thus, using Eqs. (4.7), (4.8) and (4.11), the value of δ_k is found to be

$$\delta_k = \text{Re}\{G_{cc}(\omega_k)\} \approx \frac{\psi}{C_{p,k} + C_a} . \tag{4.28}$$

In conclusion, assuming $\omega_k > \omega_a$, the stability–performance formula of Eq. (4.18) is found to be

$$R_k \approx 20\log_{10}\left(\frac{\omega_a C_{p,k} - 2\zeta_a K_p}{\omega_a(C_{p,k} + C_a)}\right),$$

(4.29)

which, according to the scaling laws found for electrodynamic proof mass actuator components and dynamic parameters gives the following scaling law for all three cases of a) constant J_a in the windings, b) constant ΔQ per unit surface area of the windings and c) constant ΔT between windings and environment:

$$R_k \propto \left[20\log_{10}\left(\frac{C_{p,k} - 2K_p}{C_{p,k} + L}\right)\right].$$

(4.30)

This formula suggests that the scaling of the actuator produces an increment of the maximum reduction of vibration that the actuator can produce at the k-th resonance frequency of the structure. This is an important result whose end product becomes even more important when it is also observed that the maximum number of control units, N_{cu}, with base surface S, that can be fitted in a panel of dimensions $l_x \times l_y$ is given by $N_{cu} = \dfrac{l_x \times l_y}{S}$. Thus the number of control units per unit surface of the structure to be controlled scales with $N_{cu} \propto \left[L^{-2}\right]$.

Therefore, this simple formulation indicates that, using a large number of decentralised control units implementing velocity feedback control with small scale actuators may be much more effective than adopting fewer control units with relatively bigger control actuators.

It is important to specify, that the formulation presented above is based on the assumption that $\omega_a < \omega_k$ which, because $\omega_a \propto \left[L^{-1}\right]$, is bound to be valid only for a limited range of scaling. Nevertheless this formulation can be used to design the best type and size of control actuator to be used to form the most convenient array of decentralised control units for the control of vibration and thus also sound radiation. Also it should be highlighted that

the stability-performance formula does not take into account cross talking effects between actuators which, as shown by Bauman and Elliott [52] tends to degrade the stability of neighbouring actuators as they get closer to each other. Thus it is likely that there is an optimal size and spatial density of the actuators that produces the best trade off between stability and control effect.

4.8 Summary

This chapter has introduced the stability and performance study of a small scale prototype proof mass actuator for the implementation of a direct velocity feedback loop on a thin panel structure. A 'stability–performance' formula that can be used to assess simultaneously the stability and control performance of the feedback control loop with the proof mass actuator has been derived from a mobility/impedance formulation. The principal scaling and design issues of the proof mass actuator have then been analysed in view of the stability requirements and control performance properties of the feedback loop. The principal outcome of this study has highlighted that the scaling of a proof mass actuator using an electrodynamic linear motor produces both positive and negative effects. Among the positive effects are the reduction of the static displacement δ_a and increment of the damping ratio ζ_a, which scale respectively with $\left[L^2\right]$ and $\left[L^{-1}\right]$. Alternatively, among the negative effects are the rise of the fundamental natural frequency ω_a and decrement of the control force f_a generated by the actuator, which scale respectively with $\left[L^{-1}\right]$ and one of the three following laws $\left[L^3\right]$, $\left[L^{2.5}\right]$, $\left[L^2\right]$ depending on which assumptions are made for the driving current in the coil. However, assuming the fundamental resonance frequency of the actuator is below the first resonance of the smart panel, the reduction of vibration for the maximum control gain that guarantees a stable feedback control loop has been found to scale with $20\log_{10}\left(\frac{C_{p,k}-2K_p}{C_{p,k}+L}\right)$, which indicates that the overall effect of scaling produces a small increment of the maximum reduction of vibration.

5 DESIGN AND TEST OF A PROTOTYPE DVFB CONTROL UNIT WITH A SMALL SCALE PROOF MASS ACTUATOR

In this chapter the design of a prototype actuator for the smart panel with five decentralised control units which is considered in Chapter 6 is presented. The stability and control performance experimental tests carried out when only the control unit listed as N.2 (see Figure 6.1) is mounted on the smart panel are presented and contrasted with theoretical predictions. In order to take into account the inertial effect of the base disc and coil components of the prototype actuator, the simulation results have been derived from a modified version of the model presented in Section 4.1 where the complex force f_c is given by:

$$f_c = -Z_{ab}\dot{w}_c + Z_a \dot{w}_m + f_a \tag{5.1}$$

where

$$Z_{ab} = \frac{K_a}{j\omega} + C_a + j\omega\, M_b, \tag{5.2}$$

and M_b is mass of the base disc and coil of the actuator. Thus, the fully coupled FRFs $G_{cc}(\omega)$ and $G_{cp}(\omega)$ used in the stability analysis and to derive the open and closed loop responses at the error sensor position with Eqs. (4.11) and (4.12) are given by:

$$G_{cc}(\omega) = \frac{\dot{w}_c}{i_c} = \frac{Y_{cc}\psi}{1 + Z_{ab}Y_{cc} + \left[Z_a + \left(Z_a^2 - Z_{ab}Z_a \right)Y_{cc} \right]Y_a}, \tag{5.3}$$

$$G_{cp}(\omega) = \frac{\dot{w}_c}{f_p} = \frac{\left(1 + Z_a Y_a\right)Y_{cp}}{1 + Z_{ab}Y_{cc} + \left[Z_a + \left(Z_a^2 - Z_{ab}Z_a \right)Y_{cc} \right]Y_a}. \tag{5.4}$$

5.1 Design of the prototype proof mass actuator

This section presents a brief summary of the design of the small scale electrodynamic proof mass actuator shown in Figure 5.1 that has been built for this study. The details of

the design are presented by Paulitsch [56]. As schematically shown in Figure 4.1a, this actuator is composed of a base disc with a cylindrical former on which the coil is wound. A cylindrical permanent magnet is mounted on three springs and a vertical bushing, which forces the magnet to oscillate in the axial direction.
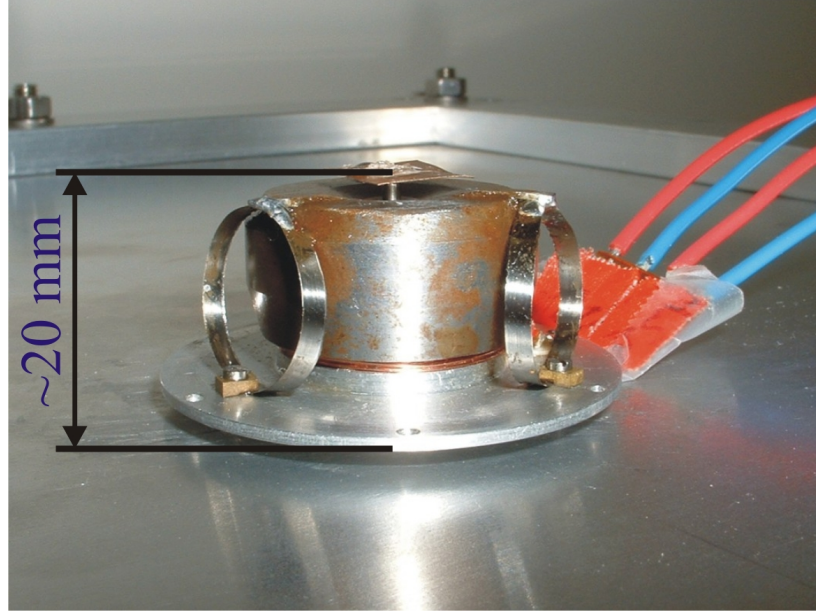
Figure 5.1: *Photo of the small scale electrodynamic proof mass actuator.*

As shown in Figure 5.1, the three springs are made of small circular rings which guarantee a relatively larger stiffness in the transverse direction than in the axial direction. In this way the fundamental axial natural frequency of the proof mass actuator can be kept rather low with a good transverse guiding which prevents non linear effects due to stick slip friction on the axial bushing. As shown in Figure 4.1a, the cross section of the magnet is shaped in such a way as to have a magnetic circuit that generates a field oriented in the direction orthogonal to the coil winding. In this way a current flow through the coil produces the reactive axial force between the coil and the magnet which is given by Eq. (4.9). The design of a small scale electrodynamic proof mass actuator is relatively complex since for each part of the actuator there are contrasting requirements. First, the number of coil windings should be large for a high transducer coefficient ψ, but the coil has to fit in the magnetic circuit and its resistance should not be high in order to minimize electrical energy dissipation. This can be achieved by appropriately designing the number of coil windings, the coil diameter and the diameter of the wire. Second, despite the small dimension requirements, a relatively large actuation force should be generated by the coil–magnet system. This can be achieved by maximizing the magnetic field perpendicular to the coil windings by appropriately choosing the size of the permanent magnet, the air gap between

the coil and the magnet, and the shape and material of the magnetic circuit. Third, the mounting springs must have very low axial stiffness in order to keep as low as possible the axial fundamental natural frequency of the proof mass actuator, although they must also bear the weight of the magnet without breaking and without too large static displacements. The design of the actuator shown in Figure 5.1 has been carried out by first setting the dimensions and shape of the magnetic circuit, second the coil dimensions and third the shape and dimensions of the circular springs. For a moving mass of 20 grams, an actuation force up to 4 N at an electrical power input of 5 W was aimed for. Different shapes of the magnetic circuit were considered and, because of the possibility to use a strong Nd-Fe-B permanent magnet, the one shown in Figure 5.1 with the given geometric dimensions was further investigated. For this geometry the actuation force is found to be [56]:

$$f_a = \frac{B_r H_l \, p h_g \left(A+2t\right) b \mu_o \left(A^2 - A_i^2\right)}{4 H_l \, p h_g \left(A+2t\right) b \mu_o + B_r q \left(A^2 - A_i^2\right) s} \sqrt{\frac{P}{\rho_{wi}}} \sqrt{\frac{1}{2d+h_g}} \sqrt{\frac{\pi s}{\left(A+2t+s\right)}} \qquad (5.5)$$

where P is the electrical power, d is the actuator stroke, ρ_{wi} is the resistivity of the coil wire, B_r, H_l, μ_0 are the electromagnetic properties of the permanent magnet and other mediums of the magnetic circuit and p, q are non-dimensional leakage factors depending on the actuator shape. The force can be plotted against the moving mass for a large number of geometric values and as a result a linear relation between the maximum force and moving mass has been determined in the considered size range. This general trend has been verified by finite element simulations [56] where the leakage factors p and q are more accurately estimated. The parameter values compiled in TABLE I in mm have been determined for a moving mass of about 20 grams.

Table 5.1: *Actuator design parameters.*

Design	A_d(mm)	A_i(mm)	h_g(mm)	s(mm)	b(mm)	D_o(mm)	B_g (T)	m (g)	F_a (N)	h_{gl}(mm)
final	12.5	2	4	3	4.8	23.5	0.2972	20.3	3.66	2.3

The number of coil windings and the coil diameter are chosen based on the geometry given by the magnetic circuit design. At a given magnetic field in the air gap B_g the actuation force

$$f_a = \frac{B_r H_l \, p h_g \left(A+2t\right) b \mu_o \left(A^2 - A_i^2\right)}{4 H_l \, p h_g \left(A+2t\right) b \mu_o + B_r q \left(A^2 - A_i^2\right) s} \sqrt{\frac{P}{\rho_{wi}}} \sqrt{\frac{1}{2d+h_g}} \sqrt{\frac{\pi s}{\left(A+2t+s\right)}} \qquad (5.6)$$

depends on the coil diameter d_w and the number of turns in the vertical direction, $N=(h_g+2d)/d_w$ and in the horizontal direction, $n=((s-t_{ol})/d_w-1)2/\sqrt{3}+1$, where t_{ol} is a constant for the thickness of the coil former and gap clearance, e.g. $t_{ol}=0.5$ mm, and l_{con} is the length of the connecting wire. In order to reduce gaps between individual wires, the wire diameter should be chosen as small as possible. Thus it is a manufacturing constraint that determines the smallest thickness of the wire. Also, the number of turns should be as big as possible according to the manufacturing and construction constraints. Only a limited amount of current of 2 A is normally generated by off the shelf electric amplifiers. It is therefore possible to determine an upper limit of the wire diameter for a given power input of 5 W and a maximum heating limit of about 150°C. As a result of all these constraints, a wire diameter of 3.15 mm with 18 vertical and 8 horizontal windings was chosen [56].
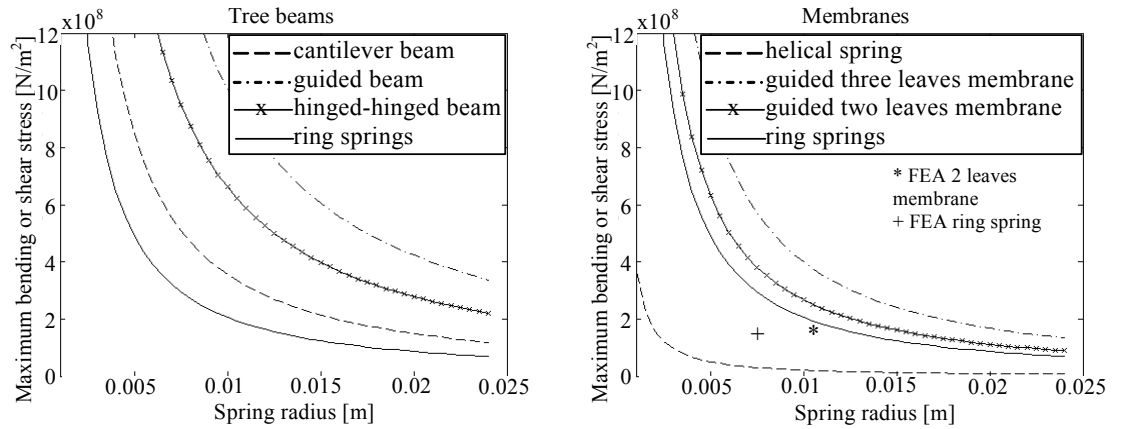
Figure 5.2: *Internal stress for a 316N/m suspension stiffness as function of spring radius.*

The supporting springs have to be designed in such a way that the fundamental resonance ω_a of the proof mass actuator is about 3 times lower than the lowest flexible resonance frequency of the plate $\omega_1 \approx 60$ Hz. As seen above, in this way, the actuator transmits a constant force, which is proportional to the reactive force f_a generated by the coil–magnet system, over the range of frequencies where the resonant response of the panel has to be controlled. The fundamental resonance frequency of the proof mass actuator scales like $[L^{-1}]$ provided that the magnitude of the moment of inertia of the suspension I_d can always be made small enough [56]. The fulfilment of the last condition is not obvious since a small moment of inertia I_d and a large stroke results in a large mechanical stress that potentially cannot be withstood by the spring material. Figure 5.2 indicates that, in comparison to other spring types, ring shaped springs are predicted to have the lowest internal mechanical stress for the size determined by the moving mass.

5.2 Open loop stability analysis

Although the stability analysis of a single control unit does not provide a clear indication on the stability when the five decentralised control systems are implemented simultaneously, it is instructive to start with this type of analysis, which gives a physical understanding of the causes of instability in each control unit.
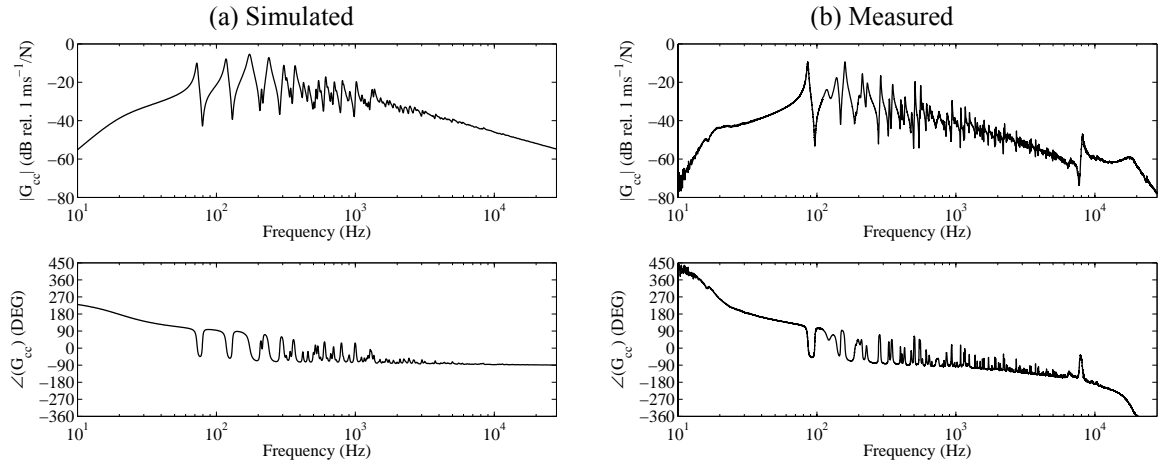
Figure 5.3: *Simulated (a) and measured (b) Bode plots of the open loop frequency response function between the error sensor signal and the input signal to the analogue control system when sole the control unit N.2 is mounted on the plate considered in the Figure 3.1.*

The Bode plots in Figure 5.3 show the simulated (a) and measured (b) open loop sensor–actuator FRF when only the control unit N.2 is mounted on the smart. The two plots agree quite well and show that there is nearly no peak of the fundamental resonance of the actuator at about 20 Hz. As discussed in section 4.2, this is due to the fact that the fundamental resonance of the actuator is well below the first resonance of the panel and to the fact that there is a rather high internal damping effect in the actuator. Also the high pass filter used to implement DC decoupling contributes to lower the amplitude of the actuator fundamental resonance. This high pass filter has been design with a 30 Hz corner frequency in order to minimise the control spillover effect at DC. Between 60 Hz and 2 KHz the FRF is characterised by a sequence of lightly damped plate resonances. At higher frequencies there is a constant amplitude roll off with frequency of the FRF, which, comparing the simulated open loop sensor–actuator FRFs in Figure 4.4a and Figure 5.3a is found to be primarily due to the inertial effect of the base disc and coil components of the actuator. At about 6 kHz there is a deep trough followed by a sharp resonance peak. A finite element analysis of the base disc and cylindrical former has shown a resonance frequency in a similar frequency range. At higher frequencies two other resonances are

visible, which are due to the flexible modes of the circular springs and the roll-off in the amplifier.

The Nyquist plots in Figure 5.4 show the simulated (a) and measured (b) open loop sensor–actuator FRF for the control unit N.2. The two plots show a small semi-circle on the left hand side which is due to the heavily damped fundamental resonance of the actuator and the high-pass filter for the DC decoupling. There are then a number of circles on the right hand side which are due to the plate resonances. The phase lag effect generated by the inductive effect of the coil gradually drifts the loci towards the imaginary axis in the bottom right quadrant so that the large circle for the base disc and cylindrical former resonance is oriented along the imaginary negative axis. At higher frequencies the loci enters the left hand side quadrants but, because of the inertial roll off effect of the base disc and coil components of the actuator, the amplitude is relatively small compared to the low frequency part located on the positive real quadrants. In conclusion, the control system is bound to be conditionally stable with a gain margin $g_{max} = -1/\delta_0 \cong 13\,\text{dB}$.

(a) Simulated   (b) Measured
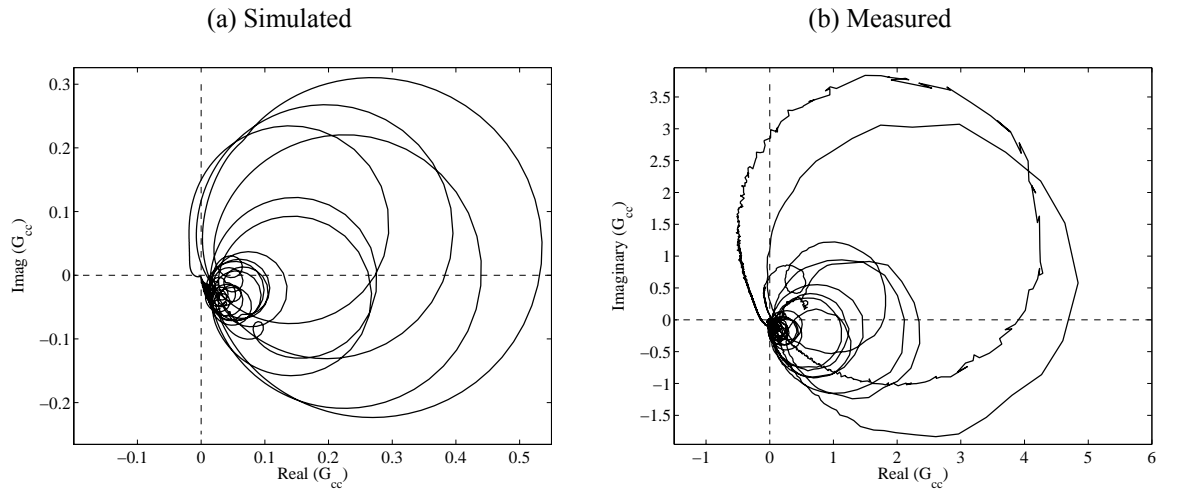
Figure 5.4: *Simulated (a) and measured (b) Bode plots loop frequency response function between the error sensor signal and the input signal to the analogue control system when sole the control unit N.2 is mounted on the plate considered Figure 3.1.*

As discussed in Section 4.3, the Nyquist plot in Figure 5.4 can also be used to estimate the maximum reduction of vibration at the control position that can be achieved at a certain resonance frequency of the panel. For the k-th resonance frequency, the maximum reduction of vibration in dB is given by $R_k = 20\log_{10}|1 + \delta_k/\delta_0|$, so that for the largest resonance circle at about 180 Hz the maximum reduction is predicted to be about 20 dB. In order to further enhance the controllability of the system, several actions could be taken.

First, the high-pass filter could be tuned such that an anti-resonance frequency lies at the intersection of the loop with the real axis. Second, the cut-off frequency of the high-pass filter could be lowered so that the low frequency bandwidth is dominated by the electrodynamic proof mass actuator resonance at about 20Hz. In this case the amplitude of the fundamental actuator resonance, at about 20 Hz, should be further lowered by either pulling down the resonance frequency or by enhancing the damping of this vibration mode. Third, the amplitudes of the two flexible resonances of the circular springs should also be lowered by enhancing the structural damping effect in the ring springs. Probably it would also be helpful to increase the amplifier bandwidth or increase damping at the cut-off frequency. In this way, the part of the locus on the left hand side quadrants of the Nyquist plot is further squeezed towards the imaginary axis and larger control gains can be implemented in the feedback control loop.

5.3 Closed loop control performance analysis

The plot in Figure 5.5 shows the simulated (a) and measured (b) spectra of velocity measured by the error sensor of the sole control unit N.2 per unit force generated by the primary shaker as.
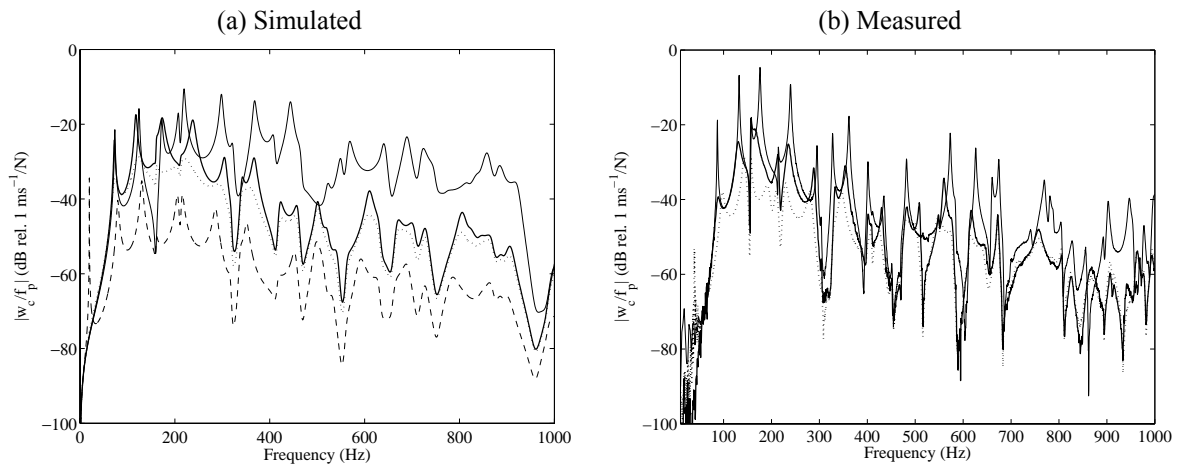
Figure 5.5: *Simulated (a) measured (b) velocity at the error sensor N.2 per unit primary force without actuator (faint line), with actuator and no control (thick line) and with actuator when a moderate feedback control gain is implemented (dotted line) and very high control gain (dashed line).*

The two plots show quite good agreement between the simulation and experimental results. The faint lines in the two plots show that the response at the error sensor when the actuator is not mounted on the panel is characterised by well separated sharp resonance peaks in nearly the whole frequency range considered. When the sole actuator N.2 is mounted on

the plate, then the resonance peaks are slightly moved down in frequency and, more importantly, are rounded off by the passive damping effect produced by the actuator (thick line). At frequencies above the fundamental resonance frequency of the actuator, the actuator proof mass acts as an inertial reference so that, for moderate internal damping effects, additional passive damping is injected to the plate [2]. Comparing the simulated results in Figure 4.5 and Figure 5.5a, it is noted that the constant roll off of the measured response in Figure 5.5b is due to the inertial effect of the base disc and coil components of the actuator. When the feedback loop is closed with a moderate gain that guarantees stability and low control spillover effect, then, as shown by the dotted line, between 80 and 250 Hz the vibration at the error sensor goes down by 5 dB to 10 dB. However at very low frequency, there is some control spillover effect which as discussed in Section 4.1 is due to the low frequency smooth 180° phase transition of the actuation force. If the maximum gain that guarantees stability was to be implemented, then, according to the dashed line in Figure 5.5a, reductions up to 20 dB would have been produced but at the cost of a very large control spillover effect at the fundamental resonance frequency of the actuator.

5.4   Summary

In this chapter the design of a small scale prototype actuator has been described in detail. The stability and control performance of one direct velocity feedback control unit with such an actuator mounted on a clamped thin rectangular panel has been assessed experimentally. The stability of this feedback loop is limited by the low frequency dynamics of the actuator which allows a maximum stable control gain $g_{max} = 13\text{dB}$. With this control gain, reductions of vibration between 5 dB and 10 dB in the frequency band between 80 and 250 Hz have been measured at the control position. However, a spillover effect has been measured at low frequency close to the fundamental resonance of the actuator.

6 IMPLEMENTATION OF DECENTRALISED CONTROL

This chapter presents the study on the practical implementation of decentralised velocity feedback control on a thin aluminium rectangular panel with miniaturised proof mass electrodynamic actuators. In the previous chapters the principal problems related to the design of a stable and effective velocity feedback loop using a small scale actuator have been presented. In particular, a scaling study (chapter 4) with reference to a 'stability–performance' formula has been introduced, which has shown the effective result of scaling on the maximum control performance of the feedback loop. The scaling of the actuator produces contrasting results: such as the undesired increase of the fundamental resonance frequency or reduction of the transmitted force of the proof mass actuator and the desirable increment of internal damping and reduction of static deflection. The final outcome of the scaling study has shown that, by reducing the size of the actuator there is no loss of control performance; on the contrary, since a bigger number of small scale control units can be fitted per unit surface of the panel to be controlled, larger control performances could be generated.

Based on these observations, a small scale prototype actuator has been designed, built and studied. In particular, its stability and control performance have been analysed experimentally in chapter 5. In this chapter the implementation on a thin rectangular panel of five decentralised feedback control units using five of these prototype small scale proof mass actuators is studied in detail. The passive and active effects of the set of five control units are assessed both theoretically and experimentally. In particular the stability of the control system is reassessed since, although each control unit has been designed with a wide range of stable control gains, the stability of the set of five decentralised control units is constrained by the 'cross talking' effects between the proof mass actuators [52].

The stability and control performance of the smart panel with five decentralised control units is first analysed theoretically in Section 6.1 using a mobility/impedance model. Section 6.2 briefly describes the prototype smart panel built for this thesis. In section 6.3, the stability and control performance at the control locations of the five decentralised control units are then assessed experimentally. Finally, in Section 6.4 the global control performance produced by the five decentralised control units is assessed in terms of the

spatially averaged response of the panel, which has been measured with a scanning laser vibrometer, and in terms of the sound power radiated measured in an anechoic room.

The experimental results presented in this chapter clearly indicate that the set of five decentralised feedback control units using proof mass actuators produce both passive and active effects which tend to efficiently reduce the resonant response of the panel at low audio frequencies. The implementation of the five decentralised feedback control loops is limited by the 'cross talking' between the five control units in correspondence to their fundamental resonance frequencies, which limits the maximum active control performance.

6.1   Stability and control performance theoretical analysis

The smart panel considered in this chapter is made of five decentralised velocity feedback control units, which, as shown in Figure 6.1, are arranged along the diagonals of the panel and at its centre. The thin rectangular panel is clamped on a rigid frame placed at the top side of a rectangular box made with thick Plexiglas walls. The panel is excited by a shaker acting on the top right hand side corner or a speaker located inside the box. The details of the dimensions and material properties of the panel and control actuators are given in Table 4.1 and Table 4.2.
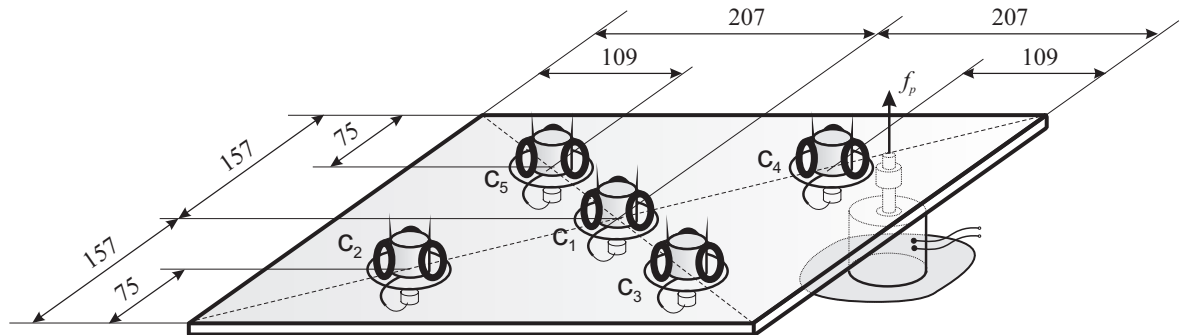
Figure 6.1: *Smart panel with five decentralised velocity feedback control units using proof mass electrodynamic actuators. The panel is excited by a shaker acting on the top left corner of the panel. Dimensions are in mm.*

6.1.1   Plate–actuators coupled model

The stability and control performance of the smart panel with five decentralised control units have been predicted with a mathematical model which is based on a mobility/impedance formulation. In order to accurately predict the response of the prototype smart panel built for this study, the dynamic effects produced by all three

mechanical components of the actuator have been taken into account. Thus, according to the sketch shown in Figure 6.2, the effects of the housing and base disc mass have been accounted for, together with the dynamic effect of the proof mass and spring-dashpot suspension system. Also, the inertial effect of the mass of the force gauge and moving part of the primary shaker has been taken into account.
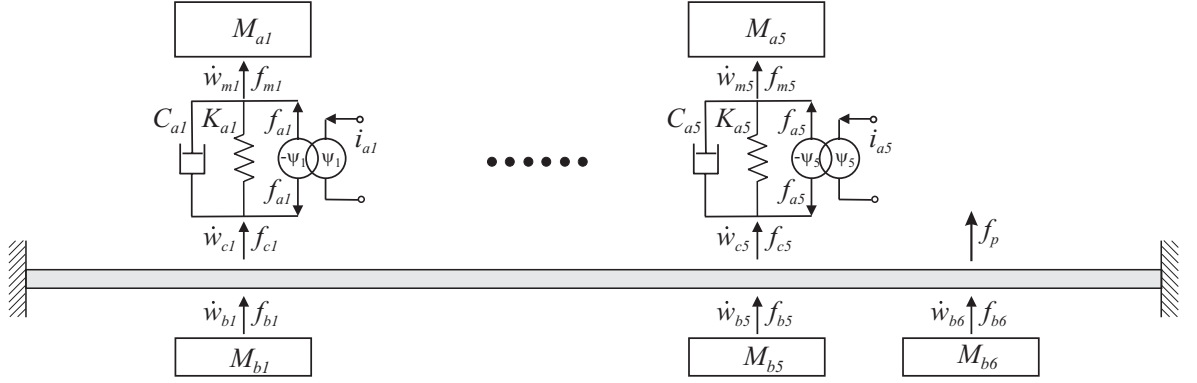
Figure 6.2: *Schematic with the notation for the velocity and force functions used in the mobility impedance model.*

The steady state response of the panel has been derived assuming the primary force disturbance to be harmonic, with time dependence of the form $\text{Re}\{\exp(j\omega t)\}$ where ω is the circular frequency and $j = \sqrt{-1}$. The mechanical and electrical functions in the model have therefore been taken to be the real part of anticlockwise rotating complex vectors, i.e., phasor, given in the form $X(\omega)e^{j\omega t}$, where $X(\omega)$ is the phasor at $t=0$.

Considering the notation shown in Figure 6.2, the phasors of the complex transverse velocities at the control positions, $\dot{w}_{cr}(\omega)$, and at the base of the actuators and primary shaker positions, $\dot{w}_{br}(\omega)$, have been grouped respectively into two column vectors $\dot{\mathbf{w}}_c(\omega) = \lfloor \dot{w}_{c1}(\omega) \quad \cdots \quad \dot{w}_{c5}(\omega) \rfloor^T$ and $\dot{\mathbf{w}}_b(\omega) = \lfloor \dot{w}_{b1}(\omega) \quad \cdots \quad \dot{w}_{b6}(\omega) \rfloor^T$. The flexural vibration at these error and base positions can be expressed by mobility matrix expressions in terms of the complex primary force, $f_p(\omega)$, and the column vectors $\mathbf{f}_c(\omega) = \lfloor f_{c1}(\omega) \quad \cdots \quad f_{c5}(\omega) \rfloor^T$ and $\mathbf{f}_b(\omega) = \lfloor f_{b1}(\omega) \quad \cdots \quad f_{b6}(\omega) \rfloor^T$ with the complex secondary excitations generated by the proof mass actuators, $f_{cs}(\omega)$, and the complex excitations generated by the inertia effects of the case and base masses of the actuators and primary shaker, $f_{bs}(\omega)$; so that:

$$\dot{\mathbf{w}}_c = \mathbf{Y}_{cc}\mathbf{f}_c + \mathbf{Y}_{cb}\mathbf{f}_b + \mathbf{Y}_{cp}f_p, \tag{6.1}$$

$$\dot{\mathbf{w}}_b = \mathbf{Y}_{bc}\mathbf{f}_c + \mathbf{Y}_{bb}\mathbf{f}_b + \mathbf{Y}_{bp}f_p. \tag{6.2}$$

The elements in the various mobility matrices have been derived with the following modal expansions:

$$Y^{r,s}(\omega) = j\omega \sum_{n=1}^{N} \frac{\phi_n(x_r,y_r)\phi_n(x_s,y_s)}{M_p\left[\omega_n^2(1+j\eta)-\omega^2\right]}. \tag{6.3}$$

In this equation $M_p = \rho h l_x l_y$ is the mass of the plate, ρ is the density of the material of the plate, l_x, l_y and h are respectively the dimensions and the thickness of the plate and η is the loss factor. Also, ω_n and $\phi_n(x,y)$ are respectively the n-th natural frequency and n-th natural mode of the plate, which have been taken from reference [44-46] for a clamped panel.

Considering the lumped models of the actuators shown in Figure 6.2, the velocities of the actuator proof masses, M_{ai}, and the forces generated by the base masses, M_{bi}, can also be expressed in terms of the following mobility and impedance matrix relations:

$$\dot{\mathbf{w}}_m = \mathbf{Y}_{mm}\mathbf{f}_m, \tag{6.4}$$

$$\mathbf{f}_b = -\mathbf{Z}_b\dot{\mathbf{w}}_b \tag{6.5}$$

where $\dot{\mathbf{w}}_m(\omega) = \lfloor \dot{w}_{m1}(\omega) \quad \cdots \quad \dot{w}_{m5}(\omega)\rfloor^T$ and $\mathbf{f}_m(\omega) = \lfloor f_{m1}(\omega) \quad \cdots \quad f_{m5}(\omega)\rfloor^T$ are the vectors respectively with the complex velocities and forces acting on the proof masses of the actuators, $\mathbf{Y}_{mm}$ is a diagonal matrix with the mobilities of the actuators proof mass; $Y_{m,i}(\omega) = 1/j\omega M_{ai}$, and $\mathbf{Z}_b$ is a diagonal matrix with the impedances of the actuators base and case masses $Z_{b,i}(\omega) = j\omega M_{bi}$.

Substituting Eq. (6.5) into Eq. (6.2), the vector with the velocities of the base masses is given by:

$$\dot{\mathbf{w}}_b = \mathbf{Q}_{bc}\mathbf{f}_c + \mathbf{Q}_{bp}f_p \tag{6.6}$$

where $\mathbf{Q}_{bc} = \left(\mathbf{I} + \mathbf{Y}_{bb}\mathbf{Z}_b\right)^{-1}\mathbf{Y}_{bc}$ and $\mathbf{Q}_{bp} = \left(\mathbf{I} + \mathbf{Y}_{bb}\mathbf{Z}_b\right)^{-1}\mathbf{Y}_{bp}$ and $\mathbf{I}$ is a 6×6 identity matrix. Also, substituting this equation into Eq. (6.5), and then into Eq. (6.1), the vector with the velocities at the control positions is obtained:

$$\dot{\mathbf{w}}_c = \mathbf{Q}_{cc}\mathbf{f}_c + \mathbf{Q}_{cp}f_p \tag{6.7}$$

where $\mathbf{Q}_{cc} = \mathbf{Y}_{cc} - \mathbf{Y}_{cb}\mathbf{Z}_b\mathbf{Q}_{bc}$ and $\mathbf{Q}_{cp} = \mathbf{Y}_{cp} - \mathbf{Y}_{cb}\mathbf{Z}_b\mathbf{Q}_{bp}$. Esq. (6.7) and (6.4) can be compiled in one mobility equation:

$$\dot{\mathbf{w}} = \mathbf{Y}_c\mathbf{f} + \mathbf{Y}_p f_p \tag{6.8}$$

where:

$$\dot{\mathbf{w}} = \begin{Bmatrix} \dot{\mathbf{w}}_c \\ \dot{\mathbf{w}}_m \end{Bmatrix}, \tag{6.9}$$

$$\mathbf{Y}_c = \begin{bmatrix} \mathbf{Q}_{cc} & \mathbf{0} \\ \mathbf{0} & \mathbf{Y}_m \end{bmatrix}, \tag{6.10}$$

$$\mathbf{f} = \begin{Bmatrix} \mathbf{f}_c \\ \mathbf{f}_m \end{Bmatrix}, \tag{6.11}$$

$$\mathbf{Y}_p = \begin{Bmatrix} \mathbf{Q}_{cp} \\ \overline{\mathbf{0}} \end{Bmatrix} \tag{6.12}$$

where $\mathbf{0}$ is a 5x5 matrix of zeros and $\overline{\mathbf{0}}$ is a 5x1 vector of zeros. The vector with the forces transmitted to the plate and to the actuators proof masses can be expressed in terms of the following impedance matrix expression:

$$\mathbf{f} = -\mathbf{Z}_c\dot{\mathbf{w}} + \mathbf{\Psi}_a\,\mathbf{I}_a, \tag{6.13}$$

with

$$\mathbf{Z}_c = \begin{bmatrix} \mathbf{Z}_{kc} & -\mathbf{Z}_{kc} \\ -\mathbf{Z}_{kc} & \mathbf{Z}_{kc} \end{bmatrix}, \tag{6.14}$$

$$\mathbf{\Psi}_a = \begin{bmatrix} +\mathbf{\Psi}_{fa} \\ -\mathbf{\Psi}_{fa} \end{bmatrix} \tag{6.15}$$

where the elements in the diagonal matrix $\mathbf{Z}_{kc}$ are given by the impedance of the spring–damper mounting system, $Z_{kc,i}(\omega) = K_{a,i}/j\omega + C_{a,i}$, and the elements in the diagonal matrix $\mathbf{\Psi}_{fa}$ are given by the voice coil coefficients of the actuators, $\Psi_{fa,i} = \psi_i$. The column vector $\mathbf{I}_a(\omega) = \lfloor i_{a1}(\omega) \quad \cdots \quad i_{a5}(\omega) \rfloor^T$ contains the current control signals driving the five proof mass actuators. At this point, substituting Equation (6.13) into Equation (6.8) the vector with the velocities both at the base and proof mass positions of each actuator is found:

$$\dot{\mathbf{w}} = \mathbf{T}_a \mathbf{I}_a + \mathbf{T}_p f_p \tag{6.16}$$

where the matrices $\mathbf{T}_a$ and $\mathbf{T}_p$ are given by $\mathbf{T}_a = \left(\mathbf{I} + \mathbf{Y}_c \mathbf{Z}_c\right)^{-1} \mathbf{Y}_c \mathbf{\Psi}_a$ and $\mathbf{T}_p = \left(\mathbf{I} + \mathbf{Y}_c \mathbf{Z}_c\right)^{-1} \mathbf{Y}_p$. The velocities at the five control positions can be extracted from Equation (6.16) simply by pre multiplying it by $\mathbf{U} = \begin{bmatrix} \mathbf{I} & \mathbf{0} \end{bmatrix}$, where $\mathbf{I}$ is a 5×5 identity matrix and $\mathbf{0}$ is a 5×5 matrix of zeros, that is:

$$\dot{\mathbf{w}}_c = \mathbf{G}_{ca} \mathbf{I}_a + \mathbf{G}_{cp} f_p \tag{6.17}$$

where $\mathbf{G}_{ca} = \mathbf{U}\mathbf{T}_{ca}$ and $\mathbf{G}_{cp} = \mathbf{U}\mathbf{T}_{cp}$.

When the five feedback control loops are closed independently with the same constant feedback gains, the control current signals are given by:

$$\mathbf{I}_a = -\mathbf{H}\dot{\mathbf{w}}_c \tag{6.18}$$

where $\mathbf{H}$ is a diagonal matrix with the five control gains; $g_1, \ldots, g_5$.
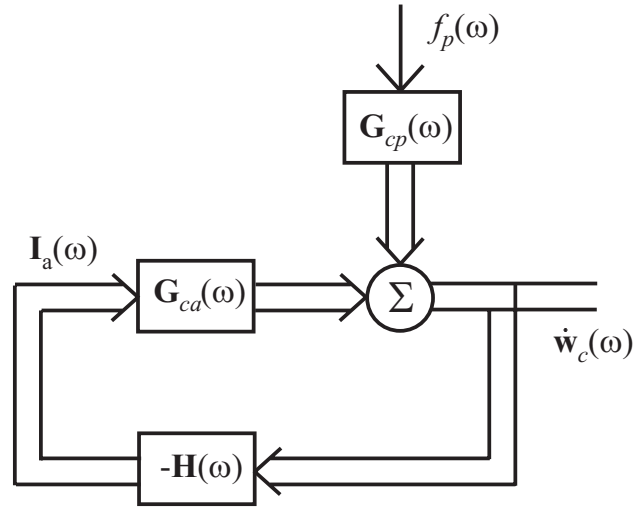
Figure 6.3: *Block diagram of the multichanel feedback control system implemented on the plate.*

The response when the five decentralised feedback control loops are closed can be described with the MIMO rejection feedback block diagram shown in Figure 6.3 so that:

$$\dot{\mathbf{w}}_c = \left(\mathbf{I} + \mathbf{G}_{ca}\mathbf{H}\right)^{-1}\mathbf{G}_{cp}f_p .$$
(6.19)

Thus, substituting Equation (6.19) into Equation (6.18) and then Equation (6.18) into Equation (6.16) the vector with the velocities both at the base and proof mass positions of each actuator can be found. This vector can then be substituted into Equation (6.13) to get the vector with the forces at the base and proof mass positions of each actuator so that the vector with the forces at the five control positions can be expressed as follows:

$$\mathbf{f}_c = -\mathbf{F}_{cp}f_p$$
(6.20)

where $\mathbf{F}_{cp} = \mathbf{U}\left[\left(\mathbf{\Psi}_a - \mathbf{Z}_c\mathbf{T}_a\right)\mathbf{H}\left(\mathbf{I} + \mathbf{G}_{ca}\mathbf{H}\right)^{-1}\mathbf{G}_{cp} + \mathbf{Z}_c\mathbf{T}_p\right]$. Also, the vector with the forces generated by the inertia effects of the case and base masses of the actuators and by the inertia effect of the force gauge and moving parts of the primary shaker is obtained by substituting Equation (6.20) into Equation (6.6) and then Equation (6.6) into Equation (6.5)

$$\mathbf{f}_b = \mathbf{F}_{bp}f_p$$
(6.21)

where $\mathbf{F}_{bp} = \mathbf{Z}_b\left(\mathbf{Q}_{bc}\mathbf{F}_{cp} - \mathbf{Q}_{bp}\right)f_p .$

The overall vibration of the plate can be assessed in terms of its total kinetic energy which, for the plate considered in this chapter, is given by the following formula [7]:

$$T(\omega) = \frac{1}{2} \int_A \rho h \left| \dot{w}(x,y,\omega) \right|^2 dA \tag{6.22}$$

where $\dot{w}(x,y,\omega)$ is the transverse velocity over the plate surface. The flexural vibration on a generic point of the panel due to the primary force, f_p, and the vectors with the control and base excitations, $\mathbf{f}_c$ and $\mathbf{f}_b$, generated by the proof mass actuators can be expressed with the following matrix relation:

$$\dot{w}(x,y) = \boldsymbol{\phi} \mathbf{A}_c \mathbf{f}_c + \boldsymbol{\phi} \mathbf{A}_b \mathbf{f}_b + \boldsymbol{\phi} \mathbf{a}_p f_p \tag{6.23}$$

where $\boldsymbol{\phi} = \lfloor \phi_1(x,y) \quad \cdots \quad \phi_R(x,y) \rfloor$ is a row vector with the amplitudes of the modes at the generic point (x,y), $\mathbf{A}_c$ and $\mathbf{A}_b$ are the matrices with the complex modal excitations functions generated by the control and base forces respectively:

$$\mathbf{A}_{c_{r,s}} = \frac{\phi_r(x_{cs}, y_{cs})}{\Lambda \left[\omega_r^2(1 + j\eta) - \omega^2 \right]}, \tag{6.24}$$

$$\mathbf{A}_{b_{r,s}} = \frac{\phi_r(x_{bs}, y_{bs})}{\Lambda \left[\omega_r^2(1 + j\eta) - \omega^2 \right]}, \tag{6.25}$$

and $\mathbf{a}_p$ is a column vector with the complex modal excitation functions generated by the primary force excitation:

$$\mathbf{a}_{p_r} = \frac{\phi_r(x_p, y_p)}{\Lambda \left[\omega_r^2(1 + j\eta) - \omega^2 \right]}. \tag{6.26}$$

Using Equations (6.19) and (6.20) the kinetic energy of the plate is found to be:

$$T(\omega) = \frac{1}{4} M_p f_p^* \left[\mathbf{a}_p + \mathbf{A}_c \mathbf{F}_{cp} + \mathbf{A}_b \mathbf{F}_{bp} \right]^H \left[\mathbf{a}_p + \mathbf{A}_c \mathbf{F}_{cp} + \mathbf{A}_b \mathbf{F}_{bp} \right] f_p. \tag{6.27}$$

This equation can be used to derive the response of the plate for various control gains of the five decentralised feedback control loops.

6.1.2 Passive effects of the actuators

Before analysing the control performances produced by the five feedback control loops, it is interesting to consider the passive effects produced by the actuators. Paulitsch et al. [42] have shown that, for moderate levels of internal damping in the actuator, above the fundamental resonance of the actuator, the proof mass vibration goes progressively to zero, so that the mass acts as a sky hook reference. As a result, the internal damping of the actuator becomes a sort of sky hook damping effect on the panel which should damp down the response of the panel at the low frequency resonances. Also, the masses of the base disc, and coil system of each actuator are directly attached to the plate. Thus they produce a substantial mass effect which tends to reduce the response of the structure as the frequency increases. Finally, the primary shaker is attached to the plate via a force gauge which also introduces a mass effect on the plate together with the moving parts of the shaker (primarily the stinger and cylindrical former and winding of the coil).

(a) Simulation (b) Experimental
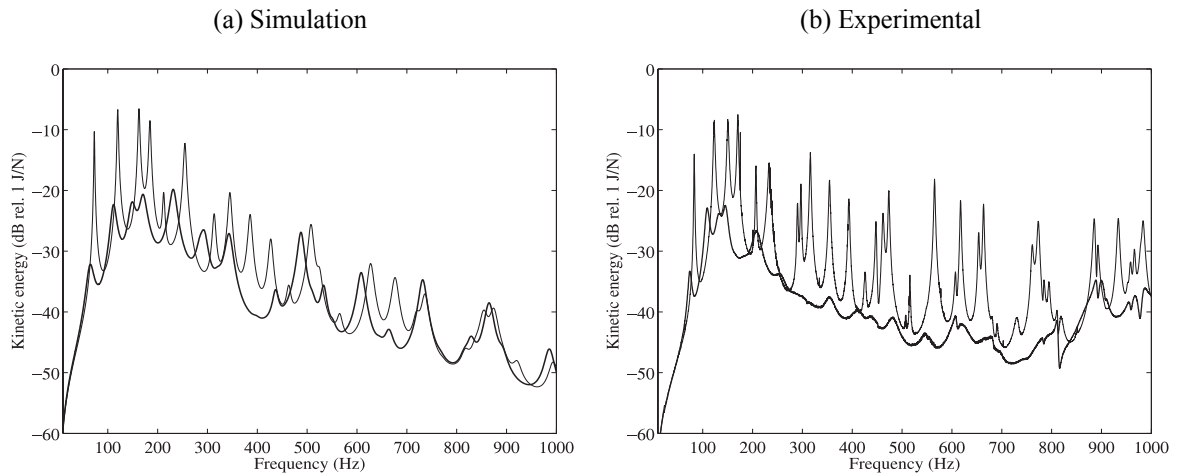
Figure 6.4: *Kinetic energy per unit primary force of the panel with no control units (faint line) and with five control units (thick line). (a) theoretical prediction; (b) experimental measurement with a scanning laser vibrometer.*

The passive effects produced by all these components can be readily analysed with the model introduced in the previous section. The plot (a) in Figure 6.4 shows the kinetic energy of the panel when there are no control units and when the five decentralised control units are mounted on the panel. The plot (b) in Figure 6.4 shows the same type of result,

where the kinetic energy has been estimated from the measured response of the smart panel built for this study over a grid of points taken with a laser vibrometer.

The result shown in the two plots of Figure 6.4 clearly illustrates the effects described above. When the five control actuators are mounted on the panel, the response tends to fall down more rapidly with frequency than in the case with no actuators because of the inertial effects of the base disc and coil system of each actuator and the inertial effect of the force gauge and moving parts of the primary shaker. Also, the resonance peaks are smoothed down by the internal damping effect of the actuators transmitted to the plate. Comparing the simulation results shown in Figure 6.4(a) and the experimental results shown in Figure 6.4(b) a good agreement is noted for both cases with and without actuators. In the case with actuators there are more discrepancies between the measured and experimental results which depend on the fact that the components of the actuators have been modelled in terms of lumped parameter elements although their size and shapes certainly have an effect on the response of the panel also at low audio frequency. Moreover, the model does not take into account the rotational inertia effects of the actuator masses which are likely to be rather important, particularly at higher audio frequencies. Nevertheless the model has certainly captured the most important features that characterise the response of the smart panel with five decentralised control units and can be used profitably to predict the response of the control system and its performances.

6.1.3 Stability of the five channel feedback control system

The control performance of the smart panel strongly depends on the stability of the five decentralised control units. Previous chapter has shown that even for the single control unit the feedback loop is only conditionally stable. The problem arises from the low frequency dynamics of the actuator, which is characterised by a resonance which introduces a 180º phase shift of the control force that is the principal cause of the instability in the feedback loop. Although the five control units implement decentralised control loops their stability has to be reassessed since, as discussed by Baumann and Elliott [52] the stability of each loop is influenced by the vibration generated by neighbouring actuators.

The stability of multiple channel feedback control loops can be analysed with the generalised Nyquist stability criterion, which states that a multichanel feedback system is

bound to be stable provided the locus of $\det[\mathbf{I} + \mathbf{G}_{ca}\mathbf{H}] = 0$ does not encircle the instability

point $(0,j0)$ as ω varies from $-\infty$ to $+\infty$ [15].
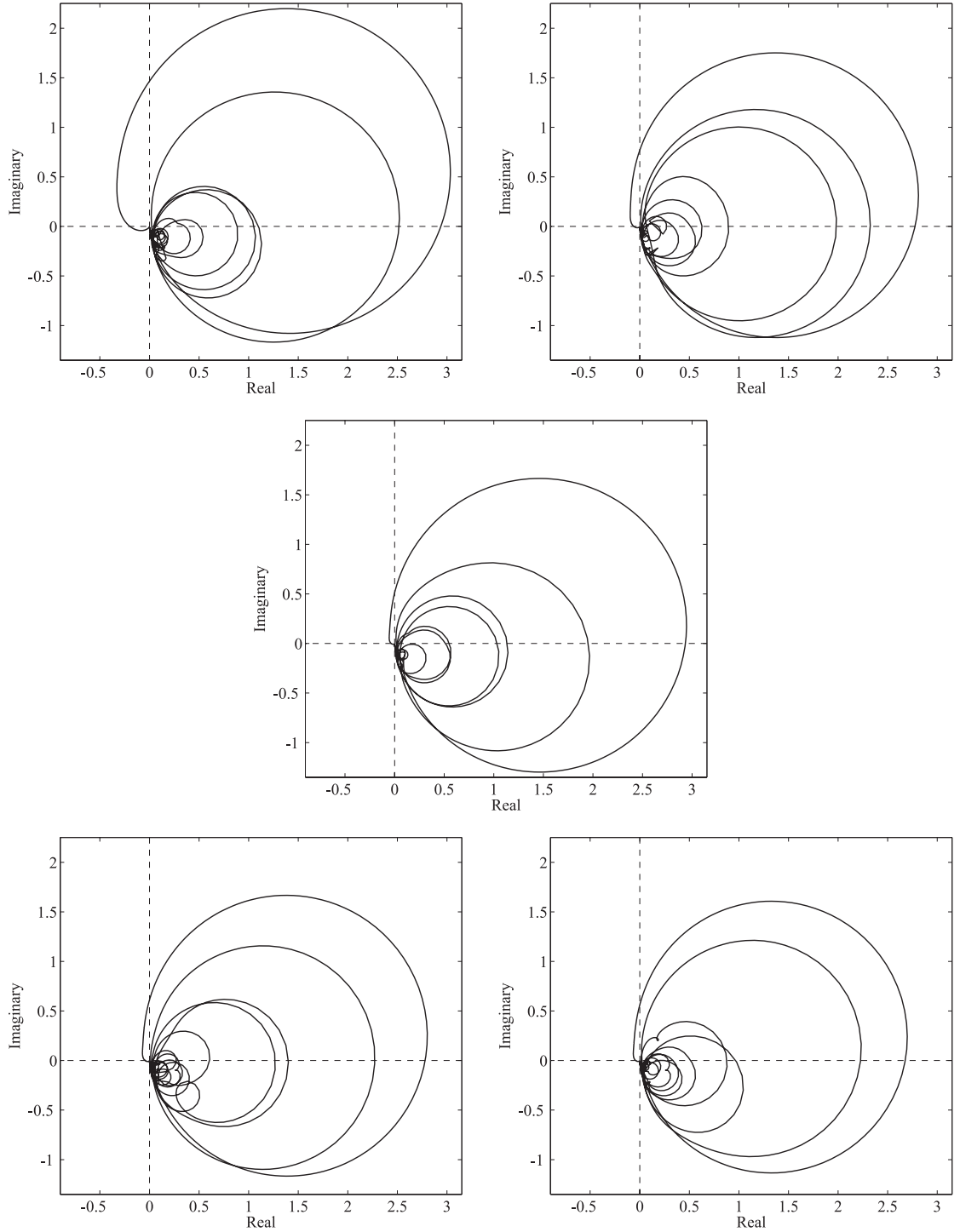
Figure 6.5: *Loci of the eigenvalues of the 5x5 matrix of sensor-actuator FRFs $G_{ca}H$ simulated between 5 Hz and 50 KHz.*

Thus, as discussed in Chapter 3, for the case of decentralised control with the same control

gains for all feedback loops, so that **H** is a diagonal matrix, the stability of the control loop

can be assessed by considering the fully populated matrix of frequency response functions (FRFs) between the five control velocities and the five input current signals to the controller driving each actuator. Moreover, the determinant of a matrix is the product of its eigenvalues [15]; that is $\det[\mathbf{I}+\mathbf{G}_{ca}\mathbf{H}] = (1+g\lambda_1)(1+g\lambda_2)\cdots(1+g\lambda_5)$, where $\lambda_i(\omega)$ is the i-th eigenvalue of $\mathbf{G}_{ca}\mathbf{H}$. Thus the stability analysis of the five channel control system can be implemented with reference to the polar plots of the five eigenvalues of $\mathbf{G}_{ca}\mathbf{H}$. In this case, in order to ensure the system is stable, the five loci should not encircle the instability point (-1, j0) as ω varies from $-\infty$ to $+\infty$.

The five plots in Figure 6.5 show the loci of the five eigenvalues of the simulated matrix of sensors-actuators FRFs $\mathbf{G}_{ca}\mathbf{H}$. They are all characterised by a low frequency loop that starts in the left hand side quadrants and then enters into the right hand side quadrants. There are then a series of smaller circles located across the real positive axis. The overall picture resulting from the analysis of the eigenvalues confirms that, the set of five decentralised feedback control loops is only conditionally stable. The stability limit is dictated by the low frequency part of the eigenvalues which is characterised by the low frequency dynamics of the actuators that produce positive, rather than negative, velocity feedback effects. As discussed by Baumann and Elliott [52], this passive feedback effect is also the principal cause of cross talking between actuators which enhances the instability problems.

6.1.4 Control performances

The performance of the five channel control system has been assessed with reference to the maximum control gain in the five control units that ensure stability as measured in the five loci in Figure 6.5, i.e. $g_{max} = 13$ dB. The plot in Figure 6.6 shows the simulated kinetic energy of the panel and five control units when there are no actuators on the panel (faint line), when there are five actuators on the panel (thick line) and when the five actuators implement the maximum control gain that guarantees stability (dotted line). This plot suggests that, the five control units can produce reductions between 3 and 10 dB at low frequencies up to 250 Hz. This result can not be considered that outstanding on its own. However if both passive and active reductions of the vibration are considered, then, comparing the kinetic energy of the panel when there are no actuators on the panel (faint line) and the kinetic energy of the panel when the five actuators are implementing feedback

loops (dotted line), it can be concluded that reductions between 10 and 20 dB or more of the low frequency resonances of the panel are generated. It is important to highlight that both the passive and active effects produced by the control units occurs at low frequencies where in fact the spectrum of the response is maximum. Thus the control effect can be interpreted as a reduction of the maximum level of the kinetic Energy spectrum from -8 dB to -27 dB, which is produced by the passive effects of the actuators (from -8 dB to -20 dB) and by the active effects of the control loops (from -20 dB to -27 dB).
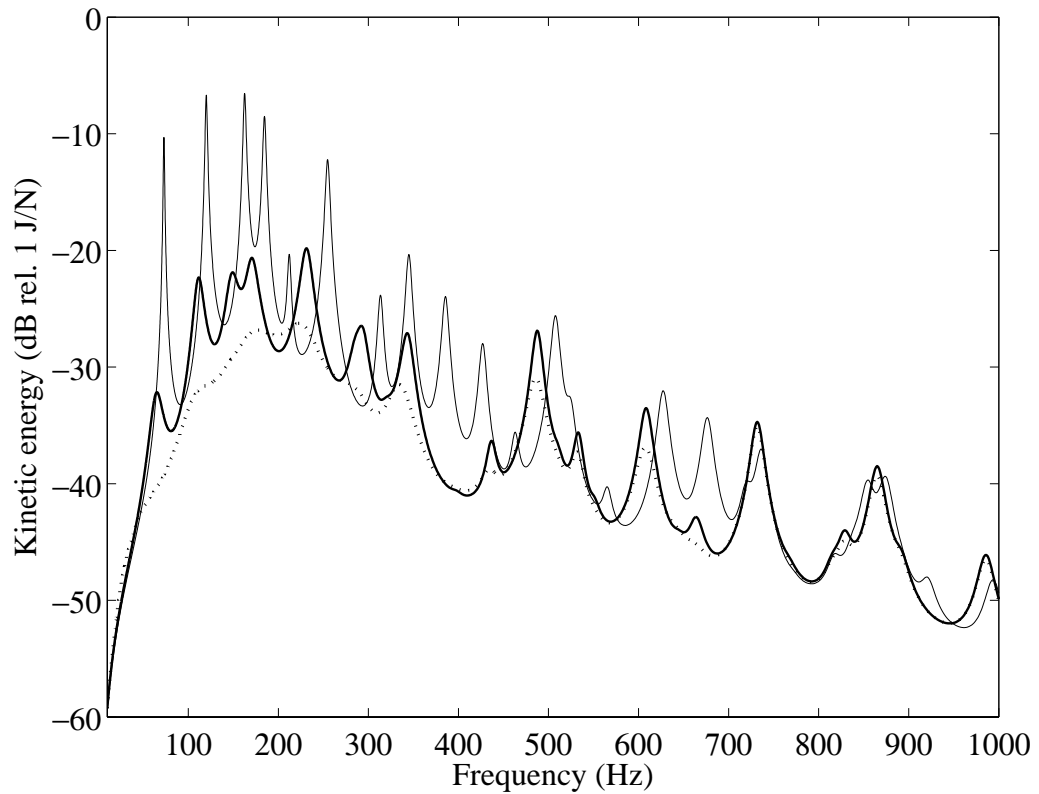
Figure 6.6: *Simulated Kinetic energy per unit primary force of the panel with no control units (faint line), with five control units when the feedback loops are left open (thick line) and when the five feedback loops are closed with the maximum control gain that guarantees stability (dotted line).*

Therefore, it can be concluded that the implementation of five decentralised velocity feedback control loops using proof mass actuators is limited by instability issues generated by the low frequency dynamics of the actuators. Also, the performance of the control system is a combination of passive and active effects. In fact there is a rather effective passive reduction of the vibration due to the internal damping of the actuator which, if it is not high enough to lock the proof mass to the housing of the actuator, it is then exerted to the plate since the proof mass acts as a sky hook reference at frequencies above the

fundamental resonance of the actuator. In addition to this passive effect, there is an active effect that further brings down the response of the panel.

These results indicate that the use of proof mass control actuators may represent a rather good control mean, particularly for low frequency disturbances which, normally, requires bulky and heavy passive treatments to be controlled. The active arrangement proposed in this chapter may provide a much more convenient approach, particularly when large numbers of small scale control units are to be used.

6.2 Prototype smart panel with five decentralised control units

Considering the theoretical analysis of the control performance of five decentralised control units, presented in the previous section of this chapter, a prototype panel has been built with five decentralised control units.
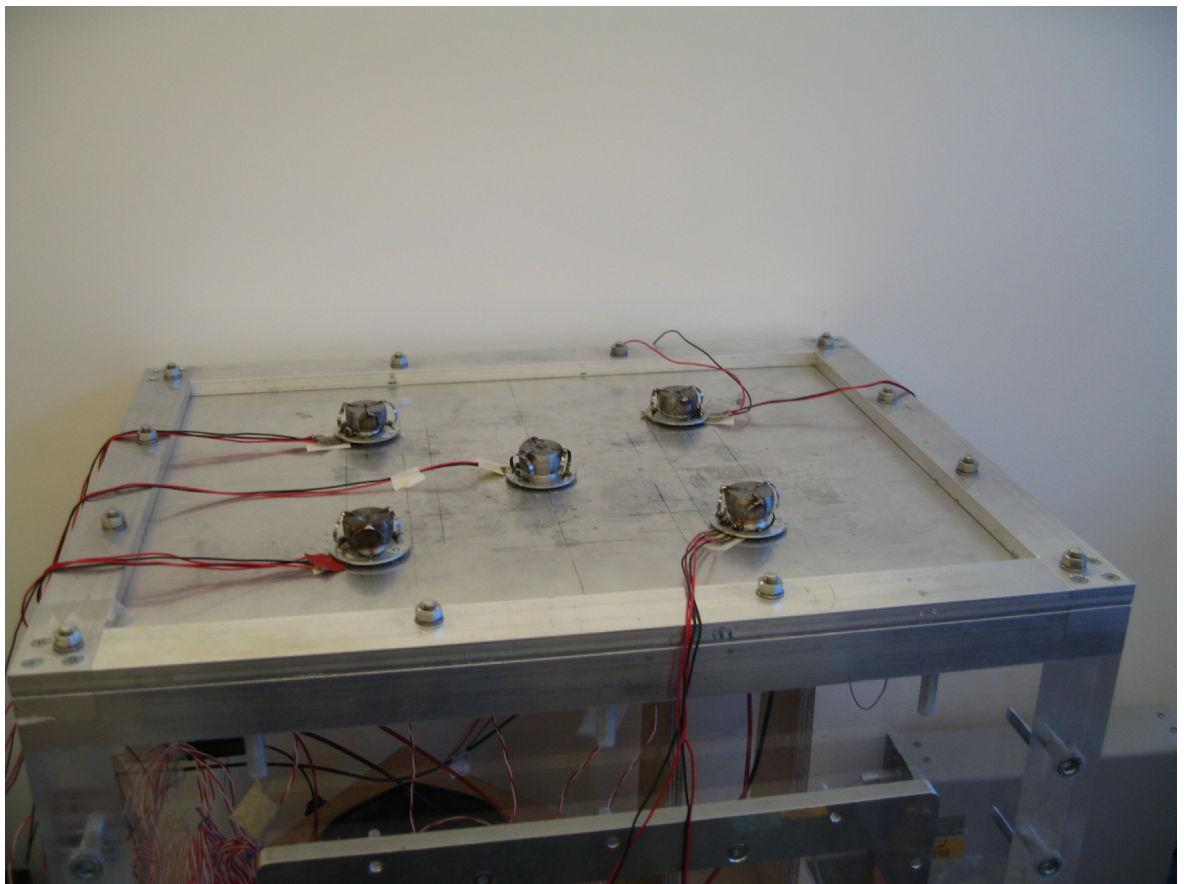
Figure 6.7: *Photograph of the box test rig and smart panel with five proof mass actuators for the implementation of decentralised velocity feedback loops.*

As shown in Figure 6.7, the panel is mounted over a rigid aluminium frame which has been fixed on the top open side of a rectangular box with thick Perspex walls. With this arrangement, the panel can be excited both acoustically, with the loudspeaker placed in the cavity, or mechanically, by the shaker which is mounted on a wooden stand located in the background right hand side corner of the box. The thick walls of the box are made of a light material so that its first resonance frequency occurs at a relatively higher frequency than the frequency range considered in the measurement. In this way, the flanking sound radiation through the side walls of the box is relatively lower than that through the top smart panel [58]. As a result it has been possible to assess the effective sound radiation by the panel with and without control.
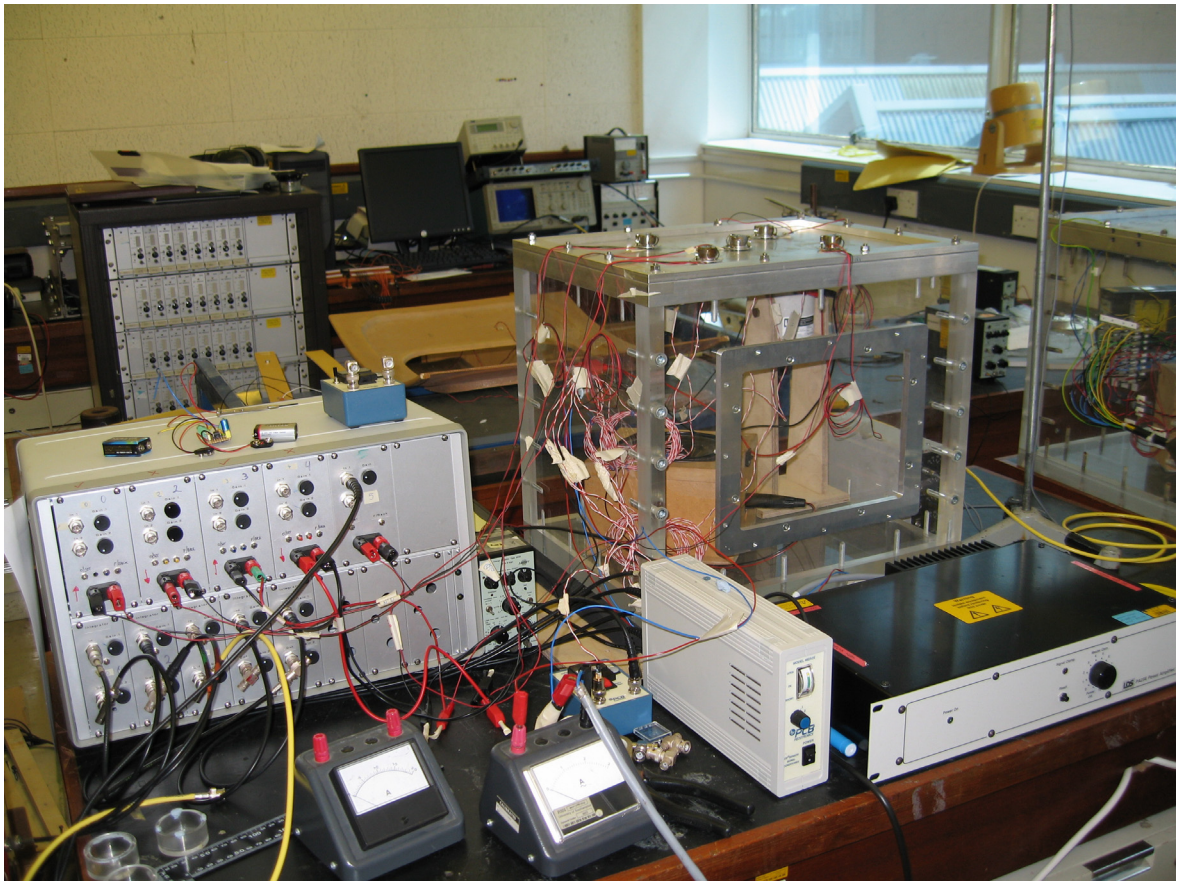
Figure 6.8: *Photograph of the complete experimental setup with the box test rig and the control equipment: signal conditioner and controller (left).*

As shown in Figure 6.7, five actuators have been built and mounted on the aluminium panel. For each actuator an accelerometer sensor has been fixed on the other side of the panel in correspondence to the axis of the actuator itself. In order to get the desired negative velocity feedback control loops for each control unit, the output signal from the accelerometer has been inverted, integrated and amplified with an analogue control system

and then fed back to the actuator. Additionally in order to reduce the DC electrical coupling a high-pass filter with a cut-off frequency of about 30Hz is used in the feedback loop.

6.3 Stability-Control performance tests

The operation of the smart panel has been tested in two stages. First the stability of the control system has been evaluated by measuring the 5×5 fully populated matrix of FRFs between the outputs of the five error sensors, passed through analogue integrators to get the velocity signals, and the five input signals to the analogue control amplifiers driving the proof mass actuators. The maximum stable gain has then been derived from the five plots with the loci of the 5×5 sensor–actuator matrix of FRFs.

Second, the implementation and performance of the five decentralised control units has been assessed by plotting the maximum reductions generated at the control positions when the maximum control gains are implemented.

6.3.1 Stability analysis

Figure 6.9 shows the loci of the eigenvalues of the 5×5 matrix of sensor–actuator FRFs measured between 5 Hz and 28 KHz. The loci are slightly irregular because they have been calculated from measured data over a particularly large frequency range. The plots show similar characteristics to those of the loci predicted from the simulated matrix of sensor–actuator open loop FRFs.

The low frequency portion of the loci are characterised by rather big loops which start in the left hand side quadrants and then drift towards the positive real right hand side quadrants. These loops appear slightly rotated in the clock wise direction. This is the result of the DC decoupling implemented in the controllers with a high pass filter with cut off frequency of about 30 Hz. As it was discussed in section 3.2.1.5, this is equivalent to their implementation of PI control. As predicted in the simulation study, there are then, a certain number of smaller loops which are approximately located across the real positive axis. According to these graphs the maximum control gain that can be implemented in the five decentralised control loops is about $g_{\max} \approx 10 \text{dB}$.
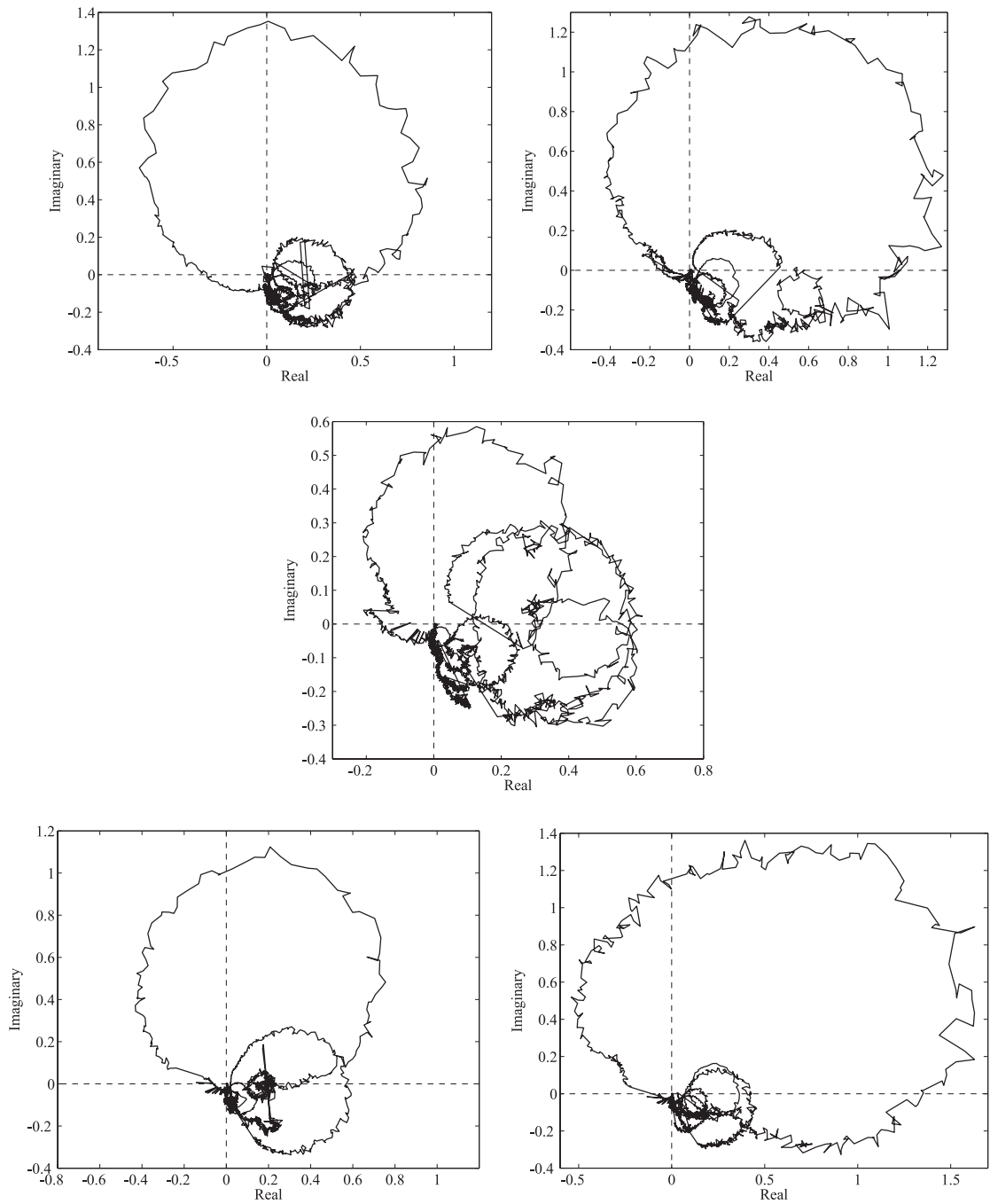
Figure 6.9: *Loci of the eigenvalues of the 5x5 matrix of sensor–actuator FRFs measured between 5 Hz and 28 KHz.*

6.3.2 Control performance

The control performance of the smart panel has been tested by implementing a moderate gain that guarantees stability and little control spillover effects at low frequency. The passive and active effects produced at the five error sensors per unit primary force excitation are plotted in Figure 6.10. As discussed in section 6.1.2, the passive damping generated by the actuators on the panel effectively smooth out the resonance peaks. Also,

the base and coil components of the actuators produce an inertial effect which further reduces the response of the panel as the frequency rises.
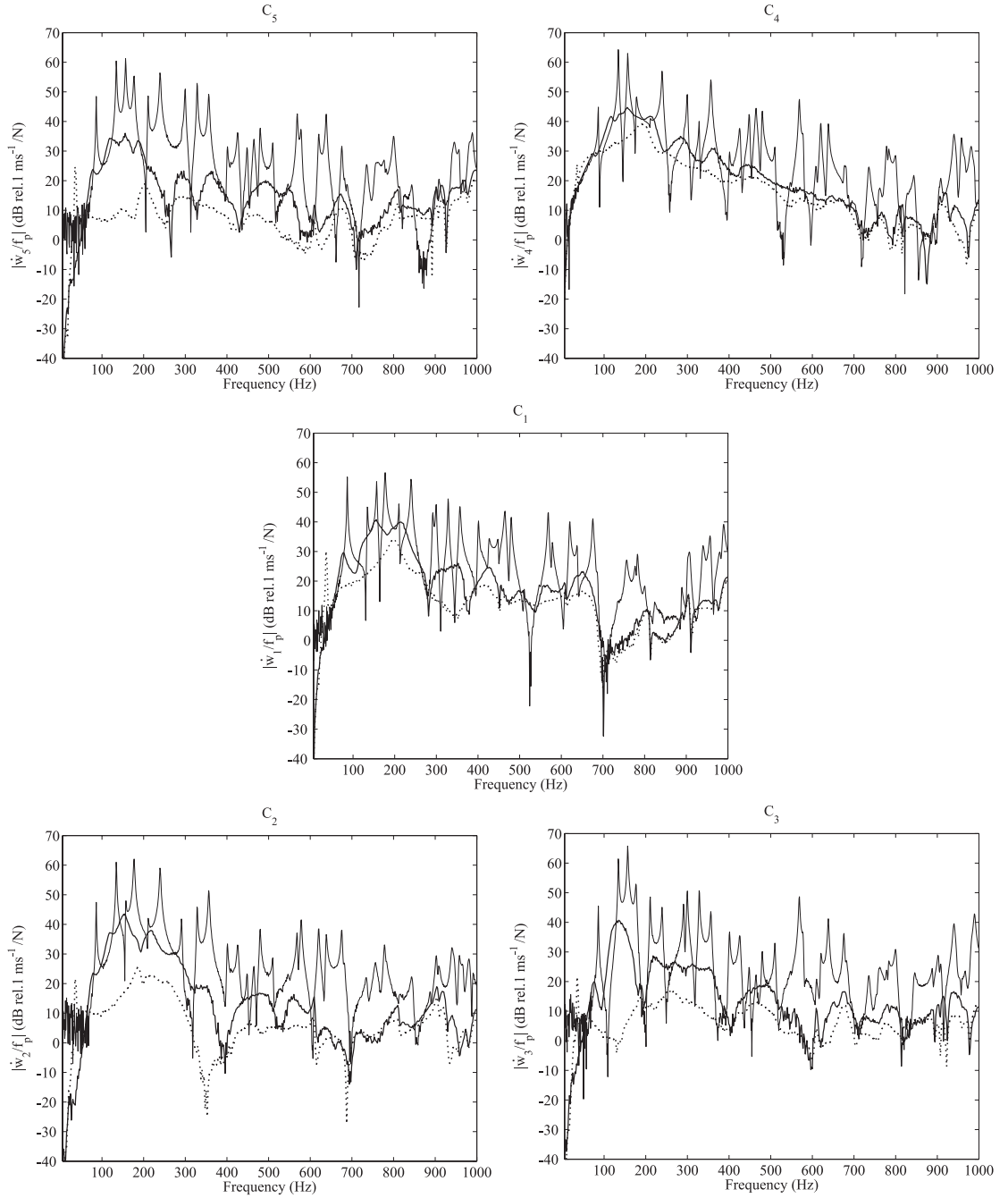
Figure 6.10: *Measured velocities at the five error sensors per unit force excitation to the plate with no actuators (faint lines), with actuators and no control (thick lines) and with actuators and implementing the maximum control gains that guarantee stability (dotted lines).*

The active control performances vary according to the location of the control units. The control unit N.4, which is closely located to the primary excitation, is the one that shows smaller vibration reductions. This is probably due to the primary excitation near field which cannot be effectively controlled by active damping. In contrast, the two control units

located further away from the primary excitation, i.e. control units N.2 and N.5, show relatively higher performances, possibly because the near field effect of the primary excitation to the panel tends to be relatively lower in those points and the active damping action efficiently reduces the steady state response at the control position.

Considering the control units N.2, N.3 and N.5 that produce the largest control effects, reductions between 20 dB and 30 dB up to 550 Hz are measured by the error sensors. In contrast the control units N.1 and N.4 produce relatively small reductions between 5 and 10 dB up to 550 Hz. It is important to note that this uneven performance result does not represent a priori a bad design of the control system. In fact it is a prerogative of this design to implement a robust control scheme that does not set the control actuators to minimise an optimal function, but instead implement active damping over the panel regardless of the positions of the actuators. Thus it is not a surprise that some control units will be more efficient than others depending on their position and the type and location of the primary excitation. Nevertheless, when a large enough number of systems is used a good control effect should be produced over the desired control frequency band.

6.4   Global control effect produced by the smart panel

The global control performance produced by the smart panel with the five decentralised control units implementing moderate feed back gains that produce little control spillover effect at the fundamental resonance frequency of the actuator has been assessed in two ways. First with the kinetic energy of the panel derived from the spatially averaged response of the panel measured with a scanning laser vibrometer (Laser Doppler Vibrometer) [8,31,41,58]. Second with the total sound power radiated derived from the measured sound pressure in nine positions around the box in an anechoic room, according to the standard procedure described by the ISO 3744 guidelines [8,31,41,58]. These measurements have been taken for two cases where the panel is excited either by the shaker force actuator, which is also located within the cavity, or the acoustic field generated in the box by a loudspeaker source.

The measurements taken with the laser vibrometer show the control performance produced by the five control units on the response of the panel. Also, they provide an indication about the near field sound radiation generated by the panel [7]. The measurement taken in

the anechoic room gives instead an indication of the far field mean sound radiation produced by the panel.

The two types of primary excitations have been chosen in such a way as to assess the control performance produced by the five control units when most of the structural modes are efficiently excited by the shaker point force excitation on the panel or only few volumetric structural modes are efficiently excited by the acoustic field in the cavity generated by the loudspeaker.

6.4.1 Kinetic energy of the panel measured with laser vibrometer

The two plots in Figure 6.11 show the narrow band spectra of the kinetic energy of the panel derived from the spatially averaged response of the panel measured with a scanning laser vibrometer. The response of the panel when there are no actuators mounted on the panel (faint line) is characterised by very lightly damped resonances in both cases where the panel is excited by the shaker or loudspeaker primary sources. As seen in Section 6.1.2, when the five control actuators are mounted on the panel, they produce a rather high passive damping and mass effects on the panel which efficiently reduces the response of the panel (thick lines). The passive effects produced by the five control units generate very high reductions of the response comprised in a range between 10 dB and 20 dB. Figure 6.11(b) shows a number of peaks, as for example those at 500 Hz, 820 Hz and 860 Hz, which are little affected by the presence of the five actuators. These resonances are not structural resonances; they are instead acoustic resonances of the cavity which are efficiently excited by the loudspeaker source placed in the cavity.

The dotted lines in the two plots of Figure 6.11 show the response of the panel in the two primary excitation cases when the five control units are used to implement decentralised velocity feedback control loops. Both plots show that the active system further reduces the response of the panel by about 3 dB to 10 dB at the low frequencies below about 250 Hz.

Figure 6.11: *Measured narrow band spectra of kinetic energy of the panel derived from the spatially averaged response of the panel measured with a scanning laser vibrometer when the panel is excited by the shaker (a) and by the loudspeaker in the cavity (b). Faint line: response of the panel with no control units; thick line: response of the panel with the five control units; dotted line: response of the panel with the five control units implementing decentralised velocity feedback control.*

Although the active control effect may look not so significant compared to the passive effect introduced by the control system, it is important to emphasise that the active control reduction of vibration occurs at low frequency where the response of the panel is relatively larger than that at mid and high audio frequencies. The passive reduction of vibration at low frequency with passive means is a challenging problem that often cannot be solved unless bulky and heavy passive treatments are applied on the structure. The combined passive and active effects produced by five control units effectively cover the whole frequency range up to 1 kHz. This is clearly shown in the third octave plots of Figure 6.12 where the significance of the additional reduction of vibration introduced by the feedback loops on top of the passive effects can be assessed by comparing the levels of the red (centre) and green (right) bars. For instance, considering the smart panel excited by the shaker, the insertion of the five control actuators brings down the maximum response of the panel from 74 to 62 dB. When the active control system is also turned on, the maximum reduction of the panel is further reduced to 58 dB. Similarly, for the system excited by the loudspeaker, the maximum response of the panel falls down from 73 dB to 58 dB when the five control units are mounted on the panel and then to 49 dB when the control units are turned on.

Figure 6.13 shows the response of the panel at the 82.97 Hz and 123.4 Hz resonance frequencies when the panel is excited by the shaker primary sources and Figure 6.14 shows the response of the panel at the 84.38 Hz and 128.9 Hz resonance frequencies when the panel is excited by the loudspeaker (note the change of scale between the top and centre bottom plots). Figures 6.12 and 6.13 show the efficacy of both passive and active effects on the panel. The passive action of the five control actuators effectively reduces the response of the panel which is controlled by the (1,1) mode at 82.97 Hz and 84.4 Hz and by the (2,1) mode at 123.4 Hz and 128.9 Hz. Then the active action of the five control units further reduces the responses in such a way as the patterns of the (1,1) and (2,1) modes are nearly completely erased so that the responses are controlled by residual modes and show a rather uniform patterns.
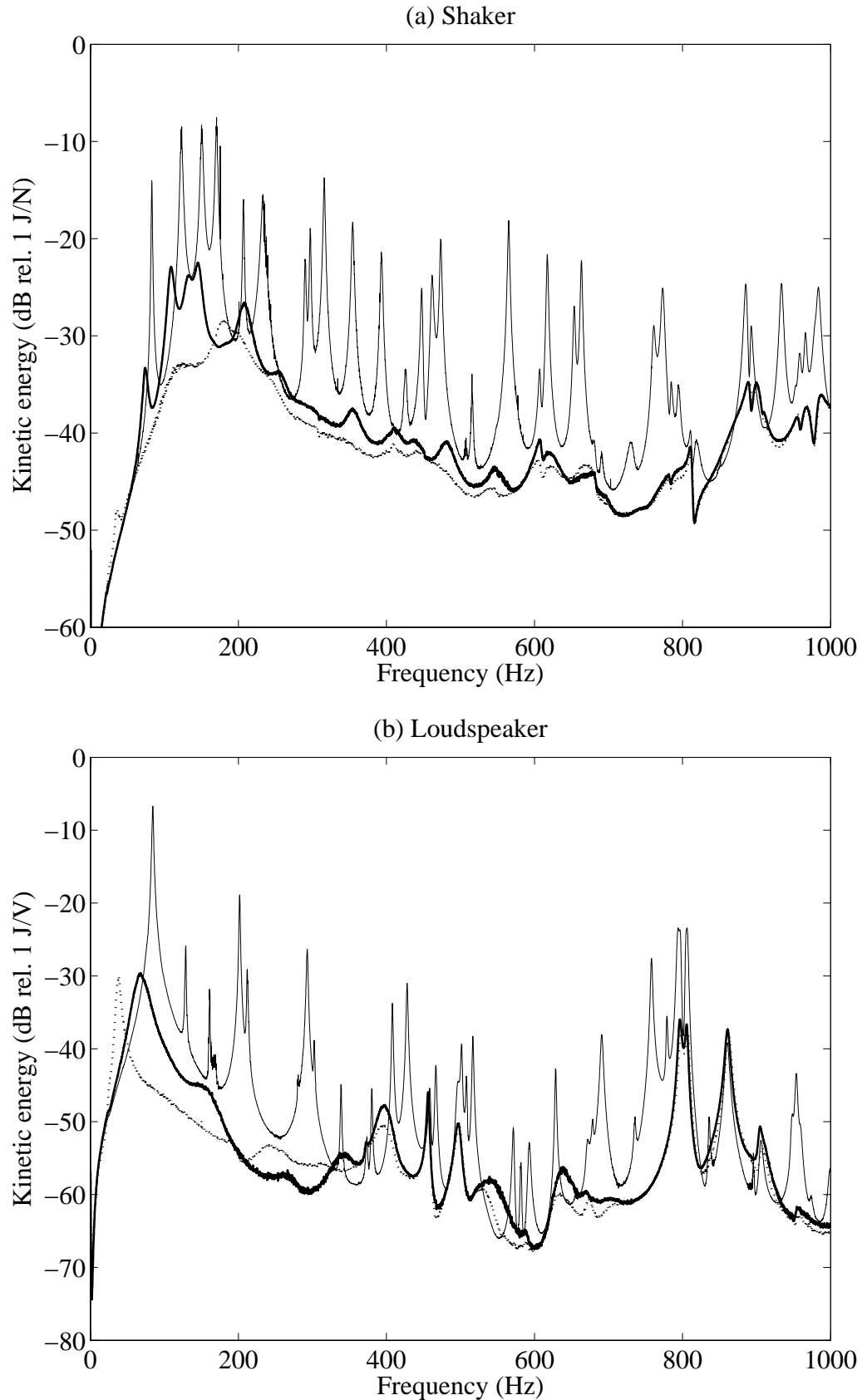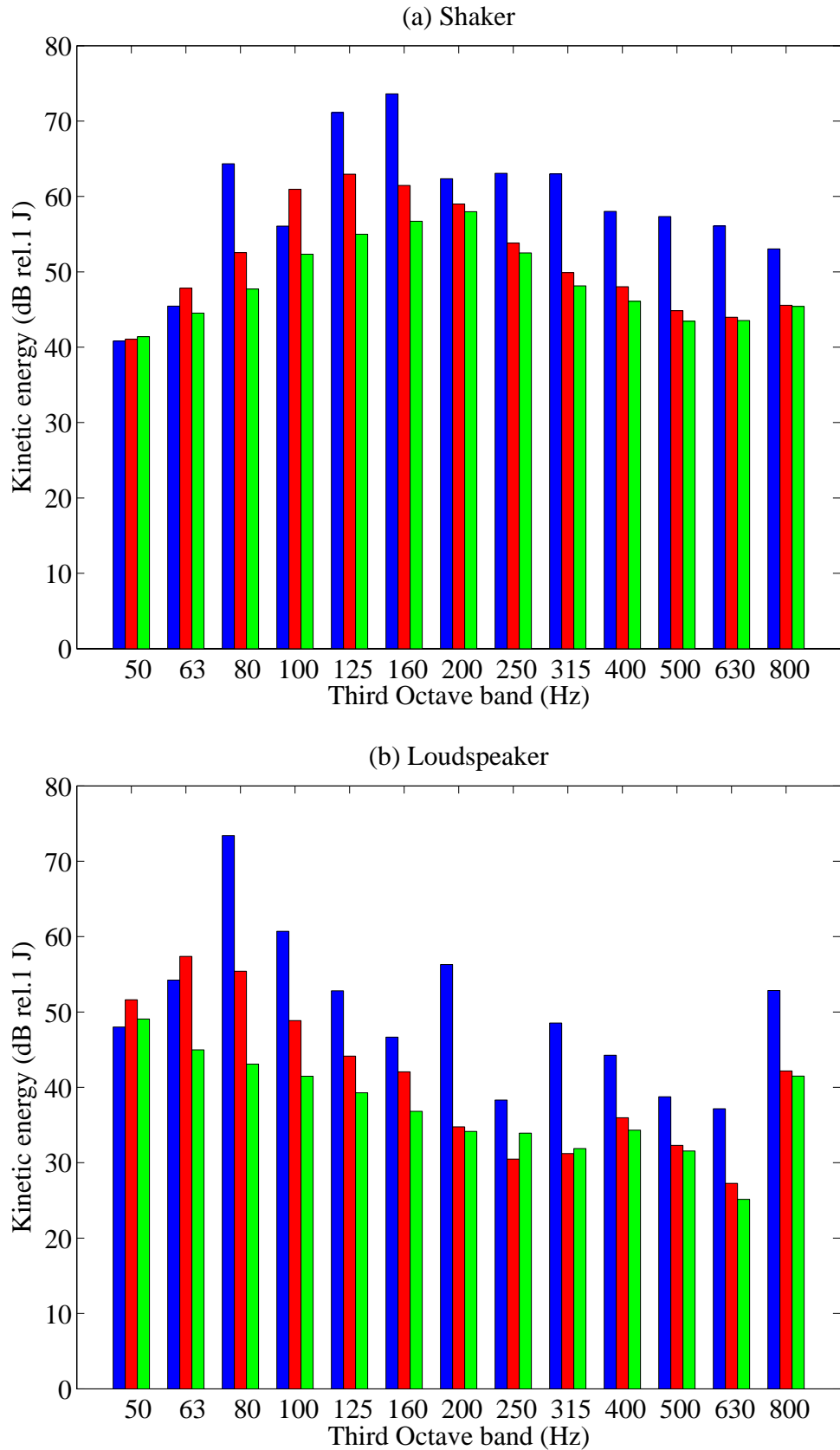
Figure 6.12: *Measured third octave band spectra of the kinetic energy of the panel derived from the spatially averaged response of the panel measured with a scanning laser vibrometer when the panel is excited by the shaker (a) and by the loudspeaker in the cavity (b). Blue (left) bar: response of the panel with no control units; red (centre) bar: response of the panel with the five control units; green (right) bar: response of the panel with the five control units implementing decentralised velocity feedback control.*

(a)

$f = 82.97$ Hz

(b)
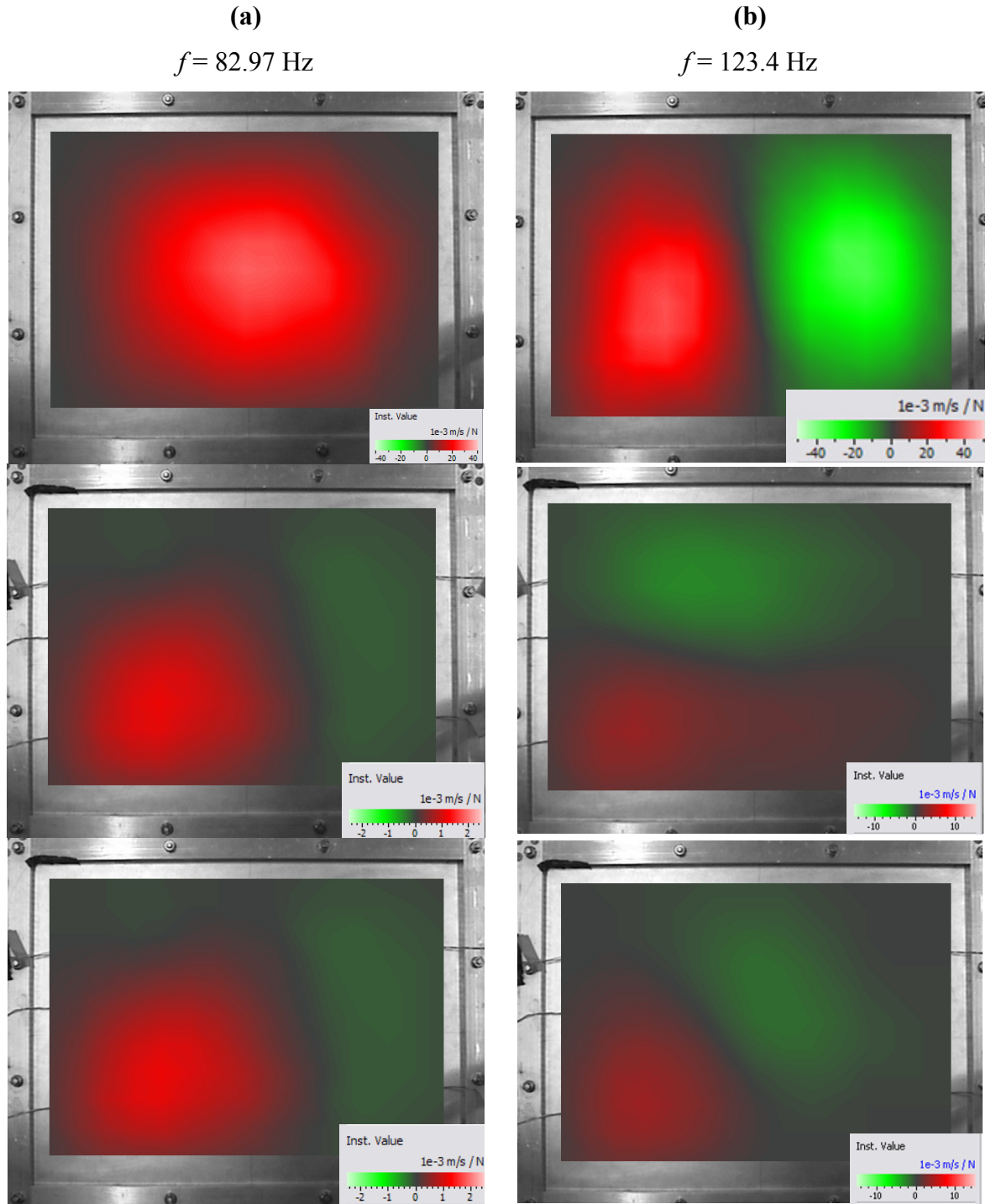
$f = 123.4$ Hz

Figure 6.13: *Response of the smart panel excited by the shaker at (a) 82.97 Hz resonance frequency, which is controlled by the (1,1) mode of the panel, and (b) at the 123.4 Hz resonance frequency, which is controlled by the (2,1) mode of the panel. Top plots response of the panels with no control actuators. Centre plots, response of the panels with the five control units. Bottom plots, response of the panels when the five units implement decentralised velocity feedback control loops.*

(a)

f = 84.4 Hz

(b)
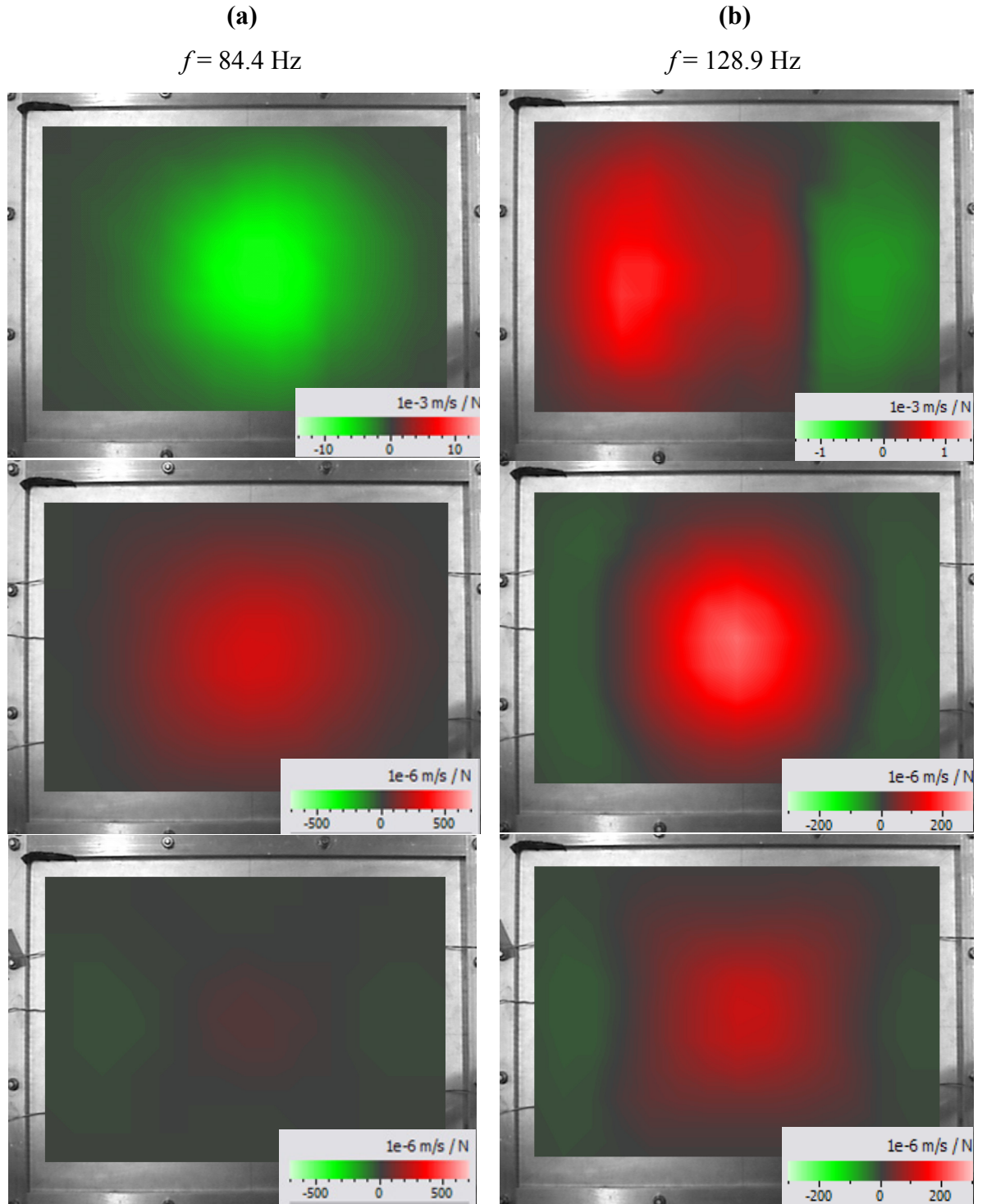
f = 128.9 Hz

Figure 6.14: *Response of the smart panel excited by the loudspeaker at the (a) 84.4 Hz resonance frequency, which is controlled by the (1,1) mode of the panel, and (b) at the 128.9 Hz resonance frequency, which is controlled by the (2,1) mode of the panel. Top plots response of the panels with no control actuators. Centre plots, response of the panels with the five control units. Bottom plots, response of the panels when the five units implement decentralised velocity feedback control loops.*

6.4.2 Total sound power radiated measured in anechoic room

The two plots in Figure 6.15 show total sound power radiated derived from the measured sound pressure in nine positions around the box in an anechoic room when the panel is excited by the shaker (a) and the loudspeaker in the cavity (b).

As found for the response of the panel, the averaged FRF by the panel without actuators (faint lines) is characterised by very lightly damped resonances in both cases where the panel is excited by the shaker or loudspeaker primary sources. In contrast to the spectrum found for the response of the panel, there are far less resonance peaks. This is due to the fact that, for frequencies below acoustic coincidence [7], the sound radiation of even resonant modes is much lower than that of odd modes. This phenomenon is even more important when the panel is excited by the acoustic field in the cavity, which efficiently couples only with a selected set of modes of the panel. When the five actuators are mounted on the panel the spectrum of the sound radiations (thick lines) is smoothed and lowered respectively by the passive damping and mass effects of the actuators. As a result of the sound radiation filtering effect and damping-mass actuators effects, the sound power radiated by the panel with the five actuators is characterised by very few heavily damped peaks at low frequencies. Also, the mean level is brought down by about 20 dB to 30 dB. It is interesting to note that the sound radiated when the panel is excited by the acoustic field in the cavity generated by the loudspeaker (Figure 6.15b), above 400 Hz there are some sharp resonances, which are due to the acoustic modes in the cavity and thus cannot be damped by the actuators.

When the five decentralised feedback control loops are implemented on the panel excited by the shaker, a reduction of the total sound power radiation between 5 dB and 20 dB is measured in the frequency range up to 400 Hz. In the second case, where the panel is excited by the acoustic field in the cavity generated by the primary loudspeaker, when the five decentralised feedback control loops are implemented, sound reductions are measured only up to 200 Hz, although a large reduction of about 16 dB is measured in correspondence to the resonance peak at 60 Hz of the (1,1) mode. This result is obtained at the expenses of a relatively large spillover effect at the fundamental resonance frequency of the five actuators. Figure 6.16 shows that the passive effect produced by the actuators extends up to 2000 Hz, particularly for the case where the panel is excited by the shaker.
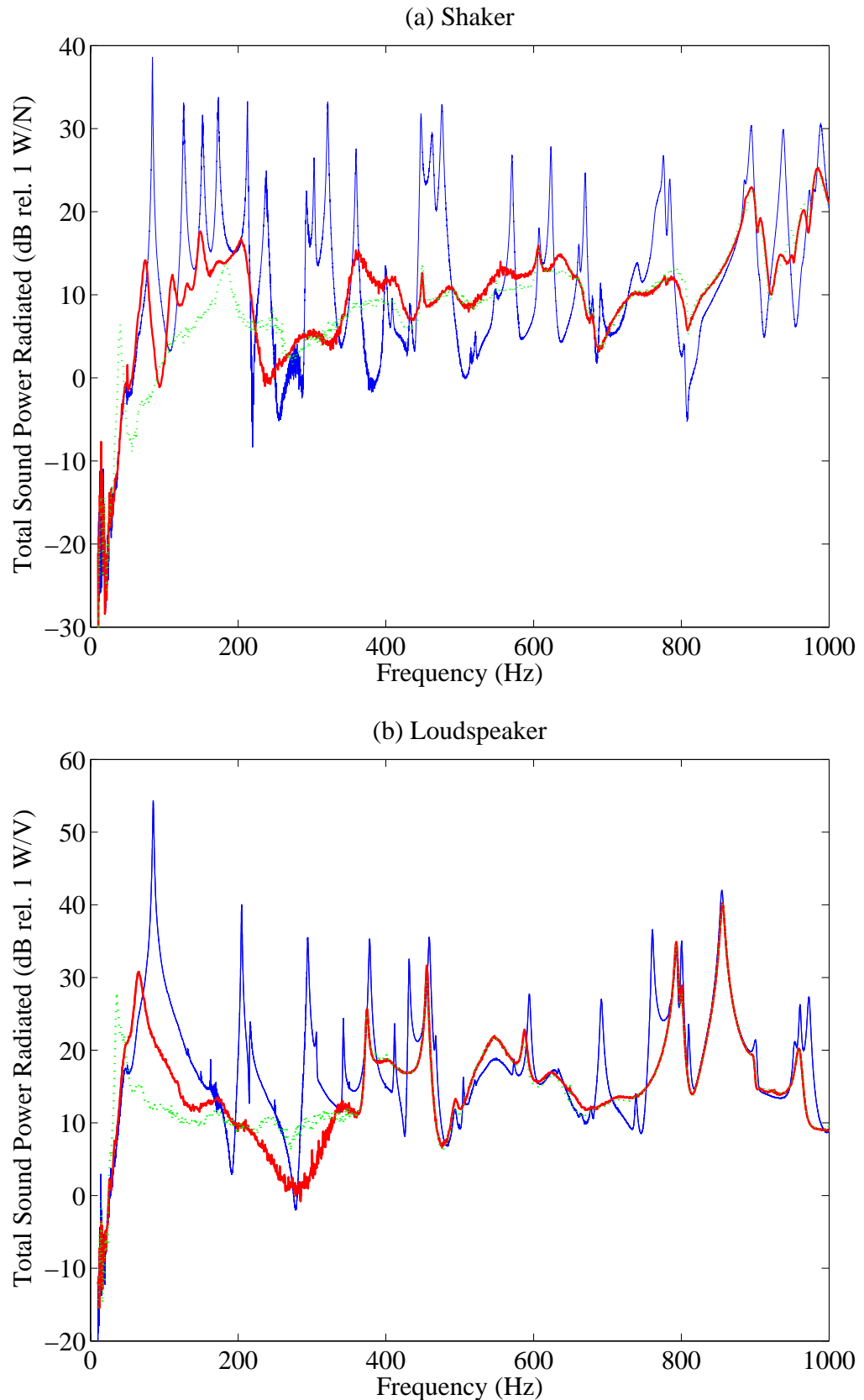
Figure 6.15: *Measured narrow band spectra of the total sound power radiated (0-1kHz) derived from the measured sound pressure in nine positions around the box in an anechoic room when the panel is excited by the shaker (a) and the loudspeaker in the cavity (b), white noise. Faint (blue) line: response of the panel with no control units; thick (red) line: response of the panel with the five control units; dotted (green) line: response of the panel with the five control units implementing decentralised velocity feedback control.*
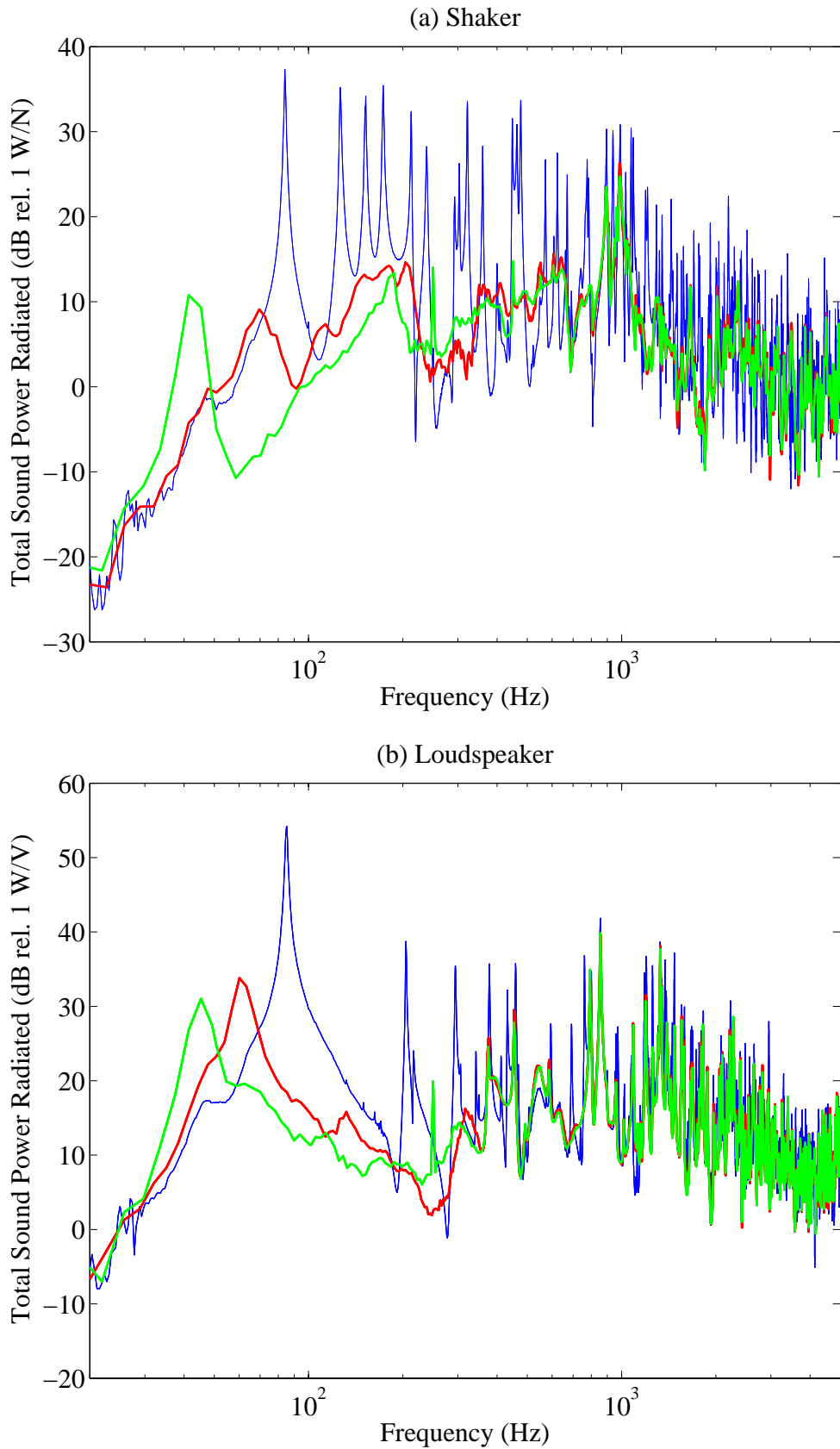
Figure 6.16: *Measured narrow band spectra of the total sound power radiated (0-5kHz) derived from the measured sound pressure in nine positions around the box in an anechoic room when the panel is excited by the shaker (a) and the loudspeaker in the cavity (b), white noise. Faint (blue) line: response of the panel with no control units; thick (red) line: response of the panel with the five control units; dotted (green) line: response of the panel with the five control units implementing decentralised velocity feedback control.*
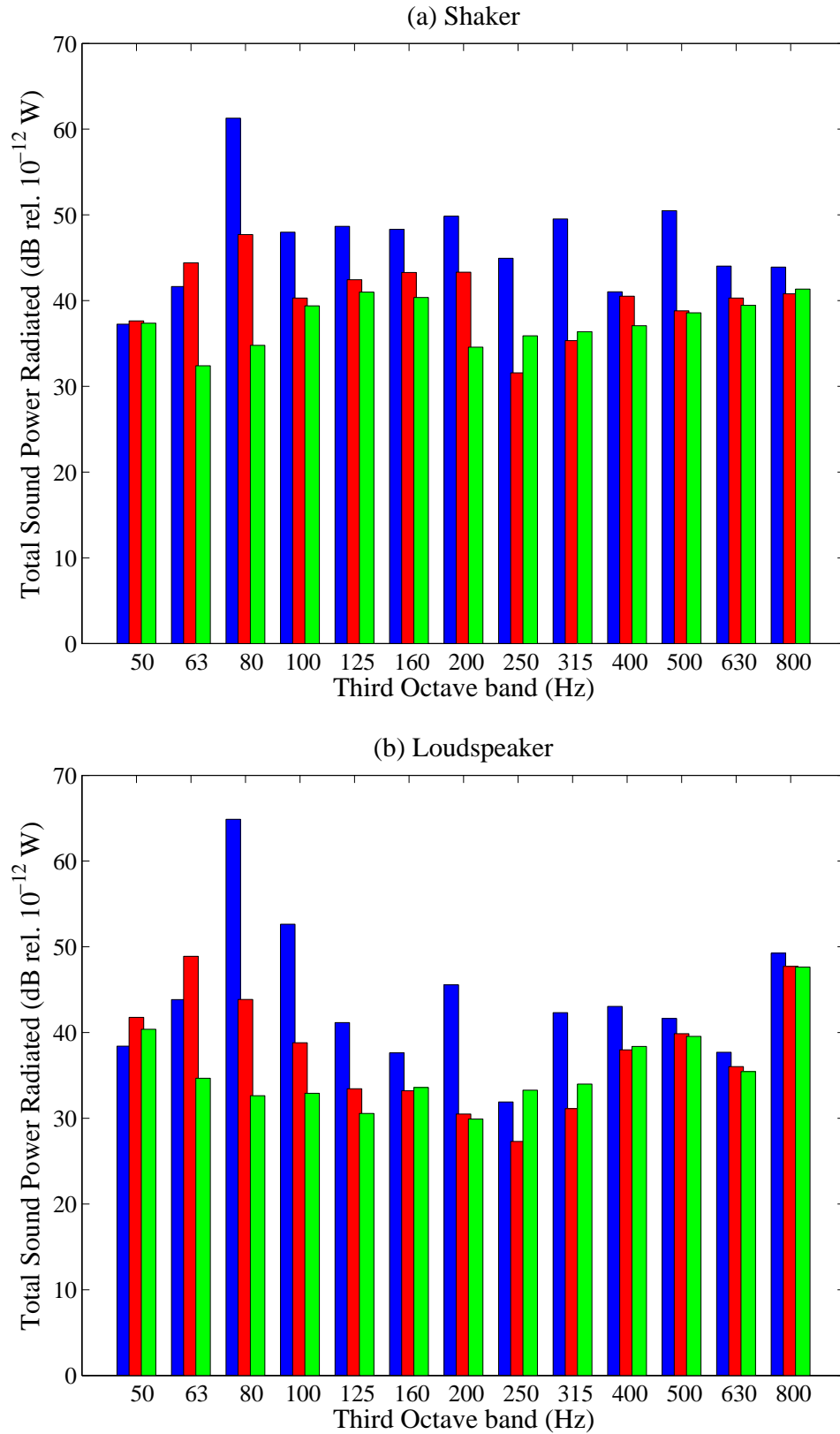
Figure 6.17: *Measured third octave band spectra total sound power radiated between 0 and 1kHz derived from the measured sound pressure in nine positions around the box in an anechoic room when the panel is excited by the shaker (a) and the loudspeaker in the cavity (b), white noise. Blue (left) bar: sound radiated by the panel with no control units; red (centre) bar: sound radiated by the panel with the five control units; green (right) bar: sound radiated by the panel with the five control units implementing decentralised velocity feedback control.*
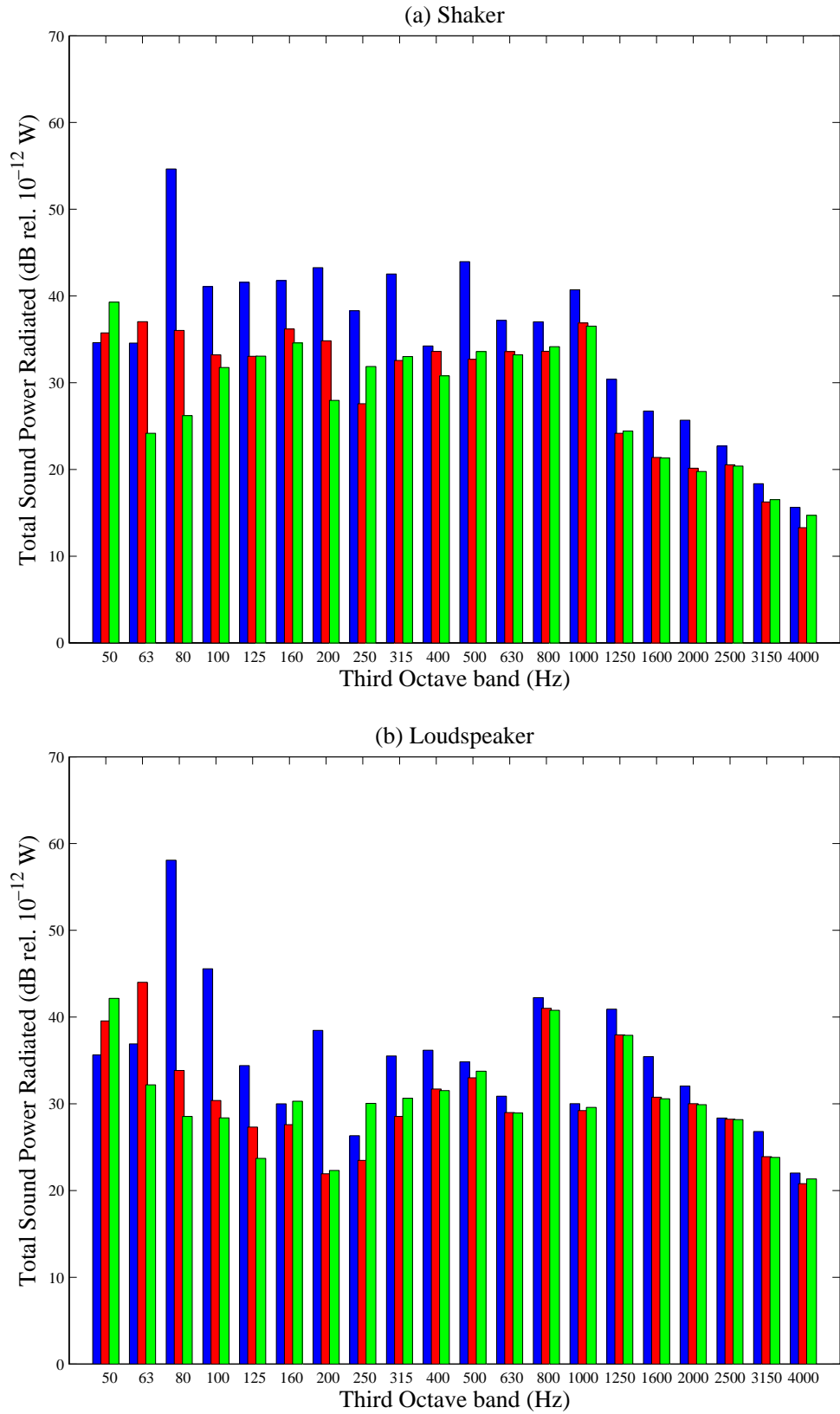
Figure 6.18: *Measured third octave band spectra total sound power radiated between 0 and 5kHz derived from the measured sound pressure in nine positions around the box in an anechoic room when the panel is excited by the shaker (a) and the loudspeaker in the cavity (b), white nose. Blue (left) bar: sound radiated by the panel with no control units; red (centre) bar: sound radiated by the panel with the five control units; green (right) bar: sound radiated by the panel with the five control units implementing decentralised velocity feedback control.*

The third octave band plots in Figure 6.17 show that the passive effects of the five proof mass actuators produce maximum reductions of the sound power radiated up to about 10 dB and 11 dB respectively for the panel excited by the shaker and acoustic field generated by the loudspeaker in the cavity. When the five control units are activated, the maximum sound radiation is further brought down by another 6 dB and 10 dB in the two primary excitation cases. This result indicates that the reduction of vibration produced by the five decentralised control units reflects a correspondent reduction of the low frequency sound radiation. As seen for the narrow frequency band sound power radiation spectral, in Figure 6.16, and Figure 6.18 show that the passive effects of the actuators extend up to about 2000 Hz.

The study presented in Chapter 4 has shown that the control effectiveness of the decentralised control unit does not decrease with scaling; thus, the reduction of vibration and sound radiation of the smart panel can be enhanced by further scaling the actuators and then arranging more control units over the surface of the panel.

6.5 Summary

This chapter has presented a study on the implementation of decentralised velocity feedback control on a panel using proof mass electrodynamic actuators. In this chapter the passive and active effects of a set of five control units have been assessed both theoretically and experimentally.

A fully coupled model of the panel with the five electrodynamic actuators has been introduced and used to single out the principal dynamic effects produced by the actuators and feedback control loops. It has been shown that the five actuators produce passive damping and mass effects, which effectively reduce the lightly damped response of the panel by 10 to 20 dB at resonance frequencies. Also, it has been shown that the stability of the five decentralised control units is affected by "cross talking" effects between the proof mass actuators. As a result the maximum control gain that guarantees stability has been predicted to be $g_{max} = 10 \, dB$. When the five control loops implement such a maximum gain, the response of the panel is further reduced by 3 to 10 dB at low frequencies below 250 Hz.

The experimental study has been carried out in two stages. First the stability and control performance at the error positions have been assessed. The stability analysis has confirmed the issue due to the "cross talking" between the actuators highlighted in the theoretical study. Nevertheless, the implementation of five decentralised feedback loops with a moderate feedback control gain that produce little control spillover effect at the fundamental resonance frequency of the actuator has produced reductions of vibration at the control positions between 10 and 20 dB up to 550 Hz.

In the second stage of the experimental study, the global control performance produced by the smart panel with the five decentralised control units has been assessed with reference to the kinetic energy of the panel derived from the spatially averaged response of the panel measured with a scanning laser vibrometer and the total sound power radiated derived from the measured sound pressure in nine positions around the box in an anechoic room. Also in this case, the two experiments have confirmed the theoretical predictions. The passive effects of the actuators efficiently bring down the lightly damped resonant response of the panel by 10 to 20 dB in the frequency range considered up to 1 kHz.

The implementation of the five decentralised control units further reduces the response by another 3 to 8 dB at frequencies below 250 Hz. This behaviour also reflects in the measured total sound power radiated, although in this case the spectrum of the sound radiated is characterised by fewer peaks due to the efficiently radiating modes of the panel. As a result the net reductions of the sound radiation are relatively smaller than those measured for the vibration response and they reach maximum values between 3 and 10 dB up to 250 Hz. Nevertheless, considering third octave plots, the system clearly produces an overall (due to both passive and active effects) reduction of the maximum response and maximum reduction of sound radiation of about 20 dB. When broad band noise is controlled, it is of great importance to bring down the maximum level which usually lies at low audio frequencies, where, normally, passive systems are not that effective while, in contrast, the system presented in this study shows promising results.

7   CONCLUSION

This thesis has presented a theoretical and experimental study on the implementation of decentralised feedback control on a panel in order to reduce its spatially average vibration and total sound power radiation at low audio frequencies where the response of the panel is characterised by well separated lightly damped resonances. The decentralised feedback control units are made of proof mass actuators with velocity sensors located at their footprints which implement basic feedback loops.

In Chapter 2 the implementation of basic feedback control laws has been analysed in details considering two simple vibration systems. First a single degree of freedom system with an ideal reactive control force actuator and a velocity sensor. Second a single degree of freedom system with a proof mass control force actuator and a velocity sensor. Both stability and control performance characteristics produced by Proportional, Integral, Derivative, PI, PD and PID feedback laws have been analysed. The details of this study are summarised in Section 2.9. In general the study has shown that Proportional control is effective at resonance frequency where the response is controlled by damping, Integral control is effective below resonance where the response is stiffness controlled and Derivative control is effective above resonance where the response is mass controlled. Thus, the best control result is produced by a PID controller tailored to produce the active stiffness, damping and mass effects respectively below, at and above resonance frequency.

In Chapter 3 the implementation of five decentralised feedback control loops on a smart panel using proof mass electrodynamic actuators has been presented. A mobility–impedance model has been developed which predicts the passive and active response of the panel in terms of its kinetic energy. The model considers the fully coupled electro-dynamic response of the actuator and structure in the two cases when the actuator is current and voltage driven. At first the stability and control performance of a single control unit have been analysed when Proportional, Integral, Derivative, PI, PD and PID control laws are implemented. As summarised in Section 3.4, when the structure under control is characterised by multiple resonant modes, Proportional control offers the most practical and effective approach and only minor advantages are produced by a PID controller. Finally the use of current driven actuators enables the implementation of larger control gains which produces larger vibration reductions. The study of five decentralised control loops has been limited to Proportional and PID control laws. As discussed in Section 3.4,

the stability and performance analysis has confirmed the results obtained for the single control unit.

In Chapter 4, the miniaturisation of the control units has been investigated. Previous studies have shown that, several decentralised control units should be mounted on a panel in order to obtain reasonable spatially averaged reductions of vibration. Thus, in order to develop a practical system it is important to design a small scale actuator. Normally the scaling of transducers is merely analysed with reference to the scaling of the control force they produce. In this chapter the effects produced by the scaling of the actuator have been analysed with reference to stability and control performance in the case Proportional control is implemented. Since the proposed system produces active damping, which is primarily effective at resonance frequencies of the structure under control, a compact formula has been derived which gives the reduction of vibration at the control position when the maximum feedback control gain that guarantees stability is implemented. This formula has then been used to assess the effects on control produced by scaling of the control units. As discussed in Section 4.8, the principal outcomes of this study have highlighted that scaling produces negative effects, such as the increase of the fundamental resonance of the actuator and the decrement of the transmitted control force, and also positive effects, such as the increase of the internal damping and the decrement of the static deflection. Finally, the stability–performance formula has shown that the overall effect of scaling produces a small increase of vibration reduction for the maximum stable control gain. The importance of this result is strengthen by the fact that the smaller is the control unit the larger is the number of system that can be fitted in the structure under control. It should be emphasised that this analysis has been carried out on a single control unit. In order to assess the effective result for multiple units the maximum stable gain should be derived taking into account the cross effects between all units.

Chapter 5 has presented the design of a prototype proof mass electrodynamic actuator that has been used to build the smart panel demonstrator with five decentralised feedback control units. The model developed in Chapter 4 has been adapted to include the mass of the cases of the actuators. In this way, simulation predictions and experimental measurements have been compared in the stability and control performance studies. The stability analysis has confirmed the low frequency problem introduced by the fundamental resonance of the actuator. As indicated by the theoretical study presented in Chapters 2 and 3, this problem has been mitigated by applying a low pass filter so that the control function

implements PI control. The low frequency Integral control part produces two benefits since, referring to the locus of the sensor–actuator FRF, it reduces the size of the low frequency circle and tends to rotate it in clock wise direction away from the instability Nyquist point and the spillover area. When the maximum control gain is implemented, reductions of vibration between 5 and 10 dB have been obtained at the control position in a frequency range between 80 and 250 Hz. It should be emphasised that excellent agreement has been found between the predicted and measured responses for the stability and control performance analyses.

In Chapter 6 the implementation of a smart panel demonstrator with five decentralised control units using the prototype proof mass electrodynamic actuator has been presented. Also in this case both simulation and experimental results have been considered. Once more excellent agreement has been found between the predicted and measured responses for the stability and control performance analyses. The stability analysis has shown that the cross talking effect between the control units allows the implementation of smaller control gains than the maximum ones that guarantees stability of a single control unit. The performance study has highlighted that the five control units produce passive damping and mass effects which efficiently bring down the lightly damped resonant response of the panel by 10 to 20 dB in the frequency range considered up to 1 kHz. The implementation of the five control loops further reduces the response and sound radiation by another 3 to 8 dB at frequencies below 250 Hz.

FUTURE WORK

The work carried out for this study has provided encouraging results for the practical construction of decentralised multiple channel feedback control systems using proof mass actuators. In particular it has investigated the effective outcome of scaling down the size of the control units with reference to the stability and control performance. However the results obtained in this analysis are limited to single control units. Thus for future work it is recommended to extend the scaling study to multiple control units. Bauman and Elliott [52] have considered the cross effects on stability by multiple decentralised control units. However their analysis refers to a set of control units of given dimensions and physical properties. It would be interesting to investigate how stability and then control performance as the size and physical properties of multiple control units are scaled down.
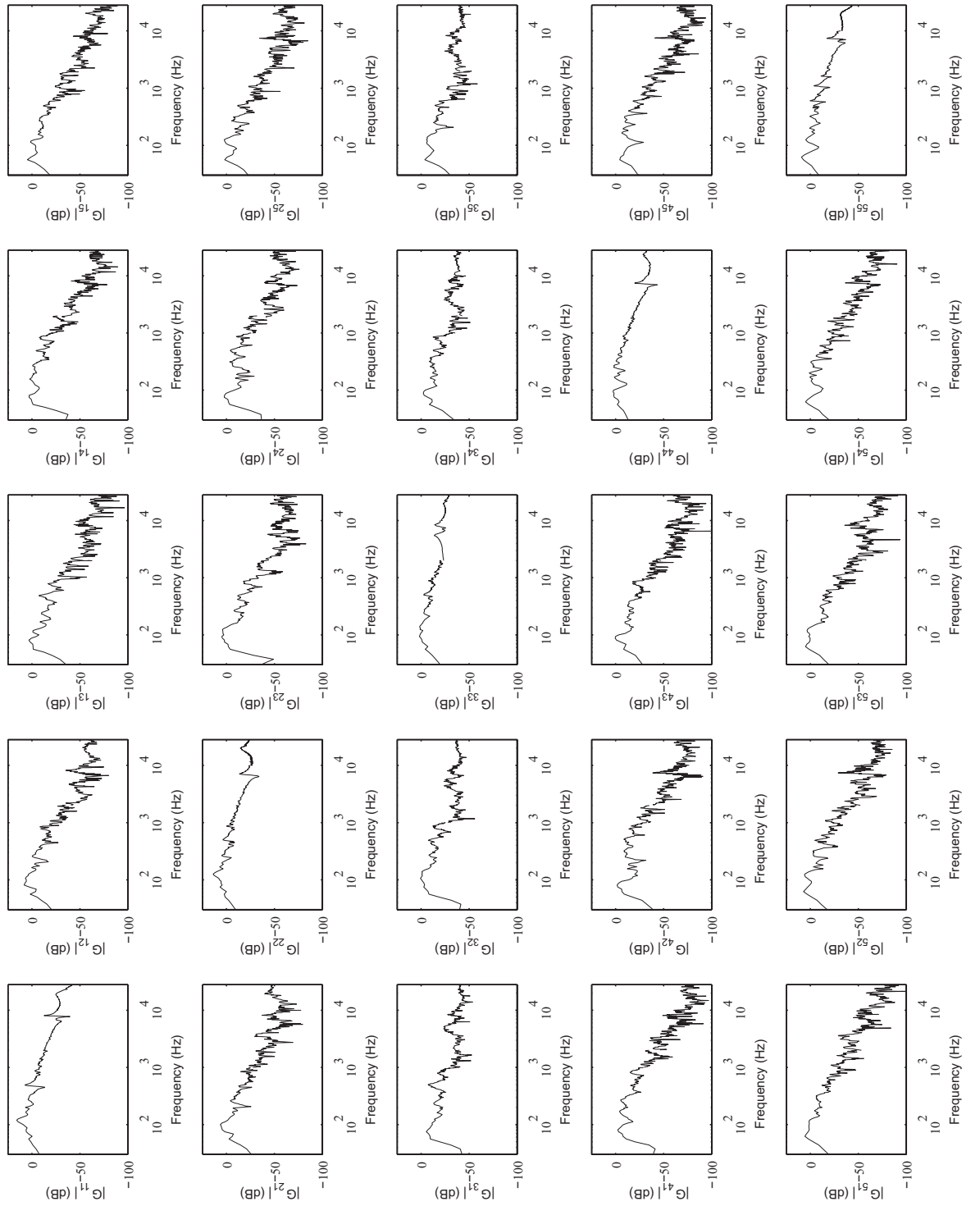
APPENDIX A

Figure A.1 *Modulus of the twenty five open loop frequency response functions between the five sensors and five actuators of the decentralised control systems.*
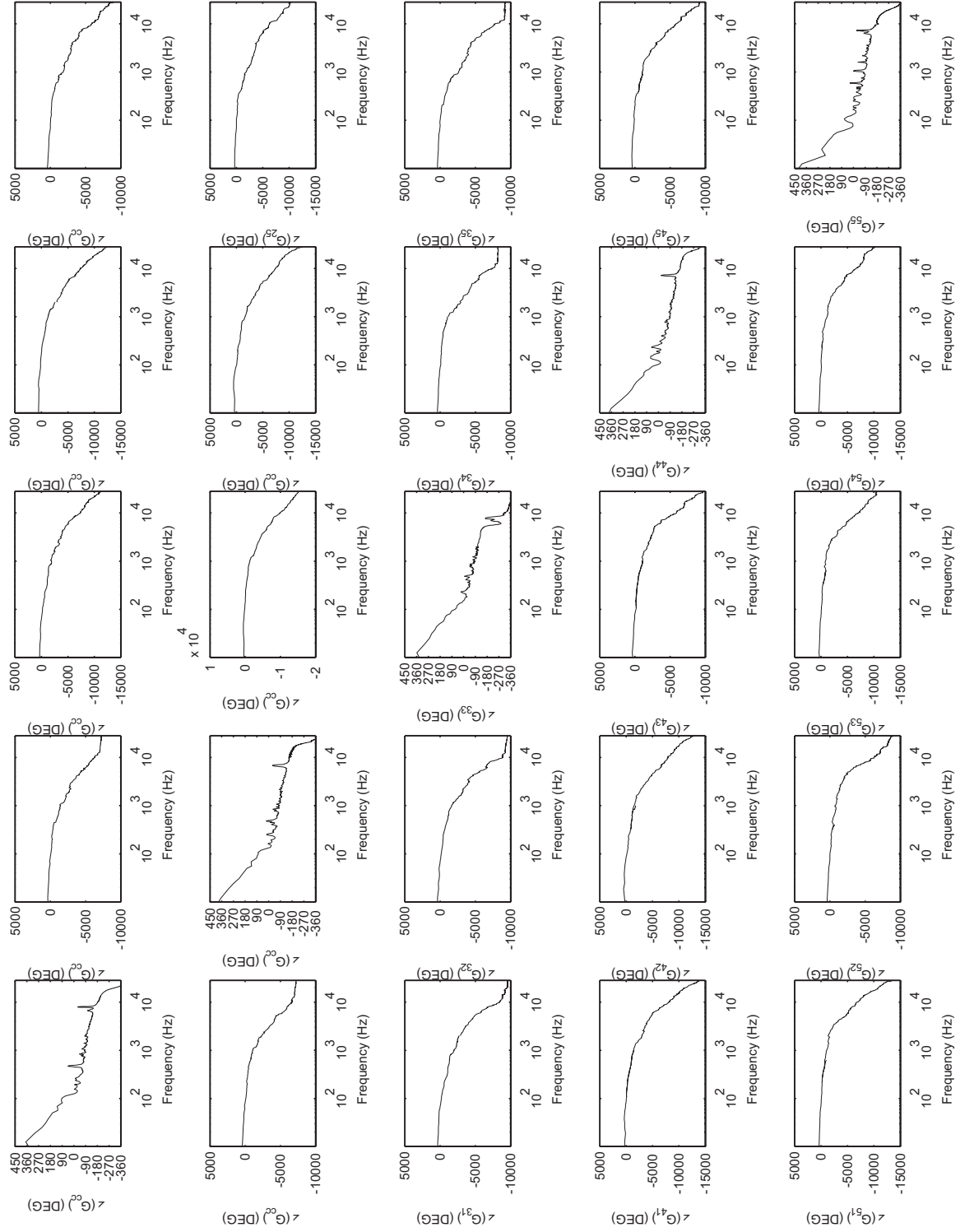
Figure A.2: *Phase of the twenty five open loop frequency response functions between the five sensors and five actuators of the decentralised control systems.*

LIST OF REFERENCES

[1] D. J. Thompson and J. Dixon, "Vehicle noise," in Frank J. Fahy and Johh G. Walker (eds.) *Advanced applications in acoustics, noise and vibration* London: E & FN Spon, 2004, pp. 236-291, Chapter 6.

[2] J. S. Mixson and J. S. Wilby, "Interior Noise," in Harvey H. Hubbard (ed.) *Aeroacoustics of Flight Vehicles, Theory and Practice* NASA Langley Research Center Hampton, Virginia, 1995, pp. 271-335, Chapter 16.

[3] P. Gardonio, *"Review of active techniques for aerospace vibro-acoustic control,"* Journal of Aircraft, vol. 39, no. 2, pp. 206-214, 2002.

[4] F. J. Fahy, "Fundamentals of noise and vibration control," in Frank J. Fahy and Johh G. Walker (eds.) *Fundamentals of noise and vibration* London: E & FN Spon, 1998, pp. 225-309, Chapter 5.

[5] M. J. Brennan and N. S. Ferguson, "Vibration Control," in Frank J. Fahy and Johh G. Walker (eds.) *Advanced applications in acoustics, noise and vibration* London: E & FN Spon, 2004, pp. 530-580, Chapter 12.

[6] L. L. Beranek, *Acoustics*, 2nd ed. New York: American Institute of Physics for the Acoustical Society of America, 1986.

[7] F. J. Fahy and P. Gardonio, *Sound and structural vibration: radiation, transmission and response*, 2nd ed. London: Academic Press, 2007.

[8] E. Bianchi, *"Smart panel with an array of decentralised control systems for active structural acoustic control."* PhD Thesis ISVR. University of Southampton., 2003.

[9] C. R. Fuller, S. J. Elliott, and P. A. Nelson, *Active Control of Vibration* New York: Academic Press, 1996.

[10] M. E. Johnson and S. J. Elliott, *"Active control of sound radiation from vibrating surfaces using arrays of discrete actuators,"* Journal of Sound and Vibration, vol. 207, no. 5, pp. 743-759, 1997.

[11] R. L. Clark, W. R. Saunders, and G. P. Gibbs, *Adaptive Structures*, 1st ed. New York: John Wiley & Sons, Inc., 1998.

[12] P. Lueg. Process of silencing sound oscillations. [2,043,416]. 1936. USA.

[13] H. F. Olsen and E. G. May, *"Electronic sound absorber,"* Journal of the Acoustical Society of America, vol. 25 pp. 1130-1136, 1953.

[14] W. B. Conover, *"Fighting noise with noise,"* Noise Control, vol. 2 pp. 78-82, 1956.

[15] S. J. Elliott, *Signal Processing for Active Control*, 1 ed. London: Academic Press, 2001.

[16] A. Roure, *"Self adaptive broadband active noise control system.,"* Journal of Sound and Vibration, vol. 101 pp. 429-441, 1985.

[17] G. B. B. Chaplin, *"Anti-sound-the Essex breakthrough.,"* Chartered Mechanical Engineer, vol. 30 pp. 41-47, 1983.

[18] P. A. Nelson and S. J. Elliott, *Active Control of Sound* New York: Academic Press, 1992.

[19] A. Preumont, *Vibration control of active structures*, 2 ed. London: Kluwer Academic, 2002.

[20] B. Petitjean and I. Legrain, *"Feedback controllers for active vibration suppression,"* Journal of Structural Control, vol. **3**, no. 1-2, pp. 111-127, 1996.

[21] S. J. Elliott, P. Gardonio, T. C. Sors, and M. J. Brennan, *"Active vibroacoustic control with multiple local feedback loops,"* The Journal of the Acoustical Society of America, vol. 111, no. 2, pp. 908-915, Feb.2002.

[22] P. Gardonio, E. Bianchi, and S. J. Elliott, *"Smart panel with multiple decentralized units for the control of sound transmission. Part I: Theoretical predictions. Part II: Design of the decentralized control units. Part III: Control system implementation,"* Journal of Sound and Vibration, vol. 274, no. 1-2, pp. 163-232, 2004.

[23] B. Petitjean, I. Legrain, F. Simon, and S. Pauzin, *"Active control experiments for acoustic radiation reduction of a sandwich panel: Feedback and feedforward investigations,"* Journal of Sound and Vibration, vol. 252, no. 1, pp. 19-36, Apr.2002.

[24] M. J. Balas, *"Direct velocity control of large space structures,"* Journal of Guidance and Control, vol. 2 pp. 252-253, 1979.

[25] J. Q. Sun, *"Some observations on physical duality and collocation of structural control sensors and actuators,"* Journal of Sound and Vibration, vol. 194 pp. 765-770, 1996.

[26] V. Jayachandran and J. Q. Sun, *"Unconditional stability domains of structural control systems using dual actuator-sensor pairs,"* Journal of Sound and Vibration, vol. 208, no. 1, pp. 159-166, Nov.1997.

[27] P. Gardonio and S. J. Elliott, *"Modal response of a beam with a sensor-actuator pair for the implementation of velocity feedback control,"* Journal of Sound and Vibration, vol. 284, no. 1-2, pp. 1-22, June2005.

[28] P. Gardonio and S. J. Elliott, *"Smart panels for active structural acoustic control,"* Smart Materials and Structures, vol. 13, no. 6, pp. 1314-1336, 2004.

[29] M. E. Johnson and S. J. Elliott, *"Active control of sound radiation using volume velocity cancellation,"* Journal of the Acoustical Society of America, vol. 98, no. 4, pp. 2174-2186, Oct.1995.

[30] P. Gardonio, Y. S. Lee, S. J. Elliott, and S. Debost, *"Analysis and measurement of a matched volume velocity sensor and uniform force actuator for active structural acoustic control,"* Journal of the Acoustical Society of America, vol. 110, no. 6, pp. 3025-3031, 2001.

[31] P. Gardonio, E. Bianchi, and S. J. Elliott, *"Smart panel with multiple decentralized units for the control of sound transmission. Part I: Theoretical predictions,"* Journal of Sound and Vibration, vol. 274, no. 1-2, pp. 163-192, 2004.

[32] S. J. Elliott and M. E. Johnson, *"Radiation modes and the active control of sound power,"* Journal of the Acoustical Society of America, vol. 94 pp. 2194-2204, 1993.

[33] M. E. Johnson and S. J. Elliott, *"Active control of sound radiation using volume velocity cancellation,"* Journal of the Acoustical Society of America, vol. 98, no. 4, pp. 2174, 1995.

[34] R. L. Clark and C. R. Fuller, *"Active structural acoustic control with adaptive structures including wavenumber considerations,"* Journal of Intelligent Material Systems and Structures, vol. 3, no. 2, pp. 298-315, 1992.

[35] R. L. Clark, R. A. Burdisso, and C. R. Fuller, *"Design approaches for shaping polyvinylidene fluoride sensors in active structural acoustic control (ASAC),"* Journal of Intelligent Material Systems and Structures, vol. 4, no. 3, pp. 354-365, July1993.

[36] S. A. Collins, D. W. Miller, and A. H. Von Flotow, *"Distributed sensors as spatial filters in active structural control,"* Journal of Sound and Vibration, vol. 173, no. 4, pp. 471-501, 1994.

[37] M. E. Johnson, *"Active control of sound transmission."* PhD Thesis ISVR. University of Southampton, 1996.

[38] S. S. Rao, "Mechanical Vibration," 3 ed. New York: Addison-Wesley Publishing Company, 1995, Chapter 10.

[39] C. K. Lee, *"Theory of laminated piezoelectric plates for the design of distributed sensors/actuators. Part I: governing equations and reciprocal relationships.,"* Journal of the Acoustical Society of America, vol. 87 pp. 1144, 1990.

[40] Y. Aoki, P. Gardonio, and S. J. Elliott. Stability of a Piezoelectric Patch-Accelerometer Active Damping Control System in Smart Panel. 2006. Euronoise 2006, Tampere, Finland.

[41] P. Gardonio, E. Bianchi, and S. J. Elliott, *"Smart panel with multiple decentralized units for the control of sound transmission. Part II: Design of the decentralized control units,"* Journal of Sound and Vibration, vol. 274, no. 1-2, pp. 193-213, July2004.

[42] C. Paulitsch, P. Gardonio, and S. J. Elliott, *"Active vibration control using an inertial actuator with internal damping,"* Journal of the Acoustical Society of America, vol. 119, no. 4, pp. 2131-2140, 2006.

[43] J. Peirs, *"Design of micromechatronic systems: scale laws, technologies, and medical applications."* PhD Thesis Katholieke Universiteit Leuven, 2001.

[44] P. Gardonio and M. J. Brennan, "Mobility and impedance methods in structural dynamics," in Frank J. Fahy and Johh Walker (eds.) *Advanced applications in acoustics, noise and vibration* London: E & FN Spon, 2004, pp. 387-388, Chapter 9.

[45] G. B. Warburton, *"The Vibration of Rectangular Plates,"* Proceedings of the Institution of Mechanical Engineers, vol. 168 pp. 371-384, 1951.

[46] P. Gardonio and S. J. Elliott, *"Driving point and transfer mobility matrices for thin plates excited in flexure."* ISVR Technical Report No.277, 1999.

[47] L. Meirovitch, *Dynamics and Control of Structures* New York: John Wiley & Sons, 1990.

[48] C. González Díaz and P. Gardonio, *"Proportional, Integral, Derivative, PID-, PI-, and PD- Velocity Feedback Control with Inertial Actuators."* ISVR Technical Memorandum No.956, 2005.

[49] S. J. Elliott, M. Serrand, and P. Gardonio, *"Feedback Stability Limits for Active Isolation Systems with Reactive and Inertial Actuators,"* Journal of Vibration and Acoustics, vol. 123, no. 2, pp. 250-261, Apr.2001.

[50] L. Benassi and S. J. Elliott, *"Active vibration isolation using an inertial actuator with local displacement feedback control,"* Journal of Sound and Vibration, vol. 278, no. 4-5, pp. 705-724, Dec.2004.

[51] S. Skogestad, *Multivariable feedback control: analysis and design* Chichester: Wiley, 1996.

[52] O. N. Baumann and S. J. Elliott, *"The stability of decentralized multichannel velocity feedback controllers using inertial actuators,"* The Journal of the Acoustical Society of America, vol. 121, no. 1, pp. 188-196, Jan.2007.

[53] P. Gardonio, *"Scaling of velocity feedback systems for vibration control,"* Journal of Smart Materials and Structures, 2007.

[54] O. N. Baumann and S. J. Elliott, *"Destabilisation of velocity feedback controllers with stroke limited inertial actuators,"* Journal of the Acoustical Society of America, 2006.

[55] W. S. N. Trimmer, *"Microrobots and micromechanical systems,"* Sensors and Actuators, vol. 19, no. 3, pp. 267-287, Sept.1989.

[56] C. Paulitsch, *"Vibration Control with electrodynamic actuators."* PhD Thesis ISVR, University of Southampton, 2005.

[57] W. C. Young and R. G. Budynas, *Roark's formulas for stress and strain*, 6th ed. New York: McGraw-Hill, 1989.

[58] E. Bianchi, P. Gardonio, and S. J. Elliott, *"Smart panel with multiple decentralized units for the control of sound transmission. Part III: Control system implementation,"* Journal of Sound and Vibration, vol. 274, no. 1-2, pp. 215-232, July2004.